ILMATIETEEN LAITOS
METEOROLOGISKA INSTITUTET
FINNISH METEOROLOGICAL INSTITUTE

144
CONTRIBUTIONS

EFFECT OF SNOW MICROSTRUCTURE AND SUBNIVEAN WATER BODIES ON MICROWAVE RADIOMETRY OF SEASONAL SNOW

ANNA KONTU

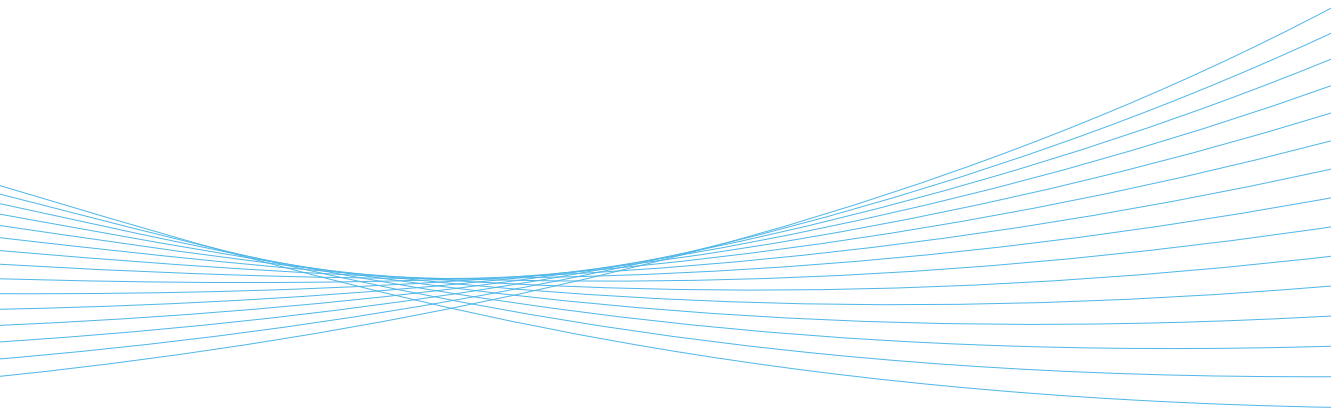

Effect of snow microstructure and subnivean water bodies on microwave radiometry of seasonal snow

Anna Kontu

A doctoral dissertation completed for the degree of Doctor of Science (Technology) to be defended, with the permission of the Aalto University School of Electrical Engineering, at a public examination held at the lecture hall AS2 of the school on 8 May 2018 at 12.

This doctoral thesis is conducted in collaboration with Aalto University and Finnish Meteorological Institute.

Aalto University
School of Electrical Engineering
Department of Electronics and Nanoengineering
Space Science and Technology

Finnish Meteorological Institute
Space and Earth Observation Centre
Earth Observation Research

Supervising professor
Professor Jaan Praks, Aalto University

Thesis advisor
Professor Jouni Pulliainen, Finnish Meteorological Institute

Preliminary examiners
Professor Leung Tsang, University of Michigan, USA
Dr. Paolo Pampaloni, Institute of Applied Physics “Nello Carrara” IFAC, Italy

Opponent
Professor Marco Tedesco, Lamont-Doherty Earth Observatory, USA

Abstract

Author Anna Kontu

Name of the doctoral dissertation

Effect of snow microstructure and subnivean water bodies on microwave radiometry of seasonal snow

Publisher School of Electrical Engineering

Unit Department of Electronics and Nanoengineering

Series

Aalto University publication series DOCTORAL DISSERTATIONS 69/2018

Finnish Meteorological Institute Contributions 144

Field of research Space science and technology

Manuscript submitted 9 December 2016 **Date of defence** 8 May 2018

Permission to publish granted 7 February 2018 **Language** English

Abstract

Remote sensing using microwave radiometry is an acknowledged method for monitoring various environmental processes in the cryosphere, atmosphere, soil, vegetation and oceans. Several decades long time series of spaceborne passive microwave observations can be used to detect trends relating to climate change, while present measurements provide information on the current state of the environment. Unlike optical wavelengths, microwaves are mostly insensitive to atmospheric and lighting conditions and are therefore suitable for monitoring seasonal snow in the Arctic.

One of the major challenges in the utilization of spaceborne passive microwave observations for snow measurements is the poor spatial resolution of instruments. The interpretation of measurements over heterogeneous areas requires sophisticated microwave emission models relating the measured parameters to physical properties of snow, vegetation and the subnivean layer. Especially the high contrast in the electrical properties of soil and liquid water introduces inaccuracies in the retrieved parameters close to coastlines, lakes and wetlands, if the subnivean water bodies are not accounted for in the algorithm. The first focus point of this thesis is the modelling of brightness temperature of ice- and snow-covered water bodies and their differences from snow-covered forested and open land areas. Methods for modelling the microwave signatures of water bodies and for using that information in the retrieval of snow parameters from passive microwave measurements are presented in this thesis.

The second focus point is the effect of snow microstructure on its microwave signature. Even small changes in the size of scattering particles, snow grains, modify the measured brightness temperature notably. The coupling of different modelled and measured snow microstructural parameters with a microwave snow emission model and the application of those parameters in the retrieval of snow parameters from remote sensing data are studied.

Tiivistelmä

Tekijä Anna Kontu
Väitöskirjan nimi
Lumen hienorakenteen ja lumen peittämien vesialueiden vaikutus lumen mikroaaltosäteilyyn
Julkaisija Sähkötekniikan korkeakoulu
Yksikkö Elektroniikan ja nanotekniikan laitos
Sarja
Aalto University publication series DOCTORAL DISSERTATIONS 69/2018
Finnish Meteorological Institute Contributions 144
Tutkimusala Avaruustiede ja -tekniikka
Käsikirjoituksen pvm 09.12.2018 **Väitöspäivä** 08.05.2018
Julkaisuluvan myöntämispäivä 07.02.2018 **Kieli** Englanti

Tiivistelmä
Muutoksia maaperässä, kasvillisuudessa, merissä, ilmakehässä ja kryosfäärissä voidaan kaukokartoittaa passiivisilla mikroaaltolaitteilla. Monen vuosikymmenen mittaisilla satelliittimittausten aikasarjoilla voidaan havaita ilmastonmuutoksen vaikutuksia, ja tuoreilla mittauksilla saadaan tietoa ympäristön nykytilasta. Mikroaaltojen etu optisiin aallonpituuksiin verrattuna on niiden riippumattomuus ilmakehästä ja valaistusoloista, joten ne sopivat hyvin lumen seurantaan pohjoisilla alueilla.

Yksi suurimmista haasteista satelliittimikroaaltoradiometrien mittausten hyödyntämisessä lumen kaukokartoituksessa on laitteiden huono alueellinen erotuskyky. Jotta monimuotoisen kohdealueen mittauksia voidaan tulkita oikein, tarvitaan monimutkaisia mikroaaltoemissiomalleja kuvaamaan mitattujen parametrien yhteyttä lumen, kasvillisuuden ja lumen alla olevan kerroksen ominaisuuksiin. Erityisesti suuri ero veden ja maaperän sähköisissä ominaisuuksissa vaikeuttaa mittausten tulkintaa rannikoilla sekä järvien ja suoalueiden lähistöllä, jos vesialueita ei huomioida. Ensimmäinen tämän väitöskirjatyön painopisteistä on lumen ja jään peittämien vesialueiden mallinnus sekä näiden alueiden mikroaaltovasteen erot metsäisiin ja avoimiin maa-alueisiin. Työssä esitetään menetelmiä, joilla vesialueiden mikroaaltovastetta voidaan mallintaa ja hyödyntää satelliittimittausten tulkinnassa.

Toinen painopiste on lumen hienorakenteen vaikutus sen mikroaaltovasteeseen. Pienetkin muutokset sirottajien eli lumikiteiden koossa voivat vaikuttaa mitattuun kirkkauslämpötilaan huomattavasti. Väitöskirjatyö tutkii lumen hienorakenteen vaikutusta sen kirkkauslämpötilaan, mitattujen ja mallinnettujen hienorakenneparametrien yhdistämistä lumen mikroaaltomallinnukseen, ja tämän tiedon hyödyntämistä kun lumen ominaisuuksia tulkitaan satelliittimittauksista.

Preface

This thesis work was conducted at the Finnish Meteorological Institute (FMI) in Sodankylä, Finland, in 2006-2017, for the Aalto University Department of Electronics and Nanoengineering. A part of the work was funded by the graduate school "Atmospheric composition and climate change: From molecular processes to global observations and models".

When I started this work over a decade ago, I had never measured or studied snow. Neither had I ever used a radiometer, even though I had left my fingerprints on the SMOS satellite. One of my first tasks in Sodankylä was to buy a snow grain size card, build a snow depth probe and head for the field, alone. A few years later I got "my" first radiometers, SodRad 1 and ELBARA-II, and have since had my hands full of maintenance work and field work. It wasn't the easiest way to learn snow measurements or microwave radiometry, but it surely was an educational experience.

I want to thank all the people who helped in making this thesis a reality. First and foremost, I am indebted to my advisor and supervisors. Prof. Jouni Pulliainen, the (former) head of FMI Arctic Research, hired me to Sodankylä, sent me to the field, acquired all the equipment and funding, and offered me the possibility to do research. Prof. Martti Hallikainen of the Helsinki University of Technology (later Aalto University) Laboratory of Space Technology was the first supervisor of this thesis, but retired before I could finish it. Prof. Jaan Praks of the Department of Electronics and Nanoengineering at Aalto University finally mentored me through the writing process. Without Jaan's encouragement it would have taken me another decade to finish. I am also grateful to my preliminary examiners, Prof. Leung Tsang of the University of Michigan, USA, and Dr. Paolo Pampaloni, of the Institute of Applied Physics "Nello Carrara" IFAC, Italy, for their thorough reading of the manuscript and for pointing out a few obvious errors. Finally, I want to thank Prof. Marco Tedesco for acting as the opponent in my defense.

I am grateful to all my past and present colleagues in Sodankylä, especially the snow team: Hanne Suokanerva, Leena Leppänen, Henna-Reetta Hannula, Markku Ahponen, Jyrki Mattanen, Anita Sassali, Ilkka Mikkola and all the other people who participated in snow and microwave measurements. Special thanks to Veikko Mylläri, who taught me to use the SWE tube.

The FMI staff in Helsinki have provided fruitful collaboration and support. Dr. Juha Lemmetyinen and Dr. Kimmo Rautiainen have influenced my whole academic career starting from the freshman year at TKK. Juha was a co-author in

four of the five papers included in this work. I also want to thank Dr. Terhikki Manninen and Dr. Outi Meinander, my colleagues in optical/UV snow measurements, for their guidance in the world of science and co-operation in snow measurements. I am grateful to Dr. Kirsti Kauristie and Dr. Timo Sukuvaara for their support as head of my group in FMI.

During these years I have collaborated with numerous international partners, whose influence cannot directly be seen in this dissertation, but who have taught me a lot about snow, fieldwork, microwave radiometry and science, especially Dr. Martin Schneebeli, Prof. Christian Mätzler, Dr. Andreas Wiesmann, Dr. Nick Rutter, Prof. Alex Langlois and Dr. Chris Derksen.

Last I thank my family, Timo, Lumi, Myrsky and Tuisku. You have kept my feet on the ground and given me a counterbalance in life. My parents have supported me all these years on the career that I already dreamed of as a kid.

This work still doesn't contain the blueprints of a space rocket, but (again) I hope it is close enough.

Sodankylä, 26.3.2018
Anna Kontu

Contents

List of Abbreviations

AMSR-E	Advanced Microwave Scanning Radiometer – Earth Observing System
AMSR-2	Advanced Microwave Scanning Radiometer 2
DF	Decomposing or fragmented precipitation particle
dFm	Dense forest on mineral soil
dFp	Dense forest on peatland
DH	Depth hoar
DISORT	Discrete Ordinates Radiative Transfer Program for a Multi-Layered Plane-Parallel Medium
DMRT-QCA	Dense Media Radiative Transfer model based on Quasi-Crystalline Approximation
DMSP	Defense Meteorological Satellite Program
EASE	Equal-Area Scalable Earth grid
EOS	Earth Observing System
ESMR	Electrically Scanning Microwave Radiometer
FC	Faceted crystal
FMI	Finnish Meteorological Institute
FOV	Field of view
H	Horizontal polarization
HUT	Helsinki University of Technology
HUTRAD	Helsinki University of Technology Radiometer
IF	Ice formation
JAXA	Japan Aerospace Exploration Agency
JULES	Joint UK (United Kingdom) Land Environment Simulator model
L	Lake

MEMLS	Microwave Emission Model for Layered Snowpacks
MF	Melt form
MM	Machine made snow
NASA	National Aeronautics and Space Administration
NIR	Near infrared
NWP	Numerical weather prediction
PP	Precipitation particle
RG	Rounded grain
rms	Root-mean-square
SD	Snow depth
sFm	Sparse forest on mineral soil
SFT	Strong Fluctuation Theory
SH	Surface hoar
SMMR	Scanning Multichannel Microwave Radiometer
SMP	SnowMicroPen
SMRT	Snow Microwave Radiative Transfer model
SodRad 1/2	Sodankylä Radiometer 1/2
SSA	Specific surface area (volume to surface ratio)
SSM/I	Special Sensor Microwave Imager
SSMI/S	Special Sensor Microwave Imager/Sounder
SWE	Snow water equivalent
TKK	Helsinki University of Technology
TOA	Top-of-atmosphere
V	Vertical polarization
W	Wetland

List of Symbols

a	Constant, a = 1.59 cm/K
B	Spectral radiance (W/(sr·m²·K))
b	Constant, b = 0 cm
c	Speed of light in vacuum, c = 2.998·10^{-8} m/s
D	Measured snow grain size parameter (mm)
D_{SP}	Grain size parameter modelled with SNOWPACK (mm)
D_0	Optical grain size (mm)
d	Snow layer thickness (cm)
d_{eff}	Effective grain size (mm)
E	Traditional snow grain size (mm)
e	Euler's number, $e \approx 2.71828$
f	Frequency (Hz or GHz)
h	Planck's constant, h = 6.634·10^{-34} J
h_s	Standard deviation of surface height (mm)
k	Wave number (1/m)
k_B	Boltzmann's constant, k_B = 1.38·10^{-23} J/K
l_n	Loss factor of layer n
p_c	Correlation length (mm)
Q	Polarization mixing parameter
q	The portion of radiation scattered in the forward direction, q = 0.96
$r_{p,F,n}$	Fresnel reflection coefficient of layer n at polarization p
$r_{p,mod}$	Empirical reflection coefficient at polarization p
T	Physical temperature (°C or K)

T_B	Brightness temperature (K)
T_c	Cosmic background radiation, T_c = 2.7 K
T_{fp}	Brightness temperature at frequency f and polarization p (K)
t_n	Fresnel transmission coefficient of layer n
V	Forest stem volume (m³/ha)
V_{high}	Saturation stem volume of forest transmissivity (m³/ha)
$\alpha_{\uparrow(\downarrow)}$	Upwards (downwards) atmospheric profile factor
β	Scaling factor relating measured and modelled grain sizes
β_μ	Fractional coverage of land cover type μ
γ	Constant, γ = 2±1
δ	Penetration depth (m) or constant, δ = 0.20±0.04
ϵ	Emissivity
ε	Permittivity (As/Vm)
ε'	Real part of relative permittivity
ε''	Complex part of relative permittivity
ε_r	Relative permittivity compared to the permittivity of vacuum ε_0
$\varepsilon_{x\infty}$	High-frequency limit of relative permittivity for material x
ε_{x0}	Low-frequency limit of relative permittivity for material x
ε_0	Permittivity of vacuum, ε_0 = 8.854·10^{-12} As/Vm
θ	Incidence angle (° or rad)
κ_a	Absorption coefficient (1/m)
κ_e	Extinction coefficient (1/m or dB/m)
κ_s	Scattering coefficient (1/m)
λ	Wavelength (m)
μ_0	Magnetic permeability of vacuum, μ_0 = 4π·10^{-7} Vs/Am
ρ	Density (kg/m³)
σ	Conductivity (S/m)
τ	Relaxation time (s)

List of Publications

This doctoral dissertation consists of a summary and of the following publications which are referred to in the text by their numerals.

1. A. Kontu, J. Pulliainen. 2010. Simulation of spaceborne microwave radiometer measurements of snow cover using in situ data and brightness temperature modeling. *IEEE Transactions on Geoscience and Remote Sensing*, 48(3), 1031-1044. doi: 10.1109/TGRS.2009.2030499.

2. J. Lemmetyinen, A. Kontu, J.-P. Kärnä, J. Vehviläinen, M. Takala, J. Pulliainen. 2011. Correcting for the influence of frozen lakes in satellite microwave radiometer observations through application of a microwave emission model. *Remote Sensing of Environment*, 115(12), 3695-3706. doi: 10.1016/j.rse.2011.09.008.

3. A. Kontu, J. Lemmetyinen, J. Pulliainen, J. Seppänen, M. Hallikainen. 2014. Observation and modeling of the microwave brightness temperature of snow-covered frozen lakes and wetlands. *IEEE Transactions on Geoscience and Remote Sensing*, 52(6), 3275-3288. doi: 10.1109/TGRS.2013.2272077.

4. L. Leppänen, A. Kontu, J. Vehviläinen, J. Lemmetyinen, J. Pulliainen. 2015. Comparison of traditional and optical grain-size field measurements with SNOWPACK simulations in a taiga snowpack. *Journal of Glaciology*, 61(225), 151-162. doi: 10.3189/2015JoG14J026.

5. A. Kontu, J. Lemmetyinen, J. Vehviläinen, L. Leppänen, J. Pulliainen. 2017. Coupling SNOWPACK-modeled grain size parameters with the HUT snow emission model. *Remote Sensing of Environment*, 194, 33-47. doi: 10.1016/j.rse.2016.12.021.

Author’s Contribution

Publication 1: “Simulation of spaceborne microwave radiometer measurements of snow cover using in situ data and brightness temperature modeling"

The paper presents a time series of snow cover microwave brightness temperatures, simulated with the HUT snow emission model using bi-weekly snow pit measurements as input, and their comparison with spaceborne measurements of the AMSR-E instrument. The author was responsible for planning and conducting the field measurements, collecting and analysing the data and writing the manuscript. J. Pulliainen initiated the original study plan.

Publication 2: “Correcting for the influence of frozen lakes in satellite microwave radiometer observations through application of a microwave emission model”

The paper studies the effect of frozen snow-covered lakes on snow water equivalent retrieved from spaceborne observations with the HUT snow emission model. J. Lemmetyinen was responsible for the retrieval algorithm implementation, data analysis and writing the manuscript. The author took part in model development, data collection and analysis and writing the manuscript. J.-P. Kärnä, J. Vehviläinen and M. Takala assisted in data collection and writing the manuscript. J. Pulliainen participated in retrieval algorithm implementation and writing the manuscript.

Publication 3: “Observation and modeling of the microwave brightness temperature of snow-covered frozen lakes and wetlands”

The publication studies the capabilities of the HUT snow emission model in simulation of the brightness temperature of different snow-covered land cover types, such as forests, open areas, wetlands and lakes. The author was responsible for the main part of data analysis and writing the manuscript, as well as planning and performing the field measurements. J. Lemmetyinen took part in field measurements and writing the manuscript. J. Seppänen was responsible for the airborne data collection. J. Pulliainen and M. Hallikainen were the scientific supervisors of the study.

Publication 4: “Comparison of traditional and optical grain-size field measurements with SNOWPACK simulations in a taiga snowpack”

The paper presents a comparison of snow microstructure parameters modelled using SNOWPACK to field measurements. L. Leppänen was responsible for data analysis and writing the manuscript. The author participated in the field measurements, data analysis and writing the manuscript. J. Vehviläinen was responsible for the SNOWPACK model runs. J. Lemmetyinen laid out the original study plan and assisted in writing of the manuscript. J. Pulliainen assisted in writing of the manuscript and was the scientific supervisor of the study.

Publication 5: “Coupling SNOWPACK-modeled grain size parameters with the HUT snow emission model”

This paper studies the coupling of snow microstructure parameters from SNOWPACK with the HUT snow emission model and applies the snow parameters from SNOWPACK in the retrieval of snow water equivalent from microwave radiometer observations using the HUT snow emission model. The author was responsible for writing the manuscript, data collection and data analysis. J. Lemmetyinen had the original research idea and assisted in data analysis and writing the manuscript. J. Vehviläinen was responsible for the SNOWPACK model runs. L. Leppänen assisted in data collection. J. Pulliainen was the scientific supervisor of the work.

1. Introduction

Seasonal snow covers approximately 40-50 million km^2, or close to 50 %, of the Northern Hemisphere land mass every year (Brown and Robinson, 2011), and about 98 % of seasonal snow is on the Northern Hemisphere (Armstrong and Brodzik, 2001). Seasonal snow cover has a significant effect on the Earth's energy balance. Due to its high albedo (0.8-0.9 for fresh snow in the visible wavelengths), snow cover reflects a large part of the incident solar radiation back to space and therefore cools the Earth's surface (Armstrong and Brun, 2008). Smaller snow covered area for a shorter period of time would cause more solar radiation being absorbed into atmosphere and land surface, and would therefore accelerate climate change. This positive feedback mechanism has potentially a major role in global warming (Hall and Qu, 2006). Snow also affects the heat and moisture fluxes between the ground surface and the atmosphere. Similarly to the Arctic sea ice cover (Simmonds, 2015), the extent and duration of seasonal snow cover can be used as a proxy for monitoring climate change (Derksen and Brown, 2012; Hernández-Henríquez et al., 2015) and to test climate models (Brutel-Vuilmet et al., 2013). Snow depth and snow cover extent are also vital parameters in initializing numerical weather prediction (NWP) models (de Rosnay et al., 2014).

Seasonal snowpack stores the wintertime precipitation and releases it in a relatively short period of time during spring snowmelt. At the same time, melting snow absorbs a large amount of energy and therefore delays warming of the snow-covered areas (Armstrong and Brun, 2008). The timing and amount of released water affect plant growth, local annual carbon balance (Aurela et al., 2004) and river run-off (Vavrus, 2007), and may cause flooding (Bell et al., 2016; Vormoor et al., 2015). Because the terrestrial run-off is dominated by meltwater from snow and glaciers in a large part of Eurasia and North America, a fifth of the Earth's population is dependent on snow as their source of potable water (Barnett et al., 2005).

All these interactions of snow with the Earth's water and carbon cycle, radiation balance, weather and climate may change in timing and magnitude due to climate change (Räisänen, 2015; Safavi et al., 2017). Therefore accurate information of the current state of the cryosphere as well as long-term climate data records of the temporal and spatial changes in seasonal snow cover are crucial for climate studies and hydrology, among other disciplines. To meet the needs of these fields, information of snow cover can be extracted from many sources: remote sensing (Dietz et al., 2012), in situ measurements (Kinar and Pomeroy,

2015), modelling (Etchevers et al., 2002) and reanalysis (Margulis et al., 2016). Unlike temporally and spatially sparse in situ measurements, passive microwave remote sensing from satellite instruments may provide continuous daily global observations. Modelling and reanalysis rely on calculating snow data from other measured parameters, but they are often used to support remote sensing methods.

Microwave remote sensing is well suited for observations at high latitudes in the wintertime, as cloudy or rainy weather conditions and the lack of sunlight do not hinder the retrieval of snow information, unlike at optical wavelengths where the measured parameter is reflected sunlight (Ulaby et al., 1981, chapter 1). Another advantage of microwaves over optical wavelengths is the possibility to extract information of the whole snowpack, not just the surface. In addition, there exists a relatively long time series of remotely sensed passive microwave data; continuous multi-frequency spaceborne measurements are available since 1978, allowing the monitoring of long-term changes in the cryosphere.

However, the spatial resolution of current spaceborne passive microwave sensors and algorithms is in the order of 10-30 km, which is not high enough for many applications. In addition, the variability in snow conditions, land cover, vegetation and topography in a measured field of view (FOV) may decrease the accuracy of snow parameters retrieved from satellite data (Vander Jagt et al., 2013; Rees et al., 2006). A small-featured mosaic of forests, fields and small lakes or the variability of snow depth and slope on mountainous areas restrict the accuracy of retrieval. One way of mitigating these problems is the inclusion of auxiliary data, such as land cover and topography, in data interpretation.

Another limiting factor is the depth of snowpack. Depending on used frequency, snow density and grain size, the measured signal saturates at some point. Typical upper limit values reported for 36.5 GHz are around 150 mm of snow water equivalent (Derksen et al., 2010; Derksen and Brown, 2012; Langlois et al., 2012; Santi et al., 2017; Takala et al., 2011). Very shallow dry snow (< 5 cm) is transparent at microwave frequencies typically used in snow measurements (Foster et al., 2005). The detection of whether there is snow on the ground or not is easier using optical wavelengths (e.g. Metsämäki et al., 2015).

The most important parameter describing the state of snowpack is snow water equivalent (SWE), which describes how much water would be released if all the snow melted at once. The extraction of this parameter from satellite measurements requires algorithms and models relating the physical snow properties to the measured signal. The first retrieval algorithms (Chang et al., 1987; Kunzi et al., 1982) were purely empirical and based on assumed fixed snow properties, such as density and grain size, to derive snow depth (SD) from spaceborne measurements. Later numerous more advanced algorithms have been developed for global (e.g. Kelly, 2009; Takala et al., 2011) and regional (e.g. Derksen et al., 2010; Sorman and Beser, 2013) applications.

Two main problems in passive microwave remote sensing of snow were studied in this thesis: the mixed pixel problem, or the variability of land cover and

snow conditions in the satellite instrument's field of view, and the presentation of snow microstructure in a microwave snow model. The mixed pixel problem was approached from the point of view of subnivean freshwater bodies, such as rivers, lakes and wetlands, typical to the taiga region. The contrast in the electrical properties of water compared to land and the differences of snow covers on land and ice may hinder SWE retrieval accuracy around water bodies. This problem was studied in Publications 2 and 3, which presented modelling results and measurements of snow cover on lakes and wetlands. Publication 3 concentrated on a case study of in situ and airborne measurements of different land cover types in a small region, while Publication 2 extended the work to spaceborne measurements over all Finland. Publication 3 presented the first microwave modelling results of ice and snow-covered wetlands. The main result was that the used snow emission model was able to simulate brightness temperatures of snow-covered water bodies well, even though only a very simple modelling scheme was used. The method presented in Publication 2 for including the modelling of lake ice and snow conditions in a SWE retrieval algorithm using a microwave snow emission model improved the SWE retrieval accuracy in lake-rich areas and coastlines notably.

The micro- and macrostructure of snowpack determine its interaction with microwave radiation. The microstructure, or the size, shape and bonding of snow grains, mainly defines how microwave radiation is scattered in the snowpack. Even though snow typically has a very complex layer structure (Colbeck, 1991), it is often represented in SWE retrieval algorithms as one homogeneous layer, and snow microstructure is simplified to one grain size-related averaged parameter. These simplifications increase the retrieval error. Publication 1 compared snow grain size derived from spaceborne measurements through a microwave model to field measurements, and presented an equation for calculating an effective grain size from field measurements. This equation reduced the simulation error notably compared to using the measured grain sizes directly.

Publications 4 and 5 studied the possibility of combining a physical snow model, which calculates snow properties from meteorological data, with a microwave model to enhance the accuracy of snow parameter retrieval. Publication 4 compared field snow measurements with physical snow model results, and Publication 5 compared measured brightness temperatures to those simulated using snow profiles from a physical snow model. These results showed that grain size from a physical snow model corresponds to grain size in a snow microwave emission model, and that coupling a physical snow model to snow parameter retrieval algorithm is achievable.

This thesis is divided into following chapters: Chapter 2 describes the general concept of remote sensing of snow and the theory of microwave radiometry. Chapter 3 focuses on snow properties. Chapter 4 presents the main results of Publications 1-5 and Chapter 5 concludes the work.

2. Passive microwave systems for snow observation

This chapter describes the general concept of remote sensing, gives a brief history of passive microwave remote sensing of snow and introduces the instruments typically used. The theory and principles of microwave radiometry, as well as different radiometers used in this work, are presented.

2.1 Remote sensing concept and instruments

Remote sensing is the acquisition of information about a target without direct contact. Considering snow, it usually means tower-based, airborne or spaceborne observations. Two frequency ranges of the electromagnetic spectrum are often used in remote sensing of snow: *microwaves* (wavelengths between 1 mm and 1 m, or frequencies between 300 MHz and 300 GHz) and *optical* (wavelengths between 100 nm and 1 mm). They are used because the atmosphere is mostly transparent in these bands. However, unlike microwaves, optical wavelengths are obstructed by clouds. Optical wavelengths typically reflect from the surface of the target and provide information of the first few centimetres of the snowpack. Depending on frequency, microwaves can penetrate through the snowpack into ground providing information of the whole snowpack and the top soil layer (Lemmetyinen et al., 2016; Zheng et al., 2016).

Remote sensing instruments can be divided into two categories: *active*, which include a transmitter and a receiver, and *passive*, which only receive natural radiation. An active microwave instrument is called a *radar* or a *scatterometer*, while a passive system is a *radiometer*. Spaceborne radars reach better spatial resolution than radiometers, but their spatial and temporal coverage is not as good as radiometers' (Dietz et al., 2012). There have been many recent studies on applying spaceborne active microwave instruments to snow parameter retrieval (Leinss et al., 2015; Pettinato et al., 2013; Rott et al., 2013), but currently they are only used in wet snow detection (Nagler et al., 2016). Radiometers are typically applied to measure SWE or SD or soil properties such as frost depth (Lemmetyinen et al., 2016; Rautiainen et al., 2014). Active optical *lidars* typically measure surface height and can therefore be used to monitor snow depth (Bhardwaj et al., 2016). Passive optical *spectrometers* measure reflected sunlight and are often used to map snow cover extent (Metsämäki et al., 2015) or albedo (Williamson et al., 2016).

The origin of microwave radiometry techniques is in radio astronomy. The first passive microwave measurements of terrestrial snowpack were conducted in the 1960's and 1970's in the USA (Edgerton et al., 1971), Switzerland (Mätzler et al., 1980) and Finland (Tiuri and Hallikainen, 1981). These systems were truck or tower-mounted and operated at frequencies between 1 GHz and 100 GHz (Foster et al., 1984). Spaceborne passive microwave measurements are available since 1972 from the Nimbus 5 Electrically Scanning Microwave Radiometer (ESMR) instrument, with a continuous time series of multi-frequency data since 1978 from the Nimbus 7 Scanning Multichannel Microwave Radiometer (SMMR).

In the 1970's and 1980's, the application of spaceborne passive microwave measurements to snow monitoring was studied using both the Nimbus ESMR's (Chang et al., 1981; Foster et al., 1980) and the SMMR instrument (Chang et al., 1987; Hallikainen and Jolma, 1986; Kunzi et al., 1982). The first global snow depth algorithm was introduced in 1987 (Chang et al., 1987) using SMMR data. Later global snow products were developed based on the Defense Meteorological Satellite Program (DMSP) series Special Sensor Microwave Imager (SSM/I) sensors (Armstrong and Brodzik, 1995; Grody and Basist, 1996) and the Advanced Microwave Scanning Radiometer – Earth Observing System (AMSR-E) instrument on board National Aeronautics and Space Administration (NASA) Aqua satellite (Kelly and Chang, 2003). After the AMSR-E failed in 2011, DMSP series Special Sensor Microwave Imager/Sounder (SSMI/S) instruments (Smith and Bookhagen, 2016; Takala et al., 2017) and the AMSR-2 on board Japan Aerospace Exploration Agency (JAXA) GCOM-W1 satellite (Santi et al., 2012) have been used for remote sensing of snow.

The first algorithms for the retrieval of snow depth (d) from spaceborne passive microwave observations were purely empirical. Chang et al. (1987) suggested a linear relationship

$$d = a \cdot (T_{18H} - T_{37H}) + b, \tag{1}$$

where T_{18H} and T_{37H} are the brightness temperatures (K) at 18 GHz and 37 GHz horizontal polarization, respectively, and a and b are constants a = 1.59 cm/K and b = 0 cm. This equation assumes a snow density of 300 kg/m^3 and a grain size of 0.3 mm (Kelly and Chang, 2003). If snow properties differ from these assumptions, the error in the retrieved SD increases (Davenport et al., 2012). Therefore Eq. (1) is not reliable in all regions at all times with the given constants a and b.

Despite these limitations, similar empirical algorithms were used for several applications in regional and global scale (e.g. Foster et al., 1997; Goodison and Walker, 1994; Hallikainen and Jolma, 1992) using either H or V polarization. Kelly and Chang (2003) recalibrated the coefficients a and b for different regions of the Earth to get a global algorithm for the SSM/I and the AMSR-E instruments. Later empirical dynamically adjusting coefficients were applied to account for the evolution of snow grain size in the AMSR-E algorithm (Kelly, 2009). While the earliest algorithms used H polarization (Chang et al., 1987;

Kunzi et al., 1982) due to its higher sensitivity to SD and SWE, nowadays V polarization is often used, because it is less sensitive to ice lenses in snow (Rees et al., 2010).

In addition to direct empirical algorithms, several other types of retrieval algorithms have been studied. For example, neural networks can be used (Santi et al., 2012) to directly retrieve SWE. Neural networks (Davis et al., 1993), genetic algorithms (Tedesco and Kim, 2006a) and numerical inversion (Roy et al., 2004; Takala et al., 2011) can also be applied to invert microwave emission models. In situ measurements can be assimilated into the algorithm to calibrate it at measurement stations (Margulis, 2006; Takala et al., 2011), and a physical snow model can be coupled with a microwave snow emission model to better address the evolution of snow parameters (Langlois et al., 2012). Markov Chain Monte Carlo methods can be applied to retrieve SWE in a multi-layer snowpack (Pan et al., 2017).

Three types of measurement set-ups are typically used in remote sensing (Figure 1): a) ground-based, b) airborne and c) spaceborne. Ground-based and airborne systems are well suited for development and testing of models, retrieval algorithms and instruments. In addition, with ground-based systems it is possible to measure long continuous time series of one target to detect changes, e.g. diurnal and seasonal variation (Macelloni et al., 2005; Meinander et al., 2008; Mätzler et al., 1980; Wang and Zender, 2011). Even close-range measurements of individual snow labs are possible (Hallikainen et al., 1987; Maslanka et al., 2016; Wiesmann et al., 1998). The measured target is known and can be characterized with high precision. Airborne systems allow wider spatial coverage, while their temporal coverage is often short or infrequent. They are typically used in measurement campaigns, not in long-term monitoring. Spaceborne systems offer the possibility for daily long-term global observations, but suffer from poorer spatial and temporal resolution.

In passive microwave systems, the variation of the measured target is completely different in these three cases. In ground-based systems, the FOV size is metres at most, and can be characterized. In airborne systems, the FOV is tens or hundreds of metres. There is typically some variation inside the FOV, but often fairly uniform FOVs, such as forest or water areas, can be selected. In spaceborne systems the instrument's FOV is large, even tens of kilometres wide, and may contain various different land covers, varying topography and different snow conditions.

A spaceborne radiometer observes radiation from several sources (Figure 2): from a) clouds, b) atmosphere, c) solar and cosmic radiation, d) vegetation, e) ground attenuated by snow, vegetation and atmosphere, and f) snow attenuated by vegetation and atmosphere. In the microwave range, clouds and rain are often negligible. Only the signal from snow is desired, all the other sources need to be removed from the signal, as well as the attenuation by atmosphere and vegetation.

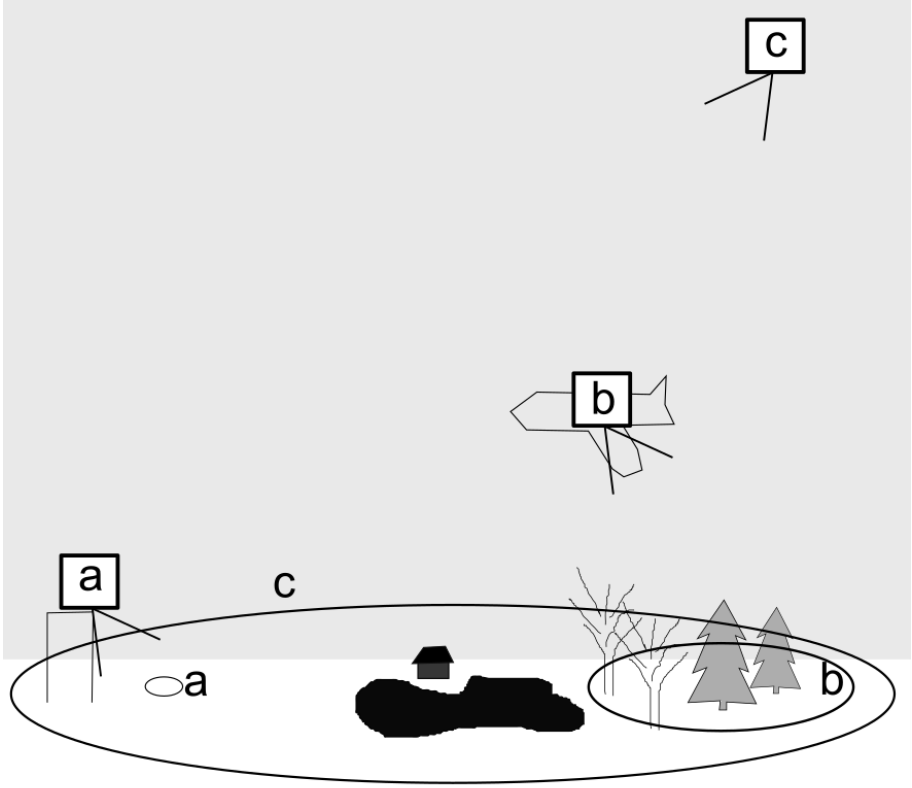

Figure 1. A conceptual image of the different fields of view of (a) ground-based, (b) airborne and (c) spaceborne measurement systems.

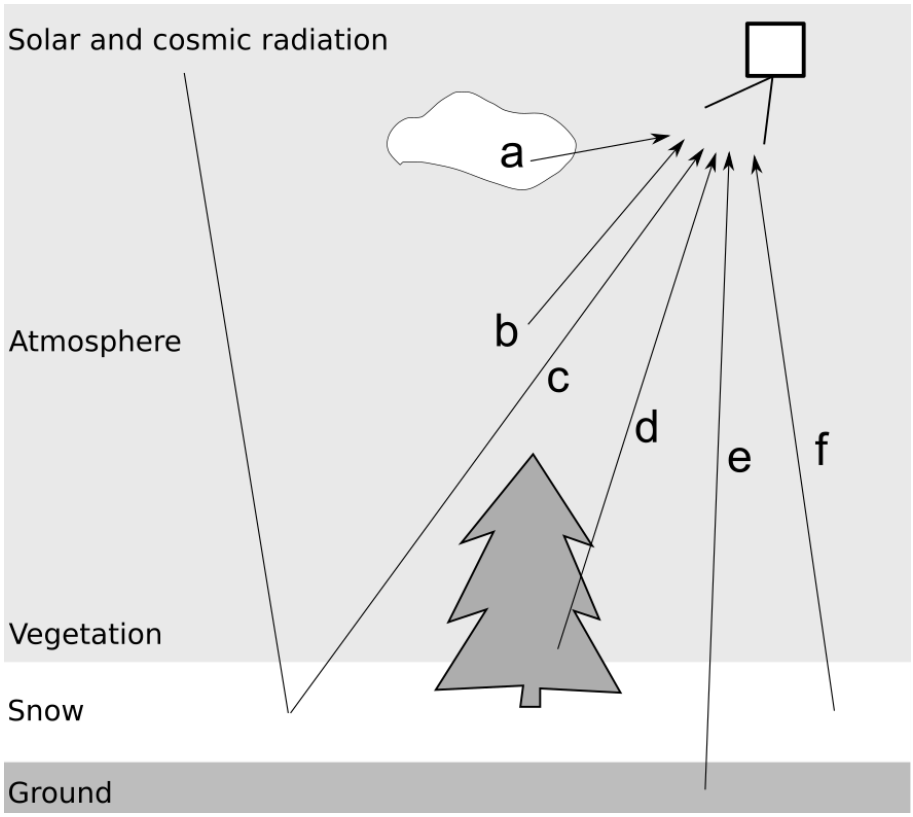

Figure 2. Radiation sources measured by a spaceborne radiometer: a) clouds, b) atmosphere, c) solar and cosmic radiation, d) vegetation, e) soil and f) snow.

2.2 Theoretical background of microwave radiometry of snow

The terminology related to this work, as well as the basic theory of microwave emission of snow, is explained in this chapter.

2.2.1 Microwave emission

All natural matter emits electromagnetic radiation caused by the thermal motion of particles. The emitted radiation is usually defined using a *blackbody*, an idealized object which absorbs all incident radiation and emits all of its thermal energy. The energy emitted by a blackbody, or its spectral radiance B (W/sr·m^2·K), can be expressed with Planck's law (Planck, 1901)

$$B = \frac{2hf^3}{c^2} \cdot \frac{1}{e^{\frac{hf}{k_B T}} - 1}, \tag{2}$$

where h = 6.634·10^{-34} J is Planck's constant, f is frequency (Hz), c = 2.998·10^8 m/s is the speed of light in vacuum, k_B = 1.38·10^{-23} J/K is Boltzmann's constant and T is the physical temperature of the radiator (K). In the microwave range, $hf \ll k_B T$, and the Rayleigh-Jeans approximation can be used instead of Planck's law (Ulaby, Moore and Fung, 1981, chapter 4):

$$B = \frac{2k_B T}{\lambda^2}, \tag{3}$$

where $\lambda = c/f$ is wavelength (m). Therefore the radiated power is linearly dependent on physical temperature.

The equations (2) and (3) hold for blackbodies, but natural targets are not perfect radiators or absorbers. Their *brightness temperature* T_B, or the physical temperature of a blackbody that would emit the same amount of energy as the target at temperature T, is

$$T_B = \epsilon(f, p, \theta, \varepsilon, \mu)T, \tag{4}$$

where ϵ is the emissivity of the target. It depends on used frequency (f), polarization (p) and incidence angle (θ), as well as on the electromagnetic properties, such as permittivity (ε) and permeability (μ), of the target. By measuring the brightness temperature with a radiometer and deducing the physical temperature of a target, its emissivity can be calculated.

The physical properties of a target, such as snow water equivalent and structure, determine its electromagnetic properties, including emissivity. Theoretical, empirical or semi-empirical models can be used to relate the physical properties to the measured signal. Since emissivity often varies with frequency, polarization and observation angle, more information about a target can be retrieved by combining multiple observations.

2.2.2 Emission, extinction, absorption and scattering

As radiation travels, it interacts with a medium through two processes: emission and extinction. *Emission* is the addition of energy from a medium, and *extinction* is the loss of energy in a medium. There are two ways for extinction of radiation: *absorption*, or the transformation of energy to other forms such as heat, and *scattering*, or energy that is diverted from the direction of the incident radiation. (Ulaby et al., 1981, chapter 4)

2.2.3 Relative permittivity

The electrical properties (such as absorption and scattering coefficients) of a medium depend on one fundamental property, *permittivity* ε, which is often expressed as *relative permittivity* ε_r compared to the permittivity of vacuum $\varepsilon_0 = 8.854 \cdot 10^{-12}$ As/Vm. Relative permittivity is complex ($\varepsilon_r = \varepsilon' - j\varepsilon''$); the real part ε' describes the material's resistance to electric fields and the complex part ε'' is related to dielectric losses in the medium. The relative permittivity of air is almost equal to that of vacuum. (Ulaby et al., 1981, chapter 4)

2.2.4 Penetration depth

Penetration depth defines how deep electromagnetic radiation can penetrate into a material. At depth δ, the radiation is $1/e$ part of the original value. For time harmonic fields, such as propagating microwave radiation (Sihvola, 1999),

$$\delta = \frac{1}{2\pi f \sqrt{\varepsilon_0 \mu_0} |\mathrm{Im}\sqrt{\varepsilon_r}|}, \tag{5}$$

where f is frequency (Hz), $\mu_0 = 4\pi \cdot 10^{-7}$ Vs/Am is the magnetic permeability of vacuum. Relative permittivity ε_r and penetration depth δ are both frequency sdependant. Lower frequencies penetrate deeper into a medium than higher frequencies enabling the retrieval of information from the whole snowpack in the microwave range. (Ulaby et al., 1982, chapter 11)

2.2.5 Polarization

The electric and magnetic fields of electromagnetic waves oscillate in directions perpendicular to each other and to the propagation direction of the wave. The orientation of the oscillation of the electric field is called *polarization*. Radiation from many natural sources, such as the Sun, is a random mixture of different polarizations and is therefore unpolarised. However, most targets monitored with microware remote sensing have strongly polarized emission. Microwave radiometers often measure two orthogonal radiation components, horizontal (H) and vertical (V) polarization. Any polarization can be expressed as a combination of these two. Microwave polarization difference can be applied to measure, for example, plant phenology (Shi et al., 2008), snow parameters (Santi et al., 2017) and soil freezing processes (Rautiainen et al., 2014).

2.2.6 Fresnel reflection

The transmission and reflection of radiation moving through an interface between two media are described with Fresnel equations. The reflection coefficients $r_{V,F}$ and $r_{H,F}$ for V and H polarization for radiation coming from above are

$$r_{V,F} = \left| \frac{\frac{\varepsilon_2}{\varepsilon_1} \cdot \cos\theta - \sqrt{\frac{\varepsilon_2}{\varepsilon_1} - \sin^2\theta}}{\frac{\varepsilon_2}{\varepsilon_1} \cdot \cos\theta + \sqrt{\frac{\varepsilon_2}{\varepsilon_1} - \sin^2\theta}} \right|^2, \quad (6)$$

$$r_{H,F} = \left| \frac{\cos\theta - \sqrt{\frac{\varepsilon_2}{\varepsilon_1} - \sin^2\theta}}{\cos\theta + \sqrt{\frac{\varepsilon_2}{\varepsilon_1} - \sin^2\theta}} \right|^2, \quad (7)$$

where ε_1 and ε_2 are the relative permittivities of the lower and upper layer, respectively, and θ is the incidence angle (rad). These equations assume that the interface is flat, which is not the case in the interfaces between soil and snow or water and ice. Therefore empirical modifications to these equations are often used in applications (Chapter 3.2.2).

2.2.7 Considerations for snow cover

Relative permittivity of liquid water (ε_w) depends on frequency and temperature and can be written as (Debye, 1929)

$$\varepsilon_w = \varepsilon_{w\infty} + \frac{\varepsilon_{w0} - \varepsilon_{w\infty}}{1 + j2\pi f \tau_w}, \quad (8)$$

where $\varepsilon_{w\infty}$ is the high-frequency limit, ε_{w0} is the low-frequency limit, f is the frequency (Hz) and τ_w is the relaxation time of water (s). The high-frequency limit is $\varepsilon_{w\infty} \approx 4.9$, but ε_{w0} and τ_w depend on temperature. For water at temperature T = 0°C, $\varepsilon_{wo} \approx 88.045$ and $\tau_w \approx 1.8$ s. The real part of relative permittivity ε'_w is above 70 at frequencies below 10 GHz and decreases to 4.9 at frequencies above 100 GHz (Ulaby et al., 1986, appendix E). The complex part ε''_w has a peak of approximately 40 around 10 GHz, but its location depends on temperature.

For permittivity of pure or freshwater ice (ε_i), the same Eq. (8) can be applied. The low-frequency limit for ice ε_{i0} is between 90 and 100 and the high-frequency limit is $\varepsilon_{i\infty} \approx 3.17$, which are quite similar to liquid water. However, the relaxation time of ice is $\tau_i \sim 10^{-5}$ s (Mätzler, 1987; Mätzler and Wegmüller, 1987), resulting in a frequency and temperature independent $\varepsilon'_i \approx 3.15$ in the microwave range (Ulaby et al., 1986, appendix E). The complex part $\varepsilon''_i \sim 10^{-3}$, but it is difficult to measure because of the low value (Matsuoka et al., 1996). The measured values of ε''_i do not agree with Eq. (8) (Ulaby et al., 1986, appendix E).

Since dry snow is mainly a mixture of ice and air, its relative permittivity ε_{ds} can be calculated from permittivity of ice ε_i e.g. using Polder-Van Santen mixing formula (Polder and Van Santen, 1946)

$$\frac{\varepsilon_{ds} - 1}{3\varepsilon_{ds}} = \frac{\rho_s(\varepsilon_i - 1)}{\rho_i(\varepsilon_i + 2\varepsilon_{ds})}, \quad (9)$$

where ρ_s and ρ_i are the densities (kg/m^3) of snow and ice, respectively. Empirical measurements of dry snow agree with this equation (Hallikainen et al., 1986; Mätzler, 1996). As the dielectric constant of water is very high compared to ice or air, the presence of any liquid water in snow changes its relative permittivity significantly. For wet snow, the Polder-Van Santen model can be used, if a mixture of dry snow and water is considered (Hallikainen et al., 1986).

The relative permittivity of soil depends on its composition, structure and especially its liquid water content. When soil freezes, some water may still remain in liquid form even in very cold temperature (He et al., 2016). Typical values for relative permittivity of frozen soil are ε' between 3 and 8 and ε'' between 0 and 1 (Hallikainen et al., 1985), which differ notably from the permittivity of liquid water.

2.2.8 Interaction of microwaves with snowpack

All three parts of the radiative transfer equation (Chandrasekhar, 1960), namely emission, absorption and scattering, are needed to describe the interaction of microwave radiation with natural snowpacks. The effect of snow cover on brightness temperature is two-fold: 1) snow emits radiation and 2) the upwelling radiation from the layer below snow (soil or ice and water, or other snow layers) is absorbed and scattered in the snowpack.

The basis for microwave remote sensing of snow parameters is that as the scattering volume (i.e. the amount of snow, or SWE) increases, the measured brightness temperature decreases (e.g. Mätzler, 1987), because more radiation is scattered away from the sensor. The inhomogeneities of snowpack (or snow grains) act as scatterers, and the scattering properties of snowpack depend on their geometry and size. However, above a certain limit in SWE, the emission from snowpack itself masks out the scattered radiation, and the measured brightness temperature increases with increasing SWE. At 36.5 GHz, this limit is ~150 mm SWE (Derksen et al., 2010; Derksen and Brown, 2012; Langlois et al., 2012; Santi et al., 2017; Takala et al., 2011). Therefore higher SWE results in ambiguities in the retrieval, if no independent source of auxiliary data is used. Lower frequencies penetrate deeper into snowpack and therefore the limit is higher. Frequencies around 10 and 18 GHz have been used and are proposed for future missions (Rott et al., 2010), even though their sensitivity to changes in SWE is lower than at 36.5 GHz (Mätzler et al., 1982).

Generally, at low frequencies (below 20 GHz), absorption is the dominating extinction mechanism, but at higher frequencies scattering becomes dominant (Ulaby et al., 1986, chapter 19) due to the size of scatterers compared to radiation wavelength. However, in practice the situation is more complex. Snow properties such as grain size and density affect the absorption and scattering coefficients separately, and the magnitude of their effect depends on frequency (Santi et al., 2017).

Typically two frequencies, one in the absorptive region and another in the scattering region (such as 18.7 and 36.5 GHz), are used in snow parameter retrieval algorithms to separate the background from the emission of snowpack. Comparison of two frequencies also removes a major part of the effect of snow physical temperature to the measured brightness temperature.

The interaction of electromagnetic radiation with a medium is described with Maxwell equations (see e.g. Ishimaru, 2013). For a strongly scattering random medium, such as snow, there are some approximations for the interaction of microwaves with the scattering particles, the most common being Rayleigh scattering and Mie scattering. *Rayleigh scattering* assumes that the scattering particles are small compared to the radiation wavelength (Ishimaru, 2013). This is generally not true in microwave remote sensing, as both snow grains and the used wavelengths are in the order of millimetres. *Mie scattering* is an exact solution to the scattering by isotropic homogenous spheres (Ishimaru, 2013). There are no limitations to the size of the scatterers, but they must be spherical.

2.3 Radiometer systems

A radiometer typically consists of an antenna (to receive radiation from a certain direction), bandpass filters (to limit the signal to a certain frequency band), amplifiers (to amplify the received signal), an oscillator and a mixer (to mix the signal from the receiver bandwidth to the detector bandwidth) and a detector (to convert the received signal to voltage). Direct detection without mixing to lower frequency is also possible. Radiometers are highly sensitive, as the received signal is typically below the local thermal noise level. A good overview of radiometer systems and their operation is given by Skou and Vine (2006).

Calibration is needed to convert the detector voltage to brightness temperature. By measuring sources whose brightness temperature is known, a calibration curve between voltage and brightness temperature can be established. Common calibration sources include liquid nitrogen-cooled absorbers, ambient temperature absorbers, and noise sources (i.e. a terminated load or a noise diode). The measurement accuracy and the stability of a radiometer are highly dependent on the quality of its calibration. External calibration targets (absorbers) are typically applied once per campaign or a few times a year, while internal targets (loads and diodes) can be applied every integration cycle, typically several times a minute, by switching the received signal between the antenna and the calibration target. (Ulaby et al., 1981, chapter 6)

Three different radiometers were used in this work. They are briefly described in the following.

2.3.1 AMSR-E

The AMSR-E instrument (Figure 3) was developed by JAXA and flew on board NASA EOS Aqua satellite on a sun-synchronous polar orbit. The instrument operated in 2002-2011. It measured at 6.9, 10.65, 18.7, 23.8, 36.5 and 89.0 GHz frequencies at H and V polarization at an incidence angle of 55°, and covered a

swath of 1445 km. The FOV ranged from approximately 6 km at 89.0 GHz to approximately 75 km at 6.9 GHz.

The AMSR-E data were used because it was one of the few high-quality spaceborne microwave radiometers available at the time. Compared to earlier SMMR and SSM/I instruments, AMSR-E had much better spatial resolution and more frequency channels. The data are also freely available.

In Publication 1, a one-winter time series of AMSR-E observations in one location were compared to brightness temperature modelled using field measurements inside the same data grid cell. In Publications 2 and 3, the AMSR-E measurements were compared to field and airborne measurements in several places across Finland.

Figure 3. The AMSR-E instrument. Photo: NASA.

2.3.2 HUTRAD

The airborne HUTRAD (Helsinki University of Technology Radiometer, Figure 4, Hallikainen et al., 1996) was built and operated by the Helsinki University of Technology (TKK). HUTRAD used the same frequencies and polarizations as the AMSR-E. The FOV depended on the flight altitude, but was typically about 40 m x 80 m.

In Publication 3, HUTRAD was used in a flight campaign with two long transfer flights across Finland in the north-south direction. The flight route crossed several lakes and rivers, where in situ measurements of snow and ice conditions were available. In addition, a dedicated campaign in the vicinity of Sodankylä in Northern Finland targeted different land covers, such as boreal forests, wetlands and lakes. An extensive field campaign of snow and ice conditions in different land cover types was conducted simultaneously. The field measurements were used to study how well the response of different land cover types could be modelled with a microwave snow model. The airborne HUTRAD measurements were used as a reference for the model. The HUTRAD data and the modelled brightness temperatures were also upscaled and compared to AMSR-E measurements.

Figure 4. The HUTRAD radiometer installed in the TKK Short SC7 Skyvan aircraft. Photo: Jaakko Seppänen.

2.3.3 SodRad 1

SodRad 1 (Sodankylä Radiometer, Figure 5) is the model RPG-8CH-DP manufactured by Radiometer Physics GmbH, Meckenheim, Germany. It measured a 2D pattern, but only observations at an incidence angle of 50° H and V polarization at 10.65, 18.7, 21.0 and 36.5 GHz frequencies were used. The SodRad 1 radiometer was installed in a 4-m tower enabling a multi-year time series of measurements of the same forest opening every 3 hours. The measurement site was equipped with numerous automated reference measurements and manual in situ snow measurements were performed weekly.

In Publication 5, the reference data enabled the modelling of snow structure with a physical snow model, and the results were used as input to a microwave model, which in turn was compared with the SodRad 1 measurements. The multi-year data set made it possible to study the differences in snow conditions between the winters.

Figure 5. Three radiometers in a tower. From left, ELBARA-II (1.4 GHz), SodRad 1 (10.65, 18.7, 21.0 and 36.5 GHz) and SodRad 2 (89.0 and 150 GHz).

3. Snow microstructure and microwave emission

In the retrieval of SWE and other snow properties from microwave radiometer measurements, it is important to understand all the parameters that affect the radiation emitted by the measured target. Therefore microwave emission models are needed to describe the relationship of emitted radiation to different electrical and physical properties of snow. The properties of snow depend on current and past meteorological and environmental conditions, and meteorological observations can be applied in the modelling of snow properties using a physical snow model.

This chapter describes the formation, structure and evolution of a natural snowpack, the modelling of snowpack properties from meteorological data with a physical snow model, and the presentation of snow properties in microwave models. The work focuses on *seasonal snow*, which melts completely every year, contrary to *perennial snow*, which stays on the ground for several years.

3.1 Snowpack structure

Snow consists of a continuous ice matrix and pore space (Fierz et al., 2009), and may contain ice, air, liquid water, water vapour and impurities such as soot, dust or algae. Snow falls in separate precipitation events, and each of these events, as well as other meteorological phenomena, form separate layers (Colbeck, 1991). An example of the layer structure is shown in Figure 6. Typically in a snowpack grain size increases downwards and with time. New layers of fine-grained snow are added on top of the old ones, but in addition, the existing layers evolve through different metamorphism processes which change the shape, size and bonding of snow grains. As snow ages it settles, i.e. the air pores get smaller and snow compacts.

Since weather and climate control the accumulation, melting and metamorphism processes in the snowpack, snow cover is not similar everywhere. One widely used classification system is presented by Sturm et al. (1995). They divide seasonal snow into six climatological classes: tundra, taiga, alpine, prairie, maritime and ephemeral, which differ by snow density and depth, typical grain shapes, layer structure and the number of layers. In addition to the six classes, mountainous areas have a highly spatially variable snow cover. The Sodankylä

area in Northern Finland is in the taiga class, which is characterized by moderate depth and low density, and composes of 50-80 % of depth hoar covered with new snow. The number of layers is high (>15). (Sturm et al., 1995) Southern Finland is mostly maritime, where melt features and wet snow are common. On the coastal area of Finland snow cover is ephemeral, which means that snow often melts after each snowfall completely. (Rasmus, 2005)

Snow properties vary in scales from millimetres to kilometres. In the smallest scale, snow is composed of bonded ice grains. Their size, shape and bonding changes between layers, but also inside a layer. In a metre scale, natural obstacles such as vegetation or rocks affect their surroundings by changing the local topography, radiation balance and wind conditions, which affect the accumulation and metamorphism processes of snow. Solar radiation and wind cause features such as crust layers or dunes in the metre scale. In a kilometre scale, the changes in land cover, vegetation type (forested or open area), soil type and topography affect snow structure.

The overall microwave signature of a snowpack is not just a weighted average of all the layers, but depends on the sequencing of the layers (Colbeck, 1991). The effects are also frequency and polarization dependent. Grain shape is relevant for microwave scattering, as scattering models typically assume spherical or some other simplified shape of scatterers. The further the actual grain shape differs from sphere, the higher is the inaccuracy of the scattering model.

3.1.1 Snow metamorphism

Snow metamorphism is driven by the energy, mass and momentum exchanges in the snow-atmosphere interface (Bartelt and Lehning, 2002; Rasmus, 2005). The mass and energy fluxes between snow and atmosphere include sensible heat (change in temperature of snow), latent heat (phase changes, such as melting, freezing, sublimation and deposition) and radiative energy (longwave and shortwave radiation). In practice, the energy, mass and momentum fluxes are controlled by meteorological conditions. Sensible and latent heat fluxes are governed by changes in air temperature. Sun elevation and cloudiness determine the incoming radiative flux. Incoming longwave radiation is affected by the existence of tree canopy. A detailed overview of snow metamorphism processes can be found from Rasmus (2005).

In the metamorphism processes, parts of the ice grains sublimate, while new ice is deposited on other parts of the grains changing their size and shape. Local environmental conditions, mainly temperature gradient and vapour pressure in the snowpack, determine whether the grains grow or shrink and also govern the shape of the resulting grains. Natural snow is close to its triple point, and therefore water transitions between ice, liquid water and water vapour phases easily.

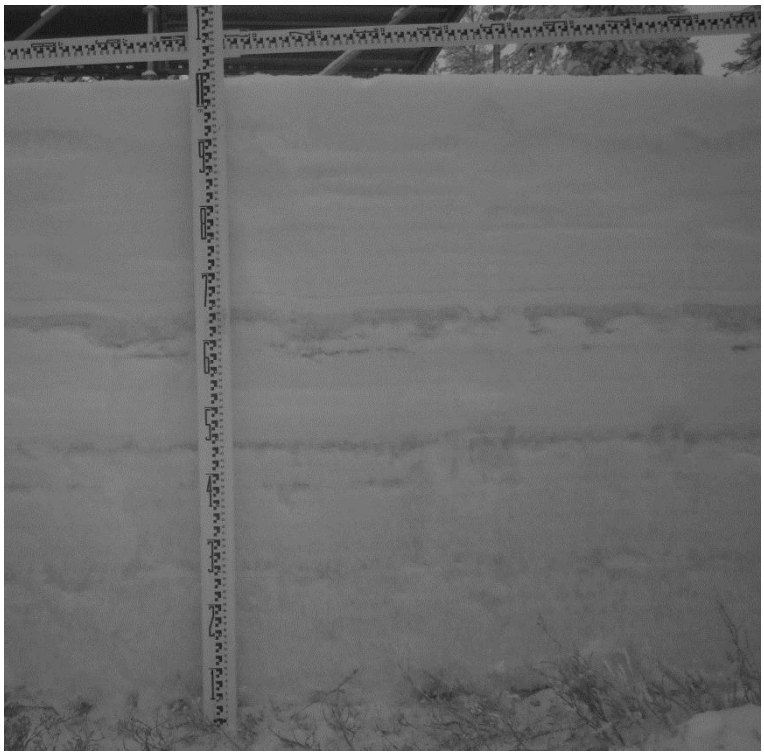

Figure 6. Near infrared (NIR) photo of a snowpack showing the layer structure on March 1, 2016 in Sodankylä, Finland. The darker layers have larger grain size, and the darkest ones are ice crusts. Snow depth is 99 cm. Photo: Tom Watts.

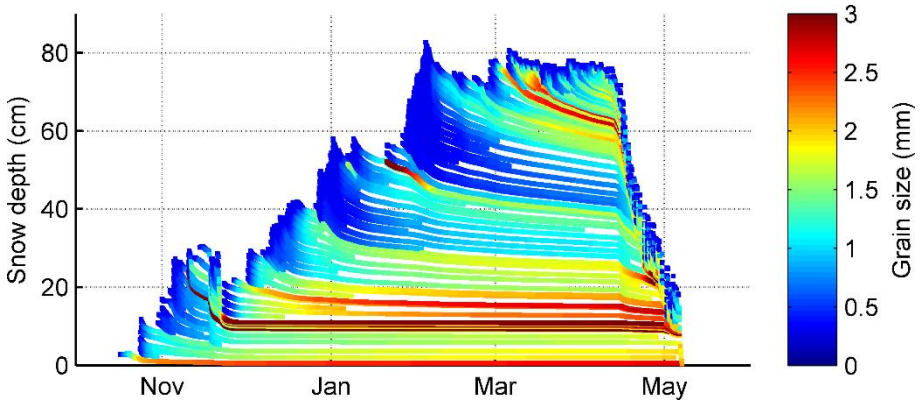

Figure 7. The evolution of snow grain size (E) in Sodankylä, Finland, in the winter of 2012-2013 modelled with SNOWPACK. Based on Figure 6b of Publication 4.

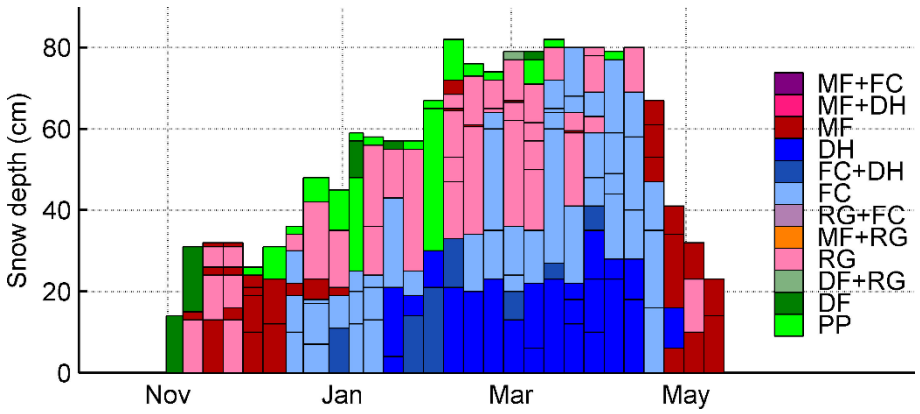

Figure 8. Weekly measurements of manually determined grain shape profiles in Sodankylä, Finland, in the winter of 2012-2013. Grain shapes are defined in Table 1.

Table 1. Snow grain shape classes according to Fierz et al. (2009).

Class	Code
Precipitation particles	PP
Decomposing and fragmented precipitation particles	DF
Rounded grains	RG
Faceted crystals	FC
Depth hoar	DH
Surface hoar	SH
Melt forms	MF
Ice formations	IF
Machine made snow	MM

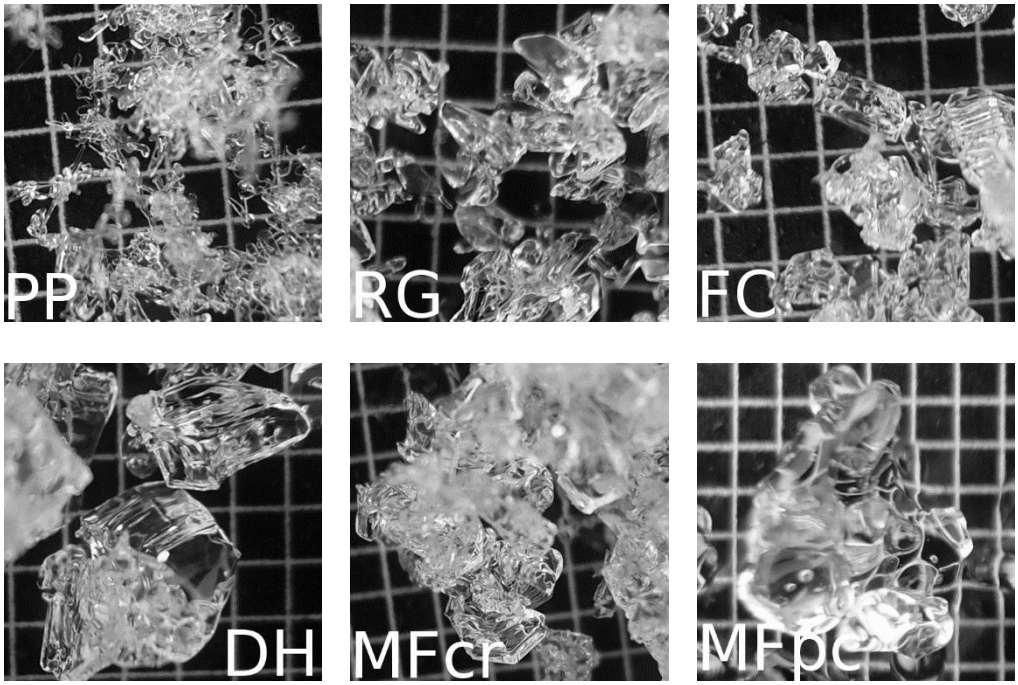

Figure 9. Six examples of snow grains on a 1-mm grid from top left: broken dendrites and other precipitation particles (PP), rounded grains (RG), faceted crystals (FC), depth hoar crystals (DH), melt-refreeze crust (MFcr) and melted polycrystals (MFpc). First five pictures are from different layers of one snow pit on February 4, 2014. The melted crystals are from May 14, 2014.

The most widely used classification system for grain shape is the International Classification for Seasonal Snow on the Ground (Fierz et al., 2009). It defines nine classes for grain shape presented in Table 1. All the classes are further divided into subclasses for more accurate characterization of grain shapes and their history. A modelled time series of snow grain size E (see Chapter 3.1.3 for definition) for one winter is shown in Figure 7. Figure 8 shows the manually determined layers and their grain shapes for the same winter.

New snow consists of precipitation particles (PP) whose shape depends on environmental conditions on their path through the atmosphere. New snow grains often have complex shapes and they are characterized by high specific surface area (SSA, see Chapter 3.1.3) and low density. One possible form is a dendritic particle (Figure 9 top left).

The most important factor in snow metamorphism is the temperature gradient between ground and atmosphere (Colbeck, 1982). Temperature cycling at snow surface due to changes in atmospheric temperature e.g. between day and

night may increase the speed of the processes (Ebner et al., 2016). If the temperature gradient in snow is small (<5 K/m), ice crystals and water vapour in snow are in equilibrium, and grain growth is very slow. This is called equi-temperature metamorphism. Despite the equilibrium, there are small temperature variations between different parts of snow grains, which cause destructive metamorphosis: the small details, such as dendrites, disappear and the grains round (Figure 9 top middle). At the same time, snow grains experience sintering, in which ice bridges and bonds grow between individual grains (Rasmus, 2005). Equi-temperature metamorphism transforms the beautiful dendritic shapes of new snowflakes to rounded grains (RG).

When the temperature gradient is 5-15 K/m, both equi-temperature and kinetic growth processes happen, and faceted crystals (FC, Figure 9 top right) grow but slowly (Rasmus, 2005). Fast kinetic growth occurs when the temperature gradient exceeds 20 K/m. Water sublimates from the warmer top of snow grains and deposits on the cold bottom surfaces of the grains in the layer above. Hexagonal striated shapes grow downwards forming typical depth hoar (DH) shapes (Figure 9 bottom left).

Wind, rain, solar radiation and melt-refreeze cycles may form hard crust layers on snow surface (Figure 9 bottom middle). Wet snow metamorphism (Brun, 1989) occurs when liquid water is present, typically late in the spring when snow is melting. This is one of the equi-temperature metamorphism processes, and the grains are round and either in clusters or as single crystals in liquid (Figure 9, bottom right).

3.1.2 Physical snow models

The determination of snowpack structure is mainly manual work (Kinar and Pomeroy, 2015; Leppänen et al., 2016); there are no automated measurement equipment for snow stratification. The traditional method requires digging a snow pit, like the one in in Figure 6, to determine snow structure manually form differences in snow hardness, wetness and grain sizes and shapes. New semi-automatic equipment such as the SnowMicroPen (SMP) can determine layer, density and SSA profiles without snow pits (Proksch et al., 2015), but they are still manual tools. Therefore physical snow models offer an enticing possibility to model snow micro- and macrostructure from automated measurement data. An example of the output of a snow model is shown in Figure 7. Compared to manual measurements in Figure 8, the temporal and vertical resolutions are much better. However, the accuracy of the output profile depends on the quality of the model and input data used.

There are several physical snow models of differing complexity, which predict various parameters of the snowpack such as thickness, density, volumetric moisture, grain size and temperature of each layer from the history of meteorological and radiation observations at a site. The most detailed models are Crocus (Brun et al., 1992; Vionnet et al., 2012) and SNOWPACK (Bartelt and Lehning, 2002; Lehning, Bartelt, Brown and Fierz, 2002; Lehning, Bartelt, Brown, Fierz, et al., 2002). Crocus was developed for the French and SNOWPACK for the

Swiss avalanche warning systems. These models calculate the macro- and microstructural processes and output detailed snowpack structure and various parameters for numerous layers. An example of a simpler snow model is the Joint UK Land Environment Simulator (JULES) model (Best et al., 2011), which models snow as part of a complete land surface system. It can be coupled with NWP or climate models. It is possible to include several snow layers in JULES, but snow physics and structure are not modelled in as much detail as in Crocus or SNOWPACK (Vionnet et al., 2012).

The SNOWPACK model was applied in Publications 4 and 5 of this thesis, because it is widely used and actively developed. It solves numerically the 1-D partial differential equations of mass, energy and momentum conservation from snow. SNOWPACK was used as a proof of concept to study whether grain size parameters from any physical snow model could be coupled with the HUT snow emission model. SNOWPACK was chosen for its complexity; it includes most of the processes governing the evolution of snowpack and is therefore quite accurate. At the same time it requires many input parameters which are often not available in the large scale, especially in real time. Further work will have to rely on some simpler snow model, which does not require so many input parameters. SNOWPACK grain metamorphism and the equations governing grain growth rate are explained in detail in Publication 5 and in Bartelt and Lehning (2002) and Rasmus (2005).

3.1.3 Snow microstructure parameters

Snow microstructure is the key variable affecting the scattering of microwave radiation in snow. The microstructural variations of snowpack ("snow grains") are about the same size as the microwave electromagnetic wavelength in snow, and even small variations in grain size alter the microwave response of snow significantly. Snow grains in a natural snowpack are bonded and form a continuous ice matrix. In addition, each layer contains a distribution of snow grain sizes and shapes. Despite this complexity, typically one grain size-related parameter for the whole snowpack is used as a proxy for scattering particle size in microwave models. This simplification does not take into account the bonding, shape or size distribution of the grains or snow stratification.

Several different snow microstructural parameters have been defined: *Correlation length* (p_c) is the slope of the autocorrelation function (Mätzler, 2002). It is arguably the best method to describe the scattering of microwave radiation is snow, but determining correlation length from structural snow samples (Wiesmann et al., 1998) is slow and not suitable for large-scale use. A novel method for determining correlation length from SMP measurements has been developed (Proksch et al., 2015), but suffers from calibration problems.

Optical grain size (D_0) is the diameter of identical ice spheres that have the same optical properties as the snow in question, i.e. the same surface area to volume ratio or specific surface area (SSA, Grenfell and Warren, 1999). Correlation length, optical grain size and SSA are theoretically defined and can be objectively measured, although there might be differences between values measured with different techniques. SSA is becoming the most widely used

snow microstructure parameter, because it is theoretically defined and fairly easy to measure in the field using various techniques, even though it is not necessarily the best parameter in the microwave region; as the largest grains scatter the most radiation, the distribution of different grain sizes in a natural snow layer cannot be represented with identical ice spheres in the microwave region (Roy et al., 2013). As the name optical grain size suggests, the properties of the identical spheres are the same as the original snow sample only at optical wavelengths.

The traditional measure of *snow grain size* (E) is the average of the greatest extension of individual grains in a layer (Fierz et al., 2009), and is defined on the field by comparing snow grains to a mm-grid (Figure 9). This method is subjective, as it requires the separation of single snow crystals, which might be tightly bonded, and the estimation of average size of a distribution of grain sizes. Empirical relationships between E and p_c can be established (Durand et al., 2008; Hallikainen et al., 1987), but they may not hold for the whole range of natural snow types. The equation for the scattering of radiation in snow used in the HUT snow emission model is based on snow grain size E.

3.2 Microwave modelling

Several snow microwave emission models with differing complexity have been presented in the literature, including the Helsinki University of Technology (HUT) snow emission model (Pulliainen et al., 1999), the Microwave Emission Model for Layered Snowpacks (MEMLS, Wiesmann & Mätzler 1999), Strong Fluctuation Theory (SFT, Wang et al. 2000), the Dense Media Radiative Transfer model based on quasi-crystalline approximation (DMRT-QCA) (Tsang et al., 2000), a parameterized multiple-scattering model by Jiang et al. (2007) which is based on the DMRT model, and the newly developed Snow Microwave Radiative Transfer (SMRT) model (Sandells et al., 2016). They range from purely theoretical to empirical, have different input and output parameters and different methods to model snow-microwave interactions (Maslanka et al., 2016; Pan et al., 2016; Tedesco and Kim, 2006b). However, comparison of different models is difficult, as they use different microstructural parameters (Tedesco and Kim, 2006b).

One of the main differences between the models is whether they consider scattering inside snowpack to be mainly coherent or incoherent; incoherent scattering includes only the average power scattered by randomly distributed particles, while coherent scattering takes into account the small random fluctuations in amplitude and phase (Ishimaru, 2013). The HUT model is incoherent, while DMRT-QCA, SFT and SMRT are coherent. MEMLS includes tuned combination of coherent and incoherent scattering. Another major difference is the parameterization of snow microstructure; SFT treats snow as a continuous random medium with permittivity fluctuations, while the other models consider snow as a collection of discrete spherical scatterers. This thesis focuses on the HUT snow emission model, which was applied in Publications 1, 2, 3 and 5.

3.2.1 The HUT snow microwave emission model

The HUT snow emission model (Lemmetyinen et al., 2010; Pulliainen et al., 1999) is a semi-empirical radiative transfer-based model. Compared to theoretical models, it is relatively simple, which enables direct iterative inverse solving of the model. The main snow parameters needed for the calculation of brightness temperature are grain size E, temperature, density and SWE of each snow layer. Snow wetness is also an important input parameter, but this work focuses on dry snow.

For a homogeneous snow layer with a thickness d, the brightness temperature at the snow-air boundary is (Pulliainen et al., 1999)

$$T_{SNOW}(\theta) = T_B(0^+,\theta)e^{-(\kappa_e - q\kappa_s)d\sec(\theta)} + \frac{\kappa_a T_s}{\kappa_e - q\kappa_s}\left(1 - e^{-(\kappa_e - q\kappa_s)d\sec(\theta)}\right), \quad (10)$$

where θ is the propagation angle of the radiation (rad), $T_B(0^+,\theta)$ is the upwelling radiation from soil (K), κ_e, κ_s and κ_a (1/m) are the extinction, scattering and absorption coefficients, respectively, and T_s is the physical snow temperature (K). The main assumption in the HUT snow emission model is that the scattering of propagating radiation is mostly concentrated in the forward direction. This assumption leads to the empirical parameter q = 0.96 in Eq. (10). The first term describes the radiation from below the snow layer and the second is the emission of the layer in question. An empirical equation is used to relate snow extinction coefficient κ_e (in dB/m) to frequency (in GHz) and snow grain size (Hallikainen et al., 1987)

$$\kappa_e = 0.0018 f^{2.8} E^{2.0}, \quad (11)$$

where E is snow grain size (mm).

The original model version (Pulliainen et al., 1999) assumes one homogeneous snow layer, but later a multi-layer version of the model (Lemmetyinen et al., 2010) was developed. The same two-flux approximation that was used in the one-layer model is applied for each layer of the multi-layer version. The up- and downwelling brightness temperatures of layer n are (Lemmetyinen et al., 2010)

$$T_{n,\uparrow} = S_n\left(T_{SNOW,n} + T_{n+1,\downarrow}\frac{t_n r_{F,n-1}}{l_n^2} + T_{n-1,\uparrow}\frac{t_{n-1}}{l_n} + T_{SNOW,n}\frac{r_{F,n-1}}{l_n}\right), \quad (12)$$

$$T_{n,\downarrow} = S_n\left(T_{SNOW,n} + T_{n+1,\downarrow}\frac{t_n}{l_n} + T_{n-1,\uparrow}\frac{t_{n-1} r_{F,n}}{l_n^2} + T_{SNOW,n}\frac{r_{F,n}}{l_n}\right), \quad (13)$$

where t_n, $r_{F,n}$ and l_n are the Fresnel transmission and reflection coefficients and the loss factor of layer n, respectively, and S_n is the geometric sum of multiple reflections in layer n:

$$S_n = \frac{1}{1 - r_n r_{n-1}/l_n^2}. \quad (14)$$

In addition to snow, ice or water layers can be included in the multi-layer system, enabling its use in the case of snow on lake ice (Publications 2 and 3). Only incoherent effects are considered when reflection and refraction at layer interfaces are calculated. All interfaces except the lowest are considered ideally smooth. Only small random variations in the surface height of the lowest snow/soil or ice/water interface (h_s in the following) are considered. The lowest layer (soil or water) is considered semi-infinite. (Publication 2)

3.2.2 Scene brightness temperature

As discussed in Chapter 2.1, the brightness temperature observed from space (the top-of-atmosphere brightness temperature $T_{B,TOA}$) is not just the contribution of snow; the subnivean medium, vegetation, atmosphere and cosmic background need to be included. In the HUT snow emission model, this is taken into account with (Pulliainen et al., 1999)

$$T_{B,TOA}(\theta) = t(\theta)T_{B,gnd}(\theta) + T_{atm,\uparrow}(\theta) + t(\theta)\left(1 - \epsilon_{gnd}(\theta)\right)\left(T_{atm,\downarrow}(\theta) + t(\theta)T_c\right), \quad (15)$$

where t is the atmospheric transmissivity, $T_{B,gnd}(\theta)$ is the brightness temperature of the ground scene (including subnivean layers, snow and vegetation, K), $T_{atm,\uparrow}$ and $T_{atm,\downarrow}$ are the up- and downwelling atmospheric brightness temperatures (K), ϵ_{gnd} is the emissivity of the ground scene and T_c = 2.7 K is the cosmic background radiation.

One way of coping with the mixed pixel problem is to take into account the fraction of different land cover types inside a FOV, e.g.

$$T_{B,gnd} = \sum_{\mu=1}^{M} \beta_\mu T_{B,\mu}, \quad (16)$$

where β_μ is the fractional coverage of land cover type μ, $T_{B,\mu}$ is the brightness temperature originating from the land cover type μ (K), and $\sum_{\mu=1}^{M} \beta_\mu = 1$. This method was applied in Publications 2 and 3.

Ice

For ice layers between or below snow layers, it is assumed that q = 1, and Eq. (10) becomes (Lemmetyinen et al., 2010)

$$T_{ICE} = T_i\left(1 - e^{-\kappa_a d \sec(\theta)}\right), \quad (17)$$

where T_i is the physical temperature of ice (K).

Soil

The Rough bare soil reflectivity model (Wegmüller and Mätzler, 1999) was applied in Publications 1, 2 and 3. However, as this model was later found to be inaccurate with frozen soil, it was replaced with another model (Wang and Choudhury, 1981) in Publication 5.

The Rough bare soil reflectivity model describes the reflectivity of soil at polarization p $r_{p,mod}$ with

$$r_{H,mod} = r_{H,F} e^{-(kh_s)\sqrt{0.10 \cos\theta}}, \quad (18)$$

$$r_{V,mod} = r_{h,mod} (\cos\theta)^{0.655}, \quad (19)$$

where $r_{p,F}$ is the Fresnel reflectivity at polarization p (Eqs. (6) and (7)), k is the wave number (1/m), and h_s is the standard deviation of the surface height (m). The Wang and Choudhury model is

$$r_{H,mod} = \left[(1-Q) r_{H,F} + Q r_{V,F}\right] e^{-h_s \cos^2\theta}, \quad (20)$$

$$r_{V,mod} = \left[(1-Q) r_{V,F} + Q r_{H,F}\right] e^{-h_s \cos^2\theta}, \quad (21)$$

where Q is a parameter for polarization mixing due to surface roughness.

Soil parameters are often considered empirical fitting parameters and optimized for the used data set or location (as in Publications 2 and 3), or typical fixed values are used (as in Publication 1). Publication 5 used measured permittivity values, but the parameters Q and h were still optimized.

Water

The emissivity of the bottom water layer is considered by calculating the dielectric constant of water according to Klein and Swift (1977), which takes into account water salinity. The reflectivity of polarization p at ice-water interface is calculated with

$$r_{p,mod} = \sqrt{{r_{p,F}}^2 e^{-4(kh)^2 \cos^2\theta}}. \quad (22)$$

Forest

Even though taiga, or the boreal forest zone, covers about 25 % of the Northern Hemisphere land mass, retrieval of snow parameters in forests is problematic due to attenuation and emission by the canopy cover. There are some studies about remote sensing of SWE in forests (Cai et al., 2017; Cohen et al., 2015; Derksen et al., 2005; Goïta et al., 2003; Vander Jagt et al., 2015; Kruopis et al., 1999), but this is still mostly an unresolved problem. Several on-going measurement campaigns, e.g. NASA SnowEx, focus on this issue.

Publications 1, 2 and 3 applied the vegetation model by Kruopis et al. (1999). Forest transmissivity t is modelled with

$$t(f,V) = t\left(f, V_{high}\right) + \left[1 - t\left(f, V_{high}\right)\right] e^{-0.035V}, \quad (23)$$

$$t\left(f, V_{high}\right) = 0.42 + 0.58 e^{-0.028f}, \quad (24)$$

where $t\left(f, V_{high}\right)$ is the empirical frequency dependent saturation value of forest transmissivity, f is frequency (GHz) and V is the forest stem volume (m^3/ha). In addition, the emission from forest, both up- ($T_\uparrow$) and downwelling ($T_\downarrow$), needs to be taken into account:

$$T_{\uparrow} = T_{veg}(1-t), \quad (25)$$
$$T_{\downarrow} = T_{veg}(1-t)(1-\epsilon_{snow})t, \quad (26)$$

where T_{veg} is the physical temperature (K) of vegetation and ϵ_{snow} is the emissivity of snow. The Kruopis et al. model was later found to be inaccurate. Nowadays a better model for boreal forests has been published (Cohen et al., 2015).

Atmosphere

Two models for atmospheric effects, a statistical (Ascbacher, 1989; Pulliainen et al., 1993) and a physical model (Ulaby et al., 1981, chapter 5), were compared in Publication 1. The statistical model was applied in Publications 2 and 3.

In the statistical model, the up- and downwelling atmospheric brightness temperatures $T_{atm\uparrow(\downarrow)}$ are modelled with the equation (Pulliainen et al., 1993)

$$T_{atm\uparrow(\downarrow)} = \alpha_{\uparrow(\downarrow)} T_s (1-t), \quad (27)$$

where T_s is the surface air temperature (K) and $\alpha_{\uparrow(\downarrow)}$ are the approximate atmospheric profile factors for determining the effective temperature $\alpha_{\uparrow(\downarrow)} T_s$ of the atmosphere:

$$\alpha_{\uparrow} = -0.073t^2 + 0.101t + 0.918, \quad (28)$$
$$\alpha_{\downarrow} = -0.035t^2 + 0.014t + 0.967. \quad (29)$$

The physical model calculates the upwelling brightness temperature and transmissivity of atmosphere from measured pressure, temperature and humidity profiles using equations presented in (Ulaby et al., 1981) for scattering and absorption of cloud liquid water and ice particles, water vapour and oxygen. This model requires e.g. balloon-borne radio sounding measurements or modelled reanalysis data of atmospheric profiles.

3.2.3 SWE retrieval with the HUT model

The HUT snow emission model is used in an operational global SWE retrieval scheme (Takala et al., 2017). There are three main steps in the retrieval:

1. The snow depth measured at weather stations and a fixed snow density value are used as input to the HUT model. Snow grain size at the weather stations is optimized by minimizing the difference in brightness temperatures between a satellite measurement and the HUT model at the frequency difference $T_{19V} - T_{37V}$.
2. The optimized snow grain sizes and the measured snow depths at the weather stations are interpolated to the satellite data grid using spatial Kriging interpolation.
3. The snow depth and grain size fields, as well as the fixed snow density value, are used as input to the HUT model. SWE is optimized by minimizing the difference between satellite measurement and the HUT model at the frequency difference $T_{19V} - T_{37V}$, taking into account the

error estimates for the snow depth and grain size parameters. In addition, the land cover is considered, and mountainous areas are filtered away and canopy cover is taken into account in forested areas.

The result is a SWE grid for the area where satellite data are available, typically for the Northern Hemisphere.

4. Improving model-based snow parameter retrieval

Publications 1-5 focus on two persisting problems in passive microwave remote sensing of snow: the modelling of snow microstructure properties and the mixed pixel problem. This chapter presents the study problems and the main results of the Publications.

4.1 Snow microstructure and scattering

4.1.1 Extinction coefficient

In the HUT snow emission model, the effect of snow microstructure on the scattering of microwave radiation is modelled using an empirical equation (Eq. (11)). The parameters of the equation were chosen based on laboratory measurements of snow slabs at 18-60 GHz frequency range in Southern Finland (Hallikainen et al., 1987). Grain size E of the slabs varied between 0.2 and 1.6 mm, and their density varied between 0.172 and 0.390 g/cm^3. Grain shape was not characterized.

The empirical equation (11) is only valid for the types of snow that were measured in the experiment, and is not necessarily applicable to different grain shapes or density and grain size values outside the measured ranges. For taiga snow, the covered densities are usually sufficient, but grain sizes up to 5 mm are common in depth hoar layers. In addition, as the grain shape was not characterized, it is difficult to estimate if enough different snow types were included, even though the samples ranged from new to refrozen snow.

Similar empirical equations for extinction coefficient have been formulated based on measurements in other locations. For example, Roy et al. (2004) suggested another semi-empirical equation based on their field measurements in Canada:

$$\kappa_e = \gamma (f^4 E^6)^\delta, \tag{30}$$

where γ and δ are empirical constants, γ = 2±1 and δ = 0.20±0.04, E is snow grain size (mm) and f is frequency (GHz). In their data set, the average grain size of a snowpack varied between 1 mm and 3 mm. The $f^4 E^6$ dependence is based on Rayleigh scattering theory, but as can be seen from the small value of

δ, Rayleigh scattering is not directly applicable to snow without correction for multiple scattering effects.

Snow conditions in Turkey are quite different from Finland and Canada, as it is classified as maritime, which has many melt features and wet snow, or prairie, which is characterized by thin and hard snow cover severely affected by wind. Turkey is also mountainous, meaning that snow cover has high spatial variability. (Sturm et al., 1995) Therefore the empirical coefficients of Eqs. (11) and (30) are not necessarily directly applicable there. The equation used in the Middle East Technical University (METU) in Turkey is similar to Eq. (11), but has differing coefficients (Publication 1):

$$\kappa_e = 0.08 f^{1.75} E^{1.8}, \tag{31}$$

where f is frequency (GHz) and E is snow grain size (mm).

The effect of grain size on the extinction coefficient of snow using the three equations is shown in Figure 10. In addition, the extinction coefficient of Eq. (11) with the effective grain size correction (Eq. (32), Chapter 4.1.2) is depicted. The extinction coefficient calculated with Eq. (30) differs from the other two, while Eqs. (11) and (31) behave quite similarly, which was expected as they have only small differences in the constants.

In Publication 1, the three models for extinction coefficients were compared in the Sodankylä area in Northern Finland. Brightness temperatures calculated with the HUT snow emission model from bi-weekly snow pit measurements during the winter of 2006-2007 were compared to AMSR-E data. None of the three equations were found to be substantially better than the others; the results depended on frequency and polarization (Figure 11). Overall in the 6.9-90 GHz range, Eq. (11) had the lowest unbiased rms (root-mean-square) error on most channels for the whole winter and for dry snow periods only, and was therefore determined to be the best for the snow types in question.

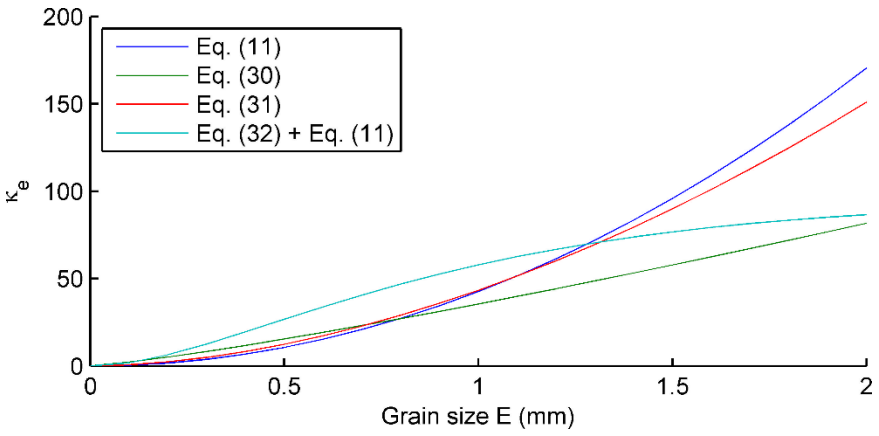

Figure 10. The effect of grain size on extinction coefficient κ_e at 36.5 GHz V-pol simulated with the three extinction coefficient models (Eqs. (11), (30) and (31)) and the effective grain size correction (Eq. (32)).

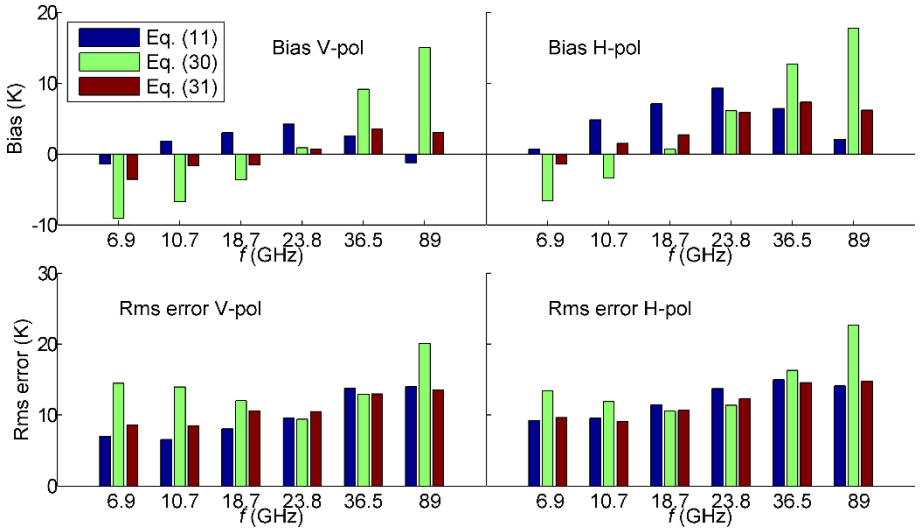

Figure 11. The biases and rms errors of one-winter time series of brightness temperature compared to AMSR-E measurements. Based on Tables IV and V of Publication 1.

4.1.2 Effective grain size

Effective grain size (d_{eff}) is the grain size which minimizes the brightness temperature difference between measurements and modelling results. It is a purely empirical fitting parameter and used to correct for simplifications in the presentation of snow microstructure in a microwave scattering model. In addition, all other modelling inaccuracies are included in the effective grain size. However, if measured or modelled grain sizes correspond with the effective grain size, they are suitable for characterizing snow microstructure in a microwave emission model. Grain size parameters used in this section are explained in Table 2.

In Publication 1, the effective grain size at $T_{18.7V} - T_{36.5V}$ was retrieved using AMSR-E measurements and HUT model simulations, which applied the in situ data of one bi-weekly snow pit. The relationship between d_{eff} (mm) and the layer-thickness weighted average of manually measured grain size E_{pit} (mm) was found to be

$$d_{\text{eff}} = 1.5\left(1 - e^{-1.5 \cdot E_{pit}}\right). \tag{32}$$

This frequency-independent equation scales down grain sizes larger than 1.5 mm and therefore removes grain sizes outside of the validity range of Eq. (11). It also changes the response of extinction coefficient as a function of grain size to be similar with Eq. (30) (Figure 10). This equation for effective grain size improved the rms error of brightness temperature simulations in Publication 1 by 20 % at 36.5 GHz V-pol. It was later used by Gunn et al. (2011), who concluded that this equation reduces errors in simulated brightness temperature substantially.

In Publication 5, the effective grain size was retrieved similarly from tower-based microwave measurements using automated snow measurements with the HUT snow emission model, and compared to SNOWPACK modelling results (Figure 12). SNOWPACK was found to model the evolution of effective grain size well, but there were large winter-dependent biases, which were attributed to

snow structure. Because the retrieved grain size is an average value for the whole snowpack, it includes the effects of stratification. The grain sizes in Figure 12 are layer SWE-weighted averages of modelled profiles. Especially the winter of 2010-2011, which differs from the others with much lower biases in both grain size parameters, was characterized by shallow snowpack and cold air temperatures, which lead to significant grain size growth and depth hoar formation compared to the other studied winters. Since the trend of modelled grain sizes followed the effective grain size, the main conclusion of Publication 5 was that grain sizes modelled with SNOWPACK are usable with the HUT snow emission model, but the biases must be taken into account.

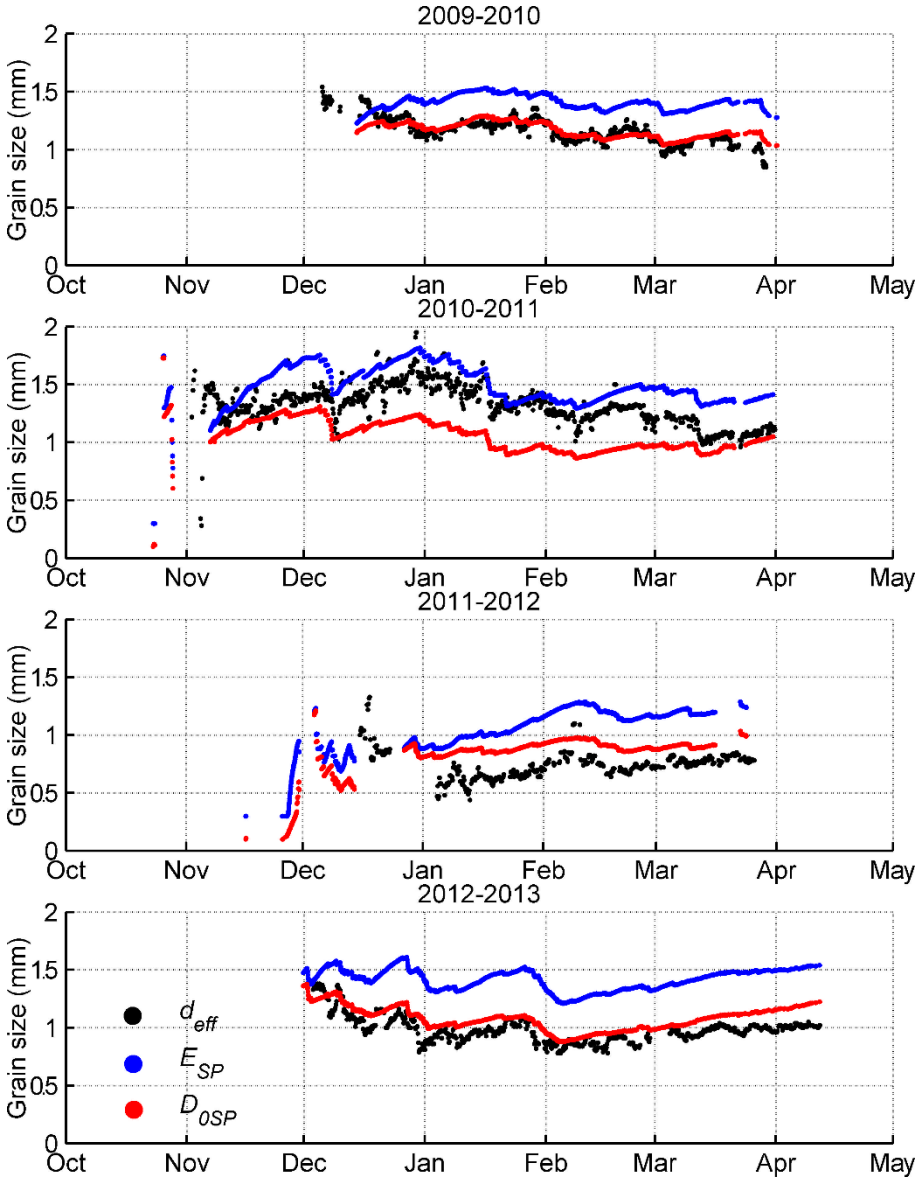

Figure 12. Time series of the effective grain size (d_{eff}) compared to E_{SP} and $D_{0\mathrm{SP}}$ values modelled with SNOWPACK in Sodankylä, Finland for four winters 2009-2013. Based on Figure 4 of Publication 5. Grain size symbols are explained in Table 2.

Table 2. Explanations of snow grain size parameters.

Parameter	Symbol	Explanation
Effective grain size	d_{eff}	The grain size which minimizes the TB difference between measurements and modelling results.
Optical grain size	D_0	The diameter of identical ice spheres that have the same surface area to volume ratio as the snow in question.
IceCube optical grain size	D_{0IC}	Average optical grain size D_0 in snowpack measured using the IceCube instrument
SNOWPACK optical grain size	D_{0SP}	Average optical grain size D_0 in snowpack modelled with SNOWPACK.
Snow grain size	E	The average of the greatest extension of individual grains in a layer.
Manual grain size	E_{pit}	Average grain size E in snowpack from manual measurements.
SNOWPACK grain size	E_{SP}	Average grain size E in snowpack modelled with SNOWPACK.

4.1.3 Grain size from a physical snow model

Even though optical and traditional grain sizes have been clearly defined, there might be differences in the calibrations of different field measurement methods or the interpretation of the parameters in microwave and physical snow models. Therefore the grain size values modelled with SNOWPACK were rigorously compared with field measurements in Publications 4 and 5. A similar comparison for Finnish snow has already been made by Rasmus (2005), but since then the SNOWPACK model has been developed further.

Publication 4 compared two winters 2011-2013 of field measurements of traditional grain size E and optical grain size D_0 (E_{pit} and D_{0IC}) to SNOWPACK output (E_{SP} and D_{0SP}) using average snowpack values (Figure 13). The E values were on the same level, but manual measurements had much more variability from one measurement to another probably due to the subjective nature of the measurement. On the other hand, the difference between D_0 values was notable; the modelled D_{0SP} was almost twice the measured D_{0IC} value. It is not clear if the measured or modelled values are more accurate. There are numerous sources of inaccuracies in both. For example, the IceCube instrument actually measures reflectivity of the snow sample surface, and D_{0IC} is calculated from SSA, which in turn is derived from reflectivity with the help of the radiative transfer model DISORT (Discrete Ordinates Radiative Transfer Program for a Multi-Layered Plane-Parallel Medium) assuming disconnected spherical scatterers (Gallet et al., 2009). However, grain shape has an effect of ± 25 % on reflectivity (Picard et al., 2009).

Based on these results, scaling factors between measured and modelled values were determined so that

$$D = \beta D_{SP}, \tag{33}$$

where D is the measured parameter (mm), D_{SP} is the modelled parameter (mm) and β is the scaling factor. For the two-winter data set shown in Figure 13, values of $\beta_E = 1.24$ and $\beta_{D_0} = 2.11$ were determined.

The resulting scaling factors β are only valid for the data set used in Publication 4. Because only snowpack average values were used, the scaling factor is in

fact a means to describe the effect of typical snow structure. Therefore it is dependent on location, time, and meteorological conditions.

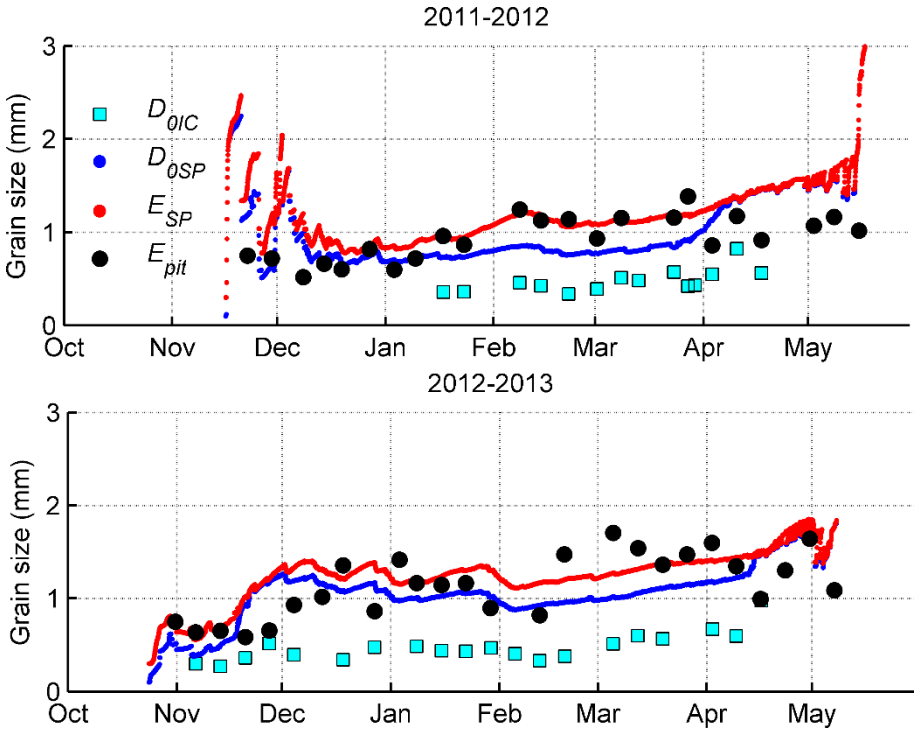

Figure 13. Time series of grain sizes E and D_0 measured in the field (E_{pit} and D_{0IC}) and modelled with SNOWPACK (E_{SP} and D_{0SP}) for 2011-2012 and 2012-2013 in Sodankylä, Finland. Based on Figure 8 of Publication 4. Grain size symbols are explained in Table 2.

In Publication 5, the SNOWPACK-modelled grain size profiles were compared to weekly manual measurements of four winters 2009-2013 using agreement score (Lehning et al., 2001), which is a means to compare measured and modelled values with differing vertical resolution. In this method, corresponding layers are searched for from the measured and modelled profiles, and values are compared layer by layer. The equations for agreement score calculation are presented in (Lehning et al., 2001) and overviewed in Publication 5. The results are summarized in 0 as mean values for each winter, and show a fairly good agreement (0.85-0.91) for E. Reflecting the results of Publication 4, the agreement score for D_0 is lower (0.74-0.75). Time series of the agreement scores are shown in Figure 14. The scores for E are lower in the beginning of each snow season than later in the winter. This can be explained by the inhomogeneity of the early shallow snow cover. For D_0, a similar trend is not obvious.

The comparisons of SNOWPACK grain sizes with manual measurements show that SNOWPACK is able to simulate the evolution of E with reasonable accuracy. However, the simulated D_0 values exhibit a large positive bias, which possibly originates from the definition of grain sizes in the SNOWPACK model; D_0 is calculated from E and two theoretical parameters, sphericity and dendricity (Publication 5), and E on the other hand is a mapping of sphericity and dendricity to field observations.

Table 3. Mean agreement scores for each winter. Based on Table 1 of Publication 5.

Parameter	2009-2010	2010-2011	2011-2012	2012-2013
E	0.85	0.87	0.88	0.91
D_0	-	-	0.75	0.74

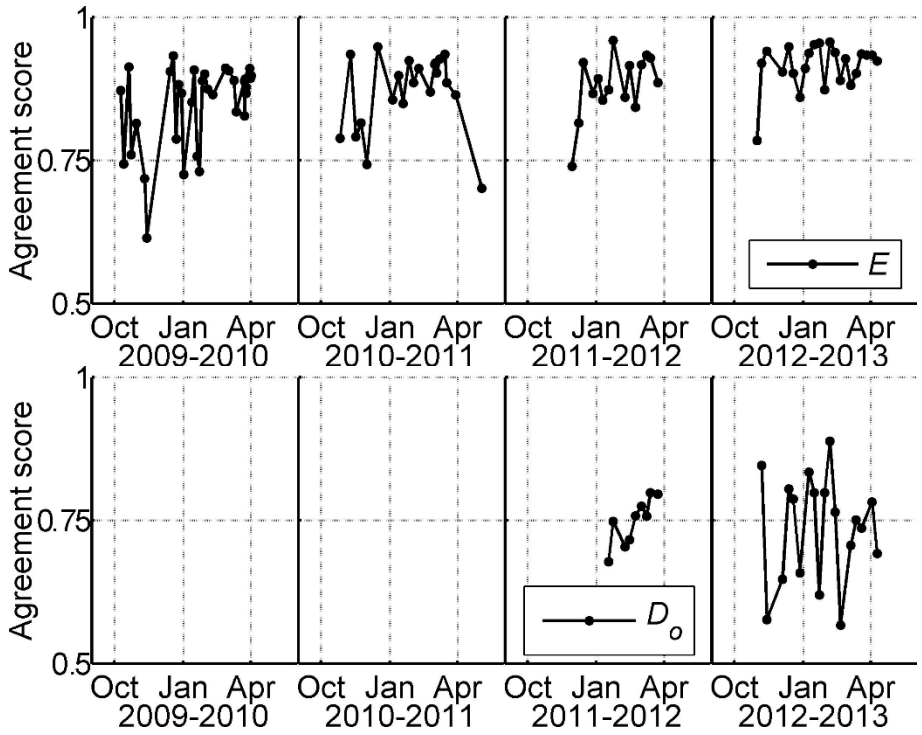

Figure 14. Time series of agreement scores for grain sizes E and D_0 between SNOWPACK profiles and manual measurements in Sodankylä, Finland in 2009-2013. Based on Figure 2 of Publication 5.

4.1.4 SWE retrieval using modelled snow parameters

The goal of Publication 5 was to find out if SNOWPACK or some other simpler physical snow model could be coupled with the HUT snow emission model in order to retrieve SWE from spaceborne brightness temperature measurements, providing ancillary information especially on snow microstructure. SNOWPACK was chosen because it includes most of the processes governing the evolution of snow. On the other hand, it requires many input parameters which often are not available in the large scale especially in real time. This study used the best data and models available, but future work focusing on operational SWE retrieval must rely on some simpler physical snow model.

The results were promising in the sense that the grain size parameter in the HUT snow emission model had a connection with the grain size of a physical snow model despite all the modelling inaccuracies.

SNOWPACK grain sizes, temperature and density profiles were used in SWE retrieval from tower-based radiometer measurements to test their applicability in a case where the radiometer footprint is well-known. Averaged snow profiles were used in the retrieval. The results are compared to SWE modelled directly by SNOWPACK and to manual field measurements in Figure 15. The comparison shows that SNOWPACK was able to model total SWE very well, in part due

to use of measured snow depth as a driving parameter in SNOWPACK instead of precipitation. However, the retrievals from microwave radiometer measurements were not as successful. Especially the difference between the two retrievals with SNOWPACK grain size parameters $D_{0,SP}$ and E_{SP} highlighted the effect of small changes in the scattering particle size to brightness temperature. There was also considerable difference between the first two and the last two winters: during the first two winters, the retrieval applying E_{SP} had very low bias and rms error (Table 4), while in the last two winters the retrieval applying D_{0SP} performed better. The most probable explanation is the structure of the snowpack; in the first two winters, the effective grain size (Figure 12) was between 1 mm and 1.5 mm, while in the last two winters it was mostly below 1 mm, indicating a smaller portion of large depth hoar crystals in the snowpack. Therefore, when grain size growth was substantial, the retrieval with grain size E_{SP} performed better.

The results show that if SNOWPACK succeeded in the modelling of snow properties, the SWE retrieval had a bias of <15 mm and an rms error of about 20 mm. However, the conditions in which SNOWPACK modelled all relevant snow parameters well could not be determined based on the measurements of four winters. Therefore direct application of snow parameters from SNOWPACK or any other physical snow model in SWE retrieval requires further study.

Table 4. The biases and rms errors of two SWE retrievals using SNOWPACK-modelled temperature, density and grain size (either D_{0SP} or E_{SP}) and SWE modelled by SNOWPACK. Based on Table 4 of Publication 5.

Winter	Bias (mm)			Rms error (mm)		
	D_{0SP}	E_{SP}	SNOWPACK	D_{0SP}	E_{SP}	SNOWPACK
2009-2010	68	4	27	76	43	32
2010-2011	108	-12	-1	123	21	16
2011-2012	-15	-68	17	19	71	21
2012-2013	1	-76	-12	22	83	17
2009-2013	48	-33	10	78	58	24

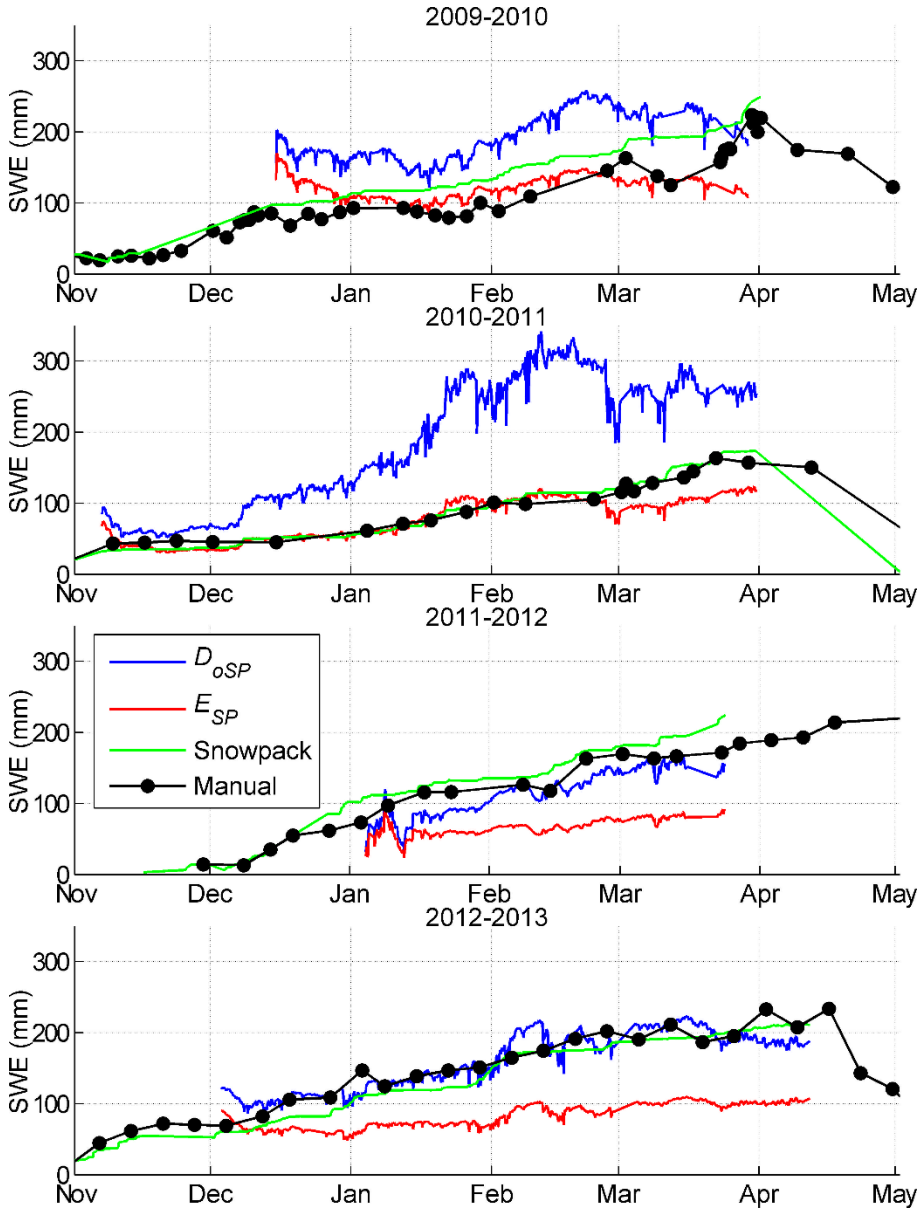

Figure 15. Time series of SWE from two retrievals using SNOWPACK profiles with D_{0SP} and E_{SP} compared to SWE modelled with SNOWPACK and measured manually. Based on Figure 7 of Publication 5.

4.2 Mixed pixel problem

In Finland and in the boreal forest region in general, small lakes and wetlands are common features in the landscape. Their effect on the microwave brightness temperature is two-fold. First, the contrast in the relative permittivity of water and soil decreases the brightness temperature in lake areas (Figure 16). As the penetration depth of microwave radiation into snow is frequency dependent, the effect of lakes is higher at lower frequencies. Second, snow depth, density and microstructure on lake ice are different from the surrounding land areas. One example of snow depth every 100 m on lake and the surrounding land area is shown in Figure 17. On lake ice the total snow depth and its variation were much smaller than on the land area with varying forest cover. The effect of snow structure on brightness temperature is visible in Figure 16 as well; the 36.5 GHz,

which is most sensitive to snow but penetrates less into ice and water, has the lowest brightness temperature on lake.

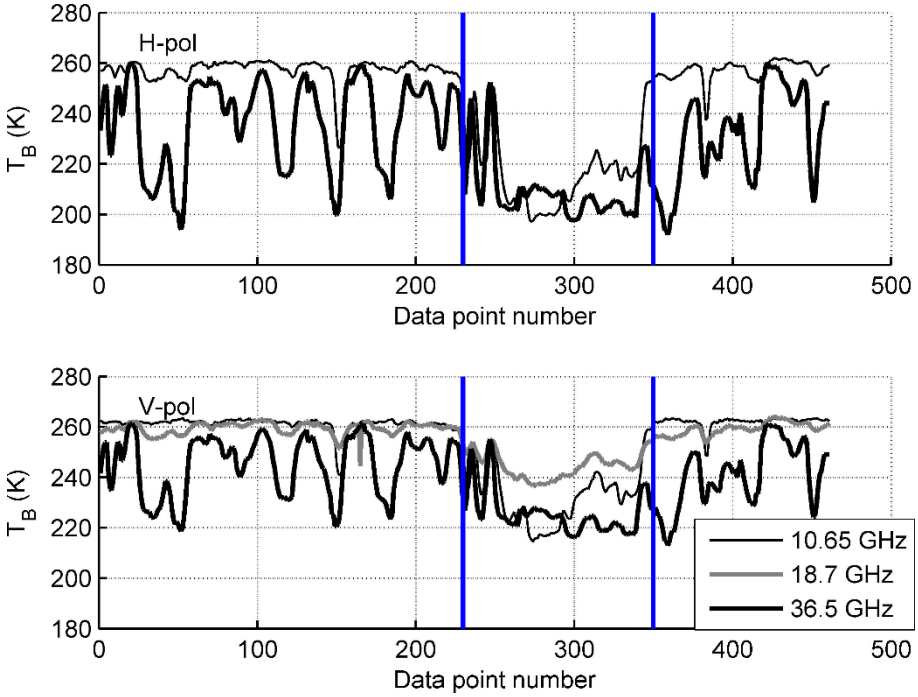

Figure 16. Brightness temperature of a snow- and ice-covered lake (marked with blue vertical lines) and the surrounding land areas from airborne HUTRAD observations. Small islands (points 230-250) and nearby shoreline (points 300-350) cause variability in the measured brightness temperature. Based on Figure 3 of Publication 3. © 2014 IEEE.

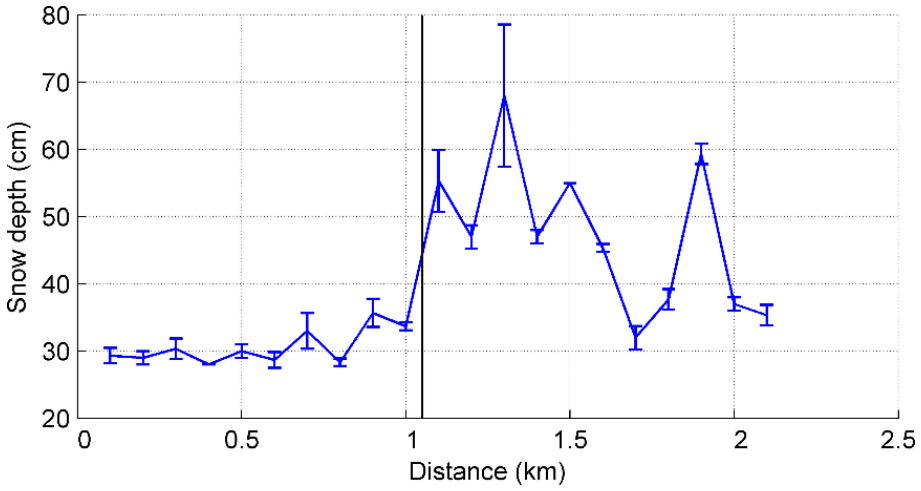

Figure 17. Snow depth on lake ice (the first 1 km) and in sparse forest (from 1.1 to 2.1 km) in the vicinity of Lake Orajärvi in Sodankylä, Finland on February 22, 2010 measured every 100 m. Mean +/- standard deviation of three measurements are shown.

Different snow conditions on lake and land areas originate from the differences in snow accumulation and freezing. Often the water areas freeze later than land areas, so that there is already accumulation of snow on land while the water areas are still open. This results in a deeper snowpack on land than on ice. During the winter, water percolates through small cracks in the congelation ice layer. When the wet snow refreezes, a layer of less dense snow ice is formed.

This process further reduces snow depth on lake and causes spatial variability in snow and ice thicknesses. On wide open areas such as lakes, wind and solar radiation alter the snowpack. Solar radiation may cause sublimation of snow, and wind enhances this process. On the other hand, wind breaks snow crystals and packs them to hard and dense dunes (Pomeroy and Gray, 1995). The result of these processes is a shallow and dense snowpack, which often has melt-refreeze features.

4.2.1 Forward modelling

Publication 3 studied the brightness temperatures of lakes, wetlands and forested and open land areas with simulations and airborne HUTRAD measurements. Lakes and wetlands were modelled as a three-layer system of water, ice and snow. In wetlands, the vegetation below and inside ice was ignored, as the first attempt to model wetlands similar to lakes as a water-ice-snow system proved to be accurate enough. Forested and open areas were simulated using equations presented in Chapter 3.2.2.

Figure 18 shows a summary of the measured and modelled response of different land cover types as a function of frequency. These results are based on long transfer flights and the selected areas all over Finland. The largest differences between the measured and modelled values were on lakes, where the simulations overestimated the brightness temperature. One possible explanation is water on ice, which was not accounted for in the simulations or included in the manual observations. Besides, there was only one in situ measurement site on each lake, and spatial variability between different parts of a lake may be significant. On wetlands, forests and open land areas the simulations and measurements agree. This is partially due to treating grain size as an empirical fitting parameter, i.e. values that minimized the sum of squared error for all selected areas of each land cover type were chosen. This approach was chosen because no in situ grain size data was available.

A more detailed in situ data set including six snow pits was available from the Sodankylä area, where there were 15 flight lines on an area of approximately 10 km x 10 km. A summary of the airborne measurements and simulations is shown in Figure 19. The variability of both brightness temperature and snow conditions in forests especially at 36.5 GHz was notable, and the mean values didn't fall on the 1:1 line. The simulation underestimated the forest brightness temperature roughly by 30 K. As simulation errors in wetland and lake areas were much smaller, it is probable that the bias was caused by the forest model (Chapter 3.2.2, Kruopis et al., 1999).

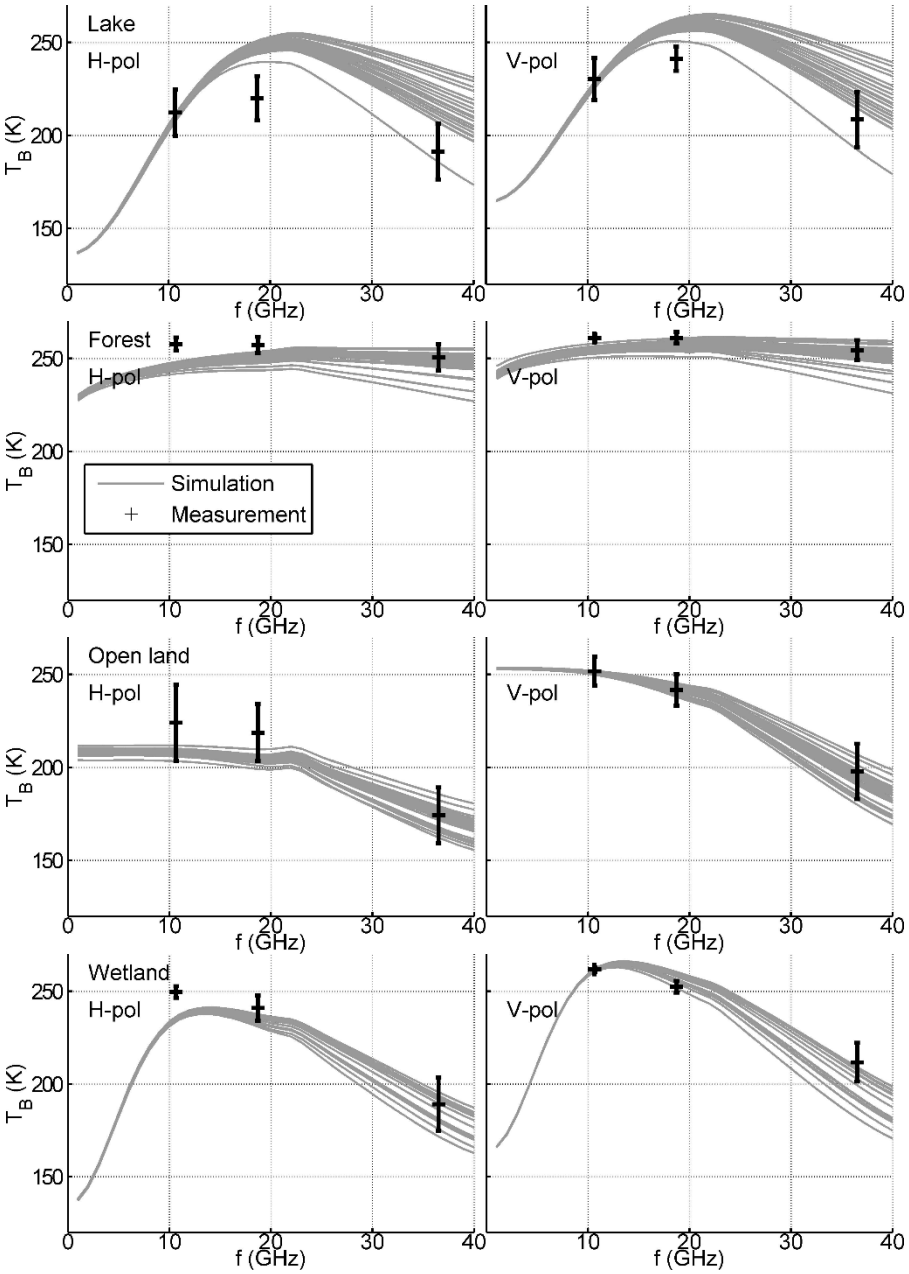

Figure 18. Airborne measurements and simulation results for four land cover types: lake, forest, open and wetland. In total 42 lakes, 39 forested areas, 14 open areas and 7 wetlands were measured and simulated. Each gray line represents one simulated transect. Mean +/- standard deviation of all measured transects of each land cover type are shown. Based on Figure 10 of Publication 3.

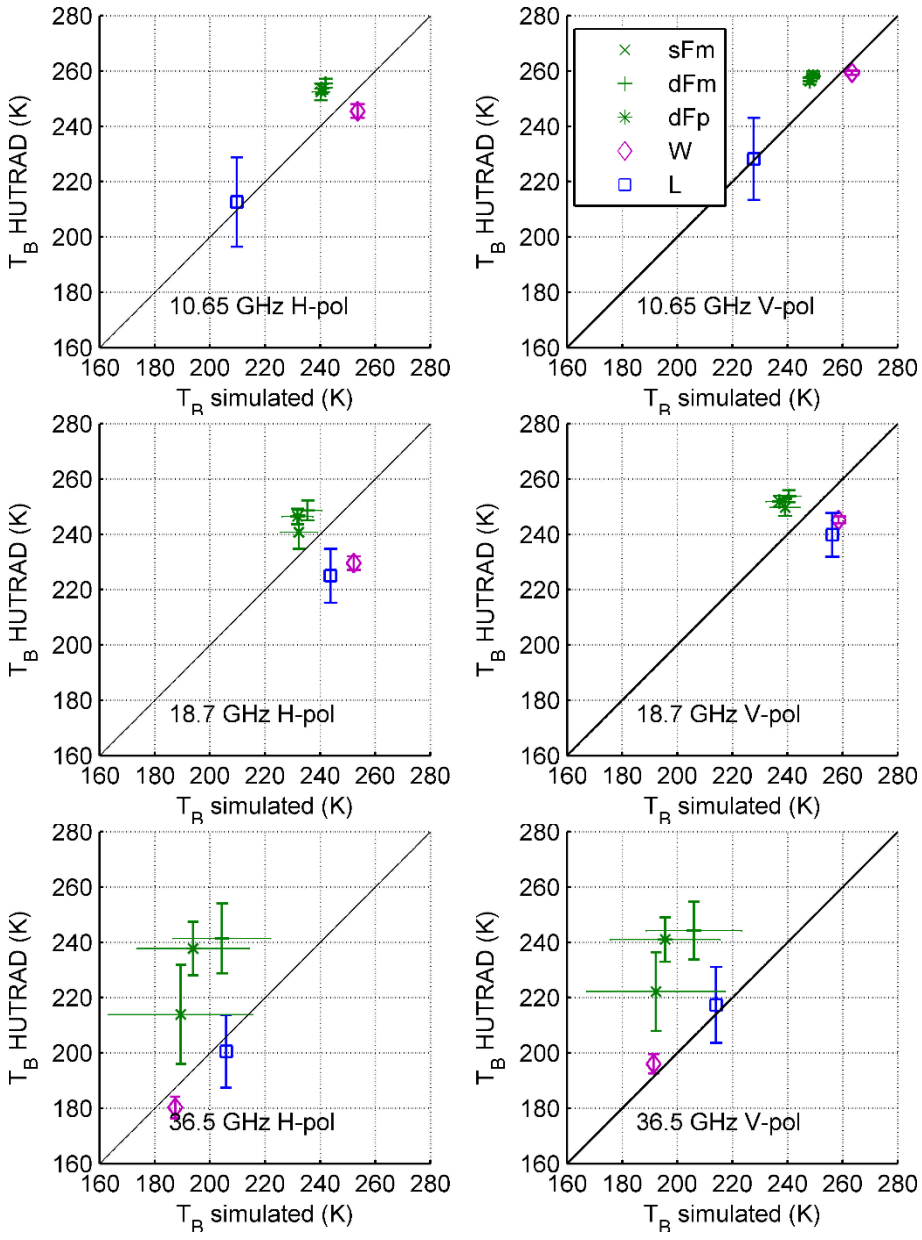

Figure 19. Airborne measurements and simulation results from the Sodankylä area for forests (sFm = sparse forest on mineral soil, dFm = dense forest on mineral soil, dFp = dense forest on peatland), wetlands (W) and lakes (L). Mean simulated or measured value +/- standard deviation is shown. Based on Figure 15 of Publication 3. © 2014 IEEE.

Upscaling is a method to transform small scale data into large scale. It is widely used for example to compare sparse in situ data with spaceborne measurements (Clewley et al., 2017; Greifeneder et al., 2016; Liu et al., 2016; Wu et al., 2017). In Publication 3, a simple weighted areal average (Eq. (16)) was used to transform airborne measurements of different land cover types into satellite grid scale. The results presented in Figure 20 show that the aggregated airborne measurements agreed with the spaceborne measurements and therefore validated the used approach. However, there were large discrepancies between the satellite-scale simulation from in situ data and the AMSR-E measurement. This was probably due to the forest emissivity model, as the earlier simulations (Figure 19) showed worst underestimation in forests. If the grain size in forests was

set to 1.0 mm instead of the measured 1.57 mm, the simulation error was reduced substantially, except at 10.65 GHz, which is least affected by snow. This approach is similar to using an optimized effective grain size in the retrieval, as all simulation errors were compensated with a modified grain size value.

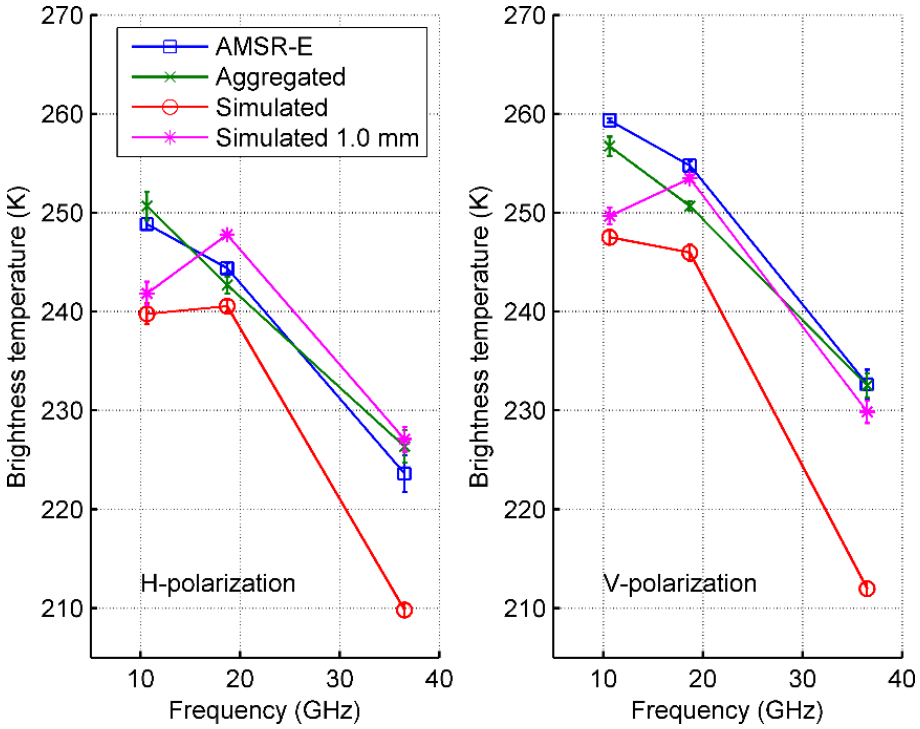

Figure 20. AMSR-E observations, aggregation of airborne measurements and simulation from in situ data. Mean values of five AMSR-E grid cells in the Sodankylä area +/- standard deviation are shown. Figure 16 of Publication 3. © 2014 IEEE.

In Publication 2, the mixed pixel problem was studied by forward modelling of brightness temperature in the satellite scale for the whole area of Finland. First the scene was simulated as land and then the water and ice layers and the differing snow conditions on lakes were included. The coverages of lakes, forests, open areas and other areas (mainly urban) were considered using Eq. (16). Measurement data of snow depth on lake ice and land areas were applied, but snow density was assumed to be constant everywhere.

Figure 21 presents the simulation results for AMSR-E grid cells with lake coverage >30 % at frequency difference $T_{18.7} - T_{36.5}$ at V and H polarizations. The brightness temperature $T_{18.7V} - T_{36.5V}$, most often used in SWE retrieval, was overestimated with a bias of 10.6 K when lakes were not included. When lakes were considered, the bias was only 2 K. This suggests that even a simple model for lakes would improve the SWE retrieval results.

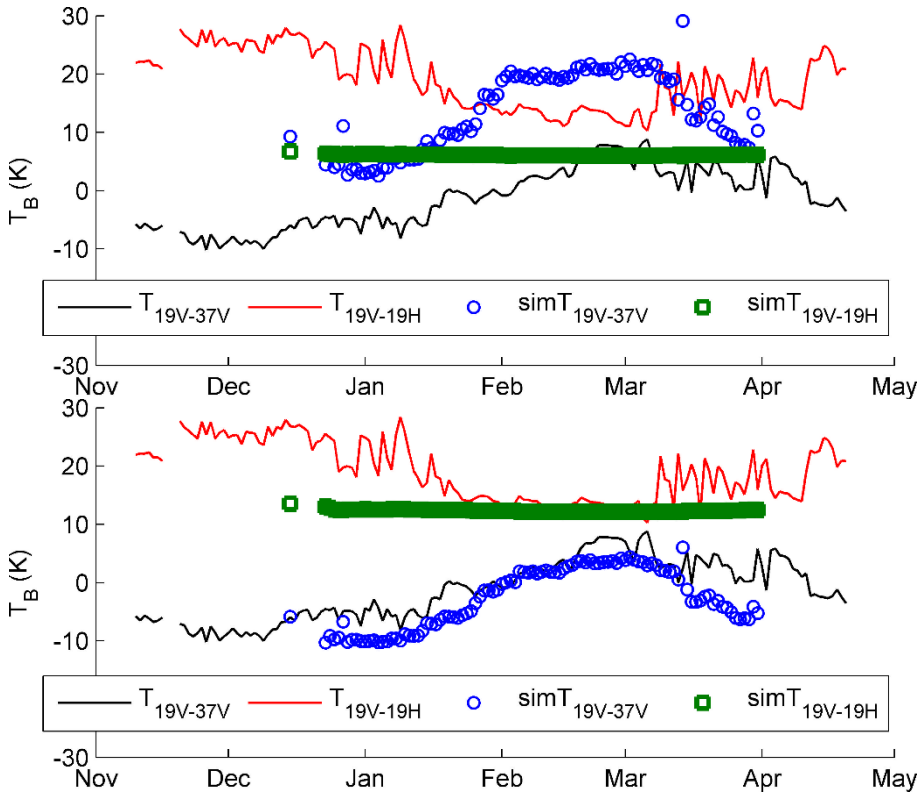

Figure 21. Time series of observed and simulated brightness temperature over lake-rich areas (lake fraction >30 %) in Finland during the winter season 2006-2007. Average of five AMSR-E EASE grid cells presented. Top: Simulation without lakes. Bottom: Lakes included. Based on Figure 7 d) and h) of Publication 2. © 2011 Elsevier Inc.

4.2.2 SWE retrieval

In Publication 2, SWE was retrieved from AMSR-E observations for the whole Finland for the winters of 2005-2008 both ignoring lakes (the normal method) and with lakes considered. With two independent parameters, SWE on land and SWE on lake, there exists an unlimited number of possible solutions to the retrieval problem. Therefore when lakes were included, their SWE was estimated to be half of the SWE on land, limiting the number of free parameters effectively to one. In situ measurements of lake ice thickness were used in the retrieval, but in an operational real-time application, data from climatology or a physical lake ice model could be used instead.

Figure 22 presents the retrieval results for one day, January 1, 2006. The inclusion of lakes modified the SWE especially in the lake-rich area in Southern Finland, where the changes in SWE were up to 50 mm. Comparison to in situ measurements revealed that for the three studied winters, the SWE estimate improved in 57-69 % of cases. The bias for the whole retrieved area decreased from -20 mm to -1.7 mm and rms error from 37.9 mm to 33.3 mm. In addition, the probability of detection of snow increased. However, on areas with significant lake cover (>30 %), the results deteriorated in some cases. This indicates that a more accurate model is needed for wide lakes. Despite this, in most cases the improvement in retrieved SWE was notable.

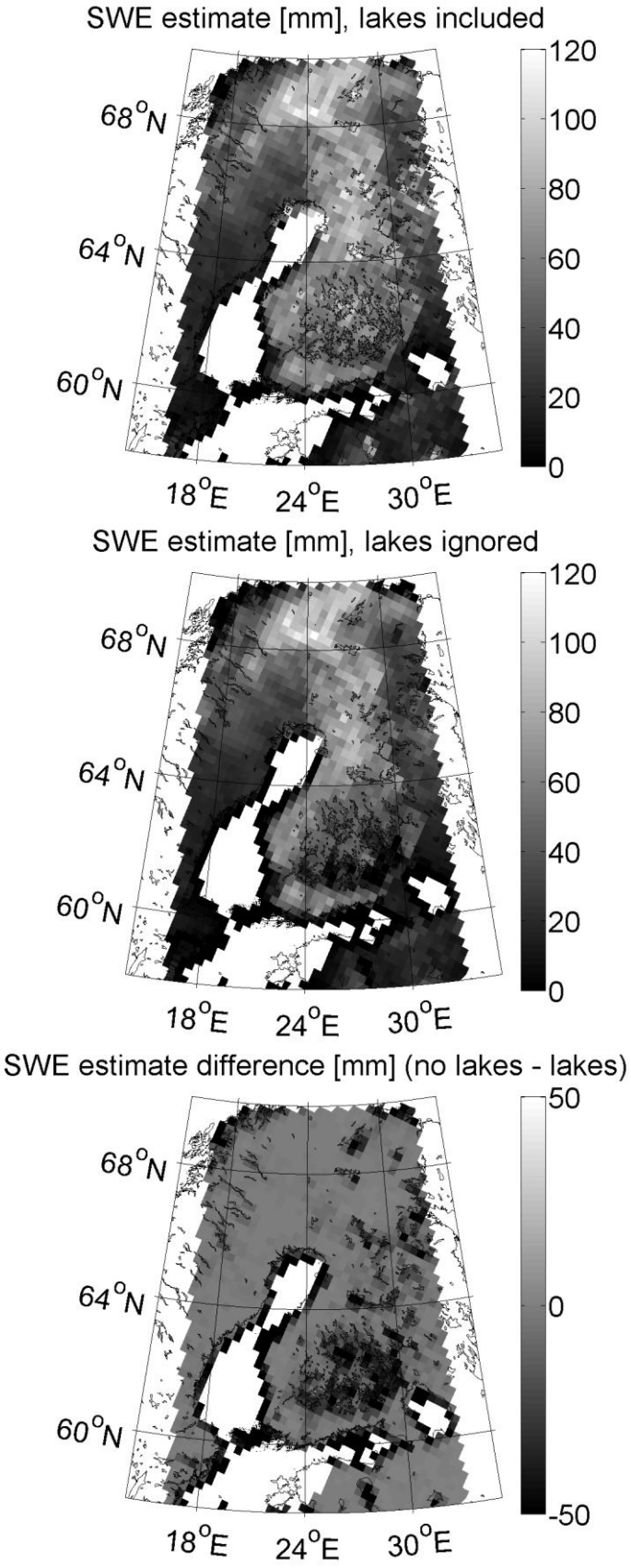

Figure 22. Gridded maps of SWE estimates (mm) for Jan 1, 2006 by a) ignoring lakes and b) including lakes in the retrieval algorithm. Difference between a) and b) is depicted in c). Figure 8 of Publication 2. © 2011 Elsevier Inc.

5. Conclusions

Passive microwave remote sensing provides an excellent means for monitoring vital elements of the Earth. Information on soil frost and snow water equivalent, among other parameters, can be extracted from spaceborne radiometer measurements. Passive microwaves are especially suitable for observing the Arctic in the wintertime and therefore essential in measurements of seasonal snow cover.

The objectives of this dissertation were 1) to find ways to mitigate the effect of subnivean water bodies on the snow parameters retrieved from spaceborne passive microwave measurements and 2) to study the usefulness of snow microstructure parameters modelled with a physical snow model in conjunction with a microwave snow emission model.

Publications 2 and 3 concentrated on modelling the microwave signatures of lakes and wetlands and including this information in the retrieval of snow water equivalent from spaceborne radiometers. Publication 3 presented the first modelling results of snow-covered frozen wetlands and found that the HUT snow emission model was able to model the airborne microwave signatures of lakes, wetlands and open terrain well. Forest simulations had higher bias suggesting that the used forest model was inaccurate. This was reflected in the satellite scale simulations, where similar underestimation as in simulations of airborne measurements over forested areas was seen. A new forest model (Cohen et al., 2015) was later developed.

Publication 2 applied the HUT snow emission model in satellite-scale simulations over all Finland to model the brightness temperature effect of snow-covered water bodies and their impact on retrieved SWE. A method for inclusion of lake effects in the retrieval algorithm was developed. It improved the probability of snow detection and the accuracy of retrieved SWE in moderately lake-covered areas. The implementation of a similar lake model in an operational SWE retrieval scheme is foreseen in the near future.

Publications 1, 4 and 5 studied the effect of snow microstructure and different microstructure parameters on brightness temperature. Special attention was paid to the use of parameters modelled with SNOWPACK together with the HUT snow emission model. SNOWPACK was found to model the evolution of grain size accurately. The seasonal trend in grain size agreed with both the manual field measurements of traditional grain size E and the effective grain size d_{eff} derived from microwave radiometer measurements with the help of the HUT snow emission model. However, there were large winter-dependent biases in the modelled grain size values, which were attributed to snow structure. Rapid

growth of thick depth hoar layer, related to cold air temperature and shallow snowpack, might be the cause for the variable biases. As only average values for the whole snowpack were used, the information of snow layer structure is lost in the process. Future work should focus on inclusion of a more detailed snow structure in the retrieval, possibly with the Monte Carlo method of Pan et al. (2017), or a simpler method using e.g. two layers for small-grained surface snow and large depth hoar crystals. In addition, as SNOWPACK requires too much measurement data for effective global use, a simpler model for grain growth should be studied.

Publication 1 presented an equation for calculating the effective grain size needed in a microwave snow emission model from field observations of traditional snow grain size. The presented equation reduces error of simulated brightness temperature notably. However, it is an empirical fix to an empirical model for the scattering of microwave radiation by snow. A more theoretical approach using more detailed measurements of snow structure and its microwave response, such as Maslanka et al. (2016), should be used.

The results of this thesis work improve the accuracy of SWE products, which in turn can be applied in monitoring of climate change related phenomena in the Arctic and for validation of climate models. The work further refines the understanding of snow microstructure parameters and their interpretation in microwave remote sensing of snow.

References

Armstrong, R.L., Brodzik, M.J. 1995. "An Earth-gridded SSM/I data set for cryospheric studies and global change monitoring", *Advances in Space Research*, 16(10), 155–163. doi: 10.1016/0273-1177(95)00397-W.

Armstrong, R.L., Brodzik, M.J. 2001. "Recent Northern Hemisphere snow extent: A comparison of data derived from visible and microwave satellite sensors", *Geophysical Research Letters*, 28(19), 3673–3676.

Armstrong, R.L., Brun, E. (Eds.). 2008. *Snow and Climate*, Cambridge University Press, Cambridge.

Ascbacher, J. 1989. *Land Surface Studies and Atmospheric Effects by Satellite Microwave Radiometry*, University of Innsbruck, Innsbruck, Austria.

Aurela, M., Laurila, T., Tuovinen, J.P. 2004. "The timing of snow melt controls the annual CO2 balance in a subarctic fen", *Geophysical Research Letters*, 31(16), 3–6. doi: 10.1029/2004GL020315.

Barnett, T.P., Adam, J.C., Lettenmaier, D.P. 2005. "Potential impacts of a warming climate on water availability in snow-dominated regions.", *Nature*, 438(7066), 303–309. doi: 10.1038/nature04141.

Bartelt, P., Lehning, M. 2002. "A physical SNOWPACK model for the Swiss avalanche warning: Part I: numerical model", *Cold Regions Science and Technology*, 35(3), 123–145. doi: 10.1016/S0165-232X(02)00074-5.

Bell, V.A., Kay, A.L., Davies, H.N., Jones, R.G. 2016. "An assessment of the possible impacts of climate change on snow and peak river flows across Britain", *Climatic Change*, 136(3), 539–553. doi: 10.1007/s10584-016-1637-x.

Best, M.J., Pryor, M., Clark, D.B., Rooney, G.G., Essery, R., Ménard, C.B., Edwards, J.M., Hendry, M.A., Porson, A., Gedney, N., Mercado, L.M., Sitch, S., Blyth, E., Boucher, O., Cox, P.M., Grimmond, C.S.B., Harding, R.J. 2011. "The Joint UK Land Environment Simulator (JULES), model description – Part 1: Energy and water fluxes", *Geoscientific Model Development*, 4, 677–699. doi: 10.5194/gmd-4-677-2011.

Bhardwaj, A., Sam, L., Bhardwaj, A., Martín-Torres, F.J. 2016. "LiDAR remote sensing of the cryosphere: Present applications and future prospects", *Remote Sensing of Environment*, 177, 125–143. doi: 10.1016/j.rse.2016.02.031.

Brown, R.D., Robinson, D.A. 2011. "Northern Hemisphere spring snow cover variability and change over 1922 – 2010 including an assessment of uncertainty", *The Cryosphere*, 5, 219–229. doi: 10.5194/tc-5-219-2011.

Brun, E. 1989. "Investigation on wet-snow metamorphism in respect of liquid-water content", *Annals of Glaciology*, 13, 22–26.

Brun, E., David, P., Sudul, M., Brunot, G. 1992. "A numerical model to simulate snow-cover stratigraphy for operational avalanche forecasting", *Journal of Glaciology*, 38(128), 13–22.

Brutel-Vuilmet, C., Ménégoz, M., Krinner, G. 2013. "An analysis of present and future seasonal Northern Hemisphere land snow cover simulated by CMIP5 coupled climate models", *The Cryosphere*, 7(1), 67–80. doi: 10.5194/tc-7-67-2013.

Cai, S., Li, D., Durand, M., Margulis, S.A. 2017. "Examination of the impacts of vegetation on the correlation between snow water equivalent and passive microwave brightness temperature", *Remote Sensing of Environment*, 193, 244–256. doi: 10.1016/j.rse.2017.03.006.

Chandrasekhar, S. 1960. *Radiative Transfer*, Dover Publications Inc., New York.

Chang, A.T.C., Foster, J.L., Hall, D.K. 1987. "Nimbus-7 SMMR derived global snow cover parameters", *Annals of Glaciology*, 9, 39–44.

Chang, A.T.C., Foster, J.L., Hall, D.K., Rango, A., Hartline, B.K. 1981. *Snow Water Equivalent Determination by Microwave Radiometry*, *NASA Technical*

Memorandum, Vol. 82074, Greenbelt, MA, USA.
Clewley, D., Whitcomb, J., Akbar, R., Silva, A., Berg, A., Adams, J., Caldwell, T., Entekhabi, D., Moghaddam, M. 2017. "A method for upscaling in situ soil moisture measurements to satellite footprint scale using Random Forests", *IEEE Journal of Selected Topics in Applied Earth Observations and Remote Sensing*, 10(6), 2663–2673. doi: 10.1109/JSTARS.2017.2690220.
Cohen, J., Lemmetyinen, J., Pulliainen, J., Heinilä, K., Montomoli, F., Seppänen, J., Hallikainen, M.T. 2015. "The effect of boreal forest canopy in satellite snow mapping-A multisensor analysis", *IEEE Transactions on Geoscience and Remote Sensing*, 53(12), 6593–6607. doi: 10.1109/TGRS.2015.2444422.
Colbeck, S.C. 1982. "An overview of seasonal snow metamorphism", *Reviews of Geophysics*, 20(1), 45–61. doi: 10.1029/RG020i001p00045.
Colbeck, S.C. 1991. "The layered character of snow covers", *Reviews of Geophysics*, 29(90), 81. doi: 10.1029/90RG02351.
Davenport, I.J., Sandells, M.J., Gurney, R.J. 2012. "The effects of variation in snow properties on passive microwave snow mass estimation", *Remote Sensing of Environment*, 118, 168–175. doi: 10.1016/j.rse.2011.11.014.
Davis, D.T., Chen, Z., Tsang, L., Hwang, J.N., Chang, A.T.C. 1993. "Retrieval of snow parameters by iterative inversion of a neural network", *IEEE Transactions on Geoscience and Remote Sensing*, 31(4), 842–852. doi: 10.1109/36.239907.
Debye, P. 1929. *Polar Molecules*, Chemical Catalog Co., New York.
Derksen, C., Brown, R. 2012. "Spring snow cover extent reductions in the 2008 – 2012 period exceeding climate model projections", *Geophysical Research Letters*, 39, 1–6. doi: 10.1029/2012GL053387.
Derksen, C., Toose, P., Rees, A., Wang, L., English, M., Walker, A., Sturm, M. 2010. "Development of a tundra-specific snow water equivalent retrieval algorithm for satellite passive microwave data", *Remote Sensing of Environment*, 114(8), 1699–1709. doi: 10.1016/j.rse.2010.02.019.
Derksen, C., Walker, A., Goodison, B. 2005. "Evaluation of passive microwave snow water equivalent retrievals across the boreal forest/tundra transition of western Canada", *Remote Sensing of Environment*, 96(3–4), 315–327. doi: 10.1016/j.rse.2005.02.014.
Dietz, A.J., Kuenzer, C., Gessner, U., Dech, S. 2012. "Remote sensing of snow – a review of available methods", *International Journal of Remote Sensing*, 33(13), 4094–4134. doi: 10.1080/01431161.2011.640964.
Durand, M., Kim, E.J., Margulis, S.A. 2008. "Quantifying uncertainty in modeling snow microwave radiance for a mountain snowpack at the point-scale, including stratigraphic effects", *IEEE Transactions on Geoscience and Remote Sensing*, 46(6), 1753–1767. doi: 10.1109/TGRS.2008.916221.
Ebner, P.P., Schneebeli, M., Steinfeld, A. 2016. "Metamorphism during temperature gradient with undersaturated advective airflow in a snow sample", *The Cryosphere*, 10(2), 791–797. doi: 10.5194/tc-10-791-2016.
Edgerton, A.T., Stogryn, A., Poe, G. 1971. *Microwave Radiometric Investigation of Snowpacks*, Aerojet General Corporation, Microwave Division, Monte, CA.
Etchevers, P., Martin, E., Brown, R., Fierz, C., Lejeune, Y., Bazile, E., Boon, A., Dai, Y.-J., Essery, R., Fernandez, A., Gusev, Y., Jordan, R., Koren, V., Kowalczyk, E., Nasonova, R., Pyles, D., Schlosser, A., Shmakin, A., Smirnova, T.G., Strasser, U., Verseghy, D., Yamazaki, T., Yang, Z.-L. 2002. "SnowMIP, an intercomparison of snow models: first results", *Proceedings of the International Snow Science Workshop*, Penticton, Canada.
Fierz, C., Armstrong, R.L., Durand, Y., Etchevers, P., Greene, E., McClung, D.M., Nishimura, K., Satyawali, P.K., Sokratov, S.A. 2009. *The International Classification for Seasonal Snow on the Ground*, *IHP-VII Technical Documents in Hydrology*, Vol. 83, UNESCO-IHP, Paris.
Foster, J.L., Chang, A.T.C., Hall, D.K. 1997. "Comparison of snow mass estimates from a prototype passive microwave snow algorithm, a revised algorithm and a snow depth climatology", *Remote Sensing of Environment*, 62(2), 132–142. doi: 10.1016/S0034-4257(97)00085-0.
Foster, J.L., Hall, D.K., Chang, A.T.C., Rango, A. 1984. "An overview of passive microwave snow research and results", *Reviews of Geophysics*, 22(2), 195–208.

doi: 10.1029/RG022i002p00195.
Foster, J.L., Rango, A., Hall, D.K., Chang, A.T.C., Allison, L.J., Diesen, B.C. 1980. *Snowpack Monitoring in North America and Eurasia Using Passive Microwave Satellite Data*, *NASA Technical Memorandum*, Vol. 80706, NASA Goddard Space Flight Center, Greenbelt, MA, USA.
Foster, J.L., Sun, C., Walker, J.P., Kelly, R., Chang, A.T.C., Dong, J., Powell, H. 2005. "Quantifying the uncertainty in passive microwave snow water equivalent observations", *Remote Sensing of Environment*, 94(2), 187–203. doi: 10.1016/j.rse.2004.09.012.
Gallet, J.-C., Domine, F., Zender, C.S., Picard, G. 2009. "Measurement of the specific surface area of snow using infrared reflectance in an integrating sphere at 1310 and 1550 nm", *The Cryosphere*, 3(2), 167–182. doi: 10.5194/tc-3-167-2009.
Goïta, K., Walker, A.E., Goodison, B.E. 2003. "Algorithm development for the estimation of snow water equivalent in the boreal forest using passive microwave data", *International Journal of Remote Sensing*, 24(5), 1097–1102. doi: 10.1080/0143116021000044805.
Goodison, B.E., Walker, A.E. 1994. "Canadian development and use of snow cover information from passive microwave satellite data", *ESA/NASA International Workshop*, pp. 245–262.
Greifeneder, F., Notarnicola, C., Bertoldi, G., Niedrist, G., Wagner, W. 2016. "From point to pixel scale: An upscaling approach for in situ soil moisture measurements", *Vadose Zone Journal*, 15(6).
Grenfell, T.C., Warren, S.G. 1999. "Representation of a nonspherical ice particle by a collection of independent spheres for scattering and absorption of radiation: 3. Hollow columns and plates", *Journal of Geophysical Research D: Atmospheres*, 104(D24), 31697–31709. doi: 10.1029/2005JD005811.
Grody, N.C., Basist, A.N. 1996. "Global identification of snowcover using SSM/I measurements", *IEEE Transactions on Geoscience and Remote Sensing*, 34(1), 237–249. doi: 10.1109/36.481908.
Gunn, G.E., Duguay, C.R., Derksen, C., Lemmetyinen, J., Toose, P. 2011. "Evaluation of the HUT modified snow emission model over lake ice using airborne passive microwave measurements", *Remote Sensing of Environment*, 115(1), 233–244. doi: 10.1016/j.rse.2010.09.001.
Hall, A., Qu, X. 2006. "Using the current seasonal cycle to constrain snow albedo feedback in future climate change", *Geophysical Research Letters*, 33, 1–4. doi: 10.1029/2005GL025127.
Hallikainen, M., Jolma, P. 1986. "Retrieval of the water equivalent of snow cover in Finland by satellite microwave radiometry", *IEEE Transactions on Geoscience and Remote Sensing*, GE-24(6), 855–862. doi: 10.1109/TGRS.1986.289700.
Hallikainen, M., Kemppinen, M., Rautiainen, K., Pihlflyckt, J., Lahtinen, J., Tirri, T., Mononen, I., Auer, T. 1996. "Airborne 14-channel microwave radiometer HUTRAD", *IEEE International Geoscience and Remote Sensing Symposium, 1996. IGARSS '96*, Vol. 4, pp. 2285–2287. doi: 10.1109/IGARSS.1996.516963.
Hallikainen, M., Ulaby, F., Van Deventer, T. 1987. "Extinction behavior of dry snow in the 18- to 90-GHz range", *IEEE Transactions on Geoscience and Remote Sensing*, GE-25(6), 737–745. doi: 10.1109/TGRS.1987.289743.
Hallikainen, M., Ulaby, F., Dobson, M., El-Rayes, M., Wu, L.-K. 1985. "Microwave dielectric behavior of wet soil-Part I: Empirical models and experimental observations", *IEEE Transactions on Geoscience and Remote Sensing*, GE-23(1), 25–34. doi: 10.1109/TGRS.1985.289497.
Hallikainen, M.T., Jolma, P.A. 1992. "Comparison of algorithms for retrieval of snow water equivalent from Nimbus-7 SMMR data in Finland", *IEEE Transactions on Geoscience and Remote Sensing*, 30(1), 124–131. doi: 10.1109/36.124222.
Hallikainen, M.T., Ulaby, F.T., Abdelrazik, M. 1986. "Dielectric properties of snow in the 3 to 37 GHz range", *IEEE Transactions on Antennas and Propagation*, AP-34(11), 1329–1340. doi: 10.1109/TAP.1986.1143757.
He, H., Dyck, M., Zhao, Y., Si, B., Jin, H., Zhang, T., Lv, J., Wang, J. 2016. "Evaluation of five composite dielectric mixing models for understanding relationships between effective permittivity and unfrozen water content", *Cold Regions Science*

and Technology, 130, 33–42. doi: 10.1016/j.coldregions.2016.07.006.
Hernández-Henríquez, M.A., Déry, S.J., Derksen, C. 2015. "Polar amplification and elevation-dependence in trends of Northern Hemisphere snow cover extent, 1971–2014", *Environmental Research Letters*, 10(4).
Ishimaru, A. 2013. *Wave Propagation and Scattering in Random Media. Volume 1: Single Scattering and Transport Theory*, Academic Press, Inc., San Diego, California.
Vander Jagt, B.J., Durand, M.T., Margulis, S.A., Kim, E.J., Molotch, N.P. 2013. "The effect of spatial variability on the sensitivity of passive microwave measurements to snow water equivalent", *Remote Sensing of Environment*, 136, 163–179. doi: 10.1016/j.rse.2013.05.002.
Vander Jagt, B.J., Durand, M.T., Margulis, S.A., Kim, E.J., Molotch, N.P. 2015. "On the characterization of vegetation transmissivity using LAI for application in passive microwave remote sensing of snowpack", *Remote Sensing of Environment*, Elsevier Inc., 156, 310–321. doi: 10.1016/j.rse.2014.09.001.
Jiang, L., Shi, J., Tjuatja, S., Dozier, J., Chen, K., Zhang, L. 2007. "A parameterized multiple-scattering model for microwave emission from dry snow", *Remote Sensing of Environment*, 111(2), 357–366. doi: 10.1016/j.rse.2007.02.034.
Kelly, R. 2009. "The AMSR-E snow depth algorithm: Description and initial results", *Journal of the Remote Sensing Society of Japan*, 29, 307–317. doi: 10.11440/rssj.29.307.
Kelly, R., Chang, A.T.C. 2003. "Development of a passive microwave global snow depth retrieval algorithm for Special Sensor Microwave Imager (SSM/I) and Advanced Microwave Scanning Radiometer-EOS (AMSR-E) data", *Radio Science*, 38(4), 1–13. doi: 10.1029/2002RS002648.
Kinar, N.J., Pomeroy, J.W. 2015. "Measurement of the physical properties of the snowpack", *Reviews of Geophysics*, 53, 481–544. doi: 10.1002/2015RG000481.
Klein, L., Swift, C. 1977. "An improved model for the dielectric constant of sea water at microwave frequencies", *IEEE Transactions on Antennas and Propagation*, 2(1), 104–111. doi: 10.1109/JOE.1977.1145319.
Kruopis, N., Praks, J., Arslan, A.N., Alasalmi, H.M., Koskinen, J.T., Hallikainen, M. 1999. "Passive microwave measurements of snow-covered forest areas in EMAC'95", *IEEE Transactions on Geoscience and Remote Sensing*, 37(5), 2699–2705.
Kunzi, K.F., Patil, S., Rott, H. 1982. "Snow-cover parameters retrieved from Nimbus-7 Scanning Multichannel Microwave Radiometer (SMMR) data", *IEEE Transactions on Geoscience and Remote Sensing*, GE-20(4), 452–467. doi: 10.1109/TGRS.1982.350411.
Langlois, A., Royer, A., Derksen, C., Montpetit, B., Dupont, F., Goïta, K. 2012. "Coupling the snow thermodynamic model SNOWPACK with the microwave emission model of layered snowpacks for subarctic and arctic snow water equivalent retrievals", *Water Resources Research*, 48(12), 1–14. doi: 10.1029/2012WR012133.
Lehning, M., Bartelt, P., Brown, B., Fierz, C. 2002. "A physical SNOWPACK model for the Swiss avalanche warning: Part III: meteorological forcing, thin layer formation and evaluation", *Cold Regions Science and Technology*, 35(3), 169–184. doi: 10.1016/S0165-232X(02)00072-1.
Lehning, M., Bartelt, P., Brown, B., Fierz, C., Satyawali, P. 2002. "A physical SNOWPACK model for the Swiss avalanche warning Part II. Snow microstructure", *Cold Regions Science and Technology*, 35(3), 147–167. doi: 10.1016/S0165-232X(02)00073-3.
Lehning, M., Fierz, C., Lundy, C. 2001. "An objective snow profile comparison method and its application to SNOWPACK", *Cold Regions Science and Technology*, 33(2–3), 253–261. doi: 10.1016/S0165-232X(01)00044-1.
Leinss, S., Wiesmann, A., Lemmetyinen, J., Hajnsek, I. 2015. "Snow water equivalent of dry snow measured by differential interferometry", *IEEE Journal of Selected Topics in Applied Earth Observations and Remote Sensing*, 8(8), 3773–3790.
Lemmetyinen, J., Pulliainen, J., Rees, A., Kontu, A., Qiu, Y., Derksen, C. 2010. "Multiple-layer adaptation of HUT snow emission model: Comparison with experimental data", *IEEE Transactions on Geoscience and Remote Sensing*,

48(7), 2781–2794. doi: 10.1109/TGRS.2010.2041357.
Lemmetyinen, J., Schwank, M., Rautiainen, K., Kontu, A., Parkkinen, T., Mätzler, C., Wiesmann, A., Wegmüller, U., Derksen, C., Toose, P., Roy, A., Pulliainen, J. 2016. "Snow density and ground permittivity retrieved from L-band radiometry: Application to experimental data", *Remote Sensing of Environment*, 180, 377–391. doi: 10.1016/j.rse.2016.02.002.
Leppänen, L., Kontu, A., Hannula, H.-R., Sjöblom, H., Pulliainen, J. 2016. "Sodankylä manual snow survey program", *Geoscientific Instrumentation, Methods and Data Systems*, 5, 163–179. doi: 10.5194/gi-5-163-2016.
Liu, S., Xu, Z., Song, L., Zhao, Q., Ge, Y., Xu, T., Ma, Y., Zhu, Z., Jia, Z., Zhang, F. 2016. "Upscaling evapotranspiration measurements from multi-site to the satellite pixel scale over heterogeneous land surfaces", *Agricultural and Forest Meteorology*, 230, 97–113. doi: 10.1016/j.agrformet.2016.04.008.
Macelloni, G., Paloscia, S., Pampaloni, P., Brogioni, M., Ranzi, R., Crepaz, A. 2005. "Monitoring of melting refreezing cycles of snow with microwave radiometers: The Microwave Alpine Snow Melting Experiment (MASMEx 2002-2003)", *IEEE Transactions on Geoscience and Remote Sensing*, 43(11), 2431–2441. doi: 10.1109/TGRS.2005.855070.
Margulis, S.A. 2006. *Feasibility of Snowpack Characterization Using Remote Sensing and Advanced Data Assimilation Techniques*, *University of California Water Resources Center Technical Completion Reports*.
Margulis, S.A., Cortes, G., Girotto, M., Durand, M. 2016. "A Landsat-era Sierra Nevada snow reanalysis (1985-2015)", *Journal of Hydrometeorology*, 17(4), 1203–1221.
Maslanka, W., Leppänen, L., Kontu, A., Sandells, M., Lemmetyinen, J., Schneebeli, M., Hannula, H., Gurney, R. 2016. "Arctic Snow Microstructure Experiment for the development of snow emission modelling", *Geoscientific Instrumentation, Methods and Data Systems*, 5, 85–94. doi: 10.5194/gid-5-495-2015.
Matsuoka, T., Fujita, S., Mae, S. 1996. "Effect of temperature on dielectric properties of ice in the range 5 – 39 GHz", *Journal of Applied Physics*, 80(10), 5884–5890. doi: 10.1063/1.363582.
Meinander, O., Kontu, A., Lakkala, K., Heikkilä, A., Ylianttila, L., Toikka, M. 2008. "Diurnal variations in the UV albedo of arctic snow", *Atmospheric Chemistry and Physics*, 6551–6563. doi: 10.5194/acpd-8-4155-2008.
Metsämäki, S., Pulliainen, J., Salminen, M., Luojus, K., Wiesmann, A., Solberg, R., Böttcher, K., Hiltunen, M., Ripper, E. 2015. "Introduction to GlobSnow Snow Extent products with considerations for accuracy assessment", *Remote Sensing of Environment*, 156, 96–108. doi: 10.1016/j.rse.2014.09.018.
Mätzler, C. 1987. "Applications of the interaction of microwaves with the natural snow cover", *Remote Sensing Reviews*, 2(2), 259–387. doi: 10.1080/02757258709532086.
Mätzler, C. 1996. "Microwave permittivity of dry snow", *IEEE Transactions on Geoscience and Remote Sensing*, 34(2), 573–581. doi: 10.1109/36.655342.
Mätzler, C. 2002. "Relation between grain-size and correlation length of snow", *Journal of Glaciology*, 48(162), 461–466.
Mätzler, C., Schanda, E., Good, W. 1982. "Towards the definition of optimum sensor specifications for microwave remote sensing of snow", *IEEE Transactions on Geoscience and Remote Sensing*, GE-20(1), 57–66. doi: 10.1109/TGRS.1982.4307521.
Mätzler, C., Schanda, E., Hofer, R., Good, W. 1980. "Microwave singatures of the natural snow cover at Weissfluhjoch", *NASA Conference Publications, CP2157*, pp. 203–223.
Mätzler, C., Wegmüller, U. 1987. "Dielectric properties of fresh-water ice at microwave frequencies", *Journal of Physics D: Applied Physics*, 20, 1623–1630. doi: 10.1088/0022-3727/21/11/522.
Nagler, T., Rott, H., Ripper, E., Bippus, G., Hetzenecker, M. 2016. "Advancements for snowmelt monitoring by means of Sentinel-1 SAR", *Remote Sensing*, 8(4), 348. doi: 10.3390/rs8040348.
Pan, J., Durand, M., Sandells, M., Lemmetyinen, J., Kim, E.J., Pulliainen, J., Kontu, A., Derksen, C. 2016. "Differences between the HUT snow emission model and

MEMLS and their effects on brightness temperature simulation", *IEEE Transactions on Geoscience and Remote Sensing*, 54(4), 2001–2019. doi: 10.1109/TGRS.2015.2493505.

Pan, J., Durand, M.T., Vander Jagt, B.J., Liu, D. 2017. "Application of a Markov Chain Monte Carlo algorithm for snow water equivalent retrieval from passive microwave measurements", *Remote Sensing of Environment*, Elsevier Inc., 192, 150–165. doi: 10.1016/j.rse.2017.02.006.

Pettinato, S., Santi, E., Brogioni, M., Paloscia, S., Palchetti, E., Xiong, C. 2013. "The potential of COSMO-SkyMed SAR images in monitoring snow cover characteristics", *IEEE Geoscience and Remote Sensing Letters*, 10(1), 9–13. doi: 10.1109/LGRS.2012.2189752.

Picard, G., Arnaud, L., Domine, F., Fily, M. 2009. "Determining snow specific surface area from near-infrared reflectance measurements: Numerical study of the influence of grain shape", *Cold Regions Science and Technology*, 56, 10–17. doi: 10.1016/j.coldregions.2008.10.001.

Planck, M. 1901. "On the law of the energy distribution in the normal spectrum", *Ann. Phys*, 4, 1–11. doi: 10.1002/andp.19013090310.

Polder, D., Van Santen, J.H. 1946. "The effective permeability of mixtures of solids", *Physica*, 12, 257–271.

Pomeroy, J., Gray, D.M. 1995. *Snowcover : Accumulation, Relocation, and Management*, Hydrological Sciences Division, NHRI; Division of Hydrology, University of Saskatchewan.

Proksch, M., Löwe, H., Schneebeli, M. 2015. "Density, specific surface area, and correlation length of snow measured by high-resolution penetrometry", *Journal of Geophysical Research F: Earth Surface*, 120(2), 346–362. doi: 10.1002/2014JF003266.

Pulliainen, J., Grandell, J., Hallikainen, M. 1999. "HUT snow emission model and its applicability to snow water equivalent retrieval", *IEEE Transactions on Geoscience and Remote Sensing*, 37(3 I), 1378–1390. doi: 10.1109/36.763302.

Pulliainen, J., Kärnä, J.-P., Hallikainen, M. 1993. "Development of geophysical retrieval algorithms for the MIMR", *IEEE Transactions on Geoscience and Remote Sensing*, 31(1), 268–277. doi: 10.1109/36.210466.

Rasmus, S. 2005. *Snow Pack Structure Characteristics in Finland - Measurements and Modelling*, *Report Series in Geophysics*, University of Helsinki.

Rautiainen, K., Lemmetyinen, J., Schwank, M., Kontu, A., Ménard, C.B., Mätzler, C., Drusch, M., Wiesmann, A., Ikonen, J., Pulliainen, J. 2014. "Detection of soil freezing from L-band passive microwave observations", *Remote Sensing of Environment*, 147, 206–218.

Rees, A., Derksen, C., English, M., Walker, A., Duguay, C. 2006. "Uncertainty in snow mass retrievals from satellite passive microwave data in lake-rich high-latitude environments", *Hydrological Processes*, 20(4), 1019–1022. doi: 10.1002/hyp.6076.

Rees, A., Lemmetyinen, J., Derksen, C., Pulliainen, J., English, M. 2010. "Observed and modelled effects of ice lens formation on passive microwave brightness temperatures over snow covered tundra", *Remote Sensing of Environment*, 114, 116–126. doi: 10.1016/j.rse.2009.08.013.

de Rosnay, P., Balsamo, G., Albergel, C., Muñoz-Sabater, J., Isaksen, L. 2014. "Initialisation of land surface variables for numerical weather prediction", *Surveys in Geophysics*, 35(3), 607–621. doi: 10.1007/s10712-012-9207-x.

Rott, H., Cline, D.W., Duguay, C., Essery, R., Etchevers, P., Hajnsek, I., Kern, M., Macelloni, G., Malnes, E., Pulliainen, J., Yueh, S. 2013. "CoReH2O: High-resolution X/Ku-band radar imaging of cold land processes", *IEEE International Geoscience and Remote Sensing Symposium, 2013. IGARSS'13*, Melbourne, Australia, pp. 3479–3482.

Rott, H., Yueh, S.H., Cline, D.W., Duguay, C., Essery, R., Haas, C., Heliere, F., Kern, M., MacElloni, G., Malnes, E., Nagler, T., Pulliainen, J., Rebhan, H., Thompson, A. 2010. "Cold regions hydrology high-resolution observatory for snow and cold land processes", *Proceedings of the IEEE*, 98(5), 752–765. doi: 10.1109/JPROC.2009.2038947.

Roy, A., Picard, G., Royer, A., Montpetit, B., Dupont, F., Langlois, A., Derksen, C.,

Champollion, N. 2013. “Brightness temperature simulations of the Canadian seasonal snowpack driven by measurements of the snow specific surface area”, *IEEE Transactions on Geoscience and Remote Sensing*, 51(9), 4692–4704. doi: 10.1109/TGRS.2012.2235842.

Roy, V., Goïta, K., Royer, A., Walker, A.E., Goodison, B.E. 2004. “Snow water equivalent retrieval in a Canadian Boreal environment from microwave measurements using the HUT snow emission model”, *IEEE Transactions on Geoscience and Remote Sensing*, 42(9), 1850–1859. doi: 10.1109/TGRS.2004.832245.

Räisänen, J. 2015. “Twenty-first century changes in snowfall climate in Northern Europe in ENSEMBLES regional climate models”, *Climate Dynamics*.

Safavi, H.R., Sajjadi, S.M., Raghibi, V. 2017. “Assessment of climate change impacts on climate variables using probabilistic ensemble modeling and trend analysis”, *Theoretical and Applied Climatology*, Theoretical and Applied Climatology, 130(1–2), 635–653. doi: 10.1007/s00704-016-1898-3.

Sandells, M., Dumont, M., Essery, R., Kontu, A., Lemmetyinen, J., Löwe, H., Maslanka, W., Mätzler, C., Morin, S., Picard, G., Wiesmann, A. 2016. *Microstructural Origin of Electromagnetic Signatures in Microwave Remote Sensing of Snow-D10: Final Report*, ESA Deliverable D10: 4000112698/14/NL/LvH.

Santi, E., Paloscia, S., Pampaloni, P., Pettinato, S., Brogioni, M., Xiong, C., Crepaz, A. 2017. “Analysis of Microwave Emission and Related Indices over Snow using Experimental Data and a Multilayer Electromagnetic Model”, *IEEE Transactions on Geoscience and Remote Sensing*, 55(4), 2097–2110. doi: 10.1109/TGRS.2016.2636363.

Santi, E., Pettinato, S., Paloscia, S., Pampaloni, P., MacElloni, G., Brogioni, M. 2012. “An algorithm for generating soil moisture and snow depth maps from microwave spaceborne radiometers: HydroAlgo”, *Hydrology and Earth System Sciences*, 16(10), 3659–3676. doi: 10.5194/hess-16-3659-2012.

Shi, J., Jackson, T., Tao, J., Du, J., Bindlish, R., Lu, L., Chen, K.S. 2008. “Microwave vegetation indices for short vegetation covers from satellite passive microwave sensor AMSR-E”, *Remote Sensing of Environment*, 112(12), 4285–4300. doi: 10.1016/j.rse.2008.07.015.

Sihvola, A. 1999. *Electromagnetic Mixing Formulas and Applications*, The Institution of Engineering and Technology, London, United Kingdom.

Simmonds, I. 2015. “Comparing and contrasting the behaviour of Arctic and Antarctic sea ice over the 35 year period 1979-2013”, *Annals of Glaciology*, 56(69), 18–28. doi: 10.3189/2015AoG69A909.

Skou, N., Le Vine, D.M. 2006. *Microwave Radiometer Systems: Design and Analysis*, 2nd ed., Artech House.

Smith, T., Bookhagen, B. 2016. “Assessing uncertainty and sensor biases in passive microwave data across High Mountain Asia”, *Remote Sensing of Environment*, 181, 174–185. doi: 10.1016/j.rse.2016.03.037.

Sorman, A.U., Beser, O. 2013. “Determination of snow water equivalent over the eastern part of Turkey using passive microwave data”, *Hydrological Processes*, 27(14), 1945–1958.

Sturm, M., Holmgren, J., Liston, G.E. 1995. “A seasonal snow cover classification system for local to global applications”, *Journal of Climate*, 8(5), 1261–1283. doi: 10.1175/1520-0442(1995)008<;1261:ASSCCS>;2.0.CO;2.

Takala, M., Ikonen, J., Luojus, K., Lemmetyinen, J., Metsamaki, S., Cohen, J., Arslan, A.N., Pulliainen, J. 2017. “New snow water equivalent processing system with improved resolution over Europe and its applications in hydrology”, *IEEE Journal of Selected Topics in Applied Earth Observations and Remote Sensing*, 10(2), 428–436. doi: 10.1109/JSTARS.2016.2586179.

Takala, M., Luojus, K., Pulliainen, J., Derksen, C., Lemmetyinen, J., Kärnä, J.P., Koskinen, J., Bojkov, B. 2011. “Estimating northern hemisphere snow water equivalent for climate research through assimilation of space-borne radiometer data and ground-based measurements”, *Remote Sensing of Environment*, 115(12), 3517–3529. doi: 10.1016/j.rse.2011.08.014.

Tedesco, M., Kim, E.J. 2006a. “Retrieval of dry-snow parameters from microwave radiometric data using a dense-medium model and genetic algorithms”, *IEEE Transactions on Geoscience and Remote Sensing*, 44(8), 2143–2151. doi: 10.1109/TGRS.2006.872087.

Tedesco, M., Kim, E.J. 2006b. “Intercomparison of electromagnetic models for passive microwave remote sensing of snow”, *IEEE Transactions on Geoscience and Remote Sensing*, 44(10), 2654–2666. doi: 10.1109/TGRS.2006.873182.

Tiuri, M., Hallikainen, M. 1981. “Microwave emission characteristics of snow covered Earth surfaces by the Nimbus 7 satellite”, *11th European Microwave Conference*, Amsterdam, pp. 233–238.

Tsang, L., Chen, C. Te, Chang, A.T.C., Guo, J., Ding, K.H. 2000. “Dense media radiative transfer theory based on quasicrystalline approximation with applications to passive microwave remote sensing of snow”, *Radio Science*, 35(3), 731–749. doi: 10.1029/1999RS002270.

Ulaby, F.T., Moore, R.K., Fung, A.K. 1981. *Microwave Remote Sensing-Active and Passive. Vol. 1: Microwave Remote Sensing Fundamentals and Radiometry*, Artech House, Norwood, MA.

Ulaby, F.T., Moore, R.K., Fung, A.K. 1982. *Microwave Remote Sensing-Active and Passive. Vol. 2: Radar Remote Sensing and Surface Scattering and Emission Theory*, Artech House, Norwood, MA.

Ulaby, F.T., Moore, R.K., Fung, A.K. 1986. *Microwave Remote Sensing-Active and Passive. Vol. 3: From Theory to Applications*, Artech House, Norwood, MA.

Vavrus, S. 2007. “The role of terrestrial snow cover in the climate system”, *Climate Dynamics*, 29(1), 73–88. doi: 10.1007/s00382-007-0226-0.

Vionnet, V., Brun, E., Morin, S., Boone, A., Faroux, S., Le Moigne, P., Martin, E., Willemet, J.M. 2012. “The detailed snowpack scheme Crocus and its implementation in SURFEX v7.2”, *Geoscientific Model Development*, 5(3), 773–791. doi: 10.5194/gmd-5-773-2012.

Vormoor, K., Lawrence, D., Heistermann, M., Bronstert, A. 2015. “Climate change impacts on the seasonality and generation processes of floods – projections and uncertainties for catchments with mixed snowmelt/rainfall regimes”, *Hydrology and Earth System Sciences*, 19, 913–931. doi: 10.5194/hess-19-913-2015.

Wang, H., Pulliainen, J., Hallikainen, M. 2000. “Application of strong fluctuation theory to microwave emission from dry snow”, *Progess in Electromagnetics Research*, 29, 39–55. doi: 10.2528/PIER00011402.

Wang, J.R., Choudhury, B.J. 1981. “Remote sensing of soil moisture content, over bare field at 1.4 GHz frequency”, *Journal of Geophysical Research*, 86(C6), 5277. doi: 10.1029/JC086iC06p05277.

Wang, X., Zender, C.S. 2011. “Arctic and Antarctic diurnal and seasonal variations of snow albedo from multiyear Baseline Surface Radiation Network measurements”, *Journal of Geophysical Research: Earth Surface*, 116(3), 1–16. doi: 10.1029/2010JF001864.

Wegmüller, U., Mätzler, C. 1999. “Rough bare soil reflectivity model”, *IEEE Transactions on Geoscience and Remote Sensing*, 37(3), 1391–1395. doi: 10.1109/36.763303.

Wiesmann, A., Mätzler, C. 1999. “Microwave emission model of layered snowpacks”, *Remote Sensing of Environment*, 70(3), 307–316. doi: 10.1016/S0034-4257(99)00046-2.

Wiesmann, A., Mätzler, C., Weise, T. 1998. “Radiometric and structural measurements of snow samples”, *Radio Science*, 33(2), 273–289.

Williamson, S.N., Copland, L., Hik, D.S. 2016. “The accuracy of satellite-derived albedo for northern alpine and glaciated land covers”, *Polar Science*, 10(3), 262–269.

Wu, X., Xiao, Q., Wen, J., Liu, Q., You, D., Dou, B., Tang, Y. 2017. “Upscaling in situ albedo for validation of coarse scale albedo product over heterogeneous surfaces”, *International Journal of Digital Earth*, 10(6), 604–622. doi: 10.1080/17538947.2016.1247300.

Zheng, X., Li, X., Jiang, T., Ding, Y., Wu, L., Zhang, S., Zhao, K. 2016. “Retrieving soil surface temperature under snowpack using special sensor microwave/imager brightness temperature in forested areas of Heilongjiang, China: an improved

method", *Journal of Applied Remote Sensing*, 10(2), 26016. doi: 10.1117/1.JRS.10.026016.

Publication 1

A. Kontu, J. Pulliainen. 2010. Simulation of spaceborne microwave radiometer measurements of snow cover using in situ data and brightness temperature modeling. *IEEE Transactions on Geoscience and Remote Sensing*, 48(3), 1031-1044. doi: 10.1109/TGRS.2009.2030499.

Simulation of Spaceborne Microwave Radiometer Measurements of Snow Cover Using *In Situ* Data and Brightness Temperature Modeling

Anna Kontu and Jouni Pulliainen, *Senior Member, IEEE*

***Abstract*—The Helsinki University of Technology (HUT) snow emission model is used to calculate the time series of brightness temperature of snow-covered sparsely forested area for the winter 2006–2007. Brightness temperature simulations that apply *in situ* observed physical parameters as input are compared with the Advanced Microwave Scanning Radiometer for Earth Observing System (AMSR-E) observations. Three models for the extinction coefficient of snow and the statistical and physical atmospheric models are compared. Simulation results are presented with full *in situ* data set and only air temperature and snow depth (SD) as input data. The obtained results indicate that the extinction coefficient model of Hallikainen *et al.* originally used with the HUT snow emission model is the best suited for the Finnish snow data set used in this paper and also on frequencies which are outside the original range of the extinction coefficient model. The simulation results obtained using only air temperature and SD input data show that the HUT snow model is quite reliable even with a minimal *in situ* data set. A time series of optimized grain sizes was calculated by minimizing the simulation error. The optimized grain size tended to saturate with large values, and therefore, a new model to calculate an effective grain size was developed. The simulation with the effective grain size as input has lower rms error and higher correlation with AMSR-E data than the simulation with the measured grain size.**

***Index Terms*—Microwave radiometry, remote sensing, snow.**

I. Introduction

SEASONAL snow cover plays an important role in the hydrological and climatological processes of the boreal zone due to the high albedo, thermal emissivity, and low thermal conductivity [1] of snow. Aside from local effects, the northern seasonal snow cover has also global climatological importance [1]–[3]. The water runoff from melting snow is a key parameter in the global water cycle. To predict the evolution of snowmelt and the runoff from melting snow, continuous information on several snow parameters, like snow water equivalent (SWE), snow depth (SD), and snow-covered area, is needed throughout the snow season. Aside from ground-based snow courses and weather stations, spaceborne microwave radiometer observations can be used to provide daily information on snow cover with a full spatial coverage.

In order to extract snow data from spaceborne brightness temperature measurements, emission from soil, vegetation, and atmosphere have to be taken into account, as well as the transmissivity and reflection of radiation in and between different media. The properties of snow (e.g., grain size and shape, and moisture content) also have an effect on its microwave emission. There are several algorithms for the modeling of microwave emission from soil, vegetation canopy, and snow cover, e.g., [4]–[9]. Empirical algorithms for estimating snow parameters are retrieved by analyzing measurement data. However, the use of empirical regression coefficients reduces the regional and temporal applicability of such algorithms. On the other hand, purely theoretical emission models with multiple layers tend to be complex and thus not feasible for the inversion of satellite data. Therefore, empirical and semiempirical models are used here to simulate spaceborne-observed scene brightness temperature. Specifically, a modeling suite, including the Helsinki University of Technology (HUT) snow emission model [4], rough bare soil reflectivity model [9], boreal forest transmissivity model [7], and statistical [10], [11] and physical [12, Ch. 5] atmospheric models, is applied for its simplicity and generality.

The validity of the chosen models is studied here by combining them to simulate a daily time series of spaceborne microwave observations of snow-covered ground from an *in situ* data set collected during winter 2006–2007 in Sodankylä, Finland. The simulations are compared with the measurements by the AMSR-E instrument onboard the EOS Aqua satellite. The main problem in the comparison is the resolution of the satellite data. One satellite pixel may contain a variety of land and vegetation types. Moreover, meteorological phenomena such as rain showers may cover a pixel only partially. However, this paper focuses on the temporal, not spatial, variation of brightness temperature. In addition, the land cover and vegetation maps of the *in situ* measurement area were available for the study. Thus, the characteristics of land cover within a satellite-observed pixel were considered in simulation experiments.

This paper concentrates on the simulation of a winter-long time series of brightness temperatures of snow-covered ground and on modeling in varying snow and atmospheric conditions. In particular, the effect of grain size is studied in detail.

Manuscript received September 29, 2008; revised January 15, 2009 and April 24, 2009. First published October 20, 2009; current version published February 24, 2010.

The authors are with the Arctic Research, Finnish Meteorological Institute, 99600 Sodankylä, Finland (e-mail: anna.kontu@fmi.fi; jouni.pulliainen@fmi.fi).

Color versions of one or more of the figures in this paper are available online at http://ieeexplore.ieee.org.

Digital Object Identifier 10.1109/TGRS.2009.2030499

II. Models

A. Snow

The HUT snow model [4] is a semiempirical microwave emission model. It is based on radiative transfer equation and measurements conducted in Finland [13] and Switzerland [14]. The main goal in developing the model was to keep the number of parameters low, ensuring its applicability to the inversion of satellite data. The model has two basic assumptions: 1) single homogenous snow layer and 2) microwave radiation is mostly scattered into the forward direction. The first assumption does not generally hold up in natural snow packs where new snowfall, thawing and refreezing cycles, and depth hoar repeatedly create layers. On the other hand, the profiles of the measured parameters are rarely available, and the average or even the estimated values for the whole snowpack have to be used even in simulation experiments. In addition, profiles measured at one site do not accurately represent the entire tens of kilometers wide satellite pixel. Nevertheless, in comparison with other models for snow, the HUT snow model has performed well [15].

The HUT snow model calculates the brightness temperature of snow-covered forest observed from space with

$$T_B = \tau \cdot T_{B,\mathrm{scene}} + \tau \cdot (1 - e_{\mathrm{scene}}) \cdot T_{\mathrm{atm},\downarrow} + T_{\mathrm{atm},\uparrow} + T_{\mathrm{cosmic}} \cdot \tau^2 \cdot (1 - e_{\mathrm{scene}}) \quad (1)$$

where τ is the atmospheric transmissivity, $T_{\mathrm{atm},\downarrow}$ and $T_{\mathrm{atm},\uparrow}$ are the down- and upwelling brightness temperatures of the atmosphere, T_{cosmic} is the cosmic background radiation, and $T_{B,\mathrm{scene}}$ and e_{scene} are the brightness temperature and emissivity of the ground scene, including the contributions of snow, soil, and forests. Moreover, multiple reflectances between soil, snow, and forest canopy are modeled by applying a noncoherent approach [12, pp. 237–245].

The HUT snow model uses several input parameters: snow temperature, grain size, SWE, density, volumetric moisture, and salinity. The effect of grain size is modeled with the extinction coefficient defined in [13]

$$\kappa_e = 0.0018 f^{2.8} d^2 \quad (2)$$

where κ_e is the extinction in decibels, f is the frequency in gigahertz, and d is the grain diameter in millimeters. Equation (2) is valid for grain sizes of 0.2–1.6 mm.

Roy *et al.* [16] suggested a different model for larger grain sizes (1.3–4.0 mm):

$$\kappa_e = \gamma (f^4 d^6)^{\delta} \quad (3)$$

where $\gamma = 2 \pm 1$, and $\delta = 0.20 \pm 0.04$. Equation (3) is based on snow measurements in Canada, where the average snow grain size varied between 1 and 3 mm. The measurement area belongs to taiga snow class [17], which is also the dominant class in northern Finland.

For comparison, also the model used in the Middle East Technical University in Turkey (A. U. Sorman, personal communication) is studied here

$$\kappa_e = 0.08 f^{1.75} d^{1.8}. \quad (4)$$

This equation is for maritime snow, which is characterized by deeper and denser snowpack and larger grain sizes than taiga snow.

Equations (2)–(4) are for dry snow. In the HUT snow model, an approximation for the extinction coefficient of wet snow is calculated with

$$\kappa_{e,\mathrm{ws}} = \kappa_{e,\mathrm{ds}} - \kappa_{a,\mathrm{ds}} + \kappa_{a,\mathrm{ws}} \quad (5)$$

where ws and ds denote the wet and dry snow, respectively, and κ_a is the absorption coefficient calculated from the complex dielectric constant [12, p. 225].

Three of the AMSR-E frequencies (6.9, 10.65, and 89.0 GHz) are outside the reported applicability range of all the three extinction coefficient models. Nevertheless, the same models were applied here also for these frequencies in order to obtain a spectral continuity. (Note that absorption dominates over scattering at lower frequencies.)

B. Soil

The rough bare soil reflectivity model [9] was developed at the same time with HUT snow model for the combined modeling of snow-covered soil and the retrieval of geophysical parameters from satellite data. The target was to develop a simple model with few parameters but a wide applicability. The model is semiempirical and is based on the measurements of soil samples on 1–100 GHz.

The behavior of reflectivity on the vertical (V) polarization is based on the results from the horizontal (H) polarization due to more problematic modeling of reflectivity at V polarization. The equations for rough bare soil reflectivity are

$$r_{h,\mathrm{mod}} = r_{h,\mathrm{Fresnel}} \cdot \exp\left\{-(ks)^{\sqrt{0.10 \cos\theta}}\right\} \quad (6)$$

$$r_{v,\mathrm{mod}} = r_{h,\mathrm{mod}} \cdot (\cos\theta)^{0.655} \quad (7)$$

where $r_{h,\mathrm{Fresnel}}$ is the Fresnel reflectivity on H polarization, k is the wavenumber, s is the standard deviation of surface height, and θ is the incidence angle. The Fresnel reflectivity is dependent on the permittivities of snow (calculated by the HUT snow model) and soil.

The relative dielectric constant of frozen soil was assumed to be constant $\epsilon_{\mathrm{soil}} = 6 - j1$ on all frequencies based on [18]. The high value, compared to the permittivity of ice $\epsilon_{\mathrm{ice}} = 3.15 - j0$, is explained by the inclusion of unfrozen water in the soil even in temperatures below $-20\,^{\circ}\mathrm{C}$. In the data set of this paper, the temperature of soil was always higher than $-8\,^{\circ}\mathrm{C}$.

C. Forest

The boreal forest transmissivity model [7] is purely empirical and based on the measurements of snow-covered forest in Oulu and Sodankylä areas, Finland. The measurements near Oulu were made on 6.8, 10.65, and 18.7 GHz and both V and H polarizations. The measurements near Sodankylä used 24, 34, 48, and 94 GHz but only V polarization. The final model used here is based on the measurements on V polarization only.

The model calculates the transmissivity t of the vegetation using stem volume V (cubic meters per hectare)

$$t(f,V) = t(f,V_{\text{high}}) + [1 - t(f,V_{\text{high}})] \cdot e^{-0.035 \cdot V}$$
$$t(f,V_{\text{high}}) = 0.42 + (1 - 0.42) \cdot e^{-0.028 \cdot f}. \quad (8)$$

The simulation of scene brightness temperature considers forest coverage fraction within a satellite pixel. Fractions of forested and open areas (bogs, lakes, etc.) of the study area were obtained from land cover data.

D. Atmosphere

The atmospheric effects are modeled with two different methods: 1) from the measurements near the ground using a statistical atmospheric model [10], [11] and 2) from the profile data using a physical atmospheric model [12, Ch. 5].

In the statistical model, the upwelling brightness temperature of the atmosphere is calculated with [10]

$$T_{\text{atm},\uparrow} = \alpha_{\uparrow} \cdot T_s \cdot (1 - \tau) \quad (9)$$

where $\alpha_{\uparrow}$ is the approximate atmospheric profile factor [11], T_s is the surface (air) temperature (K), and τ is the atmospheric transmissivity derived from statistical studies [19]. Downwelling brightness temperature is calculated analogous to (9). Since the statistical model assumes average conditions, there are always some clouds included.

The input parameters to the physical model are temperature, pressure, and absolute humidity. Since only relative humidity is measured in the daily soundings, this was converted to absolute humidity with equations from [20]. The physical model is able to calculate the effects of clouds, if there are enough input data of cloud properties.

III. Data and Measurements

All the *in situ* data used in this paper were measured at the Arctic Research Centre (67.368N, 26.633E) of the Finnish Meteorological Institute in Sodankylä, northern Finland. A map of the area is shown in Fig. 1. Most of the data are operational meteorological measurements and available in http://litdb.fmi.fi/. The snow measurement site, like Sodankylä area in general, is covered with sparse pine forest, and the undergrowth consists mainly of heather, lichen, and lingonberry. The region is a typical representative of the boreal Eurasian forest belt. In agreement with Corine Land Cover 2000 data, a forest coverage fraction of 60% was used in the simulation of spaceborne AMSR-E observations.

The reference satellite data are level 2A brightness temperatures [21] from AMSR-E. The instrument measures on both V and H polarizations on six frequencies, 6.925, 10.65, 18.7, 23.8, 36.5, and 89.0 GHz. The Aqua satellite passes directly over the Northern Finland at about 10 (ascending) and 1 (descending) UTC, corresponding to 12 and 3 local times. Two *in situ* data sets corresponding to these two overpass times were collected for all automatic measurements. These two sets are hereinafter referred to as daytime and nighttime data. Manual measurements were performed only during daytime.

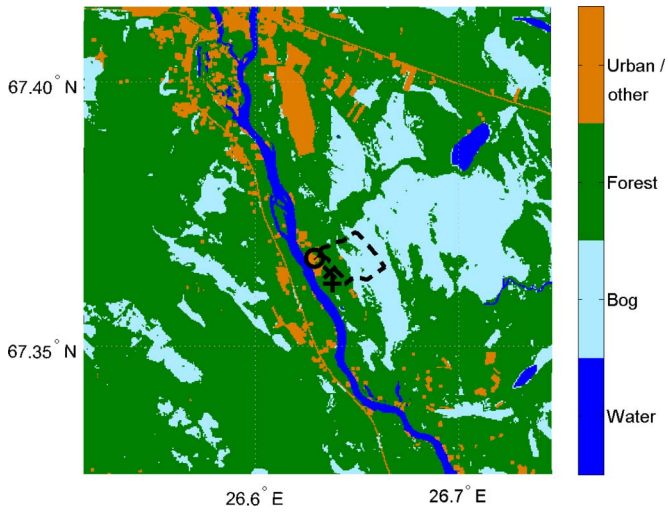

Fig. 1. Land cover map of the Sodankylä area, showing the locations of (o) AWS, (x) snow pit, (+) soil and snow temperature measurement, and (dotted line) snow course. The area of the map is 10 km × 10 km.

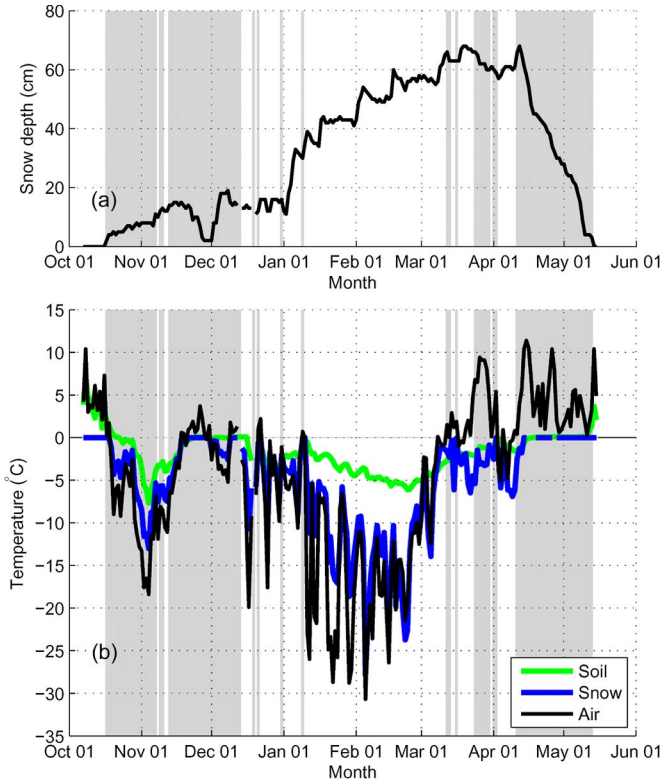

Fig. 2. (a) SD and (b) temperatures of air, snow, and soil. Wet snow periods are marked with gray.

Measurement data were collected from October 7, 2006 to May 15, 2007. The permanent snow fell on October 17 and melted finally on May 13. SD and wet snow seasons are shown in Fig. 2. The minimum, maximum, and mean values of all the measured daytime parameters are shown in Table I. The correlations between the time series of the measured parameters are shown in Table II.

A. Snow

For snow modeling, data from various sources were used. The temperatures and SD were measured automatically every

TABLE I
MINIMUM, MAXIMUM, AND MEAN VALUES AND STANDARD DEVIATIONS OF THE DAYTIME PARAMETERS

Parameter	Min	Max	Mean	Std. dev.	Unit	Type	Number of measurements
Snow temperature	-27.9	0.0	-5.15	5.78	°C	Automatic	221
Snow depth	0	68	32	23	cm	Automatic	221
Snow course mean SWE	17.7	133.8	61.9	47.1	mm	Manual	5
Snow course mean snowpack density	111	228	183	43	kg/m^3	Manual	5
Layer grain size	0.2	4.0	1.67	0.92	mm	Manual	150
Soil temperature	-7.7	6.9	-1.7	2.3	°C	Automatic	221
Air temperature	-30.7	11.4	-4.7	9.2	°C	Automatic	221
Calculated daily SWE	0	129	65	42	mm	Model	
Averaged snow grain size	0.5	2.6	1.6	0.5	mm	Model	

TABLE II
CORRELATIONS BETWEEN THE TIME SERIES OF THE PARAMETERS

	Snow temperature	Snow depth	Grain size	Soil temperature	Air temperature	$T_{B,AMSRE}$ 18.7 GHz V	$T_{B,AMSRE}$ 36.5 GHz V
Snow temperature	1.00	-0.37	0.29	0.74	0.88	0.83	0.78
Snow depth	-0.37	1.00	-0.25	-0.44	-0.11	-0.27	-0.44
Grain size	0.29	-0.25	1.00	0.22	0.35	0.39	0.35
Soil temperature	0.74	-0.44	0.22	1.00	0.67	0.68	0.70
Air temperature	0.88	-0.11	0.35	0.67	1.00	0.90	0.79
$T_{B,AMSRE}$ 18.7 GHz V	0.83	-0.27	0.39	0.68	0.90	1.00	0.96
$T_{B,AMSRE}$ 36.5 GHz V	0.78	-0.44	0.35	0.70	0.79	0.96	1.00

minute. Grain size and SWE were measured manually. For most of the parameters, the data set includes profile measurements, but since the HUT snow model is a one-layer model, the profiles could not be fully used.

For the year 2006, snow temperature was estimated as an average of the measured soil (at 5-cm depth) and air (at 2-m height) temperatures. The measurements of snow temperature profile began at the turn of the year. Automatic sensors measured the temperature every 10 cm from ground surface to 110-cm height. Since the distance between SD and temperature profile measurements is about 600 m, there are differences of a few centimeters between SDs of the two measurement sites. Usually, the temperature profile site had less snow than the SD site. Because of this, it was difficult to determine which temperature sensors were actually buried in snow. The reading of the topmost sensor at least 10 cm below the measured snow surface was used. In the simulations, the snow temperature was also limited to at most 0 °C.

Snow wetness was not measured, but dry snow conditions were estimated from AMSR-E data. Snow was considered dry (0% volumetric moisture) if [22]

$$h > 0.08\ \text{m}, \quad T_{37V} < 250\ \text{K}, \quad T_{37H} < 240\ \text{K} \tag{10}$$

where h is the SD, and T_{37V} and T_{37H} are the AMSR-E brightness temperatures on 36.5-GHz vertical and H polarizations, respectively. If these criteria were not met, snow was considered moist (0.5%) in the simulations.

SWE and SD were measured every month from a snow course by the Finnish Environment Institute (SYKE). The snow course is 4 km long and surrounds an area of 1 km^2. Every month, 80 measurements of SWE and SD were made along the snow course in pine forest, broad-leaved forest, and open bog. Since these monthly measurements of SWE are not enough for daily simulations, the SWE values used as input data in the simulations were calculated from automatic SD measurement and calibrated with monthly snow course data. Since SWE can be expressed as $SWE = \rho \cdot h$, where SWE is the SWE (in millimeters or kg/m^2) and ρ is the density of snow (in kilograms per cubic meter), a linear relationship was derived between the monthly average values of SWE from the snow course and automatic measurements of SD using density as an optimization parameter. The best fit value was $\rho = 205.2820$ kg/m^3. This constant value was used for snow density in simulations and for the calculation of daily SWE from SD. The rms error between the observed and modeled SWEs was 10.8 mm. Seasonal bias was negligible as snowpack density varied through the winter.

The grain sizes of all the layers of snow were measured twice a week from a snow pit. Throughout the winter, the measurements were conducted in the same small area. The snow layers were determined visually, and the thickness of each layer was measured with a stick with 1-cm accuracy. Grain sizes were measured using the procedures suggested by [23]. A small sample of snow was taken on a snow crystal screen with 1-mm grid. The maximum diameter of average-size grains $(D_{\max})$ was estimated visually by comparing the snow sample to the grids. If the grain size was more than 1 mm, the average grain size was estimated with an accuracy of 0.5 mm. With grains smaller than 1 mm, an accuracy of 0.25 mm was used. In cases when a layer contained a mixture of different grain sizes, the range of sizes was recorded, but the typical or average value was used for the whole layer. A picture was taken from each snow sample for later reanalysis. Fig. 3 shows the samples of snow grains from three different layers of a snow pit.

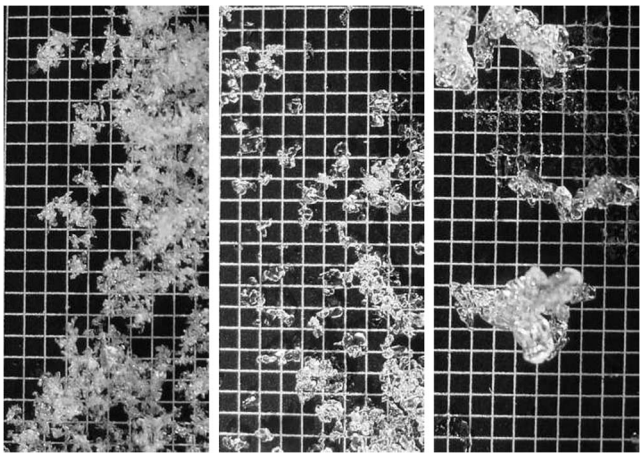

Fig. 3. Grain size measurement using a 1-mm grid. Snow grains of three different layers of one snow pit.

In this paper, we used the data of only one snow pit. In spring 2009, the spatial variability of snow parameters in typical winter conditions in the target area was studied. In total, 56 snow pits were measured in several land cover types. The standard deviation of D_{ave} (see the next paragraph) was 0.15 mm with a mean value of 0.5 mm for the whole data set (0.22 and 0.61 mm in open areas, and 0.13 and 0.48 mm in forests, respectively). Considering the measurement accuracy, the variability of grain sizes is small. Thus, the one snow pit, situated in a sparse forest typical to the area, gives a reasonably good estimate of the snow parameters in the whole area.

It is not straightforward to calculate the one-layer grain size required by the HUT snow model from these measurements, and different methods can be found from the literature (e.g., [15] and [16]). Here, the layer-thickness-weighted average (D_{ave}) of the grain sizes is used. Fig. 4 shows the stratigraphy of snowpack on three days during spring 2007. For example, on March 2, the top layer of 0.5-mm grains was newly fallen snowflakes, the second and fourth layers contained faceted crystals, and the third and bottom layers were ice. All this information is reduced to the averaged grain size of 1.35 mm.

According to [24], grain shape has a negligible effect on the scattering of microwave radiation in snow. Thus, only grain size and layering have an effect. The brightness temperature of snow depends on layering only on H polarization, not substantial on vertical [5], [25]. The effect is largest when wavelength is comparable to layer thickness, i.e., on low frequencies (6.9 and 10.65 GHz). Specifically, thin ice layers change the brightness temperature signature of snow [5], [25]. However, in natural snowpacks, ice layers are not uniform in the scale of tens of kilometers, but varying and discontinuous [25], particularly when sparse boreal forests that are characterized by forest openings are considered. Thus, for the most part, the effect of layering averages out in microwave satellite data.

B. Soil and Vegetation

Soil temperature is needed in the modeling of emission from soil. The temperature measured at 5-cm depth was used.

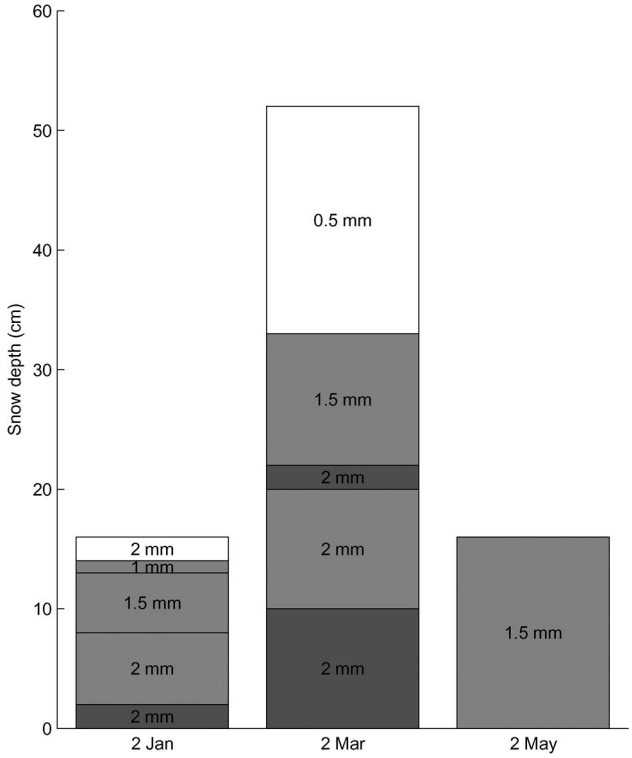

Fig. 4. Snow profiles of three days drawn to scale. Numbers denote grain size in the layer. Snow structure is marked by colors: white denotes snowflakes, light gray denotes separate crystals, and dark gray denotes ice layers.

For the forest areas, the vegetation temperature was approximated to be equal to the measured air temperature at 2 m. The forest stem volume was estimated to be 80 m^3/ha, which is a typical value for Northern Finland. Areal forest coverage fraction for the AMSR-E resolution scale was determined from digital land cover data.

C. Atmosphere

Three sources of data for atmospheric modeling were used:

1) automatic weather station (AWS) measurements of air temperature and cloud bottom height;
2) balloon-borne radiosounding profiles of pressure, temperature, and humidity up to 20 km;
3) the European Centre for Medium-Range Weather Forecasts (ECMWF) ERA-40 profiles of densities of cloud liquid water and cloud ice water.

The AWS system logged data every minute and a radiosonde were launched twice a day, at 11 and 23 UTC, which correspond well to daytime and nighttime satellite overpasses.

Due to lack of any hydrometeor data, an accurate cloud modeling was not possible with locally measured data. To include the average cloud effects, ERA-40 profiles from 1991 to 2001 were used in addition to sounding profiles to calculate the average cloud effects for those cases when AWS cloud bottom height data indicated clouds.

IV. Simulation and Analysis Methods

All in all, seven different scenarios for all the AMSR-E frequencies, both polarizations and both day and nighttime, were

TABLE III
SIMULATED SCENARIOS

Scenario	κ_e	Snow and soil data	Atmospheric data	Atmospheric model
1	Eq. (2)	All	AWS	Statistical
2	Eq. (3)	All	AWS	Statistical
3	Eq. (4)	All	AWS	Statistical
4	Eq. (2)	Snow depth	AWS	Statistical
5	Eq. (2)	All	Sounding profiles	Physical
6	Eq. (2)	All	Sounding profiles, ERA-40 and AWS	Physical
7	Eq. (2)	All, modeled grain size	AWS	Statistical

simulated. The scenarios are listed in Table III and presented in more details in the next section. In different scenarios, we compared three extinction coefficient models, two atmospheric models, and different sources of model input data.

A. Scenario Description

In all the scenarios, dry snow was estimated with (10), and otherwise, a wetness of 0.5% was assumed. Unless otherwise stated, the layer-thickness-weighted average grain size was used.

Scenario 1: This is the basic scenario. It applies the extinction coefficient model of (2). All the measured snow and soil data are used as input to the simulation. AWS data with statistical model are used to simulate the atmosphere. The average cloud conditions are included through the statistical atmospheric model.

Scenario 2: Same as scenario 1), except the snow extinction coefficient of (3) is used.

Scenario 3: Same as scenario 1), except the snow extinction coefficient of (4) is used.

Scenario 4: This was run with only SD and air temperature data. All the other input parameters were estimated from these two: ground and snow temperatures were set equal to air temperature, grain size was constant at 1 mm, and daily SWE was calculated from SD, like in all the other scenarios. The statistical atmospheric model and the extinction coefficient model of (2) were used.

Scenario 5: This was calculated with balloon-borne radiosounding profiles of pressure, temperature, and humidity. No cloud data were used. The physical atmospheric model and the extinction coefficient model of (2) were used.

Scenario 6: In this scenario, an attempt to model clouds was made. The AWS measurement of cloud bottom height was compared to ECMWF ERA-40 cloud liquid water profiles of the same calendar month from 1991 to 2001. The ERA-40 profiles are available only to year 2001; thus, historical data had to be used in this study. The averages of the best match cloud liquid and ice water profiles were used in addition to sounding profiles of temperature, pressure, and humidity. The physical atmospheric model and the extinction coefficient model of (2) were used.

Scenario 7: Same as scenario 1), except, now, a new model (see Section V-C) for an effective snow grain size was used instead of the layer-thickness-weighted averages used in the other scenarios.

TABLE IV
BIASES OF THE SIMULATED SCENARIOS

f	Scenario						
(GHz)	1	2	3	4	5	6	7
V pol							
6.9	-1.42	-9.08	-3.60	-2.16	-1.52	1.41	-1.31
10.7	1.83	-6.72	-1.65	1.36	1.74	4.82	2.12
18.7	3.02	-3.66	-1.54	4.08	3.01	6.15	4.02
23.8	4.19	0.86	0.65	6.39	3.66	6.64	5.62
36.5	2.58	9.12	3.51	8.79	-0.53	3.83	5.29
89.0	-1.25	15.01	3.01	3.67	-8.47	-6.94	0.80
H pol							
6.9	0.68	-6.65	-1.41	0.29	0.50	2.88	0.78
10.7	4.81	-3.38	1.48	4.59	4.59	7.13	5.09
18.7	7.07	0.67	2.70	8.20	6.77	9.43	8.03
23.8	9.26	6.06	5.86	11.43	8.11	10.73	10.64
36.5	6.42	12.71	7.31	12.41	2.54	6.94	9.02
89.0	2.05	17.75	6.16	6.76	-5.51	-3.99	4.02

TABLE V
RMS ERRORS OF THE SIMULATED SCENARIOS

f	Scenario						
(GHz)	1	2	3	4	5	6	7
V pol							
6.9	7.02	14.46	8.53	10.09	7.07	7.00	6.99
10.7	6.55	13.93	8.49	7.90	6.60	7.97	6.52
18.7	8.05	12.02	10.57	6.70	8.10	9.80	7.54
23.8	9.56	9.39	10.48	8.28	9.86	11.52	8.78
36.5	13.73	12.93	12.95	11.14	16.09	15.53	11.04
89.0	13.97	20.10	13.55	11.93	19.37	19.18	13.12
H pol							
6.9	9.23	13.45	9.63	10.94	9.23	9.54	9.25
10.7	9.52	11.86	9.08	9.34	9.50	11.22	9.61
18.7	11.43	10.54	10.65	10.28	11.25	13.39	11.51
23.8	13.71	11.38	12.28	13.35	13.08	15.26	13.78
36.5	14.96	16.30	14.57	14.40	15.83	16.41	13.32
89.0	14.12	22.65	14.76	13.12	17.70	17.63	13.47

B. Data Analysis

The correlations, biases, and rms errors between simulated and reference data sets for daytime data are shown in Tables IV–VII. Bias is defined as

$$\left[\sum_{1}^{n}(T_{B,\mathrm{simu}} - T_{B,\mathrm{AMSR-E}})\right] \Big/ n \qquad (11)$$

TABLE VI
UNBIASED RMS ERRORS OF THE SIMULATED SCENARIOS

f	Scenario						
(GHz)	1	2	3	4	5	6	7
V pol							
6.9	6.87	11.25	7.73	9.86	6.90	6.85	6.87
10.7	6.29	12.20	8.33	7.78	6.37	6.35	6.17
18.7	7.46	11.45	10.46	5.31	7.52	7.63	6.38
23.8	8.59	9.36	10.46	5.26	9.16	9.41	6.74
36.5	13.48	9.17	12.47	6.84	16.08	15.05	9.69
89.0	13.92	13.37	13.21	11.35	17.42	17.88	13.10
H pol							
6.9	9.44	11.94	9.77	11.21	9.43	9.21	9.45
10.7	8.74	11.85	9.49	8.76	8.79	8.97	8.68
18.7	9.85	11.38	11.14	7.44	9.74	10.05	9.17
23.8	11.31	10.95	11.99	8.54	11.19	11.59	10.09
36.5	14.05	10.81	13.17	8.15	15.93	15.20	10.49
89.0	14.35	14.33	13.77	11.66	17.08	17.43	13.26

TABLE VII
CORRELATIONS BETWEEN THE REFERENCE DATA AND THE SIMULATED BRIGHTNESS TEMPERATURES

f	Scenario						
(GHz)	1	2	3	4	5	6	7
V pol							
6.9	0.69	0.60	0.67	0.85	0.68	0.68	0.69
10.7	0.71	0.65	0.68	0.88	0.69	0.70	0.71
18.7	0.76	0.75	0.73	0.92	0.76	0.76	0.81
23.8	0.79	0.82	0.78	0.92	0.78	0.78	0.86
36.5	0.82	0.88	0.84	0.94	0.81	0.81	0.89
89.0	0.80	0.85	0.81	0.87	0.78	0.79	0.83
H pol							
6.9	0.34	0.46	0.39	0.58	0.34	0.37	0.34
10.7	0.58	0.67	0.63	0.79	0.57	0.56	0.58
18.7	0.76	0.78	0.75	0.90	0.76	0.76	0.80
23.8	0.79	0.82	0.78	0.91	0.79	0.78	0.86
36.5	0.82	0.87	0.83	0.94	0.81	0.81	0.89
89.0	0.81	0.86	0.82	0.88	0.79	0.80	0.84

where n is the number of days when both AMSR-E measurement and sufficient *in situ* data for simulations have been available. Positive bias shows overestimation in simulation. RMS error is defined as

$$\sqrt{\left[\sum_{1}^{n}(T_{B,\mathrm{simu}} - T_{B,\mathrm{AMSR-E}})^2\right] \Big/ n} \tag{12}$$

and unbiased rms error as

$$\sqrt{\left[\sum_{1}^{n}(T_{B,\mathrm{simu}} - T_{B,\mathrm{AMSR-E}} - bias)^2\right] \Big/ n}. \tag{13}$$

In the following, a simulation error is defined as

$$T_{B,\mathrm{AMSR-E}} - T_{B,\mathrm{simu}}. \tag{14}$$

TABLE VIII
BIASES AND UNBIASED RMS ERRORS OF SCENARIO 1) SIMULATIONS WITH DAYTIME AND NIGHTTIME DATA

f	Bias (K)		Unbiased rms error (K)	
(GHz)	Day	Night	Day	Night
V pol				
6.9	-1.42	-2.20	6.87	5.92
10.7	1.83	1.58	6.29	6.02
18.7	3.02	3.17	7.46	7.89
23.8	4.19	4.34	8.59	9.36
36.5	2.58	2.43	13.48	14.89
89.0	-1.25	-0.97	13.92	14.73
H pol				
6.9	0.68	-0.50	9.44	7.52
10.7	4.81	4.86	8.74	8.61
18.7	7.07	7.58	9.85	10.50
23.8	9.26	9.85	11.31	11.97
36.5	6.42	6.55	14.05	15.28
89.0	2.05	2.21	14.35	15.07

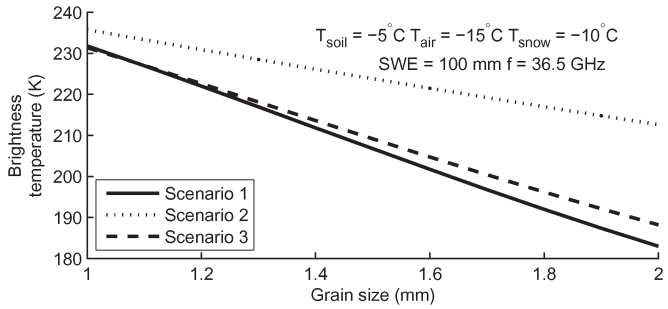

Fig. 5. Effect of grain size on brightness temperature on 36.5-GHz V polarization simulated with the three extinction coefficient models.

To study the effect of grain size on the error of the simulated brightness temperatures, grain size (D_{est}) was estimated by minimizing the difference between the brightness temperatures of simulation and AMSR-E measurements using grain size as the free optimization parameter, separately for each day and each of the 12 channels

$$\min |T_{B,\mathrm{simu}}(D_{\mathrm{est}}) - T_{B,\mathrm{AMSR-E}}|. \tag{15}$$

Grain size was limited to the range of 0–3 mm in the minimization. The results of the minimization process are given in Section V-C.

When analyzing the simulated data, it turned out that grain size is one of the main sources of errors in the simulations. A new model for calculating the effective grain size required by the HUT snow model (D_{eff}) was tested. Equation

$$D_{\mathrm{eff}} = A \cdot (1 - e^{-B \cdot D_{\mathrm{ave}}}), \tag{16}$$

where A and B are empirical constants, was fitted to the data. The derivation of parameter values for (16) is discussed in more details in Section V-C.

TABLE IX
UNBIASED RMS ERRORS OF SCENARIOS 1)–3) FOR DRY SNOW PERIODS

f	Scenario					
(GHz)	V pol			H pol		
	1	2	3	1	2	3
6.9	5.06	11.38	6.53	5.02	9.03	5.56
10.7	5.59	13.04	8.39	7.40	10.24	7.89
18.7	8.66	13.12	12.33	11.72	12.09	12.62
23.8	10.57	11.17	12.81	14.04	12.65	14.25
36.5	16.45	10.71	15.13	16.89	13.20	15.78
89.0	11.87	13.10	11.91	11.95	15.14	12.43

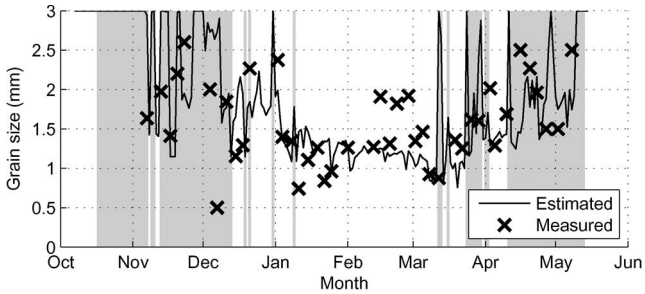

Fig. 6. Grain size estimated from scenario 1) on 36.5-GHz V polarization and the measured grain size as a function of time. Wet snow periods are marked with gray.

V. DISCUSSION

A. Comparison of Daytime and Nighttime Data

During daytime, snow absorbs solar radiation and possibly melts. Due to this, nighttime satellite data are usually preferred in the retrieval of snow parameters from spaceborne measurements. However, the manual measurements (grain size and SWE) were carried out only during daytime. Therefore, it is interesting to compare the differences in simulations calculated with daytime and nighttime automatic data. The same manual snow measurement data were used in both cases.

The difference between scenario 1) simulations with daytime and nighttime data was, except for a few isolated days, less than 5 K until the beginning of snowmelt in late March. After mid-March, the difference is large when snow is wet, as was expected. However, as shown in Table VIII, on most channels, the bias and unbiased rms errors of simulation with daytime input data are lower than those of simulation with nighttime data. Therefore, only daytime results are presented in the following.

B. Comparison of Extinction Coefficient Formulas

Scenarios 1)–3) were calculated using the three different extinction coefficient formulas. The biases, rms errors, and correlations are shown in columns 1–3 in Tables IV–VII. Scenarios 1) and 3) show very similar behavior, while scenario 2) differs much from these two. The effect of grain size on brightness temperature simulated with the three extinction coefficient formulas is shown in Fig. 5. In scenario 2), the grain size has much smaller effect on brightness temperature than in scenario 1) or 3). This explains why scenarios 1) and 3) give fairly similar results, while scenario 2) differs from the others.

Contrary to the results of [16], there is no drastic improvement from scenario 1) to 2) on 18.7- and 36.5-GHz V polarization channels in Tables IV–VII. The possible reasons for this are as follows.

1) Different snow structures. Even though the measurement areas of [16] in Canada and the area in Finland used here are all classified as taiga [17], the data set of [16] includes

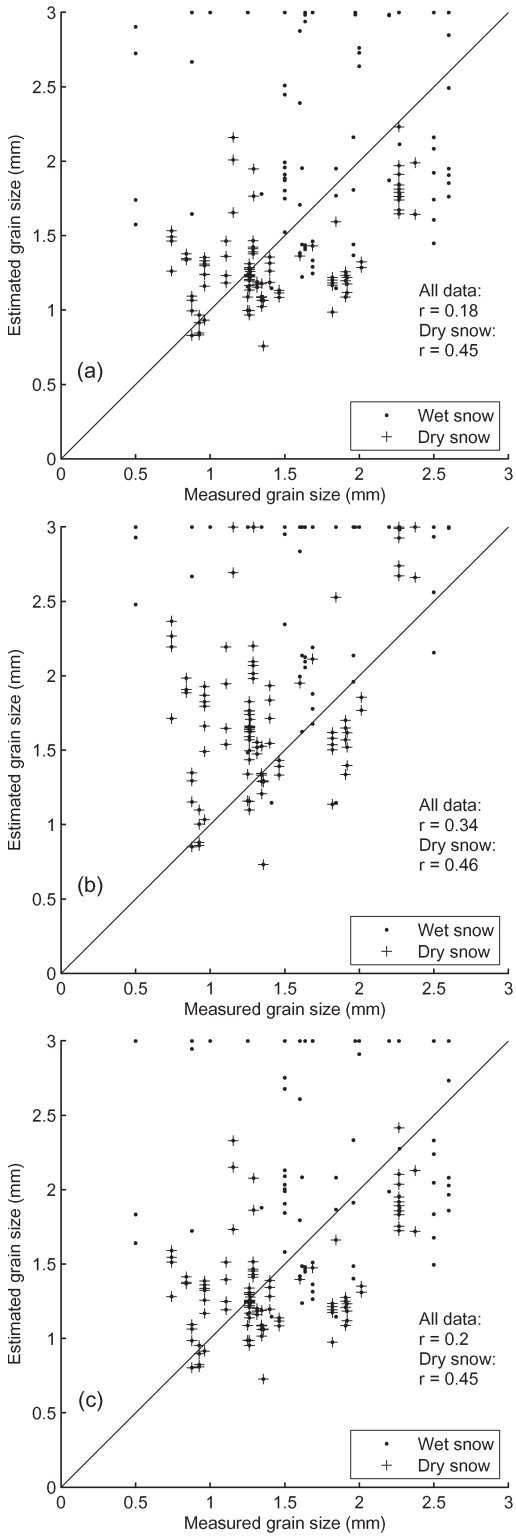

Fig. 7. Estimated and measured grain size on 36.5-GHz V polarization with (dots) the whole data set and (plusses) dry snow periods for (a) scenario 1, (b) scenario 2, and (c) scenario 3. The results are obtained by applying (15) for this single channel.

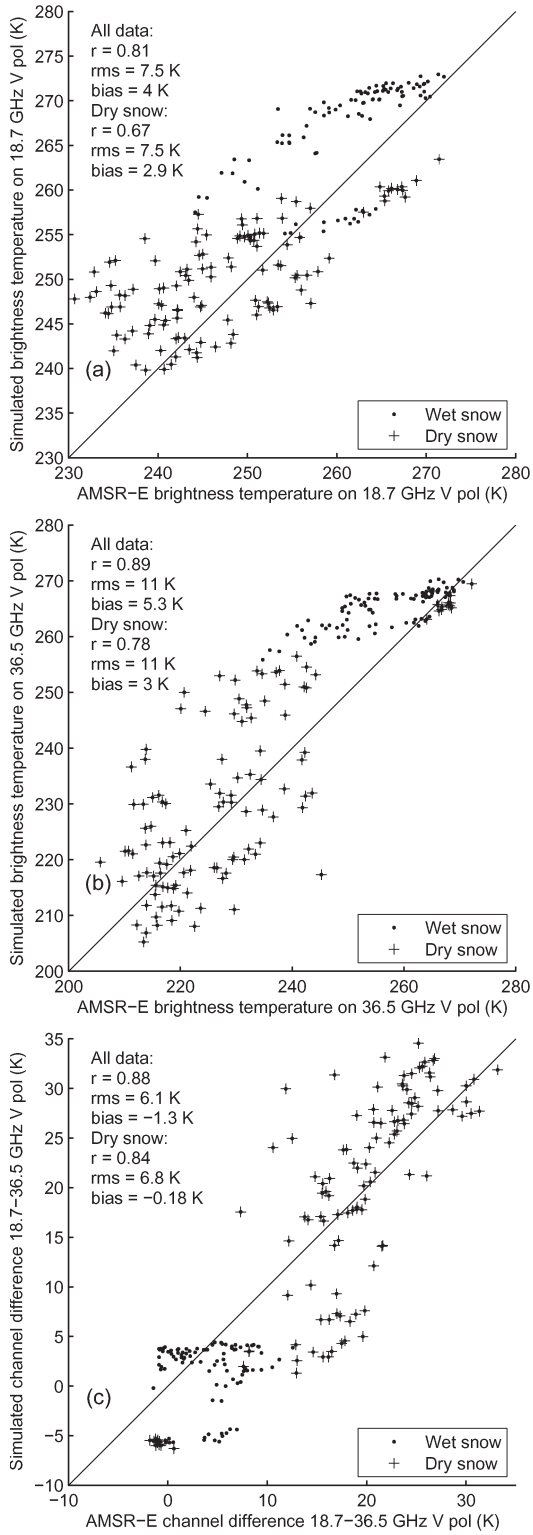

Fig. 8. AMSR-E measurement versus brightness temperature simulated using the grain size modeled with (16) (scenario 7) on (a) 18.7, (b) 36.5 GHz, and (c) channel difference 18.7–36.5 GHz on V polarization. The bias, rms errors, and correlations of the simulations are listed in column 7 of Tables IV–VII.

smaller SWE values and larger grain sizes than the one used here. Article [16] does not describe the vertical structure of the snowpack. Here, many different conditions from homogeneous snowpack to a case of nine layers with different grain sizes and shapes were included.

TABLE X
BIASES OF SCENARIO 7 FOR FIVE EPISODES OF THE WINTER

f (GHz)	Early winter	Acc.	Mid-winter	Early snowmelt	Snowmelt
V pol					
6.9	-1.21	-2.18	-5.43	-2.03	4.32
10.65	2.65	3.43	-0.93	-0.12	4.76
18.7	5.21	8.49	0.49	1.15	2.56
23.8	6.86	10.43	1.26	3.93	3.19
36.5	10.81	8.15	-4.87	0.40	3.15
89	10.08	-5.78	-4.95	-5.70	-3.15
18.7-36.5	-5.60	0.34	5.36	0.75	-0.59
H pol					
6.9	-2.42	1.85	-2.65	3.84	7.99
10.65	1.94	9.84	3.45	7.21	7.24
18.7	5.71	17.20	6.62	8.82	4.32
23.8	8.72	20.44	8.59	11.75	5.39
36.5	12.19	15.87	0.57	5.62	5.19
89	11.67	-0.97	0.91	-2.33	-0.24
18.7-36.5	-6.49	1.33	6.04	3.20	-0.87

2) Size of the data set. The data set used here covers the whole winter from the first snow to the final snow melt in the spring. Article [16] uses campaign data from ten consecutive days.
3) Reference data set. Article [16] compares simulations to airborne data, while here, satellite data are used. The choice of reference data has two major implications: With airborne data, the effects of atmosphere can be considered almost negligible, while with satellite data, the modeling of atmosphere is important. Moreover, the spatial resolution of airborne radiometer measurements is about 80 m [16], while the resolution of AMSR-E data is 5–60 km, depending on frequency [26].

Table IX shows the unbiased rms errors of scenarios 1–3 for dry snow periods. On 18.7 GHz, scenario 1 has the lowest unbiased rms error, but on 36.5 GHz, scenario 2 is better. In the whole frequency range of 6.9–89.0 GHz, scenario 1 has the lowest unbiased rms errors on most frequencies when only dry snow periods are studied but also when the whole winter data set is considered. Equation (2) used in scenario 1 works well also on the two lowest frequencies, which are outside the frequency range of this extinction coefficient model. For these reasons, model (2) was used in scenarios 4–7.

C. Grain Size Estimation and Modeling

The effect of grain size was studied further by minimizing the error of simulated brightness temperatures with (15). The time series of estimated and measured grain sizes (D_{ave}) are shown in Fig. 6. The correlations between the estimated and measured grain sizes are low, less than 0.4 when whole winter is considered and less than 0.5 when only dry snow periods are studied. The differences between scenarios 1, 2, and 3 are very small. The low correlation values were expected, since here, all the simulation errors were compensated by adjusting the grain size.

Fig. 7 shows the estimated and measured grain sizes ($D_{\rm ave}$) on 36.5-GHz V polarization for scenarios 1–3. In particular, in scenario 1 the estimated grain size of dry snow tends to saturate on large values. It is possible that the thick depth hoar layer of large grains at the bottom of the snowpack dominates the calculation of $D_{\rm ave}$ too much. Therefore, a new model was adopted for the calculation of an effective grain size $D_{\rm eff}$ from the measured layer-thickness-weighted average grain sizes $D_{\rm ave}$. In practice, the empirical formula for $D_{\rm eff}$ (16) was applied to the minimization procedure similar to (15) with parameters A and B

$$\min \sum_{i=1}^{n} \left(D_{\rm eff}(A,B) - D_{\rm est}\right)^2 \tag{17}$$

where n is the number of dry snow observation cases. Since the grain size estimation according to (15) was done separately for all channels, also the constants A and B were calculated for all channels. However, the values for different channels were so close to each other that $A = 1.5$ and $B = 1.5$ were chosen for all frequencies and both polarizations.

Scenario 7 was calculated using

$$D_{\rm eff} = 1.5 \cdot (1 - e^{-1.5 \cdot D_{\rm ave}}) \tag{18}$$

instead of $D_{\rm ave}$. The scatterplots of results on 18.7 and 36.5 GHz, as well as their difference, are shown in Fig. 8. The correlations between the measured and simulated channel differences $T_{B,18.7V} - T_{B,36.5V}$ are 0.83 in scenario 1 and 0.88 in scenario 7. Tables IV–VII show higher correlation and lower rms error on both polarizations but larger bias in scenario 7 than in scenarios 1–3. The new grain size model (18) is better able to predict the channel difference $T_{B,18.7V} - T_{B,36.5V}$, in addition to individual channels, than the simple layer-thickness-weighted average of grain size. The simulated brightness temperature time series have lower rms error when only dry snow periods are considered, as well as when the whole winter time series are studied.

D. Simulation With Limited In Situ Data

Scenario 4 was run with only SD and air temperature data, which are commonly measured from many places, and all the other input parameters were estimated from these two. The results in Tables IV–VII column 4 show higher correlation between the measured and simulated time series than in scenarios 1–3 on all channels. Moreover, the bias and rms errors are, on most channels, the lowest in scenario 4.

As Table II shows, the AMSR-E measurements correlate very well with air temperature. Thus, the air temperature, with the addition of SD, is adequate to simulate most of the variations in brightness temperature.

The results might also reflect the problems in grain size measurements: The measurement process is not very exact, but the layer thicknesses and grain sizes vary with personnel performing measurements. Moreover, the calculation of $D_{\rm ave}$ from the measured profiles causes additional errors, like the saturation of estimated grain sizes noted in Section V-C proves. Finally, grain size profiles were measured only in one location, and the snow structure is not uniform over the entire satellite pixel.

As a conclusion, the HUT snow model with only the measurements of air temperature and SD is quite reliable, at least when long time series are considered.

TABLE XI
UNBIASED RMS ERRORS OF SCENARIO 7 FOR FIVE EPISODES OF THE WINTER

f (GHz)	Early winter	Acc.	Mid-winter	Early snowmelt	Snowmelt
V pol					
6.9	7.34	3.50	1.81	7.21	7.58
10.65	7.24	3.58	2.79	5.51	6.55
18.7	6.64	5.18	4.40	5.85	5.12
23.8	6.36	6.12	4.78	7.66	4.20
36.5	7.85	9.45	5.48	9.92	4.48
89	12.71	11.57	7.70	11.18	5.91
18.7-36.5	4.57	6.10	2.90	4.98	3.49
H pol					
6.9	9.36	6.76	3.86	11.33	11.11
10.65	9.36	8.14	5.78	9.66	9.16
18.7	8.16	10.81	8.24	10.24	6.49
23.8	8.26	12.49	9.60	11.54	5.32
36.5	8.71	12.73	8.34	11.35	4.77
89	13.28	12.99	9.91	12.35	6.95
18.7-36.5	5.18	6.65	3.04	5.96	4.67

TABLE XII
CORRELATIONS BETWEEN SCENARIO 7 AND AMSR-E MEASUREMENTS FOR THE FIVE EPISODES OF THE WINTER

f (GHz)	Early winter	Acc.	Mid-winter	Early snowmelt	Snowmelt
V pol					
6.9	0.26	0.49	0.76	0.81	0.71
10.65	0.32	0.66	0.70	0.83	0.60
18.7	0.51	0.76	0.48	0.83	0.40
23.8	0.70	0.74	0.45	0.83	0.39
36.5	0.86	0.61	0.40	0.89	0.36
89	0.79	0.66	0.69	0.82	0.52
18.7-36.5	0.65	0.30	0.39	0.91	0.46
H pol					
6.9	0.01	0.02	0.71	0.08	0.21
10.65	0.10	0.47	0.66	0.70	0.23
18.7	0.45	0.76	0.46	0.83	0.24
23.8	0.66	0.77	0.41	0.84	0.28
36.5	0.87	0.62	0.31	0.88	0.32
89	0.78	0.69	0.69	0.80	0.46
18.7-36.5	0.50	0.19	0.27	0.85	0.23

E. Comparison of Ground-Based Data and Profiles

Scenario 5 was calculated with radiosounding profiles of pressure, temperature, and humidity without any input data of cloud parameters. There is not much difference in the biases and correlations of scenarios 1 and 5, but the difference of unbiased

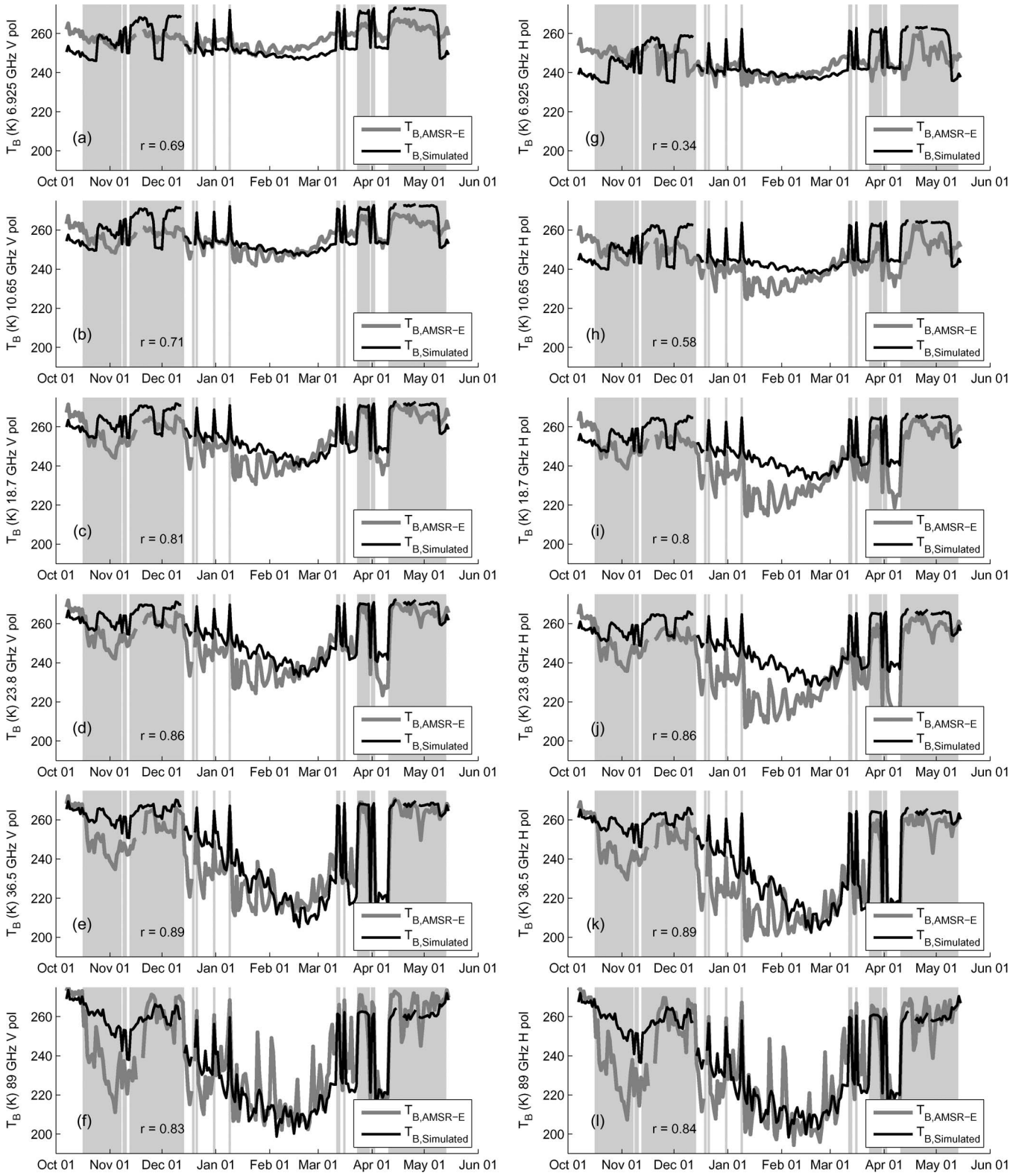

Fig. 9. AMSR-E measurement and simulation results of scenario 7 on (a) and (g) 6.9-, (b) and (h) 10.65-, (c) and (i) 18.7-, (d) and (j) 23.8-, (e) and (k) 36.5-, and (f) and (l) 89.0-GHz V and H polarizations, respectively. Wet snow periods are marked with gray.

rms errors increases with frequency, and scenario 5 has larger error values than scenario 1.

Clouds were included in scenario 6) through AWS cloud bottom height measurements and historical ECMWF ERA-40 profiles. Columns 5–6 in Tables IV–VII show that this crude method of cloud modeling does not improve the simulation results. Moreover, scenarios 1–3 with a constant statistical atmosphere still have lower bias and rms error. This implies

that the statistical atmospheric model is better than the profile data in the calculation of atmospheric effects, when the physical model [12, Ch. 5] is applied with balloon-borne sounding profile data. In addition, the use of sounding profiles does not appear to increase simulation accuracy. In addition, variations in the atmosphere appear to have only a marginal effect on brightness temperature, and significant simulation errors originate from other sources.

F. Temporal Analysis of Scenario 7

To see in more details if the HUT snow model can track the variation of brightness temperature over time, the winter was divided into five episodes.

1) Early winter (until December 31): Less than 20 cm of snow. Air temperature varies below and above 0 °C.
2) Accumulation (January 1–February 4): Snowpack deepens from 10 to 55 cm, and air temperature varies between 0 and −30 °C.
3) Midwinter (February 5–March 7): Deep snowpack (50–60 cm); air temperature below 0 °C.
4) Early snowmelt (March 8–April 10): Deep snowpack (55–68 cm). Air temperature varies below and above 0 °C.
5) Snowmelt (April 11 onward): Snow melts (from 68 to 0 cm), and air temperature is above 0 °C.

The biases, unbiased rms errors, and correlations of scenario 7 for these five periods are shown in Tables X–XII. The simulation results and AMSR-E measurements are shown in Fig. 9. As an example, more detailed results for the five episodes of the winter on channel difference 18.7–36.5 GHz on V polarization are shown in Fig. 10.

During early winter, simulations and AMSR-E measurements do not match. In particular, on low-frequency simulations and measurements are far from each other. The correlation is better on higher frequencies, but still, the biases and rms errors are quite large. One possible reason for the poor results is snow patchiness, which is not accounted for in the simulations. The consecutive melt–refreeze cycles form ice layers which, together with snow patchiness, modify the snow brightness temperature.

During the snow accumulation period, both the measured and simulated brightness temperatures generally decrease with the increasing SD. The up- and downward peaks in brightness temperature are in the same locations in both the simulations and the AMSR-E measurements, but the amplitude of variations is much larger (about 15 K) in the AMSR-E data than in the simulation results (about 5 K). The changes in the measured brightness temperature follow those in air temperature (correlation from 0.77 to 0.95, depending on channel). This reflects the results of Section V-D, where air temperature was noted to explain the changes in the measured brightness temperature very well.

In midwinter, the measured brightness temperature generally increases. Rosenfeld and Grody [27] explained the increase of brightness temperature with increasing SD in late winter by metamorphic changes in the snow crystalline structure. Despite the inclusion of grain size data in the simulation, the brightness temperature minimum of the simulation is later (at

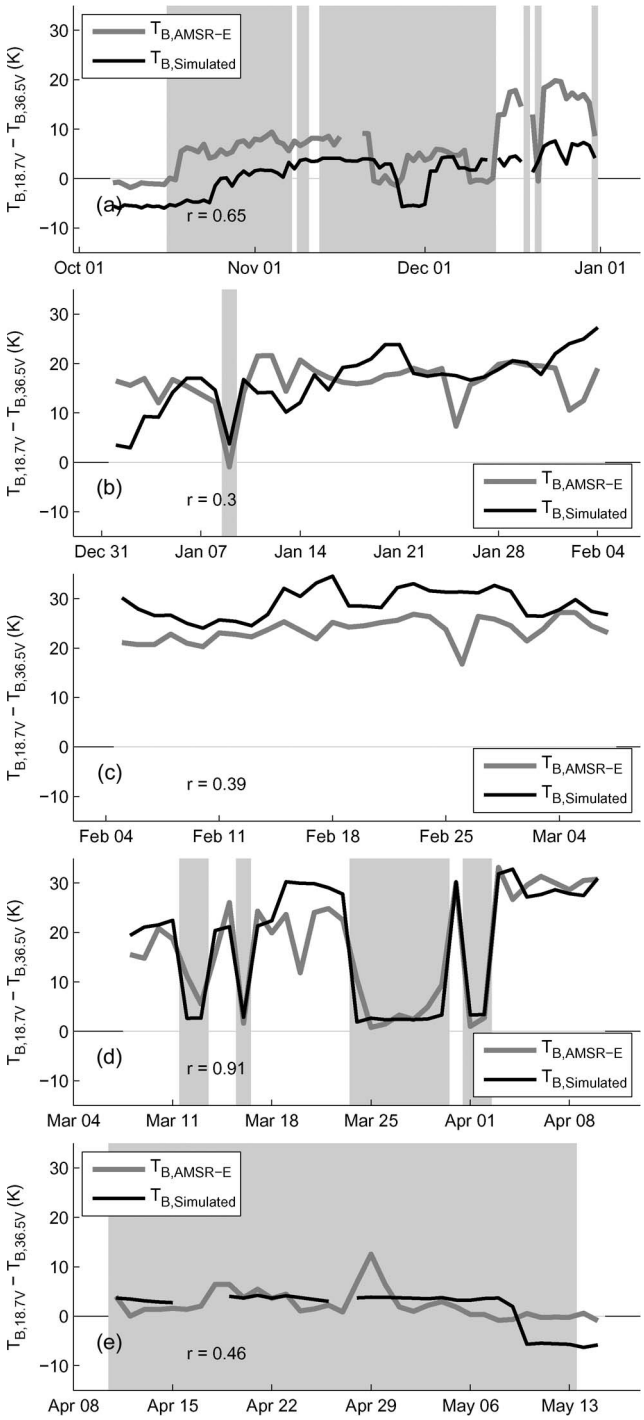

Fig. 10. Simulation 7 result and AMSR-E measurement on channel difference 18.7–36.5-GHz V polarization during (a) early winter, (b) snow accumulation, (c) midwinter, (d) begin of snowmelt, and (e) snowmelt season. Wet snow periods are marked with gray.

the end of February) than in the AMSR-E data (beginning of January). In particular, on H polarization, the measured brightness temperature actually increases during the whole dry snow season in the accumulation period and midwinter. Only at the end of midwinter, when also simulated brightness temperature increases, the simulated and measured brightness temperatures are on the same level. For the whole midwinter period, only on 89 GHz, the simulation follows the AMSR-E measurements well: The peaks are in their correct locations, and the general

trend is the same in simulations and measurements. Again, the amplitude of variations in satellite measurements is much larger than in the simulations.

During the early snowmelt period, the variation in brightness temperature is the largest of the five periods due to several melt–refreeze cycles. On 18.7 GHz, the simulations follow the measurements well. Since, in the simulations, the snow moisture content is assumed to be either 0% or 0.5%, the jumps in simulated brightness temperature are very radical, and the brightness temperature of wet snow is always about 270 K. In natural snowpacks, the moisture content changes gradually, and thus, the increases/decreases in brightness temperature are slower. The small increases of the measured brightness temperature during the first detected wet snow period and in between of the second and the third wet snow periods might be the results of moist snow with lower moisture content than 0.5%. However, with the used dry snow detection algorithm, only the first peak of these is noticed, and thus, the second peak does not appear in the simulations. The difference in brightness temperatures between dry and wet snow is the same on all the channels (about 20 K) in the simulations. In AMSR-E measurements, the difference is about 5 K on the two lowest frequencies, but from 18.7 GHz upward, the difference is modeled well.

The dry season at the end of early snowmelt period is modeled well only on the lowest and highest frequencies. Otherwise, the simulated value is much too large. On the lowest and highest frequencies, the penetration depth of microwave radiation to snow is either very large (about 10 m) or very low (about 1 cm), and thus, the snow cover does not affect the simulation results much. Even a small change of $+0.15$ mm to the snow grain size would reduce the error greatly on 18.7, 23.8, and 36.5 GHz. The same applies also for the beginning of the snowmelt period. This shows that the HUT snow model is very sensitive also to other parameters than air temperature. In particular, grain size has a large effect on the simulation results, and thus, small errors in the input parameters cause large errors in the results.

During snowmelt, except for the 89-GHz channels, the simulated brightness temperature stays at about 270 K for the whole time until all the snow has melted and the brightness temperature suddenly drops. The AMSR-E measurement decreases more gradually. Here again, snow patchiness was not accounted for: On April 27, about half of the ground was already free of snow at the snow pit site. The liquid water in snow lifts the simulated brightness temperatures to the level of 270 K until all the snow has melted on May 10.

From the point of view of satellite snow algorithms, the interesting factor is whether the difference $T_{B,18.7} - T_{B,36.5}$ is modeled better than the individual frequencies. According to Tables X–XII, generally, the rms error of the channel difference is lower and correlation higher than those of the individual frequencies. During early winter [Fig. 10(a)], there seems to be a temporal bias of a couple of days in the simulations. There is a clear explanation for the delay of the first brightness temperature jump at the end of October. Since SWE was calculated using a curve fitted to the measurements of the whole winter, SWE gets nonzero values only after the SD has reached 5 cm. The first snow (showing depths of < 5 cm) fell on the same day that the AMSR-E channel difference jumps upward. This is not considered in the simulations, as SWE is estimated to be 0 mm for this period.

At the end of November, the simulation reacts to drop (November 26) and rise (December 1) of the measured SD. Since SD does not reach zero, there is no temporal difference between the changes in SD and SWE. The AMSR-E data have two separate drops, November 22–27 and December 9–13. In both cases, there is a high peak in AMSR-E 36.5-GHz data and a little lower peak on 18.7 GHz. In December, there is a simultaneous peak in the measured air temperature and snow grain size, but there are no dramatic changes in any of the measured parameters in November. Possibly, this drop in the AMSR-E channel difference is the effect of interaction of changes in snow grain size, air temperature, snow wetness, and patchiness.

However, all these problems are related to very thin snowpack and are not present later in the winter. In particular, during snow accumulation, the bias of the channel difference is much lower than that of the individual channels. During the last three periods, the effect is not as clear, but still, the unbiased rms errors, and, in most cases, biases, are lower on the channel difference than on individual channels.

VI. Summary

The brightness temperature time series of snow-covered ground in varying snow and atmospheric conditions have been simulated using the HUT snow emission model. Seven different scenarios were simulated. The simulations calculated with input data measured during daytime had lower bias and unbiased rms error than the simulations with automatical measurements during nighttime.

Different models for snow extinction coefficient have been compared. The model [13] had the lowest unbiased rms errors on most simulated frequencies both with the whole winter data set and only dry snow periods. It performed quite well also with frequencies outside its original applicability range. The simulations with limited *in situ* data set showed that the HUT snow emission model is quite reliable even when only air temperature and SD data are available.

By comparing the ground-based air temperature measurements and a statistical atmospheric model with balloon-borne sounding profiles and a physical atmospheric model, it was found that the simulations with the statistical model had lower bias and rms error.

A time series of optimized grain sizes was calculated by minimizing the simulation error. The optimized grain size tended to saturate with large values, and therefore, a new model to calculate an effective grain size has been adopted. The simulation with the effective grain size as input has lower rms error and higher correlation with AMSR-E data than the simulation with the measured grain size. The simulation with the effective grain size was also able to model the channel difference $T_{B,18.7V} - T_{B,36.5V}$, often used in remote sensing of snow, with a bias close to zero.

REFERENCES

[1] J. Cohen and D. Rind, "The effect of snow cover on the climate," *J. Clim.*, vol. 4, no. 7, pp. 689–706, Jul. 1991.

[2] S. Vavrus, "The role of terrestrial snow cover in the climate system," *Clim. Dyn.*, vol. 29, no. 1, pp. 73–88, Jul. 2007.

[3] T. P. Barnett, L. Dümenil, U. Schlese, E. Roeckner, and M. Latif, "The effect of Eurasian snow cover on regional and global climate variations," *J. Atmos. Sci.*, vol. 46, no. 5, pp. 661–685, Mar. 1989.

[4] J. T. Pulliainen, J. Grandell, and M. T. Hallikainen, "HUT snow emission model and its applicability to snow water equivalent retrieval," *IEEE Trans. Geosci. Remote Sens.*, vol. 37, no. 3, pp. 1378–1390, May 1999.

[5] A. Wiesmann and C. Mätzler, "Microwave emission model of layered snowpacks," *Remote Sens. Environ.*, vol. 70, no. 3, pp. 307–316, Dec. 1999.

[6] L. Tsang, C.-T. Chen, A. T. C. Chang, J. Guo, and K.-H. Ding, "Dense media radiative transfer theory based on quasicrystalline approximation with applications to passive microwave remote sensing of snow," *Radio Sci.*, vol. 35, no. 3, pp. 731–749, May/Jun. 2000.

[7] N. Kruopis, J. Praks, A. N. Arslan, H. M. Alasalmi, J. T. Koskinen, and M. T. Hallikainen, "Passive microwave measurements of snow-covered forest areas in EMAC'95," *IEEE Trans. Geosci. Remote Sens.*, vol. 37, no. 5, pp. 2699–2705, Sep. 1999.

[8] T. J. Schmugge and T. J. Jackson, "A dielectric model of the vegetation effects on the microwave emission from soils," *IEEE Trans. Geosci. Remote Sens.*, vol. 30, no. 4, pp. 757–760, Jul. 1992.

[9] U. Wegmüller and C. Mätzler, "Rough bare soil reflectivity model," *IEEE Trans. Geosci. Remote Sens.*, vol. 37, no. 3, pp. 1391–1395, May 1999.

[10] J. Pulliainen, J.-P. Kärnä, and M. T. Hallikainen, "Development of geophysical retrieval algorithms for the MIMR," *IEEE Trans. Geosci. Remote Sens.*, vol. 31, no. 1, pp. 268–277, Jan. 1993.

[11] J. Aschbacher, "Land surface studies and atmospheric effects by satellite microwave radiometry," Ph.D. dissertation, Univ. Innsbruck, Innsbruck, Austria, 1989.

[12] F. Ulaby, R. Moore, and A. Fung, *Microwave Remote Sensing, Active and Passive*, vol. I, *Microwave Remote Sensing Fundamentals and Radiometry*. Reading, MA: Addison-Wesley, 1981.

[13] M. T. Hallikainen, F. T. Ulaby, and T. E. van Deventer, "Extinction behavior of dry snow in the 18- to 90-GHz range," *IEEE Trans. Geosci. Remote Sens.*, vol. GRS-25, no. 6, pp. 737–745, Nov. 1987.

[14] C. Mätzler, "Applications of the interaction of microwaves with the natural snow cover," *Remote Sens. Rev.*, vol. 2, pp. 259–387, 1987.

[15] M. Tedesco and E. J. Kim, "Intercomparison of electromagnetic models for passive microwave remote sensing of snow," *IEEE Trans. Geosci. Remote Sens.*, vol. 44, no. 10, pp. 2654–2666, Oct. 2006.

[16] V. Roy, K. Goïta, A. Royer, A. E. Walker, and B. E. Goodison, "Snow water equivalent retrieval in a Canadian boreal environment from microwave measurements using the HUT snow emission model," *IEEE Trans. Geosci. Remote Sens.*, vol. 42, no. 9, pp. 1850–1859, Sep. 2004.

[17] M. Sturm and J. Holmgren, "A seasonal snow cover classification system for local to global applications," *J. Clim.*, vol. 8, no. 5, pp. 1261–1283, May 1995.

[18] M. T. Hallikainen, F. T. Ulaby, M. C. Dobson, M. A. El-Rayes, and L.-K. Wu, "Microwave dielectric behavior of wet soil—Part I: Empirical models and experimental observations," *IEEE Trans. Geosci. Remote Sens.*, vol. GRS-23, no. 1, pp. 25–34, Jan. 1985.

[19] E. Salonen, S. Karhu, P. Jokela, S. Uppala, S. Sarkkula, and H. Aulamo, "Study of propagation phenomena for low availabilities," ESTEC, Noordwijk, The Netherlands, 1990.

[20] R. W. Hyland and A. Wexler, "Formulations for the thermodynamic properties of the saturated phases of H_2O from 173.15 K to 473.15 K," *ASHRAE Trans.*, vol. 89, no. 2A, pp. 500–519, 1983.

[21] P. Ashcroft and F. Wentz, "AMSR-E/Aqua L2A global swath spatially-resampled brightness temperatures (Tb) V008," Nat. Snow Ice Data Center, Boulder, CO, 2003.

[22] D. Hall, R. Kell, G. Riggs, A. Chang, and J. Foster, "Assessment of relative accuracy of hemisphere-scale snow-cover maps," *Ann. Glaciol.*, vol. 34, pp. 23–30, 2002.

[23] S. Colbeck, E. Akitaya, R. Armstrong, H. Gubler, J. Lafeuille, K. Lied, D. McClung, and E. Morris, *The International Classification for Seasonal Snow on the Ground*, Int. Commiss. Snow and Ice of the Int. Assoc. Sci. Hydrol. Int. Glaciol. Soc., 1992.

[24] J. L. Foster, D. K. Hall, A. T. C. Chang, A. Rango, W. Wergin, and E. Erbe, "Effects of snow crystal shape on the scattering of passive microwave radiation," *IEEE Trans. Geosci. Remote Sens.*, vol. 37, no. 2, pp. 1165–1167, Mar. 1999.

[25] S. C. Colbeck, "The layered character of snow covers," *Rev. Geophys.*, vol. 29, no. 1, pp. 81–96, Feb. 1991.

[26] *AMSR-E Data Users Handbook*, 4th ed., Jpn. Aerosp. Explor. Agency, Toky, Japan, 2006.

[27] S. Rosenfeld and N. Grody, "Anomalous microwave spectra of snow cover observed from Special Sensor Microwave/Imager measurements," *J. Geophys. Res.*, vol. 105, no. D11, pp. 14 913–14 925, Jun. 2000.

Anna Kontu was born in Espoo, Finland, in 1981. She received the M.Sc. (Tech.) degree from the Helsinki University of Technology (HUT), Espoo, in 2006, where she is pursuing the D.Sc. (Tech.) degree.

From 2005 to 2006, she was a Research Assistant with the Laboratory of Space Technology, HUT, where she worked on her Master's thesis on the testing of the Soil Moisture and Ocean Salinity (SMOS) satellite satellite calibration system. Since 2006, she has been a Research Scientist with the Arctic Research, Finnish Meteorological Institute, Sodankylä, Finland. Her current research interests include remote sensing of snow and microwave radiometry.

Jouni Pulliainen (S'91–M'95–SM'03) received the M.Sc., Lic.Tech., and D.Sc. (Tech.) degrees from the Faculty of Electrical Engineering, Helsinki University of Technology (HUT), Espoo, Finland, in 1988, 1991, and 1994, respectively.

From 1993 to 1994, he was the Acting Director of the Laboratory of Space Technology, HUT. From 2001 to 2006, he was a Professor of space technology with HUT, specializing in remote sensing. He is currently a Research Professor with the Finnish Meteorological Institute, Helsinki, Finland, where he is the Head of the Arctic Research. He has been the Principal Investigator or Project Manager for several nationally funded and international research projects, including several European Space Agency (ESA) and European Commission contracts. He has authored about 250 scientific papers and technical reports in the field of remote sensing. His research interests include direct and inverse modeling in remote sensing and, additionally, remote sensing data assimilation and application development, e.g., for the needs of climate change investigations. Recently, his work has focused on the active and passive remote sensing of boreal forests and snow cover, applying both microwave and optical data (including atmospheric correction).

Dr. Pulliainen was a member of the ESA Advisory Committee on Education (in 2001–2007). He is also a member of the ESA CoreH2O MAG (2007 onward) and the European Science Foundation European Space Sciences Committee (2008 onward).

Publication 2

J. Lemmetyinen, A. Kontu, J.-P. Kärnä, J. Vehviläinen, M. Takala, J. Pulliainen. 2011. Correcting for the influence of frozen lakes in satellite microwave radiometer observations through application of a microwave emission model. *Remote Sensing of Environment*, 115(12), 3695-3706. doi:10.1016/j.rse.2011.09.008.

Remote Sensing of Environment 115 (2011) 3695–3706

Contents lists available at SciVerse ScienceDirect

Remote Sensing of Environment

journal homepage: www.elsevier.com/locate/rse

Correcting for the influence of frozen lakes in satellite microwave radiometer observations through application of a microwave emission model

Juha Lemmetyinen [a,*], Anna Kontu [a], Juha-Petri Kärnä [b], Juho Vehviläinen [a], Matias Takala [a], Jouni Pulliainen [a]

[a] Finnish Meteorological Institute, Arctic Research, Erik Palménin aukio 1, 00560 Helsinki, Finland
[b] Finnish Environment Institute, Mechelininkatu 34a, 00251 Helsinki, Finland

ARTICLE INFO

Article history:
Received 20 April 2011
Received in revised form 18 August 2011
Accepted 12 September 2011
Available online 19 October 2011

Keywords:
Snow water equivalent
Passive microwave
Lake ice

ABSTRACT

The spatial resolution of passive microwave observations from space is of the order of tens of kilometers with currently available instruments, such as the Special Sensor Microwave/Imager (SSM/I) and Advanced Microwave Scanning Radiometer (AMSR-E). The large field of view of these instruments dictates that the observed brightness temperature can originate from heterogeneous land cover, with different vegetation and surface properties.

In this study, we assess the influence of freshwater lakes on the observed brightness temperature of AMSR-E in winter conditions. The study focuses on the geographic region of Finland, where lakes account for 10% of the total terrestrial area. We present a method to mitigate for the influence of lakes through forward modeling of snow covered lakes, as a part of a microwave emission simulation scheme of space-borne observations. We apply a forward model to predict brightness temperatures of snow covered sceneries over several winter seasons, using available data on snow cover, vegetation and lake ice cover to set the forward model input parameters. Comparison of model estimates with space-borne observations shows that the modeling accuracy improves in the majority of examined cases when lakes are accounted for, with respect to the case where lakes are not included in the simulation. Moreover, we present a method for applying the correction to the retrieval of Snow Water Equivalent (SWE) in lake-rich areas, using a numerical inversion method of the forward model. In a comparison to available independent validation data on SWE, also the retrieval accuracy is seen to improve when applying the influence of snow covered lakes in the emission model.

1. Introduction

The cryosphere is an important component in the Earth's climate system. Its importance is underlined by the variability and the change in physical properties of its components. The highly varying snow component of the climate system includes many positive feedbacks e.g. the temperature–ice-albedo feedback. These have a strong impact on the surface energy budget especially at higher latitudes (Lemke et al., 2007). Presently, the only method available for global snow cover monitoring on a revisit time sufficient for addressing needs of climate modeling studies is through satellite remote sensing. Optical and high frequency sensors provide information on snow extent and e.g. snow albedo, while microwave frequencies can be employed to detect snow volume and water content, as well as the extent of snow cover. Microwaves provide the unique advantage of being only lightly affected by weather and unaffected by lighting conditions, a critical factor in polar areas (Tedesco & Wang, 2006). Furthermore, passive microwave sensors (radiometers) provide near-global coverage with a high revisit time, up to several times a day.

However, current operational spaceborne microwave radiometers have a weak spatial resolution, originating from a large field of view, typically in the scale of tens of kilometers. As a result, the heterogeneity of land cover has an important role in the interpretation of observations. In particular, the presence of freshwater lakes and other water bodies in the field of view of a satellite instrument can cause a significant effect on the observed brightness temperature, as the emissivity of water differs considerably from that of dry ground at microwave frequencies (Rees et al., 2006). The differing background affects the total microwave emission observed, the effect depending on the penetration depth of a given frequency (Hall et al., 1981).

Several methods have been proposed for detection of snow cover properties, such as snow depth and water equivalent, through the interpretation of microwave radiometer observations. Typical inversion algorithms rely on a linear regression formula between snow depth and the difference of two observed frequency bands, as proposed by Chang et al. (1987). Different empirical fits and derivates of this approach have been proposed in the literature for both region specific and global applications (Derksen et al., 2003, 2005, 2010; Foster et

* Corresponding author. Tel.: +358 9 1929 4663.
E-mail address: juha.lemmetyinen@fmi.fi (J. Lemmetyinen).

0034-4257/$ – see front matter © 2011 Elsevier Inc. All rights reserved.
doi:10.1016/j.rse.2011.09.008

al., 1997; Goodison & Walker, 1995; Hallikainen & Jolma, 1992; Kelly et al., 2003). Variations in land cover can be taken into account through e.g. a fractional vegetation correction (e.g. Foster et al., 1997) or through the application of region-specific algorithms (e.g. Derksen et al., 2003).

Approaches have also been proposed to apply a radiative transfer model to predict the emitted microwave brightness temperature from snow covered ground, using numerical model inversion to calculate snow properties from observations (Pulliainen & Hallikainen, 2001). Compared to purely empirical methods this approach has the distinct advantage of accounting for differing snow properties, such as temperature, density or snow grain size, all of which affect the total observed brightness temperature. However, both the purely empirical algorithms and the emission modeling approach are susceptible to inaccuracies related to heterogeneity of the land cover. For SWE retrieval algorithms formulated following Chang et al. (1987), this presents a source of error as the background signal may vary depending on the amount of e.g. water bodies present in the field of view of the satellite instrument. The effect increases with increasing wavelength, due to increased penetration depth, thus affecting most the lower frequency (typically K band, e.g. 19 GHz see Gunn et al., 2011). Water bodies in a satellite's field of view will thus generate a bias on a SWE estimate based on a fixed ratio of this frequency and a higher frequency (typically at Ka band, e.g. 37 GHz). The bias is usually negative, as the water bodies in the observation lower the average K band signal, causing the typically positive K–Ka band signal difference to decrease, which is in turn interpreted as a lower value of SWE. Recent studies have shown a correlation between airborne and space-borne observations of brightness temperature of snow-covered ground and fractional lake cover (Derksen et al., 2009; Lemmetyinen et al., 2009). The resulting error in estimation of SWE holds also for approaches relying on emission model inversion, if the differing background emission is unaccounted for.

Operational SWE retrieval algorithms typically mask out areas with significant lake coverage (Takala et al., in press); however, for areas such as Finland and e.g. parts of the Canadian tundra region, this results in the exclusion a significant portion of the observations. The purpose of this study is to examine brightness temperature emissions from freshwater bodies as a potential source of error in snow parameter retrieval methods applying passive microwave observations. We employ an electromagnetic forward model to estimate the brightness temperature of snow covered ground over a lake-rich area, and examine the model's capability to account for the influence of snow covered frozen lakes. Next, we propose a method to account for fractional lake cover in the inversion of the emission model for retrieval of snow water equivalent (SWE). The goal is to extend the applicability of SWE retrieval also to cover lake rich areas, thus potentially improving overall estimations of accumulated SWE.

Despite the existing global applications for retrieval of SWE from passive microwave observations (e.g. Takala et al., in press), this study is restricted to the geographic area of Finland. Finland has an area of 338 424 km^2, of which freshwater lakes account for 34 525 km^2. Snow typically covers close to 100% of the land areas during winter months, with snow cover lasting for typically 75–100 days in southern parts of the country, and up to over 200 days in northern parts above the 67th parallel (Drebs et al., 2002). Furthermore, Finland has an extensive network of in situ observations on snow cover and lake ice available. These factors make the area ideal for applying and testing the methodology presented in this study.

2. Forward model for satellite scenery brightness temperature

In this first part of this study, we apply an electromagnetic forward model for simulation of brightness temperature sceneries at different frequencies, as observed from a satellite, during three winter seasons (2005–2008) in Finland. The applied model is the HUT snow emission model (Pulliainen et al., 1999), adapted for multiple layers of snow or ice (Lemmetyinen et al., 2010). The simulation is performed to a common grid with available AMSR-E data. Model inputs for the simulation of individual observations (grid cells) are derived from available land cover, snow and meteorological data. The simulated sceneries are compared to AMSR-E observations on several channels, in order to examine the effect of lakes and other freshwater bodies on the simulation outputs.

The aim of the forward model experiment was

1. To demonstrate how lakes and other freshwater bodies affect spaceborne passive microwave observations over the winter period,
2. To examine to what degree the effect can be simulated by applying the presented forward emission model for lakes.

2.1. Modified HUT snow emission model for snow covered lake ice

The original HUT snow emission model describes microwave emission in the frequency range of 1–90 GHz for frozen ground covered by a homogeneous snowpack (Hallikainen et al., 1987; Pulliainen et al., 1999). Separate models account vegetation and atmospheric effects (Kruopis et al., 1999; Pulliainen et al., 1997). The ground layer is treated with a semi-empirical model, modifying Fresnel reflection coefficients based on microwave observations of soils (Wegmüller & Mätzler, 1999). The effect of the vegetation layer (forests) is accounted by applying a model by Kruopis et al. (1999); the model is based on airborne observations of snow-covered forests with differing values of biomass (stem volume, m^3/ha). An expansion to the snow emission model, allowing the simulation of multiple layers of snow, was presented by Lemmetyinen et al. (2010).

The model expansion for multiple layers (Lemmetyinen et al., 2010) also allows the inclusion of ice layers within the simulated snowpack, describing the ice as a simple non-scattering layer of absorptive media. Reflection and refraction at all layer interfaces are calculated considering only incoherent effects. The emissivity of water underneath the ice-snow system is considered by calculating the dielectric constant according to Klein and Swift (1977).

A schematic diagram of the structure of snow covered frozen lakes is presented in Fig. 1. The present emission model considers only congelation (black) ice covered by snow (Fig. 1a). This is a simplification of lake ice characteristics especially in the late winter period, when slushing events cause water to surge above the ice level as the combined weight of accumulated snow and ice overcomes the buoyancy of the ice (e.g. Adams & Lasenby, 1985). Refreezing of the water after these events results in the formation of a snow-ice (or: white ice) layer between the black ice and snow cover. This is depicted in Fig. 1b. This layer of white ice differs in terms of density, and thus dielectric properties, from the pure congelation ice below and the snow cover on top. Adams and Lasenby (1978) give measured density values of 0.838–0.886 g/cm^3 for the white ice layer over lakes in Canada, compared to the value of 0.916 g/cm^3 for pure ice.

In the model, all surfaces are considered ideally smooth with the exception of the lowest boundary between soil and snow, or that between ice and water in the case of lakes. The lowest boundary roughness is considered as an empirical fitting parameter. This boundary forms the largest dielectric contrast in the model, emphasizing the effect of applying an empirical parameter for roughness. The layer beneath the lowest interface is considered to be quasi-infinite; therefore, the upwelling microwave emission is only dependant on the physical temperature of the layer, and the transmissivity characteristics of the interface. The lowest interface is considered to be a flat horizontal surface, superimposed only by small random variations of surface height. In the case of natural lake and sea ice, deformation of ice could also cause larger variations in comparison to microwave wavelengths, and would result in the appearance of incoherent

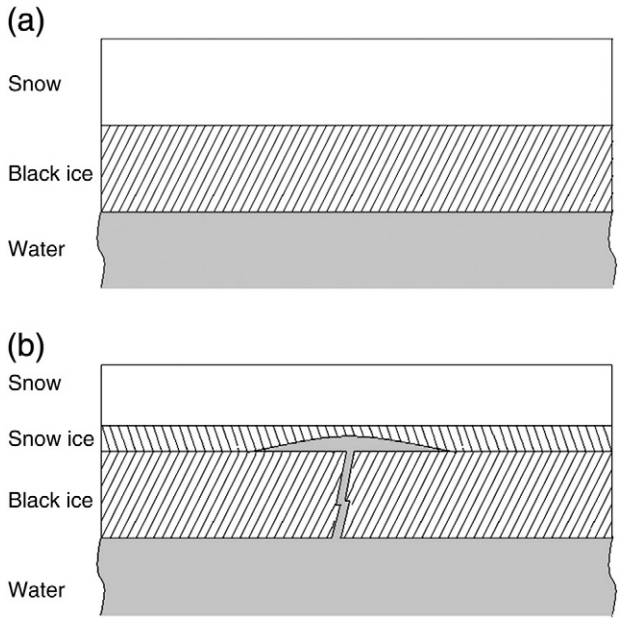

Fig. 1. Schematics of the structure of snow-covered lake ice (following Adams & Lasenby, 1985). Snow cover on top of newly formed congelation (black) ice (a). Slushing of water through cracks in congelation ice layer, and formation of snow ice (b).

reflectivity components. However, no models in predicting ice deformation magnitude are known to the authors; nor were any in situ data on lake ice deformation available for this study. Therefore, the Fresnel reflectivity coefficients are modified by small scale surface roughness variations only through the coherent reflectivity component, so that following Choudhury et al. (1979)

$$\left|r_p\right|^2 = \left|r_{p.Fresnel}\right|^2 \exp\left(-4k^2h^2\cos^2\theta\right), \quad (1)$$

where $r_{p.\,Fresnel}$ is the Fresnel reflection coefficient for polarization p, k is the wave number, h the height variation (RMS) of the rough surface and θ the incidence angle. No measurement data of the small scale RMS height variation of the water/ice boundary was available; therefore the surface roughness is considered as a purely empirical fitting parameter. The only restriction considered was that in order for (1) to be valid, the height variations should satisfy the condition $kh<<1$ (Kazumori et al., 2008).

The model has been applied previously for simulation of snow-covered lake ice emission e.g. by Gunn et al. (2011). The study compared model predictions based on in situ observations at 6.9, 19 and 37 GHz to airborne data acquired on the same frequencies in April 2008 over frozen brackish and freshwater lakes in Inuvik, Northwest Territories, Canada. Several model runs were considered; results showed that when applying a RMS height variation of 1 mm in Eq. (1) over freshwater lakes, the Root-Mean-Square Error (RMSE) of model estimates against airborne observations was 7.89 K and 11.96 K for 19 and 37 vertical polarization, respectively. Larger errors of over 18 K were found for the lower frequency 6.9 GHz model estimates, as well as for estimates made considering the ice layer an ideally smooth surface (23.85, 11.17 12.85 K for 6.9, 18.7 and 37 GHz, respectively).

2.2. Fractional proportion of land cover types

The forward model for predicting the emitted microwave brightness temperature, presented in the previous section, is applied considering that the emission of a simulation grid cell consists of varying types of land cover, each with distinct ground, snow and vegetation emission properties. Atmospheric effects over a single grid cell are considered to be uniform. The effect of topography on the local incidence angle is not considered. The fractional proportion of the total area in the observation of each ground cover type, obtained from land cover information, is used to weigh each brightness temperature in the calculation of the total scenery emission. This gives for the total brightness temperature simply as

$$T_B^{tot} = \sum_{\mu=1}^{M} \beta_\mu T_{B,\mu}, \quad (2)$$

where β_μ is the fractional (0–1) coverage and $T_{B,\mu}$ the brightness temperature originating from land cover type μ, so that $\sum_{\mu=1}^{N} \beta_\mu = 1$.

National CLC2006 (Corine Land Cover 2006, Törmä et al., 2008) data is used to obtain the fractional proportion of a given land cover type in the satellite observation; the classification divides land cover into 46 classes. The data are available at 25 m resolution. Here, the original classification is simplified to four different classes; (1) forested areas, (2) lakes, (3) open (non-forested) areas and (4) other areas, including major roadways and urban areas. The percentage of each land class type in the study area is presented in Table 1.

Forested areas include both sparsely and densely forested areas, and forests overlying several soil types (mineral soil, peat). Freshwater lakes and rivers are treated separately from coastal (sea) areas, and grid cells on coastal areas with the proportion of (sea) water of above 10% are included in class (4). Simulation grid cells with more than 10% of class (4) are excluded from the study representing a total of 7.4% of the available grid cells from the study area. The excluded cells are mostly located in coastal areas; although the presented methods would be applicable in principal also to these, this exclusion was made due to difficulties in acquiring accurate in situ information on the sea ice status.

This study uses EASE (Equal Area Scalable Earth) -gridded brightness temperature observations from AMSR-E/Aqua as a reference to model simulations and as an input in SWE retrieval experiments (Knowles et al., 2006). The EASE grids are produced by means of Inverse Distant Square interpolation from AMSR-E Global Swath Spatially-Resampled Brightness Temperatures. Determination of the fractional proportion of a given land cover type is performed simply by determining the geographic extent of each AMSR-E grid cell, based on the given center point, resolution and orientation of the EASE grid. All simulations and SWE retrieval experiments are made in the same grid.

3. In situ data

The primary data available for model input consist of daily weather station observations of snow depth and air temperature, as well as periodic observations of lake ice thickness and the depth of snow on lake ice. Weather station data on snow depth was taken from a total of 73 sites in the study area (see Fig. 2) during three winter seasons (October to May, during winter seasons between 2005 and 2008). The measurements are largely automated, being based on acoustic snow sensors The data is available at a temporal resolution of up to 10 min; however, daily averages were used.

Table 1
Division of study area into four generalized land cover classes. Appearance of each class as percentage of total area.

Class no. #	Class name	Percentage in study area [%]
1	Forest	75.0
2	Open	13.0
3	Water	10.2
4	Other	1.8

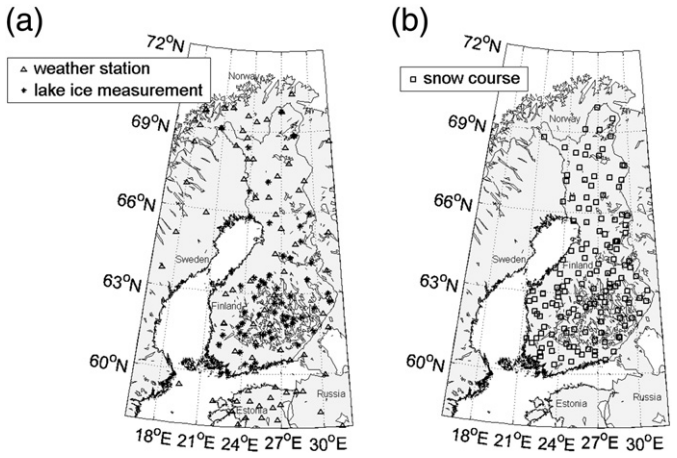

Fig. 2. Location of weather stations reporting daily snow depth in Finland and surroundings in 2005–2008, and sites of manual lake ice measurement sites (a). Location of snow courses giving reference SD and SWE information (+120 sites measured monthly) in the same period (b).

Snow course measurements by the Finnish Environment Institute (SYKE) are used as reference value of SWE. The locations of active snow courses in 2007 are shown in Fig. 2b. Each snow course consists of 40–80 measurements of snow depth and 4–8 measurements of snow density along a predefined course of 2–4 km. The measurements are typically conducted on the 15th day of each month, with some courses measured also on the 1st. The exact dates may vary by a few days depending on occasion. The snow courses are typically defined so that they cover both forested and open areas in the region, thus making possible the analysis of the snow situation by different land cover types. Data from over 120 snow courses around the country were available for this study.

For lake ice, available in situ information consists of ice depth measurements performed operationally by the Finnish Environment Institute (SYKE). Over 50 lakes are measured for ice depth, snow on ice depth and ice stratigraphy, typically every 10 days during the winter. The locations of available lake ice measurement locations used in this study are depicted in Fig. 2a. Each measurement on lake ice consists of three observations of ice thickness and stratigraphy (depth of white and black ice layers), and the average of nine observations of snow depth on ice; three snow depth values are recorded for each ice thickness measurement location, using a fixed measurement pattern.

3.1. Snow cover

To set model parameters for snow cover, available weather station observations of snow depth (see Fig. 2a) are used for each simulated date. The snow depth information is interpolated over the simulated EASE grid to form a background field of snow depth. Ordinary kriging interpolation is applied (see e.g. Isaaks & Srivastava, 1989). For the geographic area of Finland, this can be considered a relatively accurate method due to the high density of available observations and considering the aims of the experiment; even though the method does not capture the true variability of snow cover the aim of the forward model experiment is not to simulate satellite observations accurately as such, but rather to examine the influence of freshwater lakes in the simulation.

No in situ information on grain size or snow moisture content was available on the large scale required by the forward model simulations. However, grain size is one of the main parameters affecting scattering and thus total emission from a snowpack (Pulliainen et al., 1999). For the purposes of this study, the snowpack (excluding the portion of snow on ice over frozen lakes) is considered to be horizontally and vertically homogeneous for each given land cover type, with a constant effective grain size parameter. A grain size value of 1 mm is used for all simulations, regardless of land cover type or region; furthermore, the possible evolution of the grain size with increasing time and snowpack thickness is not considered. The value was obtained by fitting model estimates of brightness temperature to observations over regions with low lake coverage (<10%) for the winter period of 2005–2006. A previous study from one winter season indicated the grain size to vary from 0.5 mm to 2 mm in midwinter for the Sodankylä region in Northern Finland (Kontu & Pulliainen, 2010); the obtained value thus falls within this range. It is acknowledged that applying a constant grain size brings a degree of uncertainty to the simulations, but these are considered to be irrelevant regarding the purposes of the forward modeling experiment. The purpose of the experiment is evaluate possibilities for compensating for the effects of lakes, rather than validate the absolute accuracy of the model simulations.

Wet snow represents a source of uncertainty in brightness temperature simulations; although the HUT model includes the possibility to account for the volumetric proportion of free water in the snowpack, accurate in situ information was not available for the forward model simulations on a satellite scale. Therefore, moisture content in snow is considered by applying a wet snow mask based on satellite observations. A simple brightness temperature condition using the AMSR-E 36.5 GHz channels is applied, following Hall et al. (2002), so that the brightness temperature observed must satisfy

$$\begin{aligned} T_{B,37H} &< 240\ \text{K} \\ T_{B,37V} &< 250\ \text{K}. \end{aligned} \tag{3}$$

If the condition in Eq. (3) is not met, the snow is considered wet and the grid cell in question is excluded from the evaluation.

3.2. Lake ice

Information on lake ice depth and snow depth on lake ice is essential for the forward model experiment presented, as together with the emissivity of the underlying water, these parameters are the main factors driving emission from ice and snow covered lakes. Fig. 3a depicts a comparison of snow depth measurements on land (weather stations) and lake ice (SYKE manual measurements). The data are taken from stations and sites north of the 62nd parallel during the winter season 2006–2007. Error bars depict the standard deviation of measurements available during a single day. The data for lake ice are shown for dates when manual data was available, i.e. on average every 10 days. Fig. 3b, on the other hand, shows the average values of ice thickness measurements for the same area and time period. Error bars again depict the standard deviation of measurements. The portion of white ice measured is also plotted.

As an additional source of information, a series of snow pit measurements over lake ice were available from the winter of 2009–2010. The measurements were made at Lake Orajärvi (67.35N, 26.82E), near Sodankylä, Northern Finland. Amongst other parameters, snow density, SWE and average grain size were measured twice a month. Reference snow pit information over land is available from a site less than 10 km from the lake. The measured densities of snow on lake ice averaged at 0.21 g/cm^3; the value is comparable to densities measured on land. This is contrary to more extensive studies e.g. over tundra areas; campaigns conducted in Canada over several years reported average density values of 0.273 to 0.347 g/cm^3 for snow over land, compared to densities 0.328 to 0.371 g/cm^3 for lakes (Derksen et al., 2009). These values may be more representative of the relation of snow density on lakes and dry terrain, than the relation obtained from the single lake in Finland; nevertheless, a common density value was used in the analysis for both, following the obtained results from Lake Orajärvi, as a more extensive measurement database from the study region was not available.

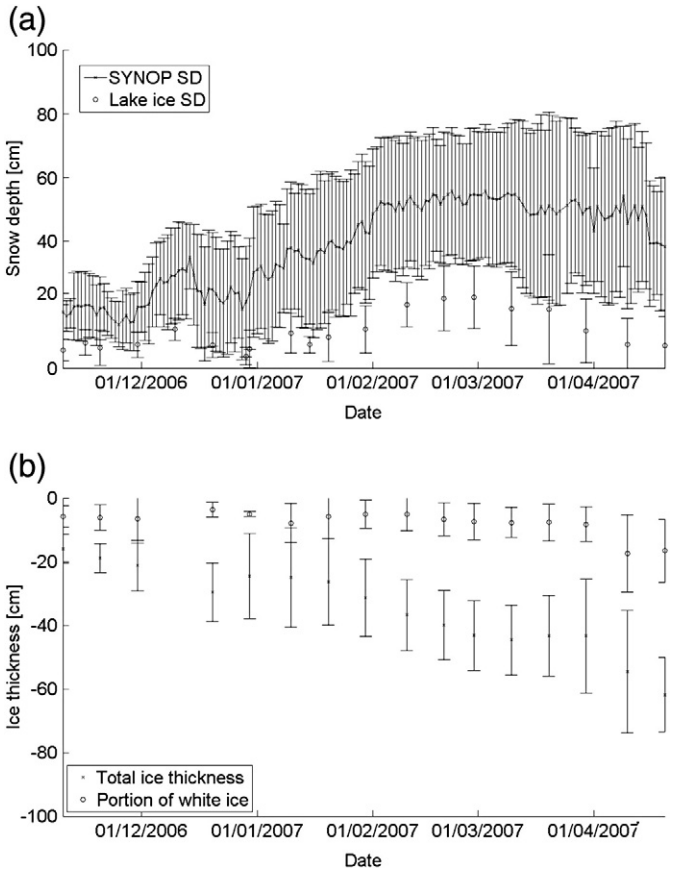

Fig. 3. (a): Average of daily values of snow depth at weather stations, and average of snow depth on lake ice measurements (every 10 days) north of 62nd parallel, winter season 2006–2007. Error bars show standard deviation of measurement readings. (b) Average of lake ice thickness measurements, including portion of white ice, above 62nd parallel, winter season 2006–2007.

The grain size (diameter) was estimated visually from photography of snow grain samples against a reference grid, following Fierz et al. (2009). A high degree of subjectivity is related to observations made in this fashion; therefore, the presented results for grain size are not considered in the modeling or retrieval experiments in this study. Nevertheless, the reported grain diameter values over land average between 0.75 and up to 2 mm at the end of the season, reflecting the presence of a depth hoar layer in the late season, with large faceted grains up to over 5 mm in diameter appearing especially in the late season. These types of large grains are lacking in the lake ice observations, where the largest grains were identified to be less than 2 mm in diameter throughout the season, the average value being typically between 0.5 and 1 mm. This is contrary to findings over tundra lakes, where the depth hoar layer formed up to over 70% of the total snow over lakes (Derksen et al., 2009). However, the available data for this study represented only one lake in Northern Finland, and no definite conclusions over snow properties could be made. As a consequence, the data was considered too scarce to define a different grain size setting for lakes compared to snow over land surfaces. The value of 1 mm was thus used for lakes in both forward modeling and retrieval experiments.

3.3. Vegetation

The vegetation stem volume, calculated for each simulated grid cell, is based on national forestry data provided by the Finnish Environment agency. Data are available at 25 m resolution, representing the average stem volume (in m^3/ha) for the forested proportion of the grid cell. For this study, these data are aggregated to the 25 km resolution of the EASE grid.

4. Forward model simulation results

4.1. Correlation of AMSR-E observations with lake cover

AMSR-E observations from the test area of simulations (corresponding to Fig. 2) were analyzed against their correlation with increasing lake coverage at different frequencies during the winter season. A strong correlation would show that lakes have a possible effect on the microwave response, although other factors may affect the outcome, such as different snow characteristics over terrestrial areas of the lake rich regions, compared to surrounding areas. Fig. 4 shows the time series of the correlation coefficient R between brightness temperature observed by AMSR-E and fractional lake cover in a grid cell, calculated over the whole study area of 16−32° E, 58−72° N during the winter season of 2006–2007. Displayed are results for three frequencies, 10.65, 18.7 and 36.5 GHz. The last two frequencies are the main frequency pair typically applied for snow parameter retrieval (e.g. Chang et al., 1987; Foster et al., 1997; Kelly et al., 2003).

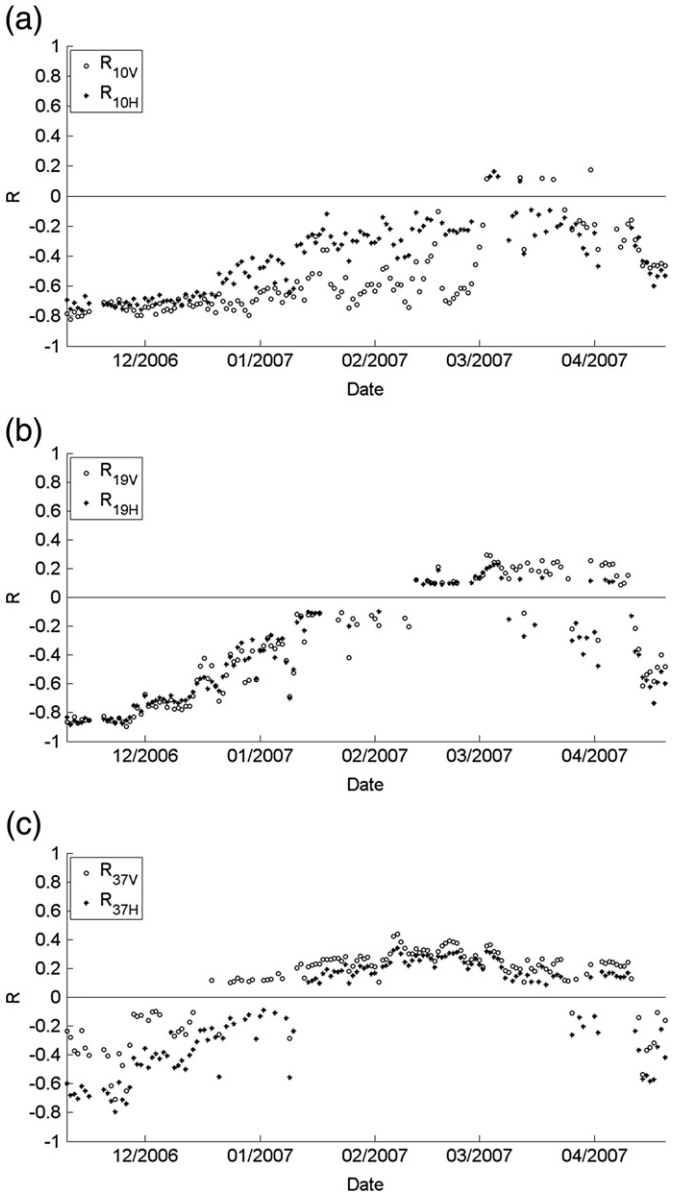

Fig. 4. Correlation coefficient R of AMSR-E brightness temperatures at (a) 10.65, (b) 18.7 and (c) 37 GHz with fractional freshwater lake cover, over geographic area of 16–32° E, 58–72° N during winter season 2006–2007. Sample size N for correlations 507. Correlations significant at 95% shown.

The motivation for examining the lower 10.65 GHz channel arises from suggested possibilities to apply also these frequencies for snow cover monitoring over deep snowpacks in tundra areas, and to overcome vegetation effects affecting the 37 GHz signal (Derksen, 2008); for the 10.65 GHz channel, the presence of lakes would be a particular problem due to the increased penetration depth of the microwave signal (Gunn et al., 2011).

The displayed timeline in Fig. 4 begins with a snow-free situation in November, when strong stable negative correlation of $R = -0.8$ is apparent on the lower two frequencies, and $-0.6/-0.3$ on 37 GHz V/H polarizations, respectively. This is due to the low apparent brightness temperature of lakes, compared to surrounding terrain. The correlation remains mostly stable on 10.65 GHz V-pol throughout the winter, with some exceptions in late December and early January. This is due to the high penetration depth at 10 GHz for dry snow cover. Sudden changes in the correlation apparent in Fig. 4 are related to snow melt events, when emission from wet snow dominates the signal for both lakes and surrounding terrain. This was verified with air temperature data from weather stations; the average daily air temperature over the grid cells used in the analysis is presented in Fig. 5. After mid-March, the correlation rapidly disappears, again possibly due to the onset of snow melt over both lakes and surrounding terrain, seen as nearly constant above-zero temperatures in Fig. 5. For 18.7 GHz, the negative correlation of the signal to increasing lake fraction decreases during the winter from the start value of −0.8 in November; similar "peaks" of zero correlation can be observed as with 10.65 GHz. The value also oscillates between positive correlations and −0.5 during the winter period, indicating rapid changes in the microwave response over lakes. The last figure shows the 36.5 GHz channel correlation with lake fraction; here the snow free negative correlation changes to a positive correlation of ~0.2 during the winter, meaning the measured brightness temperature increases with lake fraction. Higher brightness temperatures on lakes at 37 GHz, compared to surrounding open terrain, have been observed also by Kontu et al. (2008) and Derksen et al. (2009). The evolution of correlation values in Fig. 4 also follows closely those reported by Derksen et al. (2009) for Canadian Northwest Territories and Nunavut. The increasing brightness temperatures at 37 GHz can be explained by emission from the ice and snowpack covering the lake dominating over the low emissivity of the water underneath.

4.2. Forward model simulations

Model simulations were next conducted for frequencies 10.65, 18.7 and 37 GHz, horizontal and vertical polarizations, using two different model configurations. In the first scenario, lakes are not simulated but considered similarly to surrounding open terrain. In the second scenario, lakes are included as explained in Section 2.2.

The main constant parameters required for the simulation are summarized in Table 2. Density values are based on in situ measurements over land and lakes, but no geographic variability or temporal evolution is applied. Temperatures of air, snow, vegetation and the ground surface are all set to be −5 °C (with only water bodies at 0 °C). The permittivity value of soil is based on measurements of frozen soils by Hallikainen et al. (1987). The grain size value is purely empirical; the value of 1 mm was tested to fit model estimates over land with good accuracy to AMSR-E observations using a limited dataset for the winter 2005–2006, restricting simulations to areas with low lake coverage. Similarly in the simulation of emission from lakes, a moderate surface roughness of 1 mm is implemented to the water/ice interface when applying Eq. (2). This value gave good results also against airborne data, as presented in Gunn et al. (2011).

Table 2
Constant values used in the simulations for all the target areas. Vegetation data from national land cover information.

Parameter	Value
Grain size	1.0 mm
Snow density on land	0.2 g/cm^3
Snow density on lakes	0.2 g/cm^3
Ice density	0.916 g/cm^3
Snow moisture	0%
Temperature of ice	−5 °C
Temperature of water	0 °C
Temperature of ground	−5 °C
Temperature of vegetation	−5 °C
Vegetation volume (from national land cover data)	0…142 m^3/ha average 16.7 m^3/ha
Permittivity of frozen soil	6-1j
RMS height variation of soil/snow boundary	3 mm
RMS height variation of water/ice boundary	1 mm
Water salinity (lakes)	0 psu
Ice salinity (lakes)	0 psu

The remaining parameters required by the simulations, such as terrestrial snow depth and the thickness of ice on lakes, were set according to weather station observations and available in situ data on lake ice. Ordinary kriging interpolation was applied on weather station observations in order to acquire a background map of snow depth over the simulated grid. Lake ice depth and the depth of snow on ice were acquired for each grid cell from the manual observations available; kriging interpolation was applied as with the terrestrial weather station information on snow depth. However, if the number or distribution of the lake ice measurements prevented the calculation of satisfactory kriging fields, linear geographic interpolation was applied to set the ice depth value of individual grid cells. The temporally closest ice depth measurements were chosen for individual dates (no temporal interpolation was applied).

Fig. 6 gives an example of input parameter of the forward model experiment for the winter of 2006–2007. The kriging interpolated field of snow depth on land, snow depth on ice and ice thickness are depicted, as an average of values obtained for grid cells with a fractional lake cover of over 30%. The average and maximum values of the same parameters are summarized in Table 3 for all the three winters under study.

Simulated brightness temperatures are compared with observations over grid cells with over 30% lake coverage. These represent only 4% of the total 507 simulated grid cells, but give the best indication of the potential increase in simulation accuracy brought by the lake emission model. None of the lakes in the study area were large enough to cover a whole EASE grid cell (with the exception of Lake Ladoga; however, no in situ information from the lake was available). Fig. 7 shows the simulated and observed brightness temperature as an average of the grid cells with over 30% lake coverage, over the winter season 2006–2007. Results from the two simulation scenarios for the three winter periods investigated are summarized in Tables 4 and 5, for simulations omitting and including the lake emission component, respectively.

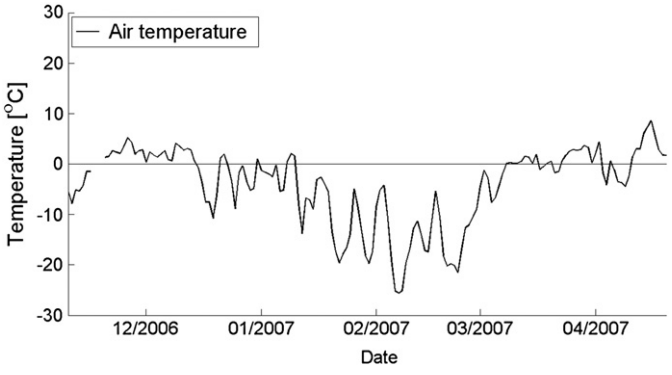

Fig. 5. Average daily air temperature for grid cells used in correlation analysis (Fig. 4).

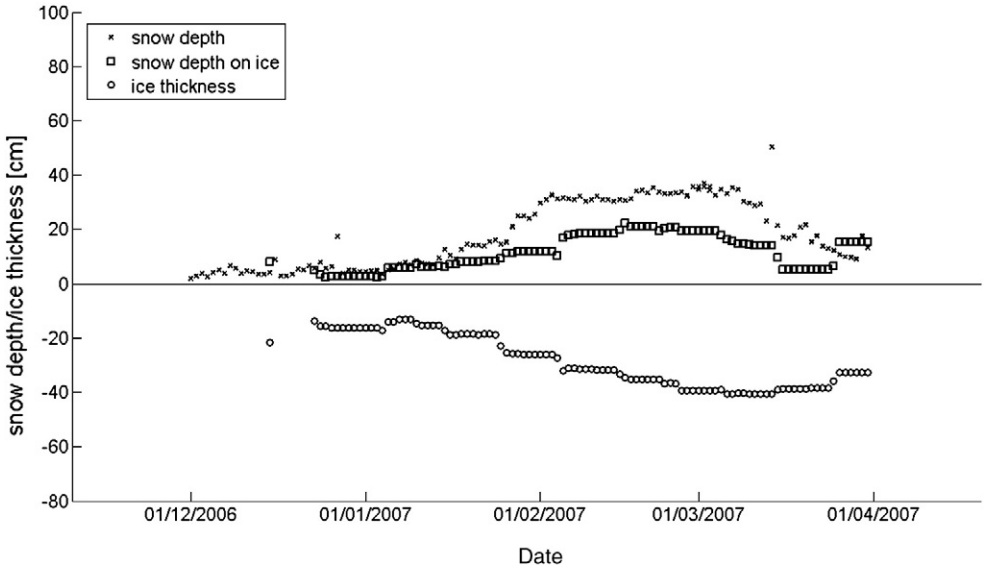

Fig. 6. Example of simulation input data for the winter 2006–2007. Snow depth (on land), and ice depth. Snow depth on lake ice, as obtained from measured values, also depicted. Average values for grid cells with over 30% lake cover.

For the simulations without inclusion of lakes during 2006–2007, both the 10.65 GHz (Fig. 7a) and 18.7 GHz (Fig. 7b) simulations overestimate the vertically polarized brightness temperature through most of the simulated period at both polarizations, with an average bias error of 10.9 and 6.7 K, respectively for the two frequencies. The simulations at 36.5 GHz, V-pol (Fig. 7c), largely follow the level of observed brightness temperatures at both polarizations; the bias error, i.e. the average difference between simulated and measured values, is −3.9 K and 3.8 K for vertical and horizontal polarizations, respectively. The brightness temperature difference of 18.7–37 GHz (Fig. 7d) is overestimated, giving a bias error of 10.6 K; as this relation is used in the inversion of SWE from observations, the use of the observed difference would, in this case, lead to an underestimation of SWE over the investigated area.

In the second scenario, applying the lake ice model clearly reduces simulation errors (Fig. 7, e–h, Table 5) for the two lower frequencies, giving bias errors of −8.4 and 1.6 K for vertical polarizations of 10.65 and 18.7 GHz, respectively, for the 2006–2007 season. The horizontal polarizations are also more accurately simulated. Compared to the simulations without lake cover inclusion, simulations at 36.5 GHz are now overestimated against observed values (bias errors are 2.6 and 6.3 for vertical and horizontal polarizations, respectively, compared to −3.9 and 3.8 K for the simulation without the lake cover component). As the model response at 36.5 GHz is most sensitive to snow cover, this is an indication that the settings of the forward model parameters for snow on lakes were not optimal. A considerable improvement in simulation accuracy, nevertheless, is seen in the difference of 18.7–36.5 GHz, vertically polarized brightness temperatures (Fig. 7h). Now, the simulated result very closely matches the observed result, as opposed to the situation depicted in Fig. 7d. Bias errors average less than 2 K for all three investigated seasons, compared to over 10 K in the original simulations not accounting for lake cover. This is important regarding the SWE estimate performed from using inversion of the forward model, as the channel difference is applied in the inversion. Also the polarization difference of 18.7 GHz can be seen to more closely match the observations. Bias and RMS error values for simulation of the other two winter periods, shown in Tables 4 and 5, show very similar behavior as the winter period of 2006–2007. When the simulation of lake ice effects is included, simulation results for the lowest two frequencies are improved both in terms of RMS errors and bias. The results on 36.5 GHz, however, are typically slightly deteriorated, with the exception of V-polarization during the winters of 2006–2007 and 2007–2008. This may be due to the grain size treatment; the grain size in the simulation is considered to be uniform for both land and lake areas, although there are indications the grain size may differ on lakes (see Section 3.2).

Table 3
Average and maximum values of snow depth on land, snow depth on lake ice and lake ice thickness over simulation grid cells with over 30% lake cover.

Year	Snow on land		Snow on lake ice		Lake ice	
	Average [cm]	Maximum [cm]	Average [cm]	Maximum [cm]	Average [cm]	Maximum [cm]
2005–2006	37	62	16	40	40	56
2006–2007	18	50	12	22	29	41
2007–2008	23	53	7	18	26	41

5. Estimation of snow properties from satellite observations

5.1. Inversion algorithm

The model inversion methodology follows the one presented for the HUT model by Pulliainen and Hallikainen (2001). The method relies on numerical iteration of the forward model to observation by applying the simulated channels and observations in a cost function, the simulated result being a function of snow depth (or water equivalent). Other parameters, such as snow density and air, snow and soil temperature values, are kept typically constant. Alternatively, these can be derived from in situ observations or other data sources, should these be available. The exception is the snow grain size parameter, which affects the model outcome primarily through an empirical relation with the snow extinction coefficient (Hallikainen et al., 1987). The grain size is included as a fitting parameter in the cost function, using an a priori estimate and an estimate of its variance as restriction parameters. The cost function then takes the form

$$W_t = \min_{W,d_0}\left\{\sum_{i=1}^{N}\frac{[y_i - f_i(\mathbf{x})]^2}{\mathrm{var}(\varepsilon_i)} + \frac{d_{0,ref,t} - d_0}{\mathrm{var}\left(d_{0,ref,t}\right)}\right\} = \min_{W,d_0}\left\{\sum_{i=1}^{N}\frac{[y_i - f_i(W_t, d_0)]^2}{\mathrm{var}\left(\varepsilon_{i,t}\right)} + \frac{d_{0,ref,t} - d_0}{\lambda^2_{d_{0,ref}}}\right\}. \quad (4)$$

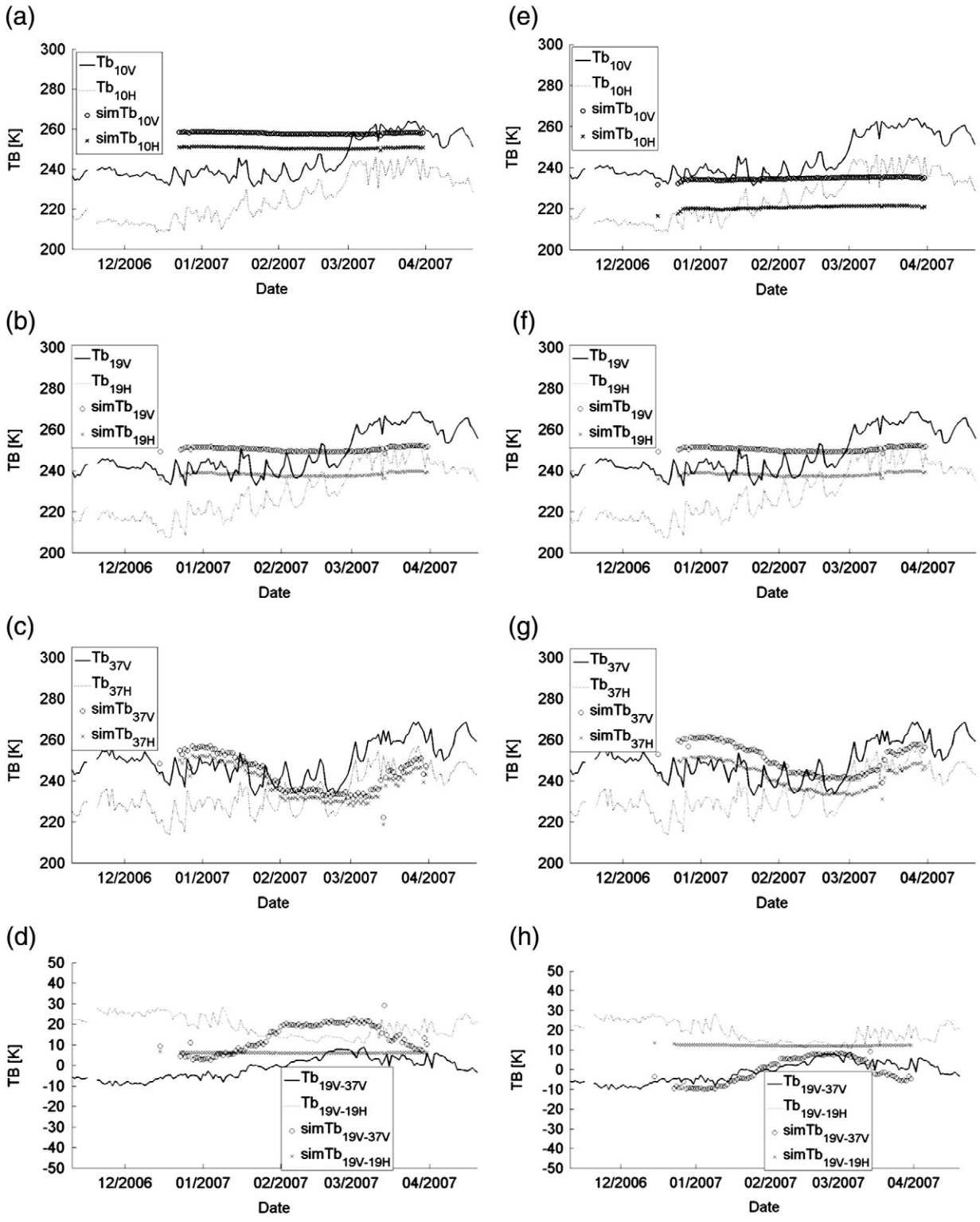

Fig. 7. Observed and simulated brightness temperature over lake-rich areas (lake fraction over 30%) in Finland during winter season 2006–2007. Average of five EASE grid cells presented. Left column, (a)–(d): simulations without lake ice simulation. Right column, (e)–(h): simulations considering lake ice, with RMS height variation of 1 mm in ice–water interface. Top to bottom: 10.65, 18.7, 36.5 GHz, H and V pol, and the channel differences 18.7–36.5 GHz (V-pol) and 18.7 V–18.7 H.

Where y_i is the observed brightness temperature of channels i, $f_i(\mathbf{x})$ is the modeled response of the same channels as a function of parameters $\mathbf{x}$. The parameters in $\mathbf{x}$ are W_t (snow water equivalent) and d_0 (grain size). $\varepsilon_{i,t}$ is the sum of model and observation errors, and $\lambda^2_{d_{0,ref}}$ the estimated variance of the reference grain size value. In the inversion tests applied here, $\varepsilon_{i,t}$ was estimated to be 1 K, and $\lambda^2_{d_{0,ref}}$ as 0.1 mm. The reference grain size $d_{0,ref}$ was set to be 1 mm, following the parameter fit performed in the forward modeling experiment. The variance of the reference grain size is a purely arbitrary value.

The method presented by Pulliainen (2006) used available in situ information of snow depth to fit the model to observations at selected channels over weather station locations, using again the grain size a free fitting parameter. This gives an effective reference grain size value at locations where weather station information is available;

Table 4
Bias, RMS and unbiased RMS errors of simulation estimates of brightness temperature against observations for grid cells with lake fraction over 30%; the effect of lakes is omitted from simulations.

		10V	10H	19V	19H	37V	37H	19V–37V	19V–19H
2005–2006	Bias	16.1	24.5	8.9	19.5	−7.5	1.4	16.4	−10.6
	RMSE	17.2	25.4	11.6	21.3	10.8	9.0	16.8	10.8
	uRMSE	6.0	6.6	7.5	8.6	7.8	8.9	3.7	1.9
2006–2007	Bias	10.9	18.9	6.7	15.5	−3.9	3.8	10.6	−8.8
	RMSE	15.3	22.9	12.7	20.7	11.8	13.7	12.3	10.4
	uRMSE	10.7	13.0	10.8	13.7	11.2	13.2	6.1	5.6
2007–2008	Bias	11.3	20.0	6.3	16.2	−6.1	2.5	12.4	−9.9
	RMSE	14.0	23.2	10.7	20.3	13.4	13.8	14.1	11.4
	uRMSE	8.3	11.8	8.7	12.3	12.0	13.6	6.7	5.5

Table 5
Bias, RMS and unbiased RMS errors of simulation estimates of brightness temperature against observations for grid cells with lake fraction over 30%; the effect of lakes is included in simulations.

		10V	10H	19V	19H	37V	37H	19V–37V	19V–19H
2005–2006	Bias [K]	−6.2	−4.5	4.7	9.1	5.4	11.6	−0.8	−4.4
	RMSE [K]	8.5	7.8	8.4	12.2	9.6	15.3	3.0	4.9
	uRMSE [K]	5.8	6.3	7.0	8.1	8.0	10.0	2.8	1.9
2006–2007	Bias [K]	−8.4	−5.9	1.6	5.3	2.6	6.3	−1.0	−3.7
	RMSE [K]	12.9	11.1	9.7	12.2	10.2	13.5	3.5	5.5
	uRMSE [K]	9.8	9.3	9.5	11.0	9.8	11.9	3.4	4.1
2007–2008	Bias [K]	−8.6	−5.6	1.4	6.1	3.2	7.6	−1.8	−4.7
	RMSE [K]	11.1	9.4	7.1	10.9	9.8	13.5	3.7	6.2
	uRMSE [K]	7.0	7.6	7.0	9.0	9.3	11.2	3.3	3.9

kriging interpolation is applied to provide effective grain size values for the whole retrieval area. However, this method is not applied in the present study, as the grain size optimization partly compensates for the lake ice effects in a given area. Therefore, the more straightforward method presented by Pulliainen and Hallikainen (2001) is applied. Two channel combinations $\mathbf{y} = f_i(\mathbf{x})$ are applied in Eq. (4):

$$\begin{aligned} \mathbf{y}_1 &= f_1(\mathbf{x}) = T_{B,19V} - T_{B,37V} \\ \mathbf{y}_2 &= f_2(\mathbf{x}) = T_{B,19V} - T_{B,19H}. \end{aligned} \tag{5}$$

The spectral difference $\mathbf{y}_1$ is the traditional passive microwave channel combination employed for detection of SWE, and also applied in Pulliainen (2006). The polarization difference of the 18.7 GHz observation ($\mathbf{y}_2$) was employed together with the spectral difference $\mathbf{y}_1$ in Pulliainen and Hallikainen (2001) to regularize the cost function in Eq. (4).

As for the forward modeling experiment, distinctive land cover types μ are accounted for in the simulations so that $f_i(\mathbf{x})$ is a sum of the fractional components of the different land cover types. Following Eq. (2),

$$f_i(\mathbf{x}) = f_i^{tot}(W, d_0) = \sum_{\mu=1}^{M} \beta_\mu f_i\left(W_\mu, d_{0,\mu}\right). \tag{6}$$

Note that W_μ and $d_{0,\mu}$ can be set to be respective of their land cover types, or assigned as common values.

5.2. Evaluation of inversion results

An experiment for inversion of SWE from satellite observations was made for three winter periods, covering the years 2005–2008. Again, two scenarios were considered: (1) influence of lakes was excluded and (2) included in the forward model. Method (1) was essentially similar to the one presented by Pulliainen and Hallikainen (2001). Method (2) is explained in Section 2. The SWE retrieval experiment applies the same lake ice depth information as the forward model experiments. This would be comparable to retrieving lake ice depth information from climatology or a physical lake ice model (e.g. Duguay et al., 2003). However, in the minimization of Eq. (4), the snow water equivalent value for lakes was set to be half of the value applied over terrestrial areas in the iteration. This assumption was taken based on the average difference between snow depth values measured over lakes, compared to terrestrial snow depth measured at weather stations (Table 3). This allows the snow depth value over lakes to fluctuate in the forward model iteration, while retaining a difference between terrestrial snow and snow over lakes.

Fig. 8 demonstrates an example of gridded SWE maps obtained using the two methods for 1 day (January 1st, 2006), and the difference of the estimated SWE value. It can be seen that including lakes in the forward model generally raises SWE estimates for the lake district in southern Finland, and over single large lakes in northern parts of the country. The difference in measured SWE is up to over 50 mm in some individual grid cells.

Validation of the SWE results was conducted against SYKE snow course measurements, which represent independent data from weather station observations of snow depth. Grid cells defined as wet snow according to Eq. (3), or with no snow cover, were excluded from the analysis. Results are shown in Fig. 9. The figures depict all retrievals obtained during the whole three-year study period from grid cells with fractional lake cover above zero. The inclusion of lake ice simulations can be seen to improve estimate accuracy to some degree; the overall bias error is reduced from −20 to −1.7 mm. The RMS error is reduced from 37.9 to 33.3; however, the bias corrected RMSE is marginally increased from 32.1 to 33.2 mm. The correlation coefficient R^2 between estimates and reference data is increased, from 0.34 to 0.35. These values are calculated from grid cells determined as snow by the algorithms; however, in particular when the lake ice simulations are omitted, the presence of snow is undetected by the algorithm. The probability of detection, i.e. the percentage of cases where snow was present according to reference data, and the inversion algorithm delivered a value of SWE>0 mm, is only 87.8% when the lakes are omitted. This increases to 98.5% when the lake ice simulation is applied.

A summary of SWE estimate accuracy against SYKE snow course data, split between the three winter periods, is shown in Table 6. The improvement in retrieval accuracy is apparent both in terms of reduced RMS and bias errors for the three seasons studied; however, the correlation coefficient and bias corrected RMSE values are slightly deteriorated for 2005–2006 and 2007–2008. The table shows also the probability of detection for the estimates; when lakes are included in the simulations, detection efficiency increases for all the three years investigated.

Fig. 10 summarizes the retrieval results in histograms, depicting the amount of improvement in retrieved values of SWE against the in situ reference values. Fig. 10a shows the improvement of grid cells with lake coverage of 5 to 15%, Fig. 10b the same for grid cells with 15 to 30% lake cover, and Fig. 10c for grid cells with over 30% lake cover. The percentage of cases where the estimate accuracy was improved through the inclusion of the lake model is shown, as well as the average improvement of retrieval accuracy (in mm SWE). An improvement in retrieval accuracy is achieved in a total of 58.8% of the cases (all cases with lake fraction over 5%). In terms of absolute SWE values, the average improvement of all cases was 2.6 mm. In 10.6% of the cases, the improvement is over 20 mm, whereas in 6.9% of the cases a deterioration of more than 20 mm is seen. As can be seen from Fig. 10c, a large part of the cases where the estimate was deteriorated occurred in areas with significant lake cover; these grid cells are typically located over large lakes. This may be an indication that the accuracy of the simplified emission model for lakes deteriorates for larger lakes.

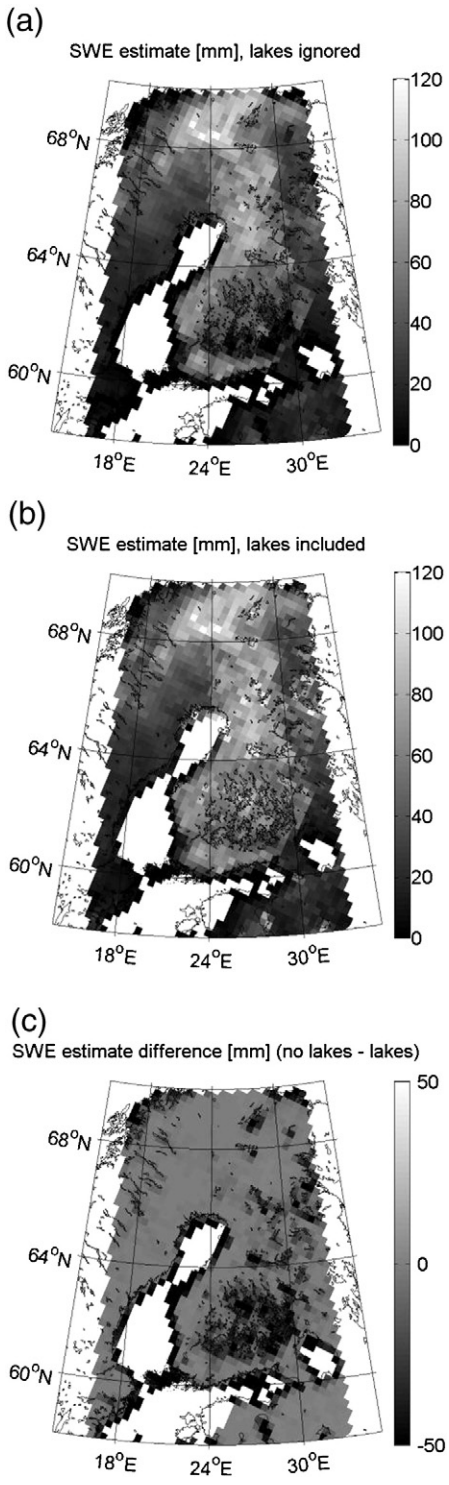

Fig. 8. Gridded maps of SWE estimates [mm] for January 1st, 2006, by (a) ignoring lakes in simulations and (b) applying lake simulations in the retrieval algorithm. Difference between estimates in (a) and (b) is depicted in (c).

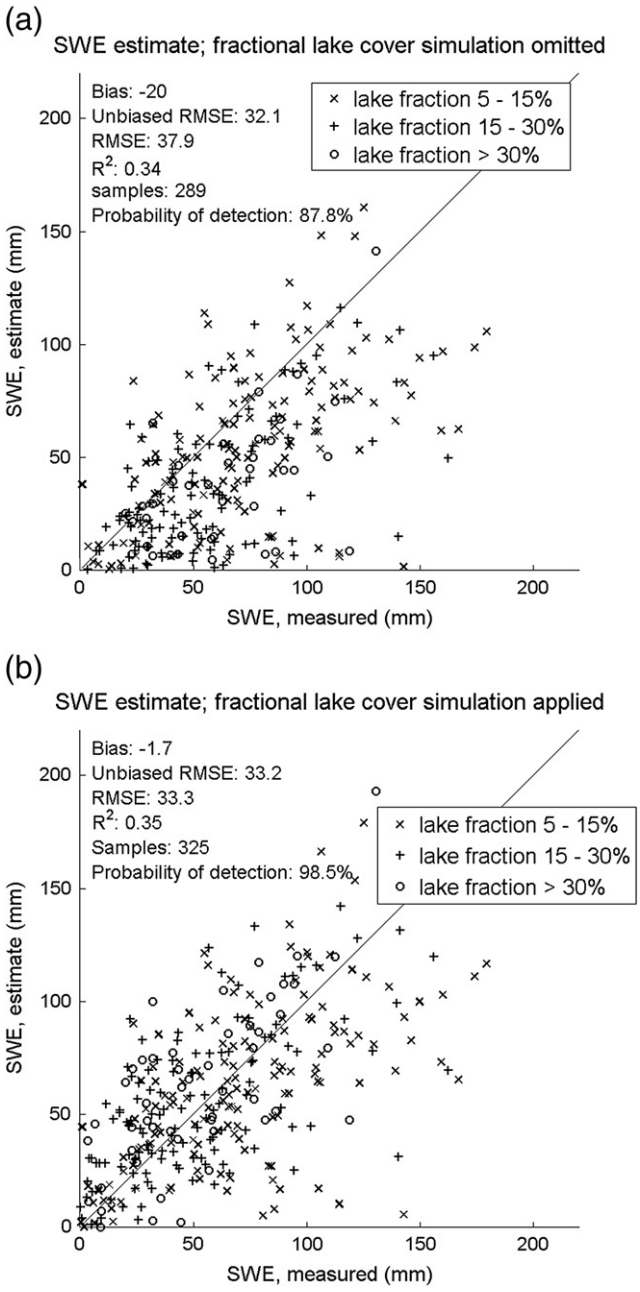

Fig. 9. Validation of SWE retrieval against SYKE snow course observations in three winter periods between 2005 and 2008. Influence of lakes omitted in forward model (a) and effect of lakes included (b). Analyzed grid cells divided into three categories according to fractional lake cover.

6. Discussion

In this study, we examined the possible influence of sub-grid scale frozen freshwater bodies on retrieval of snow parameter using passive microwave remote sensing. First, we introduced a simple method to account for fractional lake cover in a satellite observation using a forward emission model. The method was tested over the geographic area of Finland by setting model inputs using available in situ information on snow and land cover characteristics, and by comparing the simulated brightness temperatures with AMSR-E observations. The forward modeling analysis indicated that the simulation of a scenery observed by a space-borne radiometer instrument can be improved through the inclusion of frozen, snow covered lakes in the emission model as a simple layered structure consisting of water, ice and snow layers. In the studied scenarios, this was particularly the case for the signal difference of two frequencies traditionally employed in the retrieval of snow parameters, 18.7 and 36.5 GHz. However, the accuracy of the model used deteriorated with increasing fractional lake cover for the lowest frequency investigated (10.65 GHz). Other studies have shown (Gunn et al., 2011; Kontu et al., 2008) that the brightness temperature originating from snow-covered lakes is underestimated by the model on frequencies below 19 GHz; therefore, the original overestimation of brightness temperature by the model, when lakes are unaccounted for, changes into a

Table 6
Accuracy of SWE estimates in years 2005–2008. Bias, RMS, and unbiased RMS errors, R^2 values and probability of detection (PD) of SWE estimate against reference when (1) excluding and (2) including lake simulations. Grid cells with lake coverage of 5% or over included in analysis. Percentage of improved estimates and average improvement for the season in mm.

Year	Lakes excluded from simulations						Lakes included in simulations						Improvement	
	Bias [mm]	RMSE [mm]	Unb. RMSE [mm]	R^2	N	PD [%]	Bias [mm]	RMSE [mm]	Unb. RMSE [mm]	R^2	N	PD [%]	% of cases	Average impr. [mm]
2005–2006	−17	30	25	0.54	130	93.5	2	27	27	0.51	138	99.3	61	3
2006–2007	−24	44	36	0.15	66	82.1	−5	35	34	0.18	83	100.0	69	7
2007–2008	−22	44	38	0.19	87	84.8	−4	40	40	0.17	97	96.2	57	1

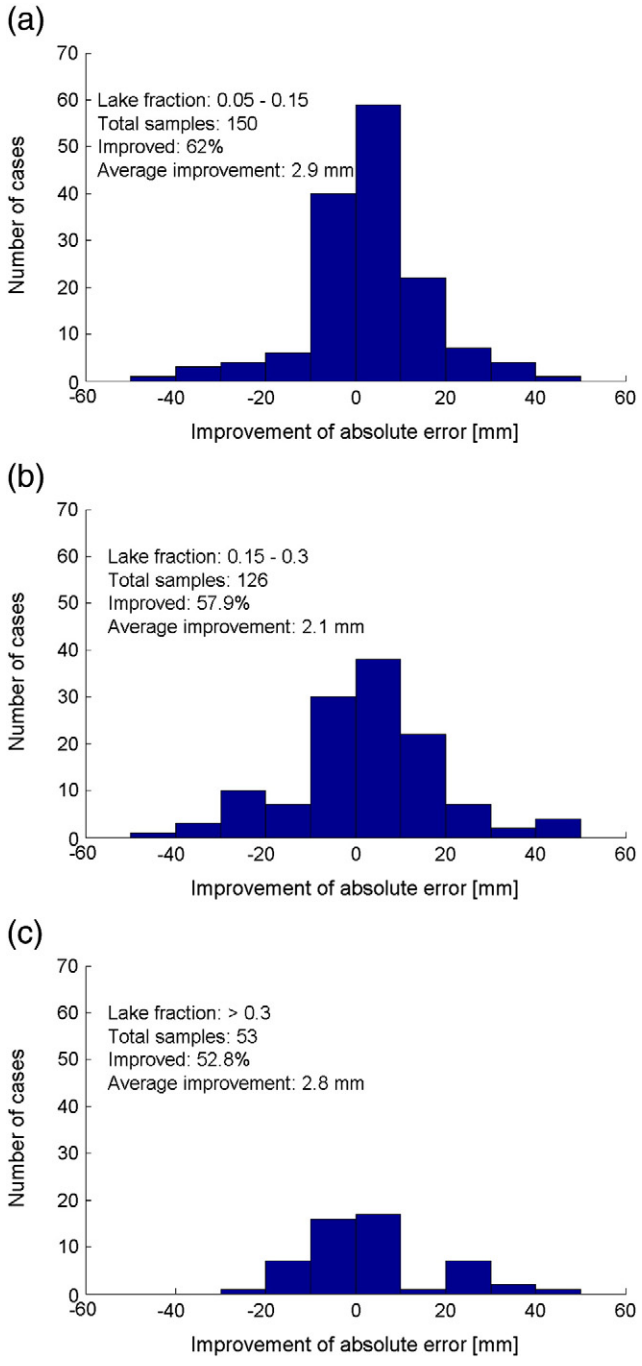

Fig. 10. Histograms of the improvement of the SWE estimate in individual grid cells with lake fraction of 5 to 15% (a), 15 to 30% (b) and over 30% (c) for three winter periods (2005–2008). Positive value indicates improvement (reduction) of error.

growing underestimation as fractional lake cover in the simulated scene increases. Further efforts should focus on adjusting the model to better simulate also the lower end of the microwave spectrum. Possible improvements include the inclusion of a white ice layer on top of the congelation ice, and the simulation of slushing events through the inclusion of a water/wet snow layer above the ice. The signature of snow covered lake ice on microwave frequencies is sensitive to all of these phenomena; the role of the ice layer is prominent on the lower frequency bands with a direct relation between ice growth and brightness temperature (Kang et al., 2010). In the latter case, it is estimated that the layer of water/wet snow would dominate the emission from the lake ice. The inclusion of a white ice layer in the simulation may, however, be problematic due to the high complexity involved in predicting the formation of snow ice (Adams & Roulet, 1980; Jeffries et al., 2005).

The modified forward model, simulating the effect of fractional lake cover, was applied in the SWE retrieval method presented by Pulliainen and Hallikainen (2001). The method applies numerical inversion of the forward model to satellite observations, using grain size as a free fitting parameter. Model input parameters concerning lake ice were set using available in situ data, as with the forward modeling experiment. It was shown that the accuracy of retrieved SWE estimates can be improved by applying the relatively simple emission model approach for lakes in the retrieval. The demonstrated improvement was comparably modest; this is partly due to the scarcity of reference information on terrestrial SWE from lake-rich areas. Another possible reason is the inability of the applied simplified forward model to capture the true variability of brightness temperature in particular over large lakes.

The present study used an extensive in situ dataset to define model input parameters for the lake ice component simulations, which was available for the studied regions in Finland. Such datasets are not available globally, at least on a consistent basis. Therefore, applying the presented method in global applications would require some other source of information to set the a priori parameters for lake ice in the retrieval. Coupling of the emission model with a thermodynamic model of lake ice can be considered an option; physical lake ice models have been shown to predict ice growth in freshwater lakes to a good accuracy, when adequate forcing data is available (e.g. Duguay et al., 2003). Another option may be through the acquisition of lake ice information from high-resolution SAR (Duguay & Lafleur, 2003; Rott et al., 2009).

Another important aspect considering the findings of this study is the inclusion of other wetland areas in a similar correction scheme using emission modeling. Bogs represent a similar source of error in SWE estimates; bogs and other wetlands, excluding lakes, represent 6% of the total land area north of the 55th latitude in Eurasia, compared to 9% of lakes and rivers (Global Land Cover 2000, http://bioval.jrc.ec.europa.eu/products/glc2000/glc2000.php). Bogs exhibit similar differing brightness temperature behavior as lakes, although with larger variability (e.g. Lemmetyinen et al., 2009). A further issue that could be addressed through the methodology presented is errors caused by effects of land cover heterogeneity over coastlines. However, simulation of the microwave emission from bogs and coastlines both represent a greater challenge than the case of lake ice

studied here. Over coastlines, in particular, the largest difficulties would arise from accounting for ice concentration, movement and deformation. Similarly, the heterogeneity of wetlands, with varying portions of soil and open water in different stages of freezing, may be difficult to simulate following the relatively simple approach applied here for lakes.

Acknowledgments

The National Snow and Ice Data Center (NSIDC) is acknowledged for providing AMSR-E observations and the Finnish Environment Institute for providing national land cover and vegetation data for Finland.

References

Adams, W. P., & Lasenby, D. C. (1978). The role of ice and snow in lake heat budgets. *Limnology and Oceanography*, *23*(5), 1025–1028.

Adams, W. P., & Lasenby, D. C. (1985). The roles of snow, lake ice and lake water in the distribution of major ions in the ice cover of a lake. *Annals of Glaciology*, *7*, 202–207.

Adams, W. P., & Roulet, N. T. (1980). Illustration of the roles of snow in the evolution of the winter cover of a lake. *Arctic*, *33*(1), 100–116.

Chang, A., Foster, J., & Hall, D. (1987). Nimbus-7 SMMR derived global snow cover parameters. *Annals of Glaciology*, *9*, 39–44.

Choudhury, B. J., Schmugge, T. J., Newton, R. W., & Chang, A. (1979). Effect of surface roughness on the microwave emission from soils. *Journal of Geophysical Research*, *84*, 5699–5706.

Derksen, C. (2008). The contribution of AMSR-E 18.7 and 10.7 GHz measurements to improved boreal forest snow water equivalent retrievals. *Remote Sensing of Environment*, *112*, 2701–2710.

Derksen, C., Sturm, M., Liston, G. E., Holmgren, J., Huntington, H., Silis, A., et al. (2009). Northwest territories and Nunavut snow characteristics from a subarctic traverse: Implications for passive microwave remote sensing. *Journal of Hydrometeorology*, *10*, 448–463.

Derksen, C., Toose, P., Rees, A., Wang, L., English, M., Walker, A., et al. (2010). Development of a tundra-specific snow water equivalent retrieval algorithm for satellite passive microwave data. *Remote Sensing of Environment*, *114*, 1699–1709.

Derksen, Walker, C. A., & Goodison, B. (2003). A comparison of 18 winter seasons of in situ and passive microwave-derived snow water equivalent estimates in Western Canada. *Remote Sensing of Environment*, *88*, 271–282.

Derksen, C., Walker, A., & Goodison, B. (2005). Evaluation of passive microwave snow water equivalent retrievals across the boreal forest/tundra transition of western Canada. *Remote Sensing of Environment*, *96*(3/4), 315–327.

Drebs, A., Nordlund, A., Karlsson, P., Helminen, J., & Rissanen, P. (2002). *Climatological statistics of Finland 1971–2000.* Report of Finnish Meteorological Institute ISSN 1458–4530.

Duguay, C., Flato, G., Jeffries, M., Menard, P., Morris, K., & Rouse, W. (2003). Ice-cover variability on shallow lakes at high latitudes: Model simulations and observations. *Hydrological Processes*, *17*, 3465–3483.

Duguay, C. R., & Lafleur, P. M. (2003). Determining depth and ice thickness of shallow subarctic lakes using spaceborne optical and SAR data. *International Journal of Remote Sensing*, *24*(3), 475–489.

Fierz, C., Armstrong, R. L., Durand, Y., Etchevers, P., Greene, E., McClung, D. M., et al. (2009). The international classification for seasonal snow on the ground. *IHP-VII Technical Documents in Hydrology* N°83 IASC Contribution N°1, UNESCO-IHP, Paris, 80 pp.

Foster, J. L., Chang, A. T. C., & Hall, D. K. (1997). Comparison of snow mass estimates from a prototype passive microwave algorithm and a snow depth climatology. *Remote Sensing of Environment*, *62*, 132–142.

Goodison, B., & Walker, A. (1995). Canadian development and use of snow cover information from passive microwave satellite data. In B. Choudhury, Y. Kerr, E. Njoku, & P. Pampaloni (Eds.), *Passive microwave remote sensing of land-atmosphere interactions* (pp. 245–262).

Gunn, G. E., Duguay, C. R., Derksen, C., Lemmetyinen, J., & Toose, P. (2011). Evaluation of the HUT modified snow emission model over lake ice using airborne passive microwave measurements. *Remote Sensing of Environment*, *115*(1), 233–244.

Hall, D., Foster, J., Chang, A., & Rango, A. (1981). Freshwater ice thickness observations using passive microwave sensors. *IEEE Transactions on Geoscience and Remote Sensing*, *GE-19*, 189–193.

Hall, D., Kelly, R. E. J., Riggs, G. A., Chang, A. T. C., & Foster, J. L. (2002). Assessment of the relative accuracy of hemispheric-scale snow-cover maps. *Annals of Glaciology*, *34*, 24–30.

Hallikainen, M. T., & Jolma, P. A. (1992). Comparison of algorithms for retrieval of snow water equivalent from Nimbus-7 SSMR data in Finland. *IEEE Transactions on Geoscience and Remote Sensing*, *30*, 124–131.

Hallikainen, M. T., Ulaby, F., & Deventer, T. (1987). Extinction behavior of dry snow in the 18- to 90-GHz range. *IEEE Transactions on Geoscience and Remote Sensing*, *GE-25*, 737–745.

Isaaks, E., & Srivastava, M. (1989). *An introduction to applied geostatistics.* : Oxford University Press 592 pp.

Jeffries, M., Morris, K., & Duguay, C. (2005). Lake ice growth and decay in central Alaska, USA: Observations and computer simulations compared. *Annals of Glaciology*, *40*(1), 195–199.

Kang, Kyung-Kuk, Duguay, C. R., Howell, S. E. L., Derksen, C. P., & Kelly, R. E. J. (2010). Sensitivity of AMSR-E brightness temperatures to the seasonal evolution of lake ice thickness. *IEEE Geoscience and Remote Sensing Letters*, *7*(4), 751–755.

Kazumori, M., Liu, Q., Treadon, R., & Derber, J. C. (2008). Impact study of AMSR-E radiances in the NCEP global data assimilation system. *Monthly Weather Review*, *136*(2), 541–559.

Kelly, R., Chang, A., Tsang, L., & Foster, J. (2003). A prototype AMSR-E global snow area and snow depth algorithm. *IEEE Transactions on Geoscience and Remote Sensing*, *41*(2), 230–242.

Klein, L. A., & Swift, C. T. (1977). An improved model for the dielectric constant of sea water at microwave frequencies. *IEEE Transactions on Antennas and Propagation*, *AP-25*, 104–111.

Knowles, K. W., Savoie, M. H., Armstrong, R. L., & Brodzik, M. J. (2006). *AMSR-E/aqua daily EASE-grid brightness temperatures, 2005–2008.* Boulder, Colorado USA: National Snow and Ice Data Center Digital media (updated 2010).

Kontu, A., Kemppainen, S., Lemmetyinen, J., Pulliainen, J., & Hallikainen, M. (2008). Determination of snow emission on lake ice from airborne passive microwave measurements. *Geoscience and remote sensing symposium, 2008, IGARSS 2008. IEEE International*, *4*. (pp. 1046–1049) 4, Paper.

Kontu, A., & Pulliainen, J. (2010). Simulation of spaceborne microwave radiometer measurements of snow cover using in situ data and brightness temperature modeling. *IEEE Transactions on Geoscience and Remote Sensing*, *48*(3), 1031–1044.

Kruopis, N., Praks, J., Arslan, A., Alasalmi, H., Koskinen, J., & Hallikainen, M. (1999). Passive microwave measurements of snow-covered forests in EMAC'95. *IEEE Transactions on Geoscience and Remote Sensing*, *37*, 2699–2705.

Lemke, P., Ren, J., Alley, R. B., Allison, I., Carrasco, J., Flato, G., et al. (2007). Observations: Changes in snow, ice and frozen ground. In S. Solomon, D. Qin, M. Manning, Z. Chen, M. Marquis, K. B. Averyt, M. Tignor, & H. L. Miller (Eds.), *Climate change 2007: The physical science basis. Contribution of working group I to the fourth assessment report of the intergovernmental panel on climate change*. Cambridge, United Kingdom and New York, NY, USA: Cambridge University Press.

Lemmetyinen, J., Derksen, C., Pulliainen, J., Strapp, W., Toose, P., Walker, A., et al. (2009). A comparison of airborne microwave brightness temperatures and snowpack properties across the boreal forests of Finland and Western Canada. *IEEE Transactions on Geoscience and Remote Sensing*, *47*(3), 965–978.

Lemmetyinen, J., Pulliainen, J., Rees, A., Kontu, A., Qiu, Yubao, & Derksen, C. (2010). Multiple-layer adaptation of HUT snow emission model: Comparison with experimental data. *IEEE Transactions on Geoscience and Remote Sensing*, *48*(7), 2781–2794.

Pulliainen, J. (2006). Mapping of snow water equivalent and snow depth in boreal and sub-arctic zones by assimilating space-borne microwave radiometer data and ground-based observations. *Remote Sensing of Environment*, *101*, 257–269.

Pulliainen, J. T., Grandell, J., & Hallikainen, M. T. (1997). Retrieval of surface temperature in boreal forest zone from SSM/I data. *IEEE Transactions on Geoscience and Remote Sensing*, *35*, 1188–1200.

Pulliainen, J. T., Grandell, J., & Hallikainen, M. T. (1999). HUT snow emission model and its applicability to snow water equivalent retrieval. *IEEE Transactions on Geoscience and Remote Sensing*, *37*(3), 1378–1390.

Pulliainen, J. T., & Hallikainen, M. T. (2001). Retrieval of regional snow water equivalent from space-borne passive microwave observations. *Remote Sensing of Environment*, *75*, 76–85.

Rees, A., Derksen, C., English, M., Walker, A., & Duguay, C. (2006). Uncertainty in snow mass retrievals from satellite passive microwave data in lake-rich high-latitude environments. *Hydrological Processes*, *20*, 1019–1022.

Rott, H., Duguay, C., Essery, R., Haas, C., Macelloni, G., Malnes, E., et al. (2009). ESA SP-1313/3 candidate earth explorer core missions report for assessment: CoReH20 — Cold regions hydrology high resolution observatory. *ESA Communication Production Office* (pp. 114).

Takala, M., Luojus, K., Pulliainen, J., Derksen, C., Lemmetyinen, J., Kärnä, J.-P., Koskinen, J., & Bojkov, B., in press. Estimating northern hemisphere snow water equivalent for climate research through assimilation of space-borne radiometer data and ground-based measurements. Remote Sensing of Environment, doi:10.1016/j.rse.2011.08.014.

Tedesco, M., & Wang, J. R. (2006). Atmospheric correction of AMSR-E brightness temperatures for dry snow cover mapping. *IEEE Geoscience and Remote Sensing Letters*, *3*(3), 320–324.

Törmä, M., Haakana, M., Hatunen, S., Härmä, P., Kallio, M., Katila, M., et al. (2008). Finnish corine 2006-project: Determining changes in land cover in Finland between 2000 and 2006. *Remote Sensing for Environment Monitoring, GIS Applications and Geology VIII. Proceedings of SPIE*, *vol. 7110*.

Wegmüller, U., & Mätzler, C. (1999). Rough bare soil reflectivity model. *IEEE Transactions on Geoscience and Remote Sensing*, *37*, 1391–1395.

Publication 3

A. Kontu, J. Lemmetyinen, J. Pulliainen, J. Seppänen, M. Hallikainen. 2014. Observation and modeling of the microwave brightness temperature of snow-covered frozen lakes and wetlands. *IEEE Transactions on Geoscience and Remote Sensing*, 52(6), 3275-3288. doi: 10.1109/TGRS.2013.2272077.

Observation and Modeling of the Microwave Brightness Temperature of Snow-Covered Frozen Lakes and Wetlands

Anna Kontu, Juha Lemmetyinen, Jouni Pulliainen, Jaakko Seppänen, and Martti T. Hallikainen, *Fellow, IEEE*

***Abstract*—Small-scale variability in land cover influences both the snow cover and the microwave response of a snow-covered surface. Since low microwave frequencies penetrate below the snowpack, the differing dielectric properties of soil and water have a significant effect on passive microwave observations and therefore cause errors in the interpretation of snow parameters from satellite data. Here, the brightness temperature of snow- and ice-covered lakes and wetlands is studied using airborne and spaceborne microwave radiometer observations and modeling of brightness temperature from *in situ* measurements. We aim at assessing the validity of the multilayer Helsinki University of Technology (HUT) snow emission model on lake- and wetland-rich areas and at examining the error from omission of water bodies in the forward modeling of brightness temperature. The results indicate that the model can estimate brightness temperatures of lakes and wetlands with rms errors of 12–28 K and 9–16 K, respectively. The inclusion of lakes in the satellite-scale simulations reduces the simulation error in 52%–100% of the simulated areas at 18.7 and 36.5 GHz. The inclusion of wetlands further improves simulations, resulting in an rms error of satellite scenes of 4–5 K at 18.7 and 36.5 GHz (5–10 K without lakes and wetlands). However, the natural variability of brightness temperature over water bodies is not entirely captured particularly at 10.65 GHz. The inclusion of lakes and wetlands can be used to reduce errors in the forward model and thus increase the accuracy of snow parameters derived from satellite data.**

***Index Terms*—Ice, passive microwave remote sensing, snow.**

I. Introduction

In the northern boreal zone, seasonal snow covers the ground for a large part of the year. During the onset of snow melt, the water stored in the snowpack is released in a short time period, causing a danger of flooding. Accurate runoff forecasting is needed in flood prevention and hydropower planning, setting a requirement for accurate information on the extent and water content [snow water equivalent, (SWE)] of snow cover before the onset of snowmelt [1].

Another application benefiting from large-scale snow information is found in climate studies. Current climate models predict large temperature increases and changes in distribution and amount of precipitation, particularly in the Arctic and during wintertime [2]. Snow and climate have a strong connection through the high albedo of pure snow; snow cover reflects most of the incident solar radiation, thus reducing the amount of heat absorbed by surface air and soil. On the other hand, diminishing snow cover increases the amount of heat being absorbed by Earth surface and thus boosts global warming [3].

Most of the northern seasonally snow-covered areas are sparsely populated, making *in situ* observations of snow rare. In addition, *in situ* data are pointwise and not necessarily representative of the large-scale snow situation [4]. Thus, remote sensing offers unique possibilities for snow studies. Both optical and microwave satellite data are used in the remote sensing of snow parameters, but microwaves have two advantages: Certain microwave wavelengths penetrate through the snowpack, giving information on, e.g., snow depth (SD) and SWE, and they are independent of sunlight and only lightly affected by the atmosphere, which are clear advantages considering the winter conditions in polar areas. Several algorithms for deriving SWE from passive microwave observations have been proposed in literature (e.g., [5]–[9]).

In a practical observation with satellite microwave radiometers, such as the Special Sensor Microwave/Imager and Advanced Microwave Scanning Radiometer for the Earth Observing System (AMSR-E), the relatively crude spatial resolution (tens of kilometers) of the instruments means that an observation originates from a heterogeneous landscape, with varying land cover, topography, vegetation, and snow cover properties, which all affect the detected brightness temperature (e.g., [10]–[13]). Considering the retrieval of snow properties, large local scale variations in, e.g., topography and vegetation cover may degrade the accuracy of the resulting snow map [14]. Further features affecting the observed microwave emission are small water bodies such as rivers, lakes, and wetlands. As a part of the microwave radiation penetrates though a dry snowpack, the underlying layer has an effect on the satellite measurement, particularly at lower microwave frequencies. The dielectric constants of water in the microwave regime (e.g., $\varepsilon \approx 40$ at 18 GHz) and ice ($\varepsilon \approx 3.2$) differ significantly from that of frozen ground (e.g., between $4 - 0.5j$ and $6 - 1j$ at 18 GHz for frozen soil at -20 °C temperature [15]), affecting emissivity and the observed microwave response. Any water bodies present in the satellite's field of view thus affect the observed total brightness temperature. The total effect is dependent on

Manuscript received April 15, 2013; revised June 11, 2013; accepted June 18, 2013. Date of publication July 22, 2013; date of current version February 27, 2014.

A. Kontu, J. Lemmetyinen, and J. Pulliainen are with the Arctic Research Unit, Finnish Meteorological Institute, 99600 Sodankylä, Finland.

J. Seppänen and M. T. Hallikainen are with the Department of Radio Science and Engineering, School of Science and Technology, Aalto University, 02150 Espoo, Finland.

Color versions of one or more of the figures in this paper are available online at http://ieeexplore.ieee.org.

Digital Object Identifier 10.1109/TGRS.2013.2272077

the size and properties (such as temperature and salinity) of the water body, frequency, and the properties of a possible ice and snow cover over the water [16], [17]. Another affecting factor is that snow cover on lake ice typically differs from snow on land with regard to depth, layer structure, and grain size [18].

Traditional snow parameter retrieval algorithms rely on direct calculation of SWE from the difference between brightness temperatures at a lower frequency (typically 18 GHz), where snow mostly absorbs radiation, and a higher frequency (typically 36.5 GHz), where scattering dominates in the snowpack. These algorithms can be applied globally (e.g., [6]) or employ region-specific empirically derived coefficients (e.g., [10] and [19]). Another approach is the use of forward model inversion, enhanced by assimilation with *in situ* data, in the interpretation of passive microwave observations (e.g., [20]). Since the penetration depth of microwave radiation into and below the snowpack is frequency dependent, the effect of varying background is also frequency dependent, causing a bias in the algorithms based on a frequency difference [21]. One possibility of correcting for this effect is to mask out the lake-rich areas in the resulting snow maps (e.g., [9]). However, in larger lake-rich areas such as Finland or Canada, this method results in omission of wide areas from the retrieval.

Wetlands are very diverse; the main common factor is that they are saturated with water. The wetlands in Finland are typically peat bogs. Even so, their coverage varies from dry forested patches to moss-covered moist peat and small lakes. Wetlands have been modeled and measured at microwave frequencies (e.g., [22] and [23]). However, these studies mainly focus on inundation and water dynamics studies, i.e., the detection of liquid water. This study concentrates on the modeling of frozen snow-covered wetlands.

The objective of this study is to investigate the effect of lakes and other small fresh water bodies in the simulation of microwave emission of a snow-covered scene. We investigate the performance of the Helsinki University of Technology (HUT) snow emission model ([24] and [25]) for simulation of microwave brightness temperature over frozen snow-covered fresh water bodies. We employ an extensive data set of *in situ* information on snow and ice properties to drive the model over various lake ice sites in Finland, where airborne reference observations were acquired. The airborne data are used to scale the model to observations over lake ice, wetland, and other land cover classes, using the surface roughness of media interfaces as fitting parameters. In addition, we study the variability of brightness temperature and snow conditions on a single lake and surrounding forests and wetlands near the town of Sodankylä, northern Finland, of which several overpasses of airborne data and the most detailed *in situ* data are available. The Sodankylä data are also used in instrument intercalibration between airborne and spaceborne observations. Finally, we examine the effect of lakes and wetlands in the satellite scale and compare the simulation results for lake- and wetland-rich areas to spaceborne microwave radiometer data.

The study is limited to the geographic area of Finland. The multilayer HUT snow emission model has previously been applied for simulation of emissions of tundra lakes in Canada [26], as well as emissions from the Great Slave Lake and the Great Bear Lake [27]. Furthermore, recent studies applied the model for heterogeneous satellite scenes to correct for the influence of lake ice both in the forward model simulations and in the retrieval of SWE [13], [28]. Several shortcomings of model performance were noted, including poor performance against reference data at low frequencies. By means of an extensive airborne data set, the present study contributes to the previous studies by increasing the understanding of the contributions of different properties of snow-covered lakes to the observed emission. Furthermore, the study allows further assessment of the impact of other land cover types, including wetlands, when considering the satellite-scale simulations of a snow-covered terrain.

The setup for model simulations is given in Section II. The available data set of airborne observations and reference data is described in Section III, and comparison of these to simulations is described in Sections IV and V. The results are discussed in Section VI. Section VII finally gives the conclusions of the study.

II. Setup for Model Simulations

A. Lake Ice

The original HUT snow emission model [24] calculates the brightness temperature of one homogeneous layer of snow covering a quasi-infinite layer of frozen ground. To model the snow–ice–water system of lakes, a multiple-layer adaptation of the model is applied here [25]. Brightness temperature emissions from the snow-covered lakes were simulated considering a three-layer structure: a semi-infinite layer of water, a homogeneous layer of ice, and a homogeneous layer of snow on top. The layer interfaces were not considered smooth; based on qualitative field observations and minimization of rms error between simulations and airborne reference measurements, reasonable fixed values for surface roughnesses were chosen.

B. Wetlands

Wetlands in the areas covered by the flights consist mainly of bogs. They are typically waterlogged in the autumn and may contain large quantities of free water beneath a layer of ice in winter; thus, regarding a simulation case, wetlands resemble more shallow lakes than dry terrain. Consequently, they were simulated similarly to lakes, with a three-layer structure of a semi-infinite layer of water, a homogeneous 30-cm-thick layer of ice, and a homogeneous layer of snow on top. The thickness of the ice layer over wetlands may also be significantly thinner than that on lake ice due to organic activity in the water and soil. Since no measurement data of wetland ice layer thickness were available, a constant value was used. The ice is also typically embedded with residual organic matter and other impurities, as is the water layer below. However, as no quantitative information of these factors was available, the simulation of wetlands was performed according to the aforementioned assumption, and possible organic impurities within the ice or water were not considered.

C. Forested and Open Land

The study also includes modeling of land surfaces for the purpose of satellite-scale simulations. For these areas, the HUT snow emission model is applied as originally proposed in [24]. Snow on open areas was modeled with two layers: a semi-infinite layer of soil and a homogeneous layer of snow. On the forested areas, an empirical vegetation model [29] was included to account for the shadowing and emission from vegetation.

D. Surface Roughness Parameterization

In conjunction with the original HUT snow emission model, an empirical rough bare soil reflectivity model [30] has been used in various studies to describe the effect of surface roughness on the emitted brightness temperature from the soil surface beneath the snowpack [9], [20], [31]. This cannot be directly applied to the water/ice interface, as the model is based on empirical measurements of soil types. Several studies characterize reflections from a rough sea surface using a two-scale model (e.g., [32] and [33]). In these, the reflection coefficient is divided into coherent and incoherent components. The coherent components arise from small-scale (compared to the wavelength λ) variations in surface height, whereas incoherent components arise from periodic or random variations of comparable order to λ. A similar approach for ground surfaces has been presented in [34]. For the purposes of ocean studies, the magnitude of small- and large-scale height variations can be derived, e.g., by applying wave spectrum models dependent on measured wind speed (e.g., [35]). For obvious reasons, these are not applicable when a frozen water surface is considered.

For the purposes of this study, the water/ice and ice/snow interfaces over lakes and wetlands are considered to be flat surfaces, superimposed only by small random variations of surface height. In the case of natural lake and sea ice, deformation of ice could also cause larger variations in comparison to microwave wavelengths and would result in the appearance of the incoherent reflectivity components described previously. However, no models predicting the ice deformation magnitude are known to the authors. Therefore, the Fresnel reflectivity coefficients are modified by surface roughness variations only through a coherent reflectivity component, so that we have the following [36]:

$$|r_p|^2 = |r_{p.\mathrm{Fresnel}}|^2 \exp(-4k^2h^2\cos^2\theta). \quad (1)$$

Here, $r_{p.\mathrm{Fresnel}}$ is the Fresnel reflection coefficient for polarization p, k is the wavenumber, h is the roughness (rms height variation) of the rough surface, and θ is the incidence angle. The roughness parameter should be considered to be an empirical fitting parameter. Nevertheless, in order for (1) to be valid, the height variations should satisfy the condition $kh \ll 1$ [32], [24].

III. Data Set

A. Airborne Radiometer Data

On March 16–18, 2011, the Department of Radio Science and Engineering of Aalto University, Finland, performed a measurement campaign with the airborne HUT Radiometer (HUTRAD) microwave radiometer. HUTRAD measures on six frequencies (6.9, 10.65, 18.7, 23.8, 36.5, and 89.0 GHz) and two polarizations (vertical and horizontal). For this study, frequencies 10.65, 18.7, and 36.5 GHz, typically used in snow studies, were examined. The main specifications of the instrument are listed in Table I. The nominal incidence angle of HUTRAD is 50°–53°, depending on the aircraft pitch. The airborne radiometer system was calibrated five times during the campaign, ideally before and after each measurement flight; on the last day of measurements, a calibration was performed only after the flight. Based on the calibrations during the first two days of operations, instrument stability was estimated to have been ±3 K for 10.65 GHz, ±3 K for 18.7 GHz, and ±1 K for 36.5 GHz.

TABLE I
SUMMARY OF THE INSTRUMENT CHARACTERISTICS AND THE OBSERVATION PARAMETERS

Parameter	Values for different channels		
Frequency [GHz]	10.65	18.7	36.5
Bandwidth [MHz]	120	130	400
Integration time [s]	0.5	0.5	0.5
Sensitivity [K]	0.6	0.6	0.3
Accuracy [K]	< 3	< 3	< 1
θ_{3dB} [°]	3	3	4
α_i [°]	50	50	50
Scan method	Along track		
Flight altitude [m]	600		
Average airspeed [m/s]	64		
Footprint size[1] (w x l) [m x m]	37 x 76	37 x 76	49 x 101

[1] Ideal instantaneous footprint for 3dB beam width field of view, for flat target from an altitude of 600 m, incidence angle 50°; actual footprint varies according to aircraft maneuvering, ground elevation, integration time and airspeed.

The campaign consisted of two transfer flights with continuous measurements, from southern to northern Finland and back, as well as 15 overpasses of a specified test area around the town of Sodankylä in northern Finland. On the second transfer flight from north to south, the 18.7-GHz horizontal channel failed and was omitted from the analysis.

From the transfer flights, a total of 42 lake transects was selected for analysis. These are marked on the map in Fig. 1. The 42 AMSR-E grid cells covering the lake transects were selected for comparison with simulations. In addition to snow-covered lake ice, simulations of forested and open land surfaces and wetlands were required for the satellite-scale analysis. Totals of 39 forest, 14 open area, and 7 wetland transects were selected from the flight lines close to the chosen lake transects (and within the same AMSR-E grid cells) to allow comparison of simulation results with the airborne data. The number of forest, open area, and wetland transects is limited due to lack of large-enough homogeneous areas on the flight track.

A land cover map of one of the lake transects and the surrounding area is shown in Fig. 2. The land cover is mainly mixed forests and lakes, which is typical in southern Finland. In the north (particularly in the Sodankylä area), the typical land cover is sparse coniferous forest and open wetland. The brightness temperatures measured from the area in Fig. 2 are shown in Fig. 3. Over land, the brightness temperatures of 10.65- and 18.7-GHz channels are similar (difference < 5 K).

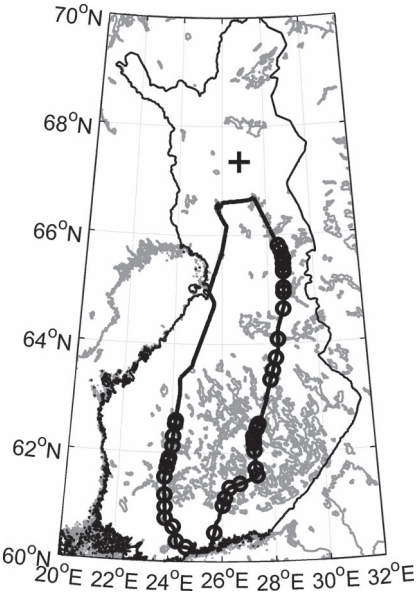

Fig. 1. Map of Finland showing the (thick black line) transfer flight routes, (o) selected lake transects, (+) the Sodankylä area, and (light gray line) shorelines.

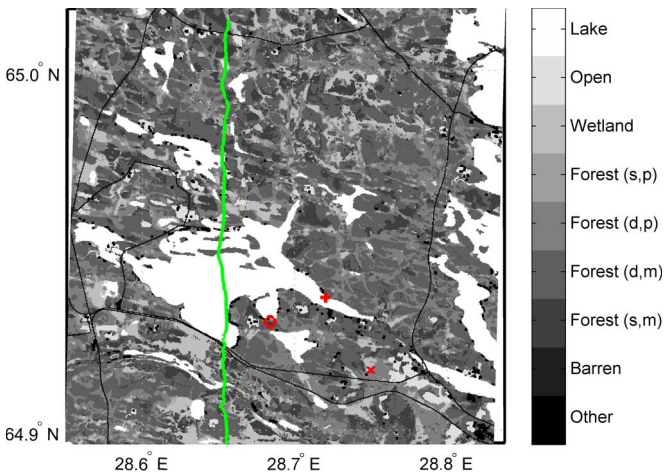

Fig. 2. Map of one of the lake transects and surrounding areas on the transfer flights with nearby *in situ* measurement sites: (o) Snow course, (+) lake ice thickness, and (×) weather station. The flight route is plotted with a green line. Flight direction is from north to south. The measured brightness temperatures are shown in Fig. 3. Forest types are (s) sparse or (d) dense forest on (m) mineral soil or (p) peat.

The lake transect can be seen as a large drop in the brightness temperature (20–60 K, depending on channel). Also, the difference of 10.65- and 18.7-GHz channels increases to 10–20 K over lake. The variation of 36.5-GHz channels is large (∼60 K) over land, while over lake, the brightness temperature is at minimum and the variation is about 10 K. The 36.5-GHz channels mostly react to changes in the snowpack; the variability is typically larger over land than over lake ice. The statistics of the airborne measurements of the lake transects on the transfer flights are presented in Fig. 4. On average, the vertically polarized channels (subsequently referred to as V-pol in the text) have a 15–18-K higher brightness temperature than the horizontally polarized channels (subsequently referred to as H-pol).

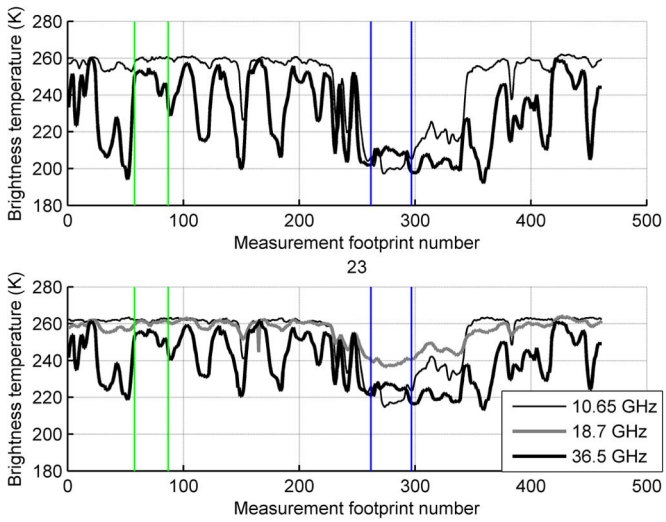

Fig. 3. Brightness temperatures measured from the area in Fig. 2: (Top) Horizontal and (bottom) vertical polarizations. The 18.7-GHz H-pol data are not shown due to receiver failure. The lake transect chosen for analysis is marked with vertical blue lines (footprints 262–297), and the forest transect is marked with vertical green lines (footprints 58–87). Only the middle part of the lake was chosen to avoid islands (in the beginning) and shoreline (at the end) in the field of view.

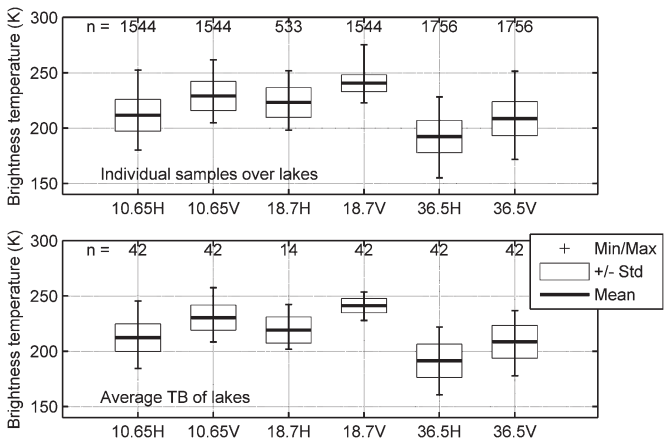

Fig. 4. Statistics of the HUTRAD measurements over the 42 lake transects of the transfer flights for frequencies 10.65, 18.7, and 36.5 GHz; (top) individual measured samples and (bottom) values averaged for each lake are shown.

The Sodankylä area data set consists of 15 flight transects over varying terrain, comprising of forests, wetlands, and a large lake (Lake Orajärvi), covering an area of approximately 10 km × 10 km. Forests account for roughly 70%, and wetlands account for 20% of the total land cover. A detailed *in situ* data set with measurements along the flight lines is available, including distributed measurements of SD and SWE of the airborne transects, ten snow pits, and an ice thickness measurement (see Section III-C). This data set is studied separately from the transfer flight data. The statistics of the brightness temperature measurements are presented in Fig. 5. A detailed map of the transects and *in situ* measurements is shown in Fig. 6.

B. Spaceborne Radiometer Data

The satellite data used are AMSR-E level-2 brightness temperatures at 10.65, 18.7, and 36.5 GHz at 12-km resolution [37].

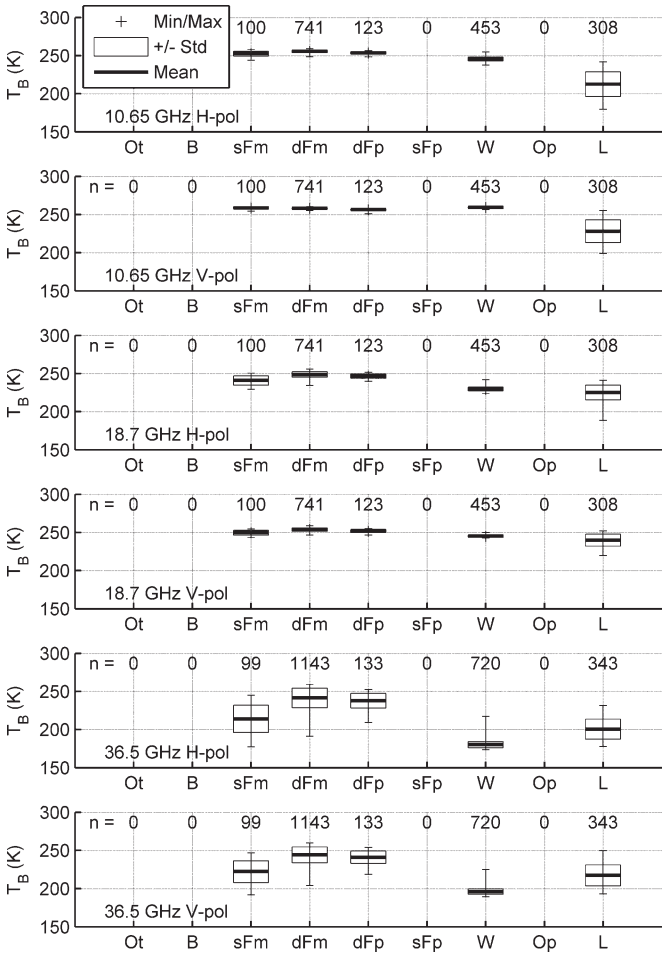

Fig. 5. Statistics of the HUTRAD measurements of the 15 flight transects in Sodankylä area for different land cover classes. See definitions of land cover classes in Section III-C.

Brightness temperatures of individual grid cells, one for each examined lake transect from the transfer flights and five for the Sodankylä test area, were used.

C. Reference In Situ Data

The layered HUT snow emission model requires several input parameters, including SWE, density, grain size, temperature, moisture, salinity, and surface roughness of each layer. In order to simulate the whole satellite scenes, additional information on the vegetation and land cover is required, including the temperature, biomass, and cover fraction of the vegetation. In addition, the transmissivity and up- and down-welling brightness temperature contributions of the atmosphere are required. For some of these parameters, *in situ* data were available (e.g., ice thickness over lakes, SD, density, and water equivalent), for the rest typical constant values were chosen (e.g., soil temperature was set to -5 °C; atmospheric transmissivity was derived from statistics [38], [39]) or the parameter was treated as an empirical fitting parameter (e.g., roughness of ice). Histograms of the most important input parameters for the transfer flight simulations are shown in Fig. 7.

Meteorological data were measured by automatic weather stations of the Finnish Meteorological Institute. Daily mean air temperature was used in the simulations. Snow temperature

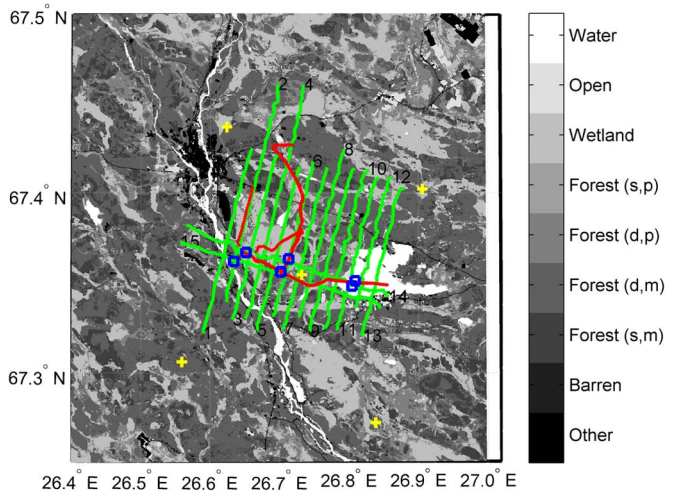

Fig. 6. Land cover, (green lines) flight transects, and *in situ* measurement sites in the Sodankylä area; (red dot) distributed SD measurements and (blue square) snow pit locations. AMSR-E grid cell center points are also marked $(+)$. Lake Orajärvi is on the eastern side of the flight area, while the Sodankylä town center is in the northwest outside of the flight area. A large wetland area is situated between these two. Forest types are (s) sparse or (d) dense forest on (m) mineral soil or (p) peat.

was not measured on any site, but a mean value of air and (constant) soil temperatures was used as a proxy value for the snowpack in simulations. Based on the snow pit measurements in Sodankylä, this assumption might cause an error of up to 5 °C in the snow temperature, resulting in a simulation error of 0.14–1.0 K, depending on frequency.

Corine land cover 2006 (CLC2006) data [41] at 25-m spatial resolution, provided by the Finnish Environment Institute (SYKE), were used to distinguish between different land cover categories. CLC2006 divides land cover into 44 categories. These were further aggregated to nine generalized classes: barren (B), sparse and dense forests on mineral soil (sFm and dFm, respectively), sparse and dense forests on peat (sFp and dFp, respectively), wetlands (W), lakes and rivers (L), open (Op; mainly fields, meadows, and other similar areas with low vegetation), and others (Ot; mainly urban area).

Data on the average forest stem volume (biomass) at 25-m resolution from year 2009 were used for the simulation of the vegetation effects following [24]. The data were provided by the Finnish Forest Research Institute.

1) Transfer Flights: SD and SWE data from snow courses form the bulk of the *in situ* snow information available. Snow courses are maintained by SYKE. A snow course is a 4-km track with 80 SD and 8 water equivalent measurements at equal distances. Each snow course covers varying terrain typical to the area and thus represents the typical snow conditions. The measurement points are classified into six land cover classes: open area, forest clearing, pine forest, spruce forest, deciduous forest, and wetland. The average values of measurements in all forests, open area, and wetland were used in the simulations. Snow grain size or stratigraphy data were not available for the transfer flight simulations; thus, the snow was considered as a single layer with a constant grain size.

Lake ice measurements, also operated by SYKE, consist of manual point measurements of SD and total ice thickness. On each lake, ice thickness is measured at three equidistant sites

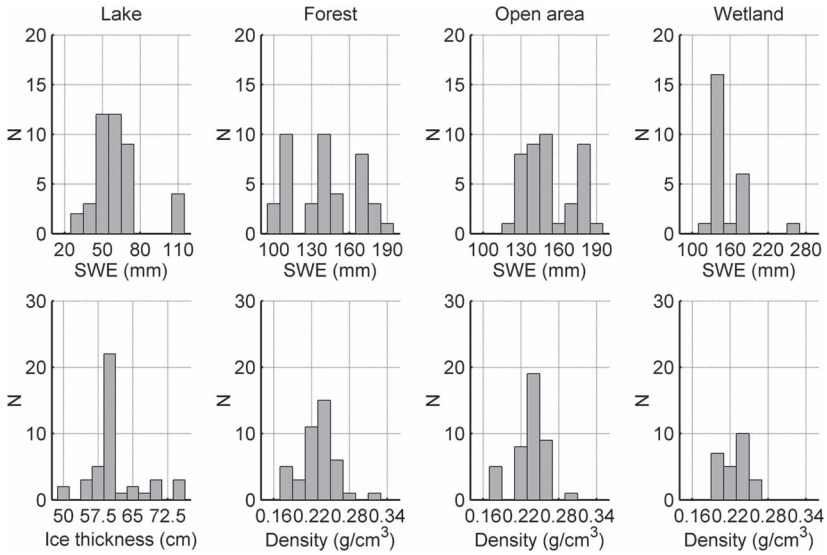

Fig. 7. Histograms of the most important input parameters for the transfer flight simulations. For lake, forest, and open area, data for all the 42 areas chosen for analysis with satellite data are shown. For wetlands, data exist only for 25 areas due to very small wetland coverage on some of the chosen areas.

with three SD measurements in a fixed pattern around each of these (nine SD measurements in total). Average values of the measurements on each lake were used. SWE and density were not measured on lake ice, but based on a five-year-long data set on Lake Orajärvi in Sodankylä and a sparsely forested site nearby, we can agree with [18] that snow on lake ice is thinner and denser and has less SWE and fewer layers than that on surrounding land areas. A constant density value of 0.270 g/cm^3 was used for snow on lakes. Snow grain size or stratigraphy information was not available, and a one-layer consideration with constant grain size was used in the simulations.

Histograms of the snow course and lake ice measurements are presented in Fig. 7.

2) Sodankylä Area: Distributed measurements of SD, density, and SWE were performed along the flight lines. SD was measured every 100 m, and SWE and density were measured every 500 m. Three values of SD were recorded at each point. The SWE measurements were used to find the mean density for each land cover class, and the SWE used in the simulations was calculated from the mean density and the distributed SD measurements [42]. The statistics of the distributed *in situ* measurements are shown in Fig. 8. The *in situ* measurements were performed for two days: on the flight day and two days earlier. Both of these were considered to be applicable as input information for simulations, since weather and snow conditions did not change significantly during this period.

In addition, on both days, snow pits were measured in five locations: two in forested sites, two on open wetland, and one on lake ice. A snow pit measurement includes profiles of snow temperature, grain size, snow layers, and density, and bulk values of SWE, density, and depth. Visual snow grain size (maximum extent of a typical grain in each layer) was measured by comparing snow grains to a 1-mm grid. The measurement procedures follow those suggested in [43]. A layer-thickness-weighted mean grain size was calculated for each measured snow pit. Then, a mean of all pits on each land cover type was calculated, resulting in grain sizes of 1.57 mm for forest, 1.24 mm for open wetland, and 1.26 mm for lakes.

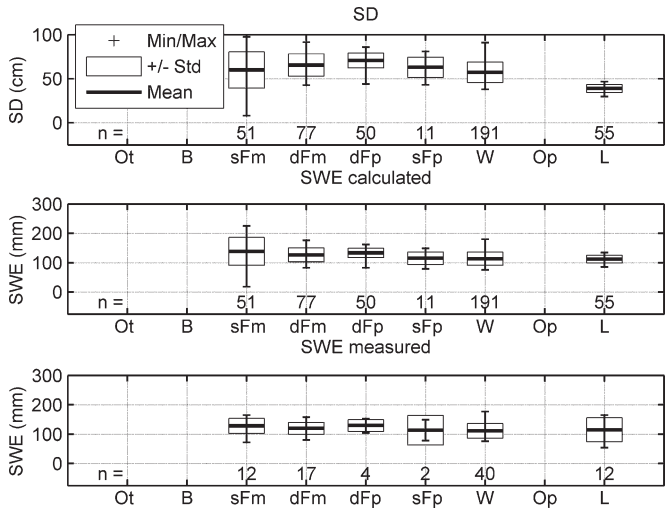

Fig. 8. Statistics of the snow parameters measured in different land cover classes in the Sodankylä area; (top) SD, (middle) SWE calculated from SD and land-cover-dependent density variations, and (bottom) SWE measured directly using a snow scale. See definitions of land cover classes in Section III-C.

Also, ice thickness and layers were measured on Lake Orajärvi on the flight day. The measurement was identical to those of the transfer flight *in situ* data set.

IV. Transfer Flight Simulation Results

A. Airborne Measurements and Simulations

The airborne measurements were used to examine the accuracy of the HUT snow emission model for homogeneous footprints and to find values for the grain size and roughness parameters, for which there were no measurement data available.

For each simulated flight transect, snow conditions were considered to be homogeneous for each land cover type. This simplification was required as no information on the spatial distribution of snow cover on the flight track or in the satellite grid cells was available for these sites; the snow course measurements only gave the typical conditions per land cover on the

surrounding area. Moreover, airborne observations over clearly heterogeneous scenes within the field of view of the instrument were discarded (e.g., shorelines). Each chosen transect had homogeneous land cover on an area clearly larger than the radiometer footprint size. Since the *in situ* snow data were classified into categories defined in Section III-C1, only four land cover categories could be simulated: forest, open area, wetland, and lake.

In the simulations of airborne measurements of the forested areas, every radiometer footprint was simulated separately with the average snow conditions but the forest stem volume of that footprint. This is needed since the forest transmissivity model used [29] is not linear. Thus, the number of forested areas examined is limited to 39 areas, where airborne measurement data were available. In addition, wetland snow data were only available from 25 areas due to scarcity of wetlands on some of the chosen areas, particularly in southern Finland.

Since there were no measurement results of snow grain sizes or water/ice, ice/snow, and soil/snow interface roughnesses, simulations with different values for these parameters were calculated in order to obtain realistic best fit values. In addition to the simulations, results of qualitative observations of ice surface roughness on Lake Orajärvi and a wetland area in Sodankylä were used. The observations indicated that, on lakes, the water/ice interface is very smooth in comparison to ice/snow interface due to slushing events and the formation of white ice over black ice (from snow and slush). However, on wetlands, the ice/snow interface might be smoother than the water/ice interface due to vegetation and soil beneath the ice. The roughness values were chosen to reflect these observations.

First, the grain size value that minimizes the sum of the rms simulation error at 36.5-GHz channels was chosen. Then, the roughness values that minimize the sum of the rms simulation errors of all the six simulated channels for the selected transects (42 lakes, 39 forests, 14 open areas, and 7 wetlands) were chosen. A contour map of the rms error with an optimum grain size of 1.5 mm for lakes is shown in Fig. 9. Based on this and similar maps for forests, open areas, and wetlands, the following values were chosen: grain sizes of 1.5 mm on lakes, 0.7 mm in forests, and 1.1 mm in open areas and wetlands; roughness values of water/ice interface of 1.5 mm on lakes and 3.0 mm in wetlands; roughness of ice/snow interface of 6 mm on lakes and in wetlands; and roughness values of soil/snow interface of 1.0 mm in open areas and 3.0 mm in forests.

In the case of Sodankylä, the measured grain size values were used instead of the optimized values. The grain size optimization, using the roughness values optimized with the transfer flight data, gives values of 1.3 mm for lakes, 0.8 mm for dense forests (dFp and dFm, separately), 1.1 mm for sparse forests (sFm), and 1.2 mm for wetlands. The values for lakes and wetlands correspond well with the measured values (1.26 and 1.24 mm, respectively), while the measured value in forest was much larger (1.57 mm) than the optimized values. This suggests that, on vegetation-free areas, the optimized and measured grain sizes agree, while in forests, the effect of vegetation might not be adequately simulated, and this is compensated with the smaller optimized grain size.

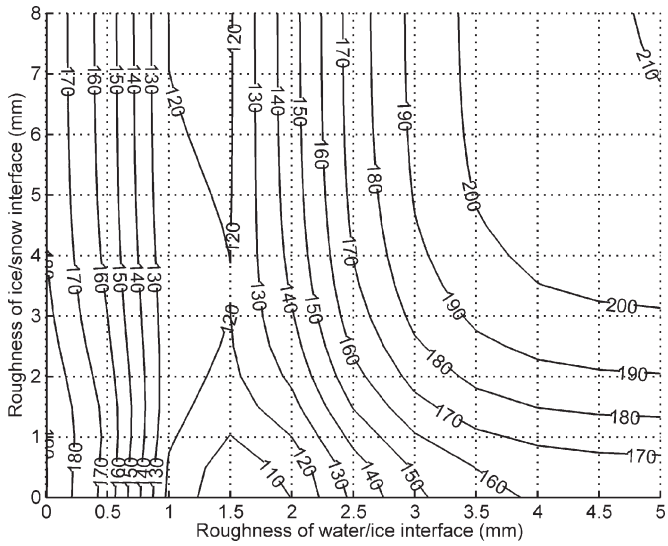

Fig. 9. Contour map of the sum of simulation errors against the HUTRAD measurements of the 42 lake transects on the transfer flights. The snow grain size is set to 1.5 mm. The minimum of the simulation error is found when the roughness of water/ice interface is 1.5 mm and the roughness of ice/snow interface is 0 mm or larger than 4 mm.

Next, the bottom-of-atmosphere brightness temperature (i.e., emitted brightness temperature without the effects of atmosphere) for lakes, forests, open areas, and wetlands was simulated for the chosen areas. The simulation results at 0–40 GHz are shown in Fig. 10 with mean value and standard deviation of airborne measurements. The best agreement between simulations and measurements is at 36.5 GHz, since the grain size was chosen to minimize the error on this frequency. Simulation bias, rms error, and unbiased rms error are shown in Table II.

B. Satellite-Scale Measurements and Simulations

The satellite-scale top-of-atmosphere (TOA) simulations included heterogeneous scenes matching the approximate size of AMSR-E L2A grid cells. The lake coverage of the grid cells was 2%–38%, forest coverage 32%–84%, and wetland coverage 0.4%–18%. The mixed land cover was considered by calculating the total brightness temperature $T_B^{\rm tot}$ from

$$T_B^{\rm tot} = \sum_{\mu=1}^{M} \beta_\mu T_{B,\mu} \tag{2}$$

where β_μ is the fractional (zero to one) coverage, $T_{B,\mu}$ is the brightness temperature originating from the land cover type μ, and $\sum_{\mu=1}^{M} \beta_\mu = 1$. The fractional coverage of forests (β_f), lakes and rivers (β_l), and wetlands (β_w) were determined from CLC2006, and five separate cases were modeled.

1) Lakes and wetlands omitted: The field of view is described by forests (β_f) and open areas $(1 - \beta_f)$.
2) Lake coverage included: The field of view is described by forests (β_f), lakes (β_l), and open areas $(1 - \beta_f - \beta_w)$. However, the snow conditions are considered identical in open areas and on lake ice (i.e., *in situ* data of open areas were used).

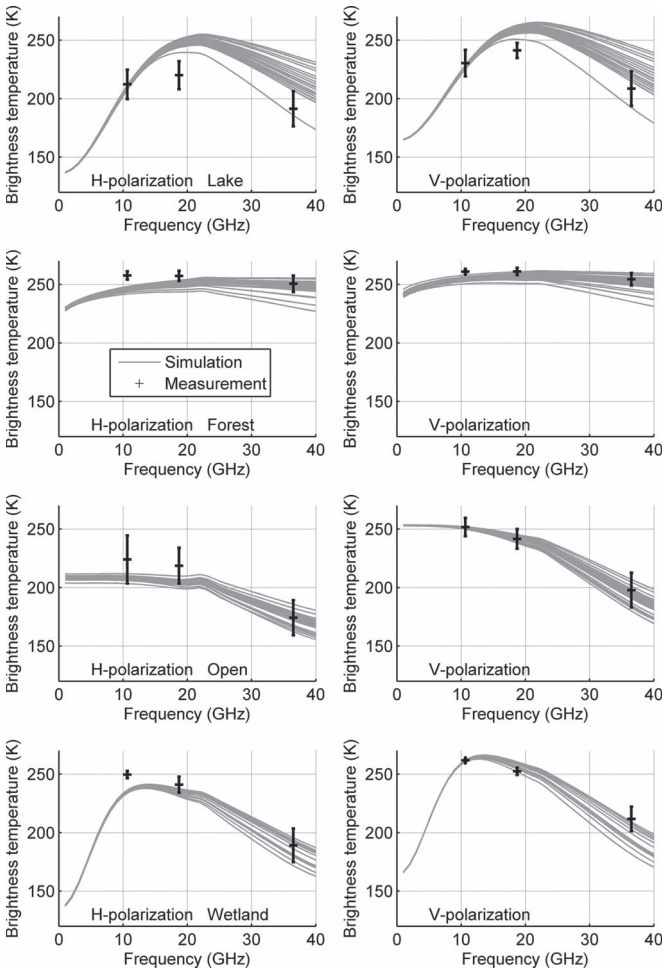

Fig. 10. Airborne simulation results using the optimized roughness and grain size values as a function of frequency for four land cover types: (Top) Lake ice, (second) forest, (third) open area, and (bottom) wetland against the HUTRAD measurements. A total of 42 individual test sites (39 for forest and 25 for wetland) was simulated. The measurement mean values of the 42 lakes, 39 forested areas, 14 open areas, and 7 wetlands indicated; the error bars depict the standard deviation of the measured values.

3) Lake snow data included: The field of view is described as in case 2. In addition, the differing snow conditions on lakes are taken into account.
4) Wetlands included: The field of view is described by forests (β_f), lakes (β_l), wetlands (β_w), and open areas ($1-\beta_f-\beta_l-\beta_w$). Snow conditions on wetlands are identical to those on open areas.
5) Wetland snow data included: The field of view is described as in case 4. In addition, the differing snow conditions on both lakes and wetlands are taken into account.

Cases 2 and 3, as well as 4 and 5, are separated to find out the effect of different backgrounds (water and ice versus ground) and different snow conditions. Due to classification of the snow data (see Section III-C1), only these land cover types (forest, open area, lake, and wetland) were considered, and the rest were simulated as open area. This assumption is reasonable since the combined coverage of all the other land cover types was, on average, 6%. Also, modeling of, e.g., urban area, which forms the major part of the other land cover classes, is out of the scope of this paper. The forested area was further divided into sparse and dense forests; the same snow parameters were used for both of these, but separate stem volumes (averages of the grid cell area) were used.

The relative simulation errors due to lake coverage in the grid cell (i.e., the difference of simulated and measured brightness temperatures is set to 0 K when the lake coverage is 0%) of the first three cases are plotted in Fig. 11. At 36.5 GHz, the simulation error decreases when the lake coverage is included and, again, when lake snow data are included. As a result, the increase of error due to increase of lake coverage in the satellite data grid cell, apparent in simulations without lake data, disappears. At 18.7 GHz, the effect of lake data is ambiguous; the underestimation of brightness temperature changes to overestimation. At 10.65 GHz, the relative simulation error increases when the lake coverage is included, but the inclusion of snow data decreases the error. Both the lake coverage and the snow data affect the simulation error, and their contributions depend on the frequency and polarization.

The effect of wetlands is depicted in Fig. 12. At 36.5-GHz H-pol, the relative error increases from the inclusion of wetlands, but at the rest of the investigated channels, the inclusion of wetland coverage and snow data decreases simulation error. The main contribution is from wetland coverage, not the differing snow conditions.

Above, the relative simulation errors were examined. The change in absolute simulation error (i.e., no scaling at 0% coverage included) between cases 1 and 3 is shown in Fig. 13. The error decreases in 52%/100% of the 42 areas at 18.7 GHz (H/V) and in 62%/88% of the areas at 36.5-GHz channels. However, at 10.65 GHz, the simulation results mainly deteriorate from the inclusion of lakes. The change between cases 1 and 4 is shown in Fig. 14. Here, the error decreases in 52%/100% of the 42 areas at 18.7 GHz and 57%/88% at 36.5 GHz. Simulation bias, rms error, and unbiased rms error are shown in Table III. At 18.7 and 36.5 GHz, case 4 (lake coverage and snow conditions, and wetland coverage included) gives the smallest biases and rms errors at vertical polarization. At horizontal polarization, cases 3 (lake coverage and snow conditions) and 5 (lake and wetland coverage and snow conditions) give the smallest errors.

The channel differences 18.7–36.5 GHz also improve from the inclusion of lakes and wetlands. At H-pol, cases 3–5 have smaller rms error than cases 1–2 (3.4–4.5 K compared to 4.5–5.9 K). At V-pol, the results are similar (rms errors of 3.7–5.1 K and 5.7–6.1 K, respectively).

V. Sodankylä Area

The aim of this section is to study the variability of brightness temperature and snow and ice conditions on a smaller scale and to investigate the effect of more detailed *in situ* data on the simulation results. We also reconstruct a satellite field of view using the flight data and a land cover map and compare the results to AMSR-E measurements for instrument intercalibration.

A land cover map of the Sodankylä area with the flight routes and *in situ* measurement sites is shown in Fig. 6. Also, the AMSR-E grid cell center points are marked on the map. The

TABLE II
SIMULATION BIAS, RMS ERROR, AND UNBIASED RMS ERROR FOR THE 42 LAKE, 39 FOREST, 14 OPEN AREA, AND 7 WETLAND TRANSECTS OF THE AIRBORNE TRANSFER FLIGHTS. THE OPTIMAL VALUES FOR SNOW GRAIN SIZE AND INTERFACE ROUGHNESS PARAMETERS WERE USED IN THE SIMULATIONS

Channel	Bias (K)				RMS error (K)				Unbiased RMS error (K)			
(GHz)	Lake	Forest	Open	Wetland	Lake	Forest	Open	Wetland	Lake	Forest	Open	Wetland
10.65 H	-5.5	-11.1	8.1	-11.6	13.2	11.8	21.7	11.7	12.0	3.8	20.1	0.5
18.7 H	24.3	-6.4	8.8	13.7	26.2	7.9	18.1	14.0	9.8	4.6	15.8	3.2
36.5 H	23.2	-1.4	12.0	12.8	28.3	7.7	21.8	13.5	16.3	7.5	18.2	4.2
18.7 H-36.5 H	-2.4	-5.0	-3.2	0.8	20.3	6.9	9.2	4.4	20.2	4.8	8.7	4.3
10.65 V	-4.5	-6.1	-7.7	-16.2	11.7	6.5	11.3	16.3	10.8	2.4	8.4	1.8
18.7 V	16.4	-3.9	-3.6	9.1	17.4	5.1	10.3	9.2	5.8	3.2	9.7	1.2
36.5 V	13.8	-1.8	-4.9	-7.4	23.0	6.3	19.3	9.0	18.4	6.1	18.7	5.1
18.7 V-36.5 V	2.6	-2.1	1.4	16.5	17.2	4.9	11.1	17.1	17.0	4.5	11.0	4.5

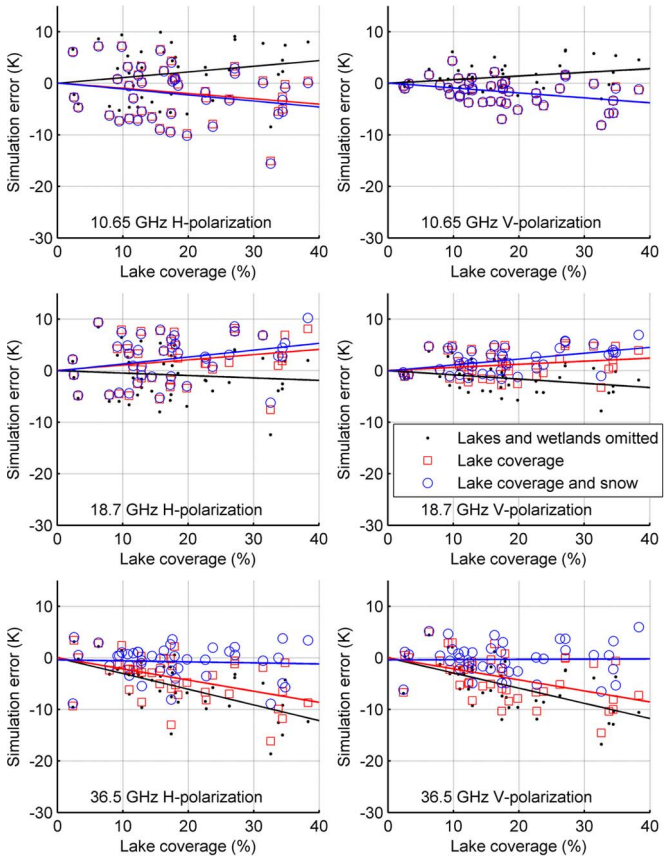

Fig. 11. Simulation error (difference of simulated and measured values) of the satellite-scale simulations against the AMSR-E observations over the 42 selected areas for (top) 10.65-, (middle) 18.7-, and (bottom) 36.5-GHz (left) horizontal and (right) vertical polarizations. The change of error relative to lake coverage is shown (i.e., error set to 0 K when the lake coverage is 0%). The simulation results are shown for the following: 1) (Black dot) Omission of lakes and wetlands; 2) (red square) lake coverage included but snow cover considered uniform; and 3) (o) snow conditions considered different for dry terrain and lake ice.

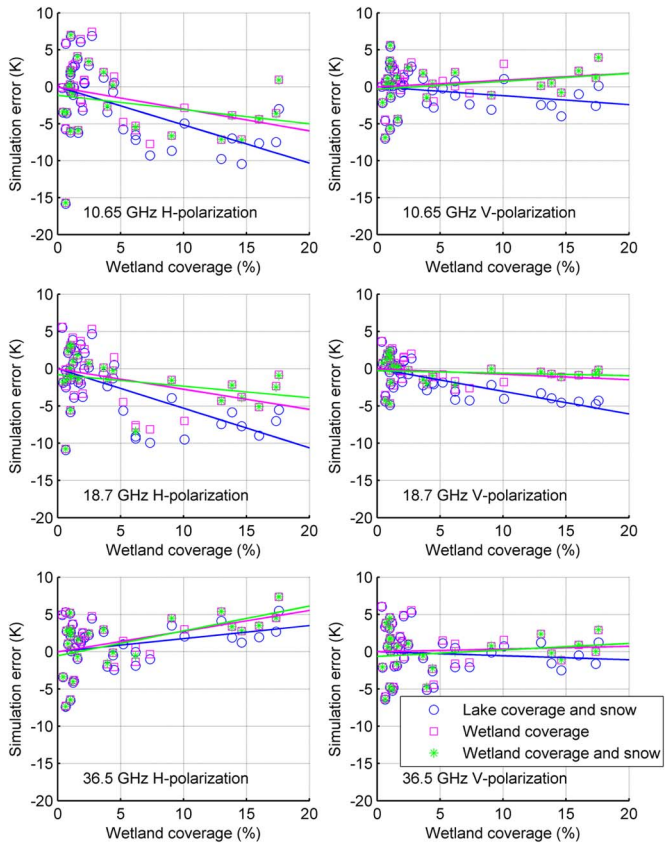

Fig. 12. Simulation error (difference of simulated and measured values) of satellite-scale simulations against AMSR-E observations over the 25 areas with wetland snow data for (top) 10.65-, (middle) 18.7-, and (bottom) 36.5-GHz (left) horizontal and (right) vertical polarizations. The change of error relative to wetland coverage is shown (i.e., error set to 0 K when the wetland coverage is 0%). Simulations are shown for the following: 1) (Blue o) Lake coverage and snow conditions considered different for dry terrain and wetlands; 2) (magenta square) in addition to previous, wetland coverage included but snow conditions considered uniform over wetland and open area; and 3) (green *) snow conditions considered different for wetland areas.

simulated area covers five AMSR-E grid cells. Five of the land cover classes are found from the flight transects: sFm (13% of the area covered by the 5 AMSR-E grid cells), dFm (41%), dFp (14%), W (20%), and L (5%). *In situ* measurements were performed also in sFp (3%). No *in situ* or airborne data were available from B, Op, and Ot areas (altogether 4%). These three were not included in the simulations, but the coverages of the other land cover classes were upscaled to fill the entire grid cell.

The *in situ* data set of distributed and point measurements was used to simulate the bottom-of-atmosphere brightness temperature for each land cover class separately. For each class, snow was considered as one homogeneous layer with SD, SWE, and grain size from average values measured in that land cover class. The mean grain size measured in forests was used for all four forest classes. For lake ice thickness, the average of the three point measurements was used. Roughness values and other constant parameters were similar to the transfer flight simulations. For comparison with the airborne measurements, every HUTRAD footprint was simulated separately with the stem volume of the footprint and average snow conditions of

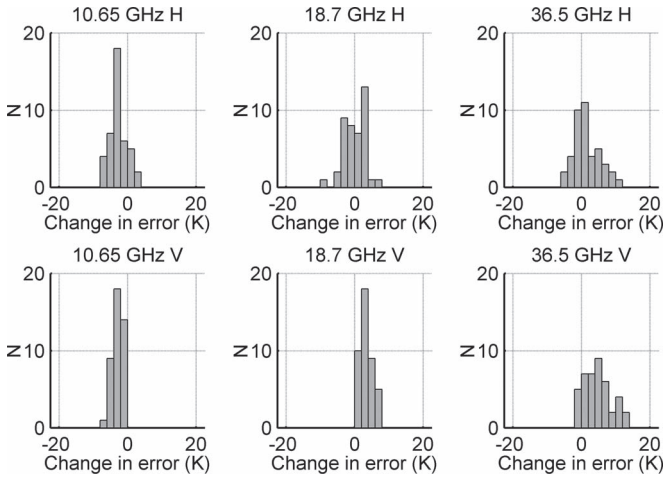

Fig. 13. Change in satellite-scale simulation error between case 1 (lakes and wetlands omitted) and case 3 (lake coverage and differing snow conditions included) for the 42 simulated areas. A positive change value indicates that the simulation result is closer to AMSR-E measurement when the lake coverage and snow conditions are included than when they are omitted.

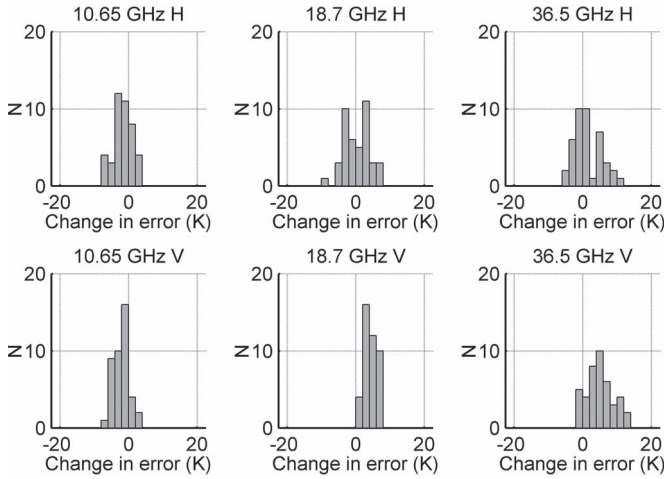

Fig. 14. Change in satellite-scale simulation error between case 1 (lakes and wetlands omitted) and case 4 (lake coverage and snow conditions and wetland coverage included) for the 42 simulated areas. A positive change value indicates that the simulation result is closer to AMSR-E measurement when wetlands and lakes are included than when they are omitted.

the forest class. In the satellite-scale measurements, the mean stem volumes of each forest class in the grid cell were used.

The simulation results of the individual land cover classes are compared to the airborne measurements in Fig. 15.

Next, the TOA brightness temperatures of the five AMSR-E grid cells were simulated using all the available *in situ* data for individual land cover classes. In addition to this "best case" scenario, cases 1–3 and 5 that were simulated from the transfer flight data were also simulated but using the distributed measurements of SWE and SD and grain sizes determined from the snow pit measurements. Case 4 could not be simulated since there were no measurement data from open areas. In other cases, the snow data from wetlands were used instead of the open area data. The optimum roughness values determined from the transfer flight data set were used.

The TOA brightness temperature was also aggregated from the mean of airborne measurements over the individual land cover classes. The airborne data collected over the Sodankylä site were used to assess the typical brightness temperature for a given class of land cover directly; then, in order to reconstruct the brightness temperature of a whole satellite scene, the measured values were aggregated by weighing these with the fraction of the land cover class in question using (2). A statistical atmospheric correction was applied to the airborne measurements using equations from the HUT snow emission model

$$T_{\mathrm{TOA}} = \mathrm{Tr}_{\mathrm{atm}} \cdot t_{\mathrm{BOA}} + T_{\mathrm{up}'} \tag{3}$$

where t_{TOA} is the TOA brightness temperature of a single land cover class, t_{BOA} is the bottom-of-atmosphere (airborne) measurement, and $\mathrm{Tr}_{\mathrm{atm}}$ and T_{up} are the atmospheric transmissivity and upwelling radiation, respectively [38]–[40]. The area covered by the five AMSR-E grid cells was thus aggregated for each channel. The same atmospheric correction was also used in the satellite-scale simulations.

Both the forward model simulations and the aggregated satellite scenes were compared to actual AMSR-E measurements. The results in Fig. 16 indicate good agreement between HUTRAD and AMSR-E observations. The difference is 0–4 K, depending on the channel. The remaining differences can be attributed to, e.g., inadequate modeling of the HUTRAD footprint coverage and the land cover classes without airborne observations. However, the "best case" simulation underestimates the brightness temperature by 4–21 K. If a grain size of 1.0 mm is used for forests, the simulation results are on the same level (difference of 1–6 K) with AMSR-E measurements. Simulation biases, rms errors, and unbiased rms errors are shown in Table IV for the different simulation setups described in Section IV-B. The four cases with the less detailed input data set show even larger underestimation. The "best case" scenario gives the smallest biases and rms errors, and case number 5 (lake and wetland coverages and snow conditions included) gives the second smallest errors.

VI. Discussion

The simulations and the airborne measurements of the transfer flights show that the brightness temperature as a function of frequency is quite different for forests than for the other simulated land covers. In forests, the main contribution to brightness temperature is from the vegetation. Thus, results for lakes, wetlands, and open areas give more information on the behavior of the snow model itself, while simulations of forested areas show the behavior of the applied vegetation model. Differences between lakes, wetlands, and open land areas are apparent at frequencies below 20 GHz, where the brightness temperature of lakes and wetlands decreases dramatically. This is the effect of the ice and water below snow, where the low microwave frequencies are able to reach.

The collected airborne data set indicates a large variability of brightness temperature over different snow-covered lakes (see Fig. 4). The difference of maximum and minimum measured average brightness temperatures of lakes was 26–61 K, depending on the channel. The differences between lakes were

TABLE III
SIMULATION BIAS, RMS ERROR, AND UNBIASED RMS ERROR FOR THE 42 GRID CELLS OF THE SATELLITE-SCALE SIMULATIONS ON TRANSFER FLIGHTS FOR THE FIVE SIMULATED CASES: (1) LAKES AND WETLANDS OMITTED, (2) LAKE COVERAGE INCLUDED, BUT SNOW CONSIDERED UNIFORM, (3) DIFFERING SNOW CONDITIONS ON LAKE ICE INCLUDED, (4) WETLAND COVERAGE INCLUDED BUT SNOW CONSIDERED UNIFORM, AND (5) DIFFERING SNOW CONDITIONS IN WETLANDS INCLUDED

Channel	Bias (K)					RMS error (K)					Unbiased RMS error (K)				
(GHz)	1	2	3	4	5	1	2	3	4	5	1	2	3	4	5
10.65 H	-3.2	-6.9	-7.2	-6.2	-7.1	6.1	8.6	8.8	7.8	8.5	5.2	5.1	5.1	4.6	4.7
18.7 H	-2.1	0.6	1.1	2.2	1.8	4.9	4.5	4.5	4.3	3.7	4.5	4.5	4.4	3.7	3.3
36.5 H	-3.6	-2.0	1.1	1.6	1.6	5.9	4.8	3.4	3.8	3.9	4.7	4.3	3.2	3.4	3.6
18.7 H-36.5 H	1.4	2.6	-0.1	0.6	0.2	5.0	5.7	4.7	4.1	3.9	4.7	5.0	4.6	4.1	3.9
10.65 V	-6.8	-9.7	-9.7	-8.8	-8.9	7.3	10.1	10.0	9.2	9.4	2.6	2.6	2.5	2.5	2.8
18.7 V	-7.7	-5.1	-4.2	-3.2	-3.3	8.1	5.7	4.8	3.7	3.7	2.6	2.5	2.3	1.8	1.7
36.5 V	-9.0	-7.5	-4.0	-3.6	-3.9	10.1	8.7	5.1	4.8	4.8	4.6	4.3	3.1	3.1	2.8
18.7 V-36.5 V	1.3	2.4	-0.2	0.4	0.6	3.2	4.1	2.6	2.3	2.2	2.9	3.4	2.5	2.3	2.2

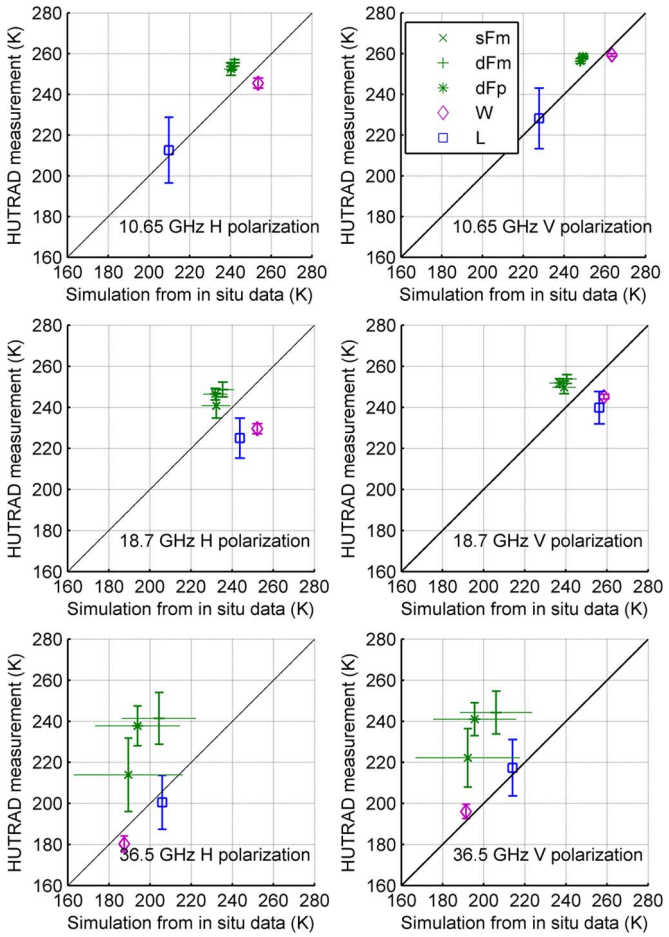

Fig. 15. Airborne measurements and simulations from Sodankylä area *in situ* data for different land cover classes at (top) 10.65-, (middle) 18.7-, and (bottom) 36.5-GHz (left) horizontal and (right) vertical polarizations. Each individual HUTRAD footprint has been simulated with mean *in situ* data of the land cover class and the forest stem volume of that footprint. For simulation results, mean simulated value ± standard deviation is shown. For HUTRAD data, mean measured value ± standard deviation is shown.

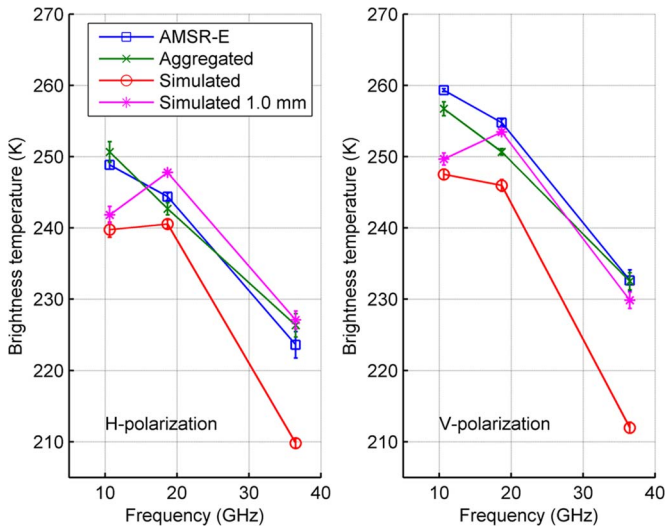

Fig. 16. (Blue square) AMSR-E observations, (green ×) aggregated satellite scenes from airborne measurements, (red o) simulation results, and (magenta *) simulation results with a grain size of 1.0 mm for forested areas for the Sodankylä area. The mean values of the five AMSR-E grid cells with error bars of standard deviation are shown for (left) horizontal and (right) vertical polarizations.

much smaller in the simulations, about 4 K at 10.65 GHz, 12 K at 18.7 GHz, and 51–53 K at 36.5 GHz. Large variations in brightness temperature were apparent also over individual lakes; the difference of maximum and minimum measured brightness temperatures of Lake Orajärvi was 32–62 K (Fig. 5). The measured variability was thus not apparent in the simulation results, particularly for the lower frequencies investigated. This suggests either of the following: 1) The input data set was not detailed enough to represent the physical variations between lake sites, or 2) the model itself underestimates the effect of variability in the ice and snow layers. Similar findings were reported in [26]. One parameter missing from our *in situ* data set is the possible appearance of water over lake ice due to slushing events. Our simulations assumed that the snow on ice is dry, since air temperature was clearly below 0 °C. While other snow parameters have little effect at the lower microwave frequencies, they are very sensitive to liquid water. There are some notes in the distributed measurement data about water below snow in some places on Lake Orajärvi, while at the snow pit site, the snowpack was completely dry. Patches of wet snow might explain the high variation in the measured brightness temperature, even though the simulations for Lake Orajärvi matched the average measured brightness temperature (Fig. 15) quite well with the assumption of a dry snowpack.

The large variation might be due to both natural and anthropogenic effects. During winter, the lake ice slowly sinks, causing water to flood over ice. Also, wind-driven dunes may cause large variation in local SD and density. On the other hand, snowmobiling and other travels on lake ice, as well as drilling holes for ice fishing, may similarly affect the structure of snow.

TABLE IV
SIMULATION BIAS, RMS ERROR, AND UNBIASED RMS ERROR FOR THE FIVE SATELLITE-SCALE SIMULATIONS OVER THE SODANKYLÄ AREA. "BEST" REFERS TO THE "BEST CASE SCENARIO" WITH ALL THE AVAILABLE *IN SITU* DATA, WHILE NUMBERS 1–5 REFER TO THE SCENARIOS SIMULATED ALSO FOR THE TRANSFER FLIGHTS: (1) LAKES AND WETLANDS OMITTED, (2) LAKE COVERAGE INCLUDED, BUT SNOW CONSIDERED UNIFORM (DATA FOR WETLANDS USED), (3) DIFFERING SNOW CONDITIONS ON LAKE ICE INCLUDED, AND (5) WETLAND COVERAGE AND SNOW DATA INCLUDED. SINCE NO MEASUREMENT DATA OF OPEN AREAS WAS AVAILABLE, IT WAS NOT POSSIBLE TO SEPARATE CASES 4 (LAKE COVERAGE AND SNOW CONDITIONS, AND WETLAND COVERAGE INCLUDED) AND 5

Channel	Bias (K)					RMS error (K)					Unbiased RMS error (K)				
(GHz)	Best	1	2	3	5	Best	1	2	3	5	Best	1	2	3	5
10.65 H	-5.6	-9.6	-10.5	-10.5	-6.1	5.6	9.6	10.5	10.6	6.1	0.6	0.6	0.8	0.8	0.6
18.7 H	-3.8	-10.5	-9.7	-9.7	-4.4	3.9	10.5	9.7	9.7	4.5	0.8	0.6	0.7	0.7	0.6
36.5 H	-13.8	-18.1	-17.7	-16.9	-14.8	14.0	18.2	17.8	17.1	14.9	2.2	1.9	2.0	2.1	2.0
18.7 H-36.5 H	-24.2	-26.0	-24.8	-24.7	-23.9	24.2	26.0	24.8	24.7	24.0	1.3	1.5	1.3	1.3	1.5
10.65 V	-7.8	-11.9	-12.5	-12.5	-8.2	7.8	11.9	12.6	12.5	8.2	0.6	0.5	0.8	0.8	0.7
18.7 V	-8.8	-14.9	-14.2	-14.0	-9.3	8.8	14.9	14.2	14.0	9.3	0.9	0.5	0.5	0.6	0.7
36.5 V	-20.7	-24.8	-24.4	-23.5	-21.5	20.8	24.8	24.4	23.5	21.6	1.9	1.6	1.6	1.8	1.7
18.7 V-36.5 V	11.9	9.8	10.2	9.5	12.3	12.0	9.9	10.2	9.6	12.4	1.4	1.2	1.2	1.2	1.4

In the satellite observations, the variability of snow conditions is even more prominent than that in the airborne observations due to, e.g., the effect of variable land cover and vegetation. Despite this, our results show that the accuracy of the satellite-scale simulation is increased at 18.7 and 36.5 GHz and the channel differences when 1) the water/ice/snow layer structure and coverage of lakes and wetlands and 2) the differing snow conditions on lake ice and wetland are taken into account in the simulation. The increase of simulation accuracy results in more accurate SWE values from the inversion of satellite measurements, as was shown in [28]. The fact that, contrary to the Sodankylä area, the transfer flight simulations did not significantly improve from inclusion of wetland snow data may indicate the quality of *in situ* data. Due to scarcity of wetlands on many of the selected areas, there were no *in situ* measurements of wetlands on 17 of the 42 selected areas. In addition, some of the wetlands may be drier than the ones in the Sodankylä area data set, and thus, the assumption of a lakelike layer structure may not be valid for all of the wetlands in the transfer flight data set.

The measurements of the Sodankylä area (Fig. 5) show considerable variability in both the microwave signature and snow conditions 1) between land cover classes and 2) within each class. The *in situ* input data to Sodankylä area simulations were much more detailed than the *in situ* data on transfer flights: There were numerous SD and SWE measurements for several land cover classes, and grain sizes for different classes were determined from a total of ten snow pits. This reflects in the simulation results for individual land cover classes (Fig. 15), which show good agreement between airborne measurements and simulations from *in situ* data, except at 36.5 GHz for forests. An underestimation of 4–21 K is also seen in the satellite-scale simulations (Fig. 16). However, if a snow grain size of 1.0 mm were used for forests instead of the 1.57 mm derived from the snow pit data, the difference of simulations and AMSR-E measurements decreases to 1–6 K. This is in accordance with previous studies [44]. In addition, the four cases simulated with less detailed *in situ* data (similar to transfer flight simulations) show even larger underestimation. The difference of AMSR-E observations and the brightness temperature aggregated from HUTRAD measurements over individual land cover classes is < 4 K. Based on this, the HUTRAD measurements are a good reference data set for the AMSR-E observations and the simulations.

VII. CONCLUSION

A multiple-layer adaptation of the HUT snow emission model has been used to simulate the emitted brightness temperature of individual AMSR-E grid cells containing mixed land cover, particularly snow- and ice-covered lakes and wetlands. The rms errors of the 42 simulated grid cells were 4–5 K at 18.7- and 36.5-GHz channels, 8–9 K at 10.65-GHz channels, and 2–4 K at 18.65–36.5-GHz channel differences. When applied to the satellite scale, including the effect of subgrid-scale water bodies on the total emitted brightness temperature was shown to improve the model estimates when compared to the observations at 18.7 and 36.5 GHz. However, on the lowest investigated frequency, i.e., 10.65 GHz, simulation results deteriorated as the model overestimated the decrease of brightness temperature caused by the lake cover. This confirms earlier studies (e.g., [26]) that the applied relatively simple forward model may not adequately represent the varying conditions over natural lakes. The inclusion of lake coverage and snow conditions on lakes improved the simulation accuracy at 18.65 and 36.5 GHz and the channel difference 18.7–36.5 GHz. The inclusion of wetland coverage further improved the accuracy, particularly at the lower simulated frequencies.

Airborne observations over the same 42 areas were used to find realistic best fit values for the snow grain size and the layer interface roughnesses. Simulations were driven using *in situ* information of the average snow and ice conditions for a given area. In comparison with the airborne data, using the optimal parameters, the model simulated the measured brightness temperature of lakes with an rms error of 12–28 K, depending on the channel, and wetlands with an rms error of 9–16 K.

ACKNOWLEDGMENT

The Finnish Environment Institute provided the *in situ* data for the transfer flights. The Finnish Forest Research Institute provided the forest stem volume data. The authors would like to thank Mr. J. Cohen for processing the CLC2006 and stem volume data. The authors would also like to thank the personnel of the Finnish Meteorological Institute Arctic Research Centre in Sodankylä, Finland, for performing the *in situ* sampling of the Sodankylä area.

REFERENCES

[1] S. J. Metsämäki, S. T. Anttila, M. J. Huttunen, and J. M. Vepsäläinen, "A feasible method for fractional snow cover mapping in boreal zone based on a reflectance model," *Remote Sens. Environ.*, vol. 95, no. 1, pp. 77–95, Mar. 2005.

[2] *Arctic Climate Impact Assessment*. Cambridge, U.K.: Cambridge Univ. Press, 2005, p. 1042. [Online]. Available: http:///www.acia.uaf.edu/

[3] P. Y. Groisman, T. R. Karl, and R. W. Knight, "Observed impact of snow cover on the heat balance and the rise of continental spring temperatures," *Science*, vol. 263, no. 5114, pp. 198–200, Jan. 1994.

[4] P. M. Atkinson and R. E. J. Kelly, "Scaling-up point snow depth data in the U.K. for comparison with SSM/I imagery," *Int. J. Remote Sens.*, vol. 18, no. 2, pp. 437–443, Jan. 1997.

[5] K. F. Künzi, S. Patil, and H. Rott, "Snow cover parameters retrieved from Nimbus-7 Scanning Multichannel Microwave Radiometer (SMMR) data," *IEEE Trans. Geosci. Remote Sens.*, vol. GE-20, no. 4, pp. 452–467, Oct. 1982.

[6] A. Chang, J. Foster, and D. Hall, "Nimbus-7 SMMR derived global snow cover parameters," *Ann. Glaciol.*, vol. 9, pp. 39–44, 1987.

[7] B. Goodison and A. Walker, "Canadian development and use of snow cover information from passive microwave satellite data," in *Passive Microwave Remote Sensig of Land-Atmosphere Interactions*, B. J. Choudhury, Y. H. Kerr, E. G. Njoku, and P. Pampaloni, Eds. Leiden, The Netherlands: VSP International Science Publishers, 1995.

[8] R. E. Kelly, A. T. Chang, L. Tsang, and J. L. Foster, "A prototype AMSR-E global snow area and snow depth algorithm," *IEEE Trans. Geosci. Remote Sens.*, vol. 41, no. 2, pp. 230–242, Feb. 2003.

[9] M. Takala, K. Luojus, J. Pulliainen, C. Derksen, J. Lemmetyinen, J.-P. Kärnä, J. Koskinen, and B. Bojkov, "Estimating northern hemisphere snow water equivalent for climate research through assimilation of space-borne radiometer data and ground-based measurements," *Remote Sens. Environ.*, vol. 115, no. 12, pp. 3517–3529, Dec. 2011.

[10] M. T. Hallikainen and P. A. Jolma, "Retrieval of the water equivalent of snow cover in Finland by satellite microwave radiometry," *IEEE Trans. Geosci. Remote Sens.*, vol. GE-24, no. 6, pp. 855–862, Nov. 1986.

[11] J. Foster, A. Chang, D. Hall, and A. Rango, "Derivation of snow water equivalent in boreal forests using microwave radiometry," *Arctic*, vol. 44, no. 5, pp. 147–152, 1991.

[12] J. Lemmetyinen, C. Derksen, J. Pulliainen, W. Strapp, P. Toose, A. Walker, S. Tauriainen, J. Pihlflyckt, J.-P. Kärnä, and M. Hallikainen, "A comparison of airborne microwave brightness temperatures and snowpack properties across the boreal forests of Finland and Western Canada," *IEEE Trans. Geosci. Remote Sens.*, vol. 47, no. 3, pp. 965–978, Mar. 2009.

[13] C. Derksen, P. Toose, J. Lemmetyinen, J. Pulliainen, A. Langlois, N. Rutter, and M. C. Fuller, "Evaluation of passive microwave brightness temperature simulations and snow water equivalent retrievals through a winter season," *Remote Sens. Environ.*, vol. 117, pp. 236–248, Feb. 2012.

[14] J. L. Foster, C. Sun, J. P. Walker, R. Kelly, A. Chang, J. Dong, and H. Powell, "Quantifying the uncertainty in passive microwave snow water equivalent observations," *Remote Sens. Environ.*, vol. 94, no. 2, pp. 187–203, Jan. 2005.

[15] M. T. Hallikainen, F. T. Ulaby, M. C. Dobson, M. A. El-Rayes, and W. Lil-Kun, "Microwave dielectric behavior of wet soil—Part 1: Empirical models and experimental observations," *IEEE Trans. Geosci. Remote Sens.*, vol. GE-23, no. 1, pp. 25–34, Jan. 1985.

[16] C. Derksen, A. Walker, and B. Goodison, "Evaluation of passive microwave snow water equivalent retrievals across the boreal forest/tundra transition of western Canada," *Remote Sens. Environ.*, vol. 96, no. 3/4, pp. 315–327, Jun. 2005.

[17] A. Rees, C. Derksen, M. English, A. Walker, and C. Duguay, "Uncertainty in snow mass retrievals from satellite passive microwave data in lake-rich high-latitude environments," *Hydrol. Process.*, vol. 20, no. 4, pp. 1019–1022, Mar. 2006.

[18] M. Sturm and G. E. Liston, "The snow cover on lakes of the Arctic Coastal Plain of Alaska, U.S.A.," *J. Glaciol.*, vol. 49, no. 11, pp. 370–380, Jun. 2003.

[19] C. Derksen, P. Toose, A. Rees, L. Wang, M. English, A. Walker, and M. Sturm, "Development of a tundra-specific snow water equivalent retrieval algorithm for satellite passive microwave data," *Remote Sens. Environ.*, vol. 114, no. 8, pp. 1699–1709, Aug. 2010.

[20] J. Pulliainen, "Mapping of snow water equivalent and snow depth in boreal and sub-arctic zones by assimilating space-borne microwave radiometer data and ground-based observations," *Remote Sens. Environ.*, vol. 101, no. 2, pp. 257–269, Mar. 2006.

[21] D. Hall, J. Foster, A. Chang, and A. Rango, "Freshwater ice thickness observations using passive microwave sensors," *IEEE Trans. Geosci. Remote Sens.*, vol. GE-19, no. 4, pp. 189–193, Oct. 1981.

[22] A. Mialon, A. Royer, and M. Fily, "Wetland seasonal dynamics and inter-annual variability over northern high latitudes, derived from microwave satellite data," *J. Geophys. Res., Atmos.*, vol. 110, no. D17, pp. D17102-1–D17102-9, Sep. 2005.

[23] S. Zhang and J. Shi, "A microwave wetland surface emissivity calibration scheme using SCE-UA algorithm and AMSR-E brightness temperature data," *Proc. Environ. Sci.*, vol. 10, pp. 2731–2739, 2011.

[24] J. T. Pulliainen, J. Grandell, and M. T. Hallikainen, "HUT snow emission model and its applicability to snow water equivalent retrieval," *IEEE Trans. Geosci. Remote Sens.*, vol. 37, no. 3, pp. 1378–1390, May 1999.

[25] J. Lemmetyinen, J. Pulliainen, A. Rees, A. Kontu, Y. Qiu, and C. Derksen, "Multiple layer adaptation of HUT snow emission model: Comparison with experimental data," *IEEE Trans. Geosci. Remote Sens.*, vol. 48, no. 7, pp. 2781–2794, Jul. 2010.

[26] G. E. Gunn, C. Duguay, C. Derksen, J. Lemmetyinen, and P. Toose, "Evaluation of the HUT modified snow emission model over lake ice using airborne passive microwave measurements," *Remote Sens. Environ.*, vol. 115, no. 1, pp. 233–244, Jan. 2011.

[27] K. Kang, C. Duguay, J. Lemmetyinen, and Y. Gel, "Estimation of ice thickness on large northern lakes from AMSR-E brightness temperature measurements," *Remote Sens. Environ.*, to be published.

[28] J. Lemmetyinen, A. Kontu, J.-P. Kärnä, J. Vehviläinen, M. Takala, and J. Pulliainen, "Correcting for the influence of frozen lakes in satellite microwae radiometer observations through application of a microwave emission model," *Remote Sens. Environ.*, vol. 115, no. 12, pp. 3695–3706, Dec. 2011.

[29] N. Kruopis, J. Praks, A. N. Arslan, H. M. Alasalmi, J. T. Koskinen, and M. T. Hallikainen, "Passive microwave measurements of snow-covered forest areas in EMAC'95," *IEEE Trans. Geosci. Remote Sens.*, vol. 37, no. 5, pp. 2699–2705, Nov. 1999.

[30] U. Wegmüller and C. Mätzler, "Rough bare soil reflectivity model," *IEEE Trans. Geosci. Remote Sens.*, vol. 37, no. 3, pp. 1391–1395, May 1999.

[31] J. Pulliainen and M. T. Hallikainen, "Retrieval of regional snow water equivalent from space-borne passive microwave observations," *Remote Sens. Environ.*, vol. 75, no. 1, pp. 76–85, Jan. 2001.

[32] M. Kazumori, Q. Liu, R. Treadon, and J. C. Derber, "Impact study of AMSR-E radiances in the NCEP global data assimilation system," *Mon. Weather Rev.*, vol. 136, no. 2, pp. 541–559, Feb. 2008.

[33] F. J. Wentz, "A two-scale scattering model for foam-free sea microwave brightness temperatures," *J. Geophys. Res.*, vol. 80, no. 24, pp. 3441–3446, Aug. 1975.

[34] T. Mo and T. Schmugge, "Calculations of microwave brightness temperature for rough soil surfaces: Bare field," *IEEE Trans. Geosci. Remote Sens.*, vol. GE-25, no. 1, pp. 47–54, Jan. 1987.

[35] W. M. Drennan, P. K. Taylor, and M. J. Yelland, "Parameterizing the sea surface roughness," *J. Phys. Oceanogr.*, vol. 35, no. 5, pp. 835–848, May 2005.

[36] B. J. Choudhury, T. J. Schmugge, R. W. Newton, and A. Chang, "Effect of surface roughness on the microwave emission from soils," *J. Geophys. Res.*, vol. 84, no. C9, pp. 5699–5706, Sep. 1979.

[37] K. W. Knowles, M. H. Savoie, R. L. Armstrong, and M. J. Brodzik, *AMSR-E L2A Global Swath Spatially-Resampled Brightness Temperatures*. Boulder, CO, USA: National Snow and Ice Data Center, Digital media.

[38] J. Aschbacher, "Land surface studies and atmospheric effects by satellite microwave radiometry," Ph.D. dissertation, Institute for Meteorology and Geophysics, Univ. of Innsbruck, Innsbruck, Austria, 1989.

[39] E. Salonen, S. Karhu, P. Jokela, S. Uppala, S. Sarkkula, and H. Aulamo, "Study of propagation phenomena for low availabilities," ESA, Paris, France, Final Rep. under ESTEC Contract 8025/88/NL/F'R, pp. 193–244, 1990.

[40] J. Pulliainen, J.-P. Kärnä, and M. Hallikainen, "Development of geophysical retrieval algorithms for the MIMR," *IEEE Trans. Geosci. Remote Sens.*, vol. 31, no. 1, pp. 268–277, Jan. 1993.

[41] M. Törmä, M. Haakana, S. Hatunen, P. Härmä, M. Kallio, M. Katila, T. Kiiski, K. Mäkisara, J. Peräsaari, H. Piepponen, R. Repo, R. Teiniranta, and E. Tomppo, "Finnish Corine 2006-project: Determining changes in land cover in Finland between 2000 and 2006," in *Proc. SPIE Remote Sens. Environ. Monit., GIS Appl. Geol. VIII*, 2008, vol. 7110, p. 71100V.

[42] C. Derksen, A. E. Walker, B. E. Goodison, and J. W. Strapp, "Integrating in situ and multiscale passive microwave data for estimation of subgrid scale snow water equivalent distribution and variability," *IEEE Trans. Geosci. Remote Sens.*, vol. 43, no. 5, pp. 960–972, May 2005.

[43] C. Fierz, R. L. Armstrong, Y. Durand, P. Etchevers, E. Greene, D. M. McClung, K. Nishimura, P. K. Satyawali, and S. A. Sokratov, "The international classification for seasonal snow on the ground," UNESCO-IHP, Paris, France, 2009, I HP-VII Tech. Doc. in Hydrol., 83, IACS Contribution no. 1.

[44] A. Kontu and J. Pulliainen, "Simulation of spaceborne microwave radiometer measurements of snow cover using in situ data and brightness temperature modeling," *IEEE Trans. Geosci. Remote Sens.*, vol. 48, no. 3, pp. 1031–1044, Mar. 2010.

Anna Kontu was born in Orimattila, Finland, in 1981. She received the M.Sc.(Tech.) degree from Helsinki University of Technology (TKK), Espoo, Finland, in 2006. From 2005 to 2006, she worked on her Master's thesis in the TKK Laboratory of Space Technology in the characterization and testing project of the European Space Agency Soil Moisture and Ocean Salinity satellite calibration subsystem units.

Since 2006, she has been with the Arctic Research Unit, Finnish Meteorological Institute, Sodankylä, Finland, working as a Scientist and preparing her D.Sc. thesis on microwave remote sensing of snow.

Juha Lemmetyinen received the D.Sc.(Tech) degree from Aalto University [former Helsinki University of Technology (TKK)], Espoo, Finland, in 2012.

From 2004 to 2008, he was a Researcher with the TKK Laboratory of Space Technology and the TKK Department of Radio Science and Engineering, where he specialized in radiometer calibration techniques and remote sensing. Since 2009, he has been a Scientist with the Arctic Research Unit, Finnish Meteorological Institute, Sodankylä, Finland. His present research interests include radiative transfer modeling and applications of synthetic aperture radar and microwave radiometers in remote sensing of snow.

Jouni Pulliainen, photograph and biography not available at the time of publication.

Jaakko Seppänen received the M.Sc.(Tech.) degree from the Helsinki University of Technology (TKK), Espoo, Finland, in 2008. Since 2008, he has been working toward the Ph.D. degree in the Department of Radio Science and Engineering, School of Science and Technology, Aalto University, Espoo, specializing in microwave remote sensing.

His current research interests include applications of microwave radiometers, radiative transfer modeling, and remote sensing of vegetation.

Martti T. Hallikainen (M'83–SM'83–F'93) received the Doctor of Technology degree from the Faculty of Electrical Engineering, Helsinki University of Technology, Espoo, Finland, in 1980.

He was a Postdoctoral Fellow with the Remote Sensing Laboratory, The University of Kansas, Lawrence, KS, USA, in 1981–1983. Since 1987, he has been a Professor of space technology with Helsinki University of Technology (Aalto University since 2010). He was a Visiting Scientist at the Jet Propulsion Laboratory and National Aeronautics and Space Administration Goddard Space Flight Center/University of Maryland Goddard Earth Sciences and Technology Center, Baltimore, MD, USA, in 2007–2008 and at the Institute for Remote Sensing Applications, Joint Research Centre, European Union, Ispra, Italy, in 1993–1994. He led the development of the airborne HUT-2-D interferometric L-band radiometer, which provided the first end-to-end demonstration of the European Space Agency (ESA) Soil Moisture and Ocean Salinity (SMOS) mission concept. His team contributed to the design of the noise injection radiometers and the onboard calibration system of SMOS and characterized the two systems. The SMOS onboard calibration system was first tested on the HUT-2-D radiometer. He also led the development of the airborne HUTRAD 16-channel 6.9–94-GHz microwave radiometer and the airborne HUTSCAT profiling 8-channel (5.4 and 9.8 GHz, four linear polarizations) scatterometer. He is the responsible Leader of the development of the Aalto-1 and Aalto-2 nanosatellites presently under construction. His team has contributed to the development of the national operational satellite-based systems for monitoring sea ice, snow, and water quality. His research interests include the development of microwave sensors for airborne and spaceborne remote sensing, development of methods to retrieve the characteristics of geophysical targets from satellite and airborne measurements, cryospheric applications of remote sensing, and nanosatellite technology.

Dr. Hallikainen has been an IEEE Geoscience and Remote Sensing Society (GRSS) Honorary Life Member since 2007 and a Fellow of the Electromagnetics Academy since 2007. Since 1985, he has been a member of the European Association of Remote Sensing Laboratories (EARSeL) Council. Since 1988, he has been the national official member of the International Union of Radio Science (URSI) Commission F, and he served as Chair of the URSI Finnish National Committee in 1997–2005. He was the Secretary General of EARSeL in 1989–1993 and the Chair of the Organizing Committee for the 1989 EARSeL General Assembly and Symposium held in Espoo. He was the General Chair of the 1991 International Geoscience and Remote Sensing Symposium (IGARSS) held in Espoo and a member of the GRSS Administrative Committee in 1988–2006. He served as President of the IEEE GRSS in 1996–1997 and as Vice President in 1994–1995. He was a member of the ESA Earth Science Advisory Committee in 1998–2001. He was the Chair of GRSS Nominations Committee in 1999–2001 and 2003–2006, and he has served as member since 2007. He served as Vice Chair of the Finnish National Committee of Committee on Space Research in 2000–2011. He served as Chair of URSI Commission F (Wave Propagation and Remote Sensing) in 2002–2005, and he was the Vice President of URSI in 2005–2011. Since 2007, he has served as Chair of GRSS Publications Awards Committee. He serves as General Chair for the 2013 URSI Commission F Microwave Signatures Symposium in Espoo. He was a recipient of the 1994 GRSS Outstanding Service Award, the 1996 IGARSS Interactive Paper Award, and the 1999 IEEE GRSS Distinguished Achievement Award. He was also a recipient of the Microwave Prize for the best paper in the 1992 European Microwave Conference, the IEEE Third Millennium Medal in 2000, and the Fiorino Oro Award in 2010.

Publication 4

L. Leppänen, A. Kontu, J. Vehviläinen, J. Lemmetyinen, J. Pulliainen. 2015. Comparison of traditional and optical grain-size field measurements with SNOWPACK simulations in a taiga snowpack. *Journal of Glaciology*, 61(225), 151-162. doi: 10.3189/2015JoG14J026.

Comparison of traditional and optical grain-size field measurements with SNOWPACK simulations in a taiga snowpack

L. LEPPÄNEN, A. KONTU, J. VEHVILÄINEN, J. LEMMETYINEN, J. PULLIAINEN

Arctic Research Centre, Finnish Meteorological Institute, Sodankylä, Finland
Correspondence: L. Leppänen <leena.leppanen@fmi.fi>

ABSTRACT. Knowledge of snow microstructure is relevant for modelling the physical properties of snow cover and for simulating the propagation of electromagnetic waves in remote-sensing applications. Characterization of the microstructure in field conditions is, however, a challenging task due to the complex, sintered and variable nature of natural snow cover. A traditional measure applied as a proxy of snow microstructure, which can also be determined in field conditions, is the visually estimated snow grain size. Developing techniques also allow measurement, for example, of the specific surface area (SSA) of snow, from which the optical-equivalent grain size can be derived. The physical snow model SNOWPACK simulates evolution of snow parameters from meteorological forcing data. In this study we compare an extensive experimental dataset of measurements of traditional grain size and SSA-derived optical grain size with SNOWPACK simulations of grain-size parameters. On average, a scaling factor of 1.2 is required to match traditional grain-size observations with the corresponding SNOWPACK simulation; a scaling factor of 2.1 was required for the optical equivalent grain size. Standard deviations of scaling factors for the winters of 2011/12 and 2012/13 were 0.36 and 0.42, respectively. The largest scaling factor was needed in early winter and under melting conditions.

KEYWORDS: remote sensing, snow, snow metamorphosis, snow physics

INTRODUCTION

In the Northern Hemisphere, observation of seasonal snow cover is essential to, for example, climate change monitoring, flood forecasting and avalanche warning systems (e.g. Martinec and Rango, 1986; Brown, 2000; Mognard, 2003; Shaffrey and others, 2009). Snow microstructure is important for physical modelling of snow evolution and remote-sensing algorithms. Grain size is a critical parameter in the analysis of snowpack development and metamorphism (Colbeck, 1982). It is also used as a proxy of snow microstructure in many remote-sensing applications (Tsang and others, 1985; Pulliainen and others, 1999).

Global mapping of snow cover is possible with optical and microwave satellite instruments (e.g. Hall and others, 2002). The extent of the snow-covered area can be observed by using visual and near-infrared wavelengths (e.g. Hall and others, 1995; Maurer and others, 2003), and snow water equivalent (SWE) can be determined from passive microwave measurements (e.g. Chang and others, 1982; Pulliainen and Hallikainen, 2001). Radiative transfer models are used to simulate microwave radiation from experimental measurements, and model inversion can be applied in retrieval of snow parameters from microwave observations. Among other snow parameters, snow emission models use grain size (Tsang and others, 1985; Pulliainen and others, 1999) or correlation length (Tsang and Kong, 1981; Stogryn, 1986; Wiesmann and others, 1998; Wiesmann and Mätzler, 1999) to describe the effect of snow microstructure on microwaves. The models are very sensitive to changes in the parameter describing the microstructure; thus its parameterization has a direct impact on the accuracy of the inverted SWE (e.g. Grenfell and Warren, 1999; Mätzler and Wiesmann, 1999; Roy and others, 2004).

Natural snowpacks consist of morphologically different layers (Colbeck, 1991); layers have typically distinct grain size, grain type, density, hardness and wetness. Several methods of defining the snow microstructure have been presented. The physical size of snow grains (E) is traditionally defined visually as the largest diameter (mm) of a typical particle (Colbeck and others, 1990; Fierz and others, 2009). However, an acknowledged problem concerning E is that it is difficult to define and measure with good repeatability in field conditions (e.g. Domine and others, 2006). Baunach and others (2001) present a comparison of E estimations made by several experts; the difference in estimation of E varied between 0.25 and 1.25 mm. Estimations were closest when grains were at an early stage of metamorphosis, i.e. grains were quite small and round. Other measures of individual grains more descriptive of the microwave behavior have been proposed by, for example, Mätzler (2002).

The optical grain size (D_0), on the other hand, is defined as the diameter of independent spheres that have the same optical hemispherical reflectance properties as the snow, and which are proportional to the volume–surface ratio of the grains (Giddings and LaChapelle, 1961; Wiscombe and Warren, 1980; Dozier and others, 1987; Grenfell and Warren, 1999). Therefore, D_0 is not the same as E of a particle, with the exception of material consisting of perfect spheres (Wiscombe and Warren, 1980). Theoretical correlation length, on the other hand, describes the distribution of scattered radiation, and is related to grain size, shape and volumetric distribution of snow grains (e.g. Debye and others, 1957; Jin, 1993). However, three-dimensional measurements of the correlation length are difficult.

The physical snow evolution model SNOWPACK (Lehning and others, 2002a) can be used to simulate the evolution of different characteristics of snow. Simulation of E is not a simple process, because the physical processes are variable and the shapes of snow crystals are complex; therefore, several equations and semi-empirical parameterizations are

needed. In the non-dendritic case, when grains are not branched, D_0 is dependent on E. Independent equations are applied for the dendritic branched grains.

D_0 can be derived from specific surface area (SSA) measurements. SSA is a geometrical characteristic of porous sintered materials such as snow, and is related to chemical, physical and electromagnetic properties of the medium (Grenfell and Warren, 1999; Domine and others, 2008; Matzl and Schneebeli, 2010). SSA can be measured by stereology (e.g. Matzl and Schneebeli, 2010), X-ray computed microtomography (Flin and others, 2005; Chen and Baker, 2010), the methane adsorption method (Domine and others, 2001; Legagneux and others, 2002) and optical methods (Matzl and Schneebeli, 2006; Painter and others, 2007; Gallet and others, 2009; Langlois and others, 2010; Arnaud and others, 2011). Reflectance, and therefore optically measured SSA, also depends on grain shape (Picard and others, 2009). In this study, SSA was measured with the optical reflectance method presented by Gallet and others (2009).

The aim of the presented research was to: (1) compare in situ measured values to those modelled using the SNOWPACK thermodynamic snow model and (2) investigate the source and magnitude of measurement errors related to these parameters.

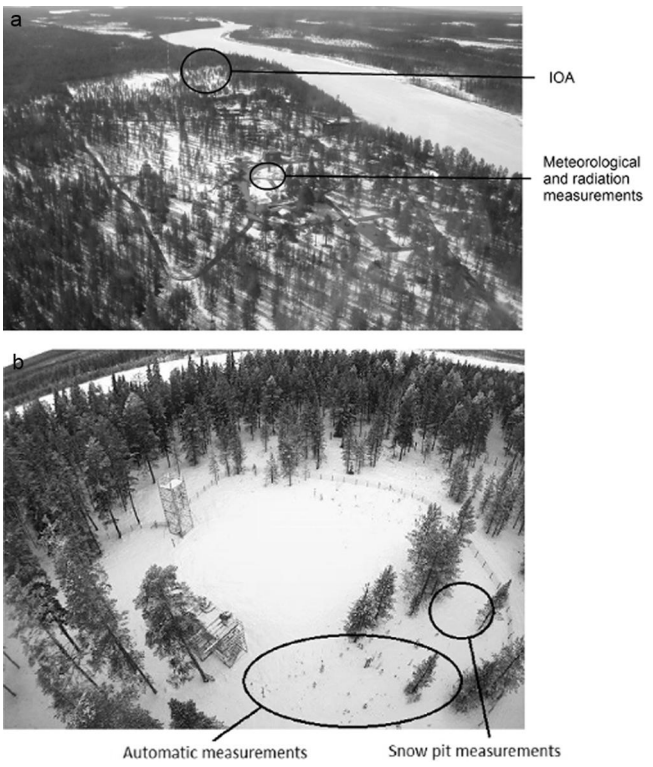

Fig. 1. (a) Aerial photograph of the Sodankylä facilities. IOA is the intensive operation area. Meteorological and radiation measurements, used to force the SNOWPACK model, were made 500 m from IOA in a similar environment. (b) The measurement field covered with snow on a natural forest floor.

THEORY AND MEASUREMENT METHODS

Grain growth

The shape and size of ice particles (referred to as snow grains from now on) change throughout the winter. Growth of snow grains is caused by changes in ambient physical conditions (Adams and Brown, 1982; Colbeck, 1982); the strongest effects are caused by changes in temperature and density.

Temperature differences in the snowpack are related to differences in air temperature, thermal conductivity of snow, terrain, vegetation, elevation and the amount of sunlight. Land-cover type affects the structure of the snowpack (e.g. an ice layer over a bog forms a different base for the snowpack than dry ground). Furthermore, even if the ambient temperature remains stable, the snowpack exhibits a vertical temperature gradient in conditions where the ambient and subnivean temperatures differ because of the low thermal conductivity of snow. Changes in snow density are also induced by temperature changes; however, the snowpack also compacts at constant temperatures, new snow increases the pressure in the older snow, and density of the snow increases.

Changes in temperature and density affect the state of grain metamorphism in the snowpack. Generally, metamorphism drives the formation of different grain shapes (Fierz and others, 2009). Colbeck (1982) describes grain shape changes through the winter; grains can form again several times, and a rule of thumb is that the average size of snow grains increases with age and depth of snowpack.

Snow class definitions

Snow grains can be classified by shape. In this paper, definitions following Fierz and others (2009) are used: grain classifications include precipitation particles (PP), decomposing and fragmented precipitation particles (DF), rounded grains (RG), faceted crystals (FC), depth hoar (DH), melt forms (MF) and ice formations (IF).

Measurement site

Snow profiles were measured at the Arctic Research Centre of the Finnish Meteorological Institute (FMI), Sodankylä, northern Finland, (67.368° N, 26.633° E) over two snow seasons. Measurements were made between January 2012 and April 2013. The measurement site (IOA (intensive observation area)) was located in a clearing surrounded by a sparse pine forest (Fig. 1). The site hosted several automated measurements (e.g. snow temperature profile, soil temperature profile, soil moisture and SWE). The meteorological and radiation data used for modelling were measured at a distance of 500 m from the IOA, where surroundings were similar to the IOA.

Snow cover at the site persists on average for 200 days, between the end of October and the end of May (Pirinen and others, 2012). The thermal winter, when the daily average temperature falls below zero, typically begins near the end of September and ends near the end of May. The maximum amount of snow is, on average, 80 cm in March, followed by a snowmelt period lasting until May. For the two winter seasons (2012 and 2013) used in this research, the measured snow depth and temperature profiles are presented in Figure 2.

The seasonal snowpack in Sodankylä has large variations in grain size and density, and impurities from, for example, tree litter and inorganic soot. Vertical layering caused by weather effects is inherent in snowpacks; however, natural snow also exhibits a high degree of horizontal variability in layering and snow structure caused by wind, vegetation and terrain effects (Sturm and others, 1998). In the case of new snow, the surface of the

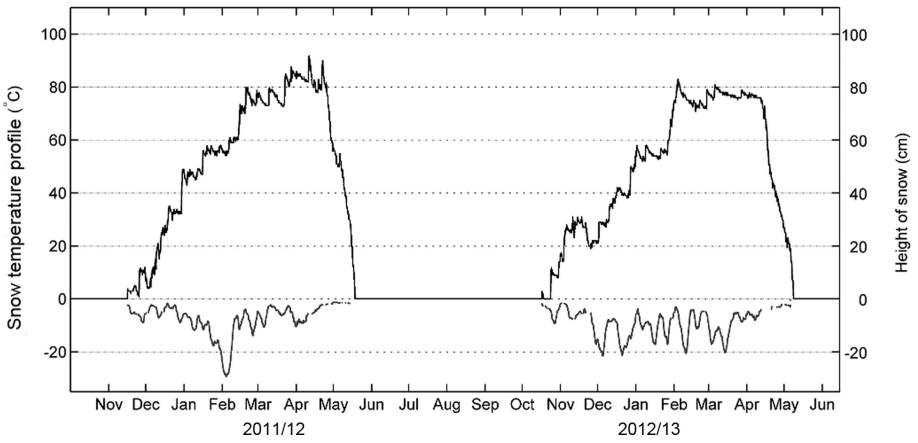

Fig. 2. Height of snow (upper, black curves) and temperature profile (difference of temperature at surface and base) of snowpack (lower, grey curves) during winters 2011/12 and 2012/13.

snowpack is typically light, and new snowflakes are large and dendritic. For older snowpacks, densification typically increases towards the bottom layers. In the middle of the snowpack, snow grains are smaller and rounder than in the surface layers. Grain size further increases towards the ground; near the ground, snow consists of grains with a large range of different sizes. During winter, the thickness of the bottom layer (mostly DH crystals) increases, the proportion of small and large grains changes, and the proportion in the layer increases near ground. The structure of the snowpack varies annually, in particular as a function of the temperature gradient over the snowpack (between air and soil temperatures).

The most common grain shapes in Sodankylä are PP, DF, RG, FC, DH and MF. Occasionally over the winter, SH crystals occur. Melting and recrystallization of the surface snow during a warm period, followed by a cold period, creates a hard crust layer, which is classified as MFcr or sometimes as IF.

The average grain-size value for the whole snowpack was considered appropriate when analysing the time series of snowpack evolution. As snow pits are forcibly made at a different location each time, the dataset at hand encompassed both temporal and spatial variations in snow structure, which are difficult to separate from one another. A weighted average was calculated to alleviate the effects of spatial (horizontal) variability of grain size in the snowpack. As the propagation of electromagnetic radiation in snow is closely related to the SWE (depth × density), weighting with SWE gives a better proxy of the relative weight of the grain size in each layer in terms of microwave interactions, compared to simple depth-weighted averaging. Other methods include weighing the grain size of each layer by the assumed optical depth of respective overlying layers (e.g. Tedesco and Kim, 2006).

Snow-pit measurements

The research was based on manual snow-pit measurements made over the 2011/12 and 2012/13 winter seasons. The collected data include estimates of E as well as SSA measurements. SSA was measured with a commercial IceCube instrument (Gallet and others, 2009). Grain-size measurements of E were performed by visually analysing macro-photographs of grain samples against a reference grid. Automated meteorological and radiation data from the test site were used to drive the SNOWPACK model; model estimates of E and D_0, given as E_{spi} and $D_{0\mathrm{sp}}$, aggregated over the snowpack to improve comparability, were analysed against the in situ measurements. The different grain-size parameters are presented in Table 1.

The collected dataset includes 35 snow-pit measurements, made over the two winters. Typically, the snow pits were measured at 1 week intervals. However, several extra measurements were arranged. Due to the destructive nature of the measuring process, the exact location of the snow pit changed each time; new pits were made at a minimum distance of 1 m from previous pits to avoid changes in snow structure caused by previous pit measurements. The data thus also include the effect of small-scale spatial variability, in addition to temporal variability caused by weather events and snow metamorphism.

All measurements from a snow pit were taken from a vertical cut of ~50 cm width made in the snowpack. Layers were determined manually from the snow-pit wall by changes in snow structure (e.g. density, hardness, grain size and shape). The measured snow-pit data include snow layer thicknesses, E for each layer, temperature profile (every 10 cm), density profile measured by weighting a snow sample (every 5 cm), and SSA measurements (every 3 cm). However, reliable density and SSA measurements from 5–10 cm above ground level were not always possible due to hard packed or very coarse-grained snow.

Table 1. Grain-size definitions

Grain size	Symbol	Description
Traditional	E	The classical grain size of a snow layer is the average size of its grains. The largest extension of a grain is measured in mm.
Optical	D_0	Diameter of optically equivalent ice spheres which have the same optical properties (surface-to-volume ratio) as original particles. Derived from the reflectance measurements made with the IceCube instrument.
SNOWPACK traditional	E_{sp}	Simulated with SNOWPACK model.
SNOWPACK optical	$D_{0\mathrm{sp}}$	Simulated with SNOWPACK model.

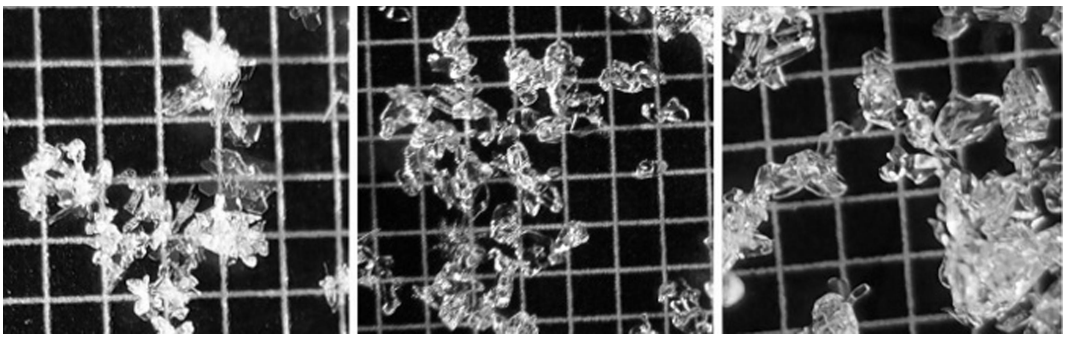

Fig. 3. Macro-photographs taken against a 1 mm reference grid in Sodankylä. Examples of dendritic (left) and non-dendritic (middle) grains. Grain shape in the left panel is PPsd, in the middle panel RGxf and in the right panel right FCxr. Grain size exhibits large variability in the right panel, likely causing observer-related bias. Grain size is more uniform in the other two photographs.

E was estimated visually for each snow layer by comparing snow grains to a 1 mm reference grid. The methodology differed from the traditional measurement (Fierz and others, 2009), because estimation was made during post-processing from macro-photographs. Occasionally, layers contained very hard snow and grains, and could not be distinguished without breaking the snow structure. Some of the photographs were also of low quality, so the grain-size estimation could not be made. Only one snow sample was taken from each layer, so errors in the definition of snow layers may have affected the representativity of the results. E was recorded to the nearest 0.25 mm. Photographs of different types of grains are presented in Figure 3. The snow type was determined visually from the same macro-photographs.

SSA measurements

A novel method of measuring D_0, the diameter of optical-equivalent ice spheres, is to derive it from measurements of reflectance (Gallet and others, 2009). SSA ($m^2\,kg^{-1}$) is defined as the surface area of particles per unit mass:

$$\mathrm{SSA} = S/M = S/(\rho_i V), \quad (1)$$

where S is surface area, M is mass of the sample, ρ_i is the density of ice ($917\,kg\,m^{-2}$) and V is volume of the sample (Legagneux and others, 2002). The optical diameter of ice spheres is presented by Kokhanovsky and Zege (2004) as

$$D_0 = 6V/S. \quad (2)$$

The theoretical relation between D_0 and SSA from Eqns (1) and (2) is

$$D_0 = 6/(\rho \mathrm{SSA}). \quad (3)$$

The SSA decreases with increasing grain size, as there is more empty space between large grains than between smaller grains.

For SSA measurements, we used the IceCube manufactured by A2 Photonic Sensors, France, which is a commercial single-frequency instrument similar to DUFISSS (Gallet and others, 2009). The instrument measures the hemispherical infrared reflectance of the snow samples, which can be linked to SSA (e.g. Domine and others, 2006; Matzl and Schneebeli, 2006). The whole snowpack was sampled at 3 cm intervals; the measurements were made from the same cut in the snowpack (i.e. pit) as the E estimations.

IceCube measurements consisted of calibration measurements and measurements of snow samples. The surface of the sample had to be smooth for the measurement to succeed; ice layers and very hard snow layers were difficult to measure, and several measurements were omitted as a result. Moreover, large crystals at the bottom of the snowpack proved difficult to sample correctly, so these measurements may carry additional errors. The sample also had to be compacted in the sample holder to avoid absorption of radiation at the bottom of the holder, which obscures reflections from the snow sample. For clustered grains (e.g. MFcl or MFpc), the SSA value was smaller, because grains were closer to each other than free grains of the same size would be (Dozier and Painter, 2004). During the measurement the sample holder was set below the instrument. Calibration measurements of the IceCube were made before and after every measurement occasion. The calibration result depended on, for example, the laser temperature, the cleanness of the spectralon surfaces and the mechanics of the instrument. The IceCube was calibrated by measuring the reflectances of six different spectralon plates and the background radiation. A least-squares polynomial was fitted to these seven measurements, and the success of the calibration was determined from the fit. The programme gives the user an estimate of the quality of the calibration from the success of the curve fit, by using a scale of very poor, poor, good and excellent. Error estimation of calibration is important, because the success of the calibration was not seen during measurement and some of the calibration measurements were often of poor quality. Errors may have originated from any single calibration measurement or multiple calibration measurements. Theoretically, it was also possible for all calibration measurements to be shifted systematically to the same direction to indicate good calibration, but the magnitude of the result (signal-to-reflectance relationship) would then be erroneous.

Snowpack model

SNOWPACK is a one-dimensional (1-D) physically based finite-element model developed at the WSL Institute for Snow and Avalanche Research SLF, Switzerland. The characteristics of the numerical set-up, the microstructure and the initial and driving parameters of the model are described by Lehning and others (2002a,b). The number of individual layers in the model is not restricted, and increases in response to snow precipitation.

SNOWPACK simulates three types of snow metamorphism: equilibrium metamorphism, temperature gradient metamorphism and wet snow metamorphism. Only the first two metamorphism simulations were investigated in this study.

The snow grains are parameterized using size parameters (grain size and bond size) and shape parameters (dendricity and sphericity). The sphericity describes the ratio of rounded versus faceted shapes, and the dendricity describes the part of original grain shapes that remain in a snow layer. Both parameters vary from 0 to 1. The dendricity and sphericity were set to 1 and 0.5, respectively, for new snow. In old rounded snow grains, the dendricity decreases to zero. The shape parameters are based on the French snow model Crocus. Further details can be found in, for example, Brun and others (1992).

Grain growth and thus grain size (E_{sp}) is defined by several equations in the SNOWPACK model depending on the physical conditions in the snowpack. The grain growth during equilibrium metamorphism, as the temperature gradient is small, is based on a mixture theory model described by Brown and others (1999, 2001). E_{sp} during equal temperature metamorphism is the diameter of a sphere. The grain growth rate (r_g) is presented by Lehning and others (2002b) in the equal temperature metamorphism as

$$\dot{r}_g(T,t) = s\left(A_1 + \frac{A_2}{r_g}\right)e^{A_3(1/T_R - 1/T)}, \quad (4)$$

where T is temperature, t is time, s is sphericity, A_1, A_2 and A_3 are coefficients, r_g is grain size, and T_R is reference temperature (273.15 K). The temperature gradient metamorphism used in SNOWPACK is described by Baunach and others (2001). It assumes that snow grains grow as plates, while the thickness of the plate stays constant. The length of a side of these plates is the temperature gradient metamorphism grain size in SNOWPACK. The grain growth rate is presented by Lehning and others (2002b) in the temperature gradient metamorphism as

$$\dot{r}_g(T) = \frac{a^2\left(J_L(t) - \frac{a^3(t)}{\Delta z}\Delta J_{L2L}(t)\right)}{2f_{gg}\rho_i r_g(0) r_g(t)}, \quad (5)$$

where $r_g(0)$ is initial grain size, ρ_i is density of pure ice, f_{gg} is the adjustable geometrical factor for better approximation of the real grain shape (Baunach and others, 2001; Lehning and others, 2002b), J_L is interlayer mass, J_{L2L} is layer-to-layer mass, $r_g(t)$ is actual growing grain size, a is lattice constant and z is snow height. Grain-size simulation of SNOWPACK has been fitted to grain-size measurements by adjusting model parameters empirically with cold laboratory experiments.

The optical grain size (D_{0sp}), which is simulated with SNOWPACK, is presented in Vionnet and others (2012) in the dendritic case as

$$D_{0sp} = 10^{-4}[d + (1-d)(4-s)] \quad (6)$$

and in the non-dendritic case as

$$D_{0sp} = E_{sp}(1-s)\max\left(4\times10^{-4}, \frac{E_{sp}}{2}\right), \quad (7)$$

where D_{0sp} (m) is the SNOWPACK optical grain size, d is dendricity, s is sphericity and E_{sp} (m) is SNOWPACK traditional grain size. Thus the D_{0sp} in the non-dendritic grains depends on E_{sp}.

In this study, version 3.1.0 of SNOWPACK was used to simulate E_{sp} and D_{0sp} for winters 2011/12 and 2012/13. Air temperature, relative humidity, wind speed and direction, incoming and outgoing shortwave radiation and snow depth observations were collected from an operational weather station (WMO code 02836) operated by the FMI at the Sodankylä Arctic Research Centre. These observations were augmented with automatic ground temperature observations and snow temperature observations close to the operational station. Incoming and outgoing longwave radiation observations were available, but the longwave radiation data contained gaps preventing their application in simulations. Therefore, only shortwave radiation data were used. In simulations for this study, SNOWPACK was driven by snow depth observations instead of precipitation data. Density of new snow was determined following Lehning and others (2002a). The data used to drive the model have 30 min intervals, and the data used for the simulations are listed in Table 2 and in the Appendix. The SNOWPACK model outputs the parameters of snow profiles at 60 min intervals.

Table 2. Summary of automated measurements used to drive the SNOWPACK model

Measurements in Sodankylä	Unit	Distance from IOA*
		m
Air temperature	°C	500
Air relative humidity	%	500
Incoming shortwave radiation	$W m^{-2}$	500
Outgoing shortwave radiation	$W m^{-2}$	500
Snow depth	cm	500
Snow temperature profile	°C	0
Soil temperature profile	°C	0
Wind speed	$m s^{-1}$	500
Wind direction	°	500

*Intensive operation area.

SNOWPACK grain size has been compared to measured grain size and grain type in several recent studies (Schweizer and others, 2006; Rasmus and others, 2007; Hirashima and others, 2008). Rasmus and others (2007) calculated agreement scores for measured and simulated grain sizes in Finland; agreement was generally good in northern Finland, where the snowpack was more stable. On the other hand, Schweizer and others (2006) compared measured and simulated grain size for each grain type, finding no large differences between measured and simulated grain sizes. Langlois and others (2012) compared the correlation length derived from D_0 measured by InfraRed Integrating Sphere (Montpetit and others, 2012) and SNOWPACK model results, and scaled D_0 lower to fit measurements to simulations. Huang and others (2012) researched grain sizes predicted by different models. Their result was that SNOWPACK predictions for E and D_0 are as good as predicted by using two other models (Flanner–Zender Grain Size Model (Flanner and Zender, 2006) and Jordan Grain Size Model (Sun and others, 1999)) which both predict the size parameters well.

RESULTS

Comparison of experimental and snowpack modelled grain sizes

Time series of E, D_0 and density profiles in Sodankylä snowpack

Profiles of E and D_0 are presented in Figure 4 for a single snow pit in February. The layered structure of the snowpack was visible in both the E and D_0 profiles. Generally, the magnitude of E was larger than the magnitude of D_0.

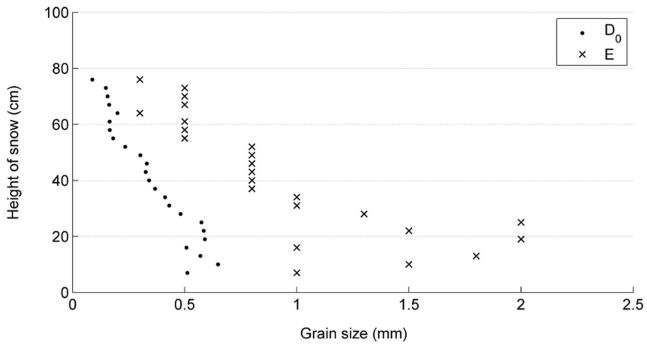

Fig. 4. E (crosses) and D_0 (dots) compared using measurements made at 3 cm intervals for a single snow pit.

Nevertheless, both measures indicated a similar trend of increasing grain size towards the bottom snow layers. Both methods indicated relatively small variation in grain size above a snow height of 20 cm. However, in lower layers the grain-size variability increased significantly.

Density, E_{sp} and D_{0sp} were modelled with SNOWPACK from meteorological and radiation data as described above and in Table 2 and the Appendix. Manual density measurements are compared to SNOWPACK simulations in Figure 5.

The bias in snow thickness between manually measured and automatic observations, used as forcing for SNOWPACK simulations, was ~5 cm during the dry snow season (Fig. 5). Both measured and simulated density values exhibit an increasing trend from snow surface towards the ground, from 50–150 to 300–500 g cm^{-3} in simulated and 50–200 to 250–450 g cm^{-3} for typical measured values in top and bottom layers, respectively. During the dry snow season, average densities for the 2011/12 winter were 208 and 175 g cm^{-3} and for the 2012/13 winter were 187 and 217 g cm^{-3} for measurements and simulations, respectively. During the melt season, density increased by up to 50% in both simulated and measured values. Some differences were apparent between two winter seasons: For instance, during the 2011/12 winter, density was notably large during the melt season, with measured values reaching 470 g cm^{-3}. However, for the 2012/13 winter, the maximum measured densities during the melt season were 400 g cm^{-3}, although the density in bottom layers was larger during the dry-snow season than for the 2011/12 season.

Time series of E, E_{sp}, D_0 and D_{0sp} profiles are presented in Figures 6 and 7. The range of values for E was 0.25–2.75, for E_{sp} was 0–2.5, for D_0 was 0–1.25 mm and for D_{0sp} was 0–1.5 mm. Typically, grain growth towards the bottom of the snowpack was apparent both in SNOWPACK simulations and measured data. The simulated layering profile can be compared to manually determined layering structure based on Figure 6; the measured E for manually determined layers is marked on the upper edge of the respective layer. Typically, SNOWPACK simulated more layers (up to >40) than could be determined by the snow-pit observation (typically not more than ten layers). In order to allow intercomparison of E, E_{sp}, D_0 and D_{0sp} in a consistent fashion, E_{sp} and D_{0sp} were weighted with the SWE of each layer. A similar method was applied for in situ data. This was seen as a necessary process due to ambiguities in relating the many simulated layers to the relatively few layers apparent in manual observations. Furthermore, as described earlier, snow-pit observations do not represent temporal evolution of a discrete location but also contain the effect of spatial variability in the natural snowpack.

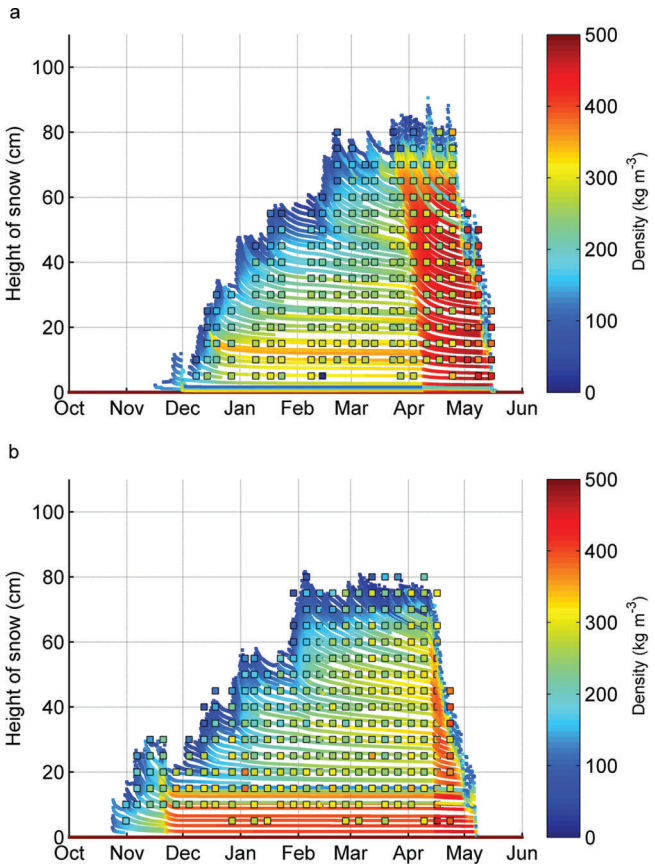

Fig 5. Snow density simulated with SNOWPACK compared to manual density measurements. Coloured boxes represent manually measured values; solid lines represent SNOWPACK simulations: (a) 2011/12; (b) 2012/13.

Averaged time series of E and D_0 in Sodankylä snowpack

The time series of both manually measured and simulated E and D_0 are presented in Figure 8. Root-mean-square (rms) errors, unbiased rms errors, biases and correlation coefficients (R^2) of datasets are presented in Table 3. For the time series of E and E_{sp} in winter 2011/12, R^2 was 0.56 and the bias 0.12 mm. For winter 2012/13 the variations were larger (with a bias of 0.26 mm) and the R^2 was 0.36. R^2 during January–March was 0.91 and 0.28 during the first and second winters, respectively. R^2 was 0.14 and 0.54 in October–December, and 0.20 and 0.32 in the melt season of the same two seasons respectively.

D_{0sp} and D_0 trends were similar for both winters, and R^2 for the whole season was 0.75 for both seasons. During January–March 2012, R^2 was 0.42, and during January–March 2013, 0.76. R^2 was 0.27 and 0.94 respectively in the melting seasons and 0.79 in October–December 2012. However, D_{0sp} was constantly larger than D_0. Therefore, the bias and rms error between D_0 and D_{0sp} were larger than between E and E_{sp}.

A linear scaling factor β_{sp} describing the ratio between measured and simulated grain size can be defined so that

$$D = \beta_{sp} D_{sp}, \quad (8)$$

where D is measured grain size and D_{sp} is simulated grain

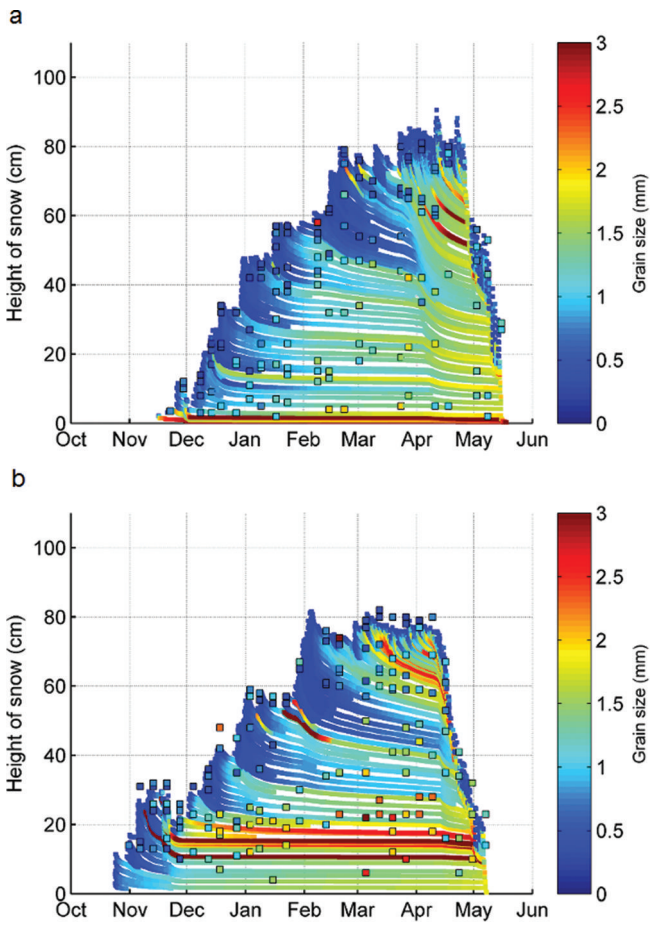

Fig. 6. SNOWPACK simulation of E_{sp} compared to manual measurements of E. Coloured boxes represent manually measured values; solid lines represent SNOWPACK simulations: (a) 2011/12; (b) 2012/13.

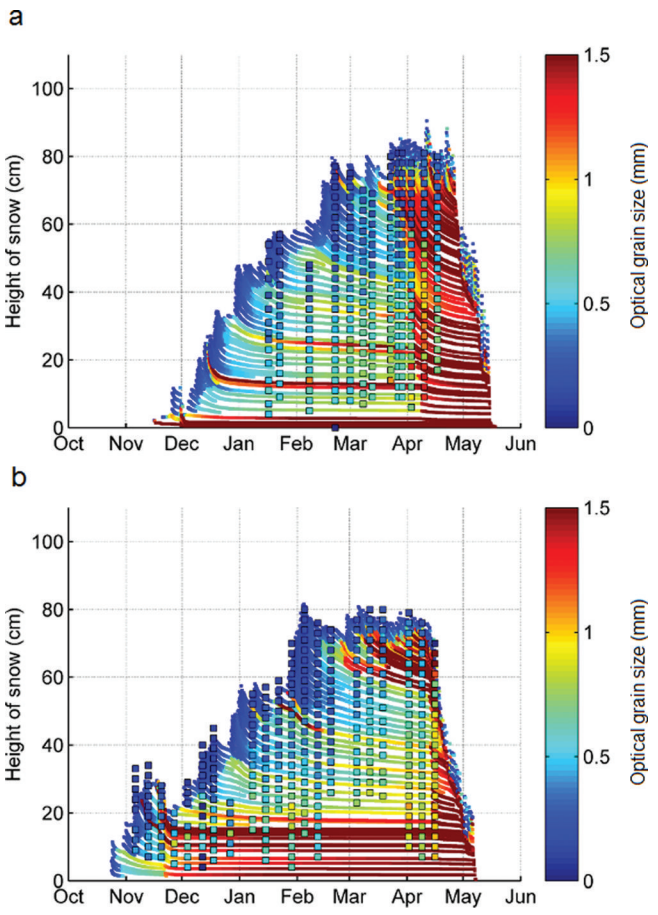

Fig. 7. SNOWPACK simulation of D_{0sp} compared to manual measurements of D_0 for snow pit 14 February 2013. Coloured boxes represent manually measured values; solid lines represent SNOWPACK simulations: (a) 2011/12; (b) 2012/13,

size. Values for β_{sp} and standard deviations are presented in Table 4 and Figure 9 for the two snow seasons. Average scaling factors between the two years were within 0.1 of each other on average. Considering both winters, the scaling factor, β_{D0sp}, between measured D_0 and simulated D_{0sp} was 2.1, and β_{Esp} between measured E and simulated E_{sp} was 1.2. The standard deviations were 0.42 and 0.36 respectively. β_{Esp} varied between 0.8 and 2.1 over both winters. β_{Esp} was more stable during the first winter than the second, with values in the range 0.9–2.3 compared to 0.8–1.8 for the first and second winters, respectively. β_{Esp} was largest during October–December and the late melting season, reaching

Table 3. Correlation coefficient (R^2), bias, rms error and unbiased rms error between measured and SNOWPACK simulated grain sizes. Grain sizes are defined in Table 1

	E_{sp}	D_{0sp}
R^2		
E	0.47	0.38
D_0	0.69	0.74
Bias		
E (mm)	0.19	0.01
D_0 (mm)	0.71	0.50
rms error		
E (mm)	0.37	0.38
D_0 (mm)	0.72	0.53
Unbiased rms error		
E (mm)	0.32	0.38
D_0 (mm)	0.14	0.16

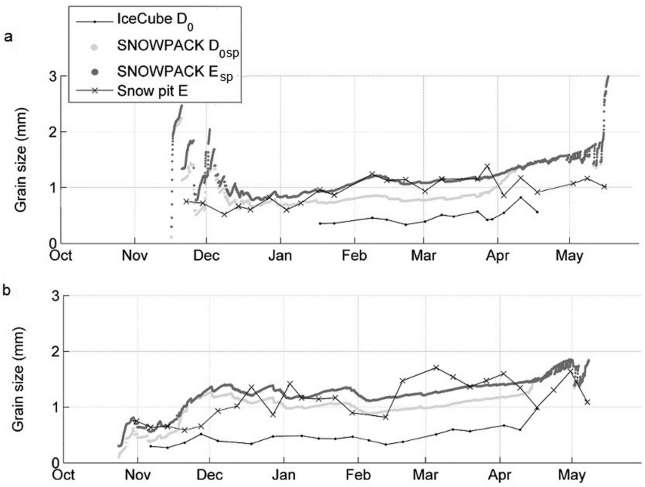

Fig. 8. Time series of measured E and D_0 and SNOWPACK simulated E_{sp} and D_{0sp}. (a) 2011/12; (b) 2012/13.

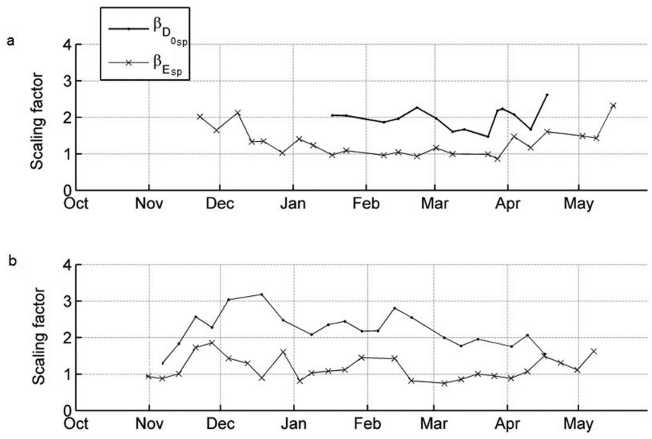

Fig. 9. Time series of scaling factors β_{Esp} and β_{D0sp} between measured E and D_0 and SNOWPACK simulated E_{sp} and D_{0sp}: (a) 2011/12; (b) 2012/13.

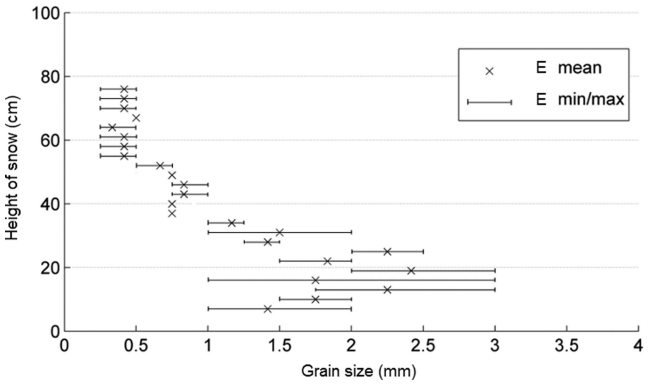

Fig. 10. An example of observer-related errors in E estimations. The macro-photographs taken by 3 cm intervals were analysed separately by three observers; the mean value of E (crosses) is marked with error bars between minimum and maximum values.

values up to 2.3. In January–March, $\beta_{Esp}$was 1.1 on average. Also β_{D0sp} was more variable during the second winter (range 1.3–3.2) than the first (range 1.8–2.8). For β_{D0sp}, there was no clear seasonally related trend, but measurements in December 2012 required the largest β_{D0sp} (average 3.1) while measurements in the 2013 melting season required the smallest β_{D0sp} (average 1.75). In January–March, β_{D0sp} was ~2.2. It can also be noticed that trends of β_{D0sp} and β_{Esp} were similar during the second winter.

Sources of measurement errors

Several factors contribute to the uncertainty of estimates of E, including random errors arising from preparation of the snow sample, and systematic errors arising from the estimation process itself. Errors are mainly caused by layer definition in the field, placing grains in the reference plate from the snowpack, unsuccessful photographing, failure to distinguish the single grains in the macro-photograph, failure to measure the size of a grain using a 1 mm reference scale or choosing the typical average grain in the macro-photograph. Other contributions to the error may be made by (1) the snow structure being disturbed when a sample of grains is placed on the reference plate, and (2) separation of the grain boundaries in the macro-photographs not always being clear.

Determining the layered stratification of the snowpack was an important aspect of the snow-pit measurement, because E may vary both horizontally and vertically. However, the process was also subject to observer error.

Table 4. The scaling factor beta between measured and SNOWPACK simulaled grain sizes. β_{Esp} is for traditional grain size E, and β_{D0sp} is for optical grain size D_0. Standard deviations (std) are also presented

	2011–13	2011/12	2012/13
β_{Esp}	1.24	1.16	1.3
std(β_{Esp})	0.36	0.31	0.39
β_{D0sp}	2.11	2.21	1.97
std(β_{D0sp})	0.42	0.47	0.30

The method applied for manual layer definition has been described above. Separation of layers was occasionally difficult because differences between the layers were not always clear. An alternative instrument for the definition of snow layer boundaries is the Snow Micro Penetrometer (SMP) (Pielmeier and Schneebeli, 2003), which may allow more objective separation of the layering structure.

An example of comparison for E estimations made by three observers from the same photographs is determined in Figure 10. Estimation of E was made from samples taken at intervals of 3 cm, in order to acquire more samples for comparison, and on the other hand, in order to compare with D_0 from the same snow sample. The snow pit chosen for comparison included several layers and snow types. The difference between estimations was largest at the bottom of the snowpack, where the sample contained a large scale of different grain sizes (Fig. 3). Even if all the grains in the photograph were almost the same size, there was a potential error of up to 0.25 mm (the precision of our estimation). More comparative data are needed for a more complete error analysis of E.

The errors in the IceCube measurement were a sum of random errors originating from the sampling process as well as systematic errors in instrument calibration. Preparation of the samples for the IceCube instrument involved several uncertainties caused by the compaction level of the snow in the sample holder (reflection from the bottom of the sample holder) and the sample surface smoothness (reflection from the sample surface). The errors in instrument calibration were caused by the cleanness of calibration spectralons (shade of the spectralons) and the descent temperature of the instrument and laser (power of the laser). Additional errors were caused by instrument properties. For example, scattering from grains below the sample surface resulted in underestimation of the reflectance, which appeared to be reduced by the limited field of view (Gallet and others, 2009). Moreover, the radiation penetration depth depends on snow density, which was usually ~1 cm; however, radiation did not penetrate the calibration spectralon plates as porous snow, which increased the amount of reflected radiation and worsened the accuracy of the calibration.

A total of 27 measurements included IceCube calibration data before and after the measurement. The average

difference in D_0 between two calibrations was 0.044 mm. The reflectance data of the largest and smallest differences between calibrations were used to derive D_0 in Figure 11. The largest difference (average from pit) was 0.113 mm on 10 April 2012, and the smallest average difference (average from pit) was 0.001 mm on 12 March 2013. Root-mean-square errors between these calibrations were 0.121 mm and 0.0025 mm respectively. Contrary to expectation, the largest differences in D_0 were between very poor and good calibrations, and the smallest were between good and poor calibrations, when the above scale is used. The average difference between D_0 of two calibrations made on the same day was still <0.05 mm

DISCUSSION

The magnitude of E was clearly larger than D_0 in both the measured and simulated cases. However, the magnitude difference between E_{sp} and D_{0sp} was not as large as between E and D_0. Underestimation of D_0 may result partly from a lack of measurements from the bottom of the snowpack. Previous results also scaled D_{0sp} lower than in this study (Langlois and others, 2012). The best correlation (from R^2, bias rms error and unbiased rms error) was between D_0 and D_{0sp} and then E and E_{sp}. The average scaling factor β_{Esp} varied 13% from one winter to another, and β_{D0sp} was within 11%. Standard deviations of yearly scaling factors were in the range 0.3–0.5.

According to our results, SNOWPACK simulations of E_{sp} and D_{0sp} showed the best agreement with field measurements during January–March conditions. For early winter in November and the snowmelt season in April and May, E_{sp} and D_{0sp} varied most, and a clear disconnect from field measurements was also apparent. During October–December, only a few snow layers were identified in field measurements; thus the variability in individual observations of E and D_0 affected the overall bulk average and the calculated average scaling factor. Overestimation of SNOWPACK density also affected the weak correlation of E and D_0 measurements with simulations during the melt season. Furthermore, measurements of E and D_0 also exhibit more uncertainties during the melt season in wet snow conditions.

Determination of layers, placing the grains in the reference plate and observer-related estimation causes the largest errors in E. Choosing the average E from the macro-photograph is the most sensitive part for error estimation. A comparison of estimates from three observers of the same macro-photographs indicated errors up to 1 mm. D_0, measured using the IceCube instrument, however, was less sensitive to observer-related errors than E estimates, but several stages of the measurement process (sampling, calibration of original values, deriving D_0 from SSA) may still result in inaccuracies. The light newly fallen snow (density $\sim 50\,g\,L^{-1}$) had to be compacted in the sample holder, and the quality of the sample was affected by different sampling techniques, smoothness of the sample surface, etc. The calibration-related error was relatively small (average 0.05 mm; maximum 0.12 mm). Error is very small because calibrations are made during the same measurement occasion. Calibration errors were further reduced by cleaning calibration spectralons, and stabilizing the instrument and laser temperatures before the calibration.

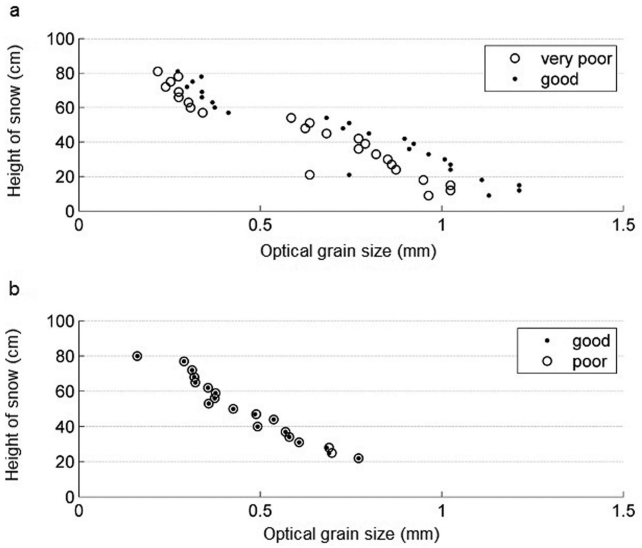

Fig. 11. The effect of repeated calibration of the SSA measurements on D_0. The same IceCube measurement is calibrated twice. On 10 April 2012, the mean difference between very poor (unfilled circles) and good (dots) calibrations of D_0 was 0.113 mm; on 12 March 2013 the difference between good (dots) and poor (unfilled circles) calibrations of D_0 was 0.001 mm.

CONCLUSIONS

A description of the snow microstructure is essential for physical snow models and radiative transfer models. A typical measure applied as a proxy indicator of snow microstructure has been the grain size (E). However, there are several ambiguities related to defining and measuring E. An alternative parameter describing snow microstructure, the optical grain size (D_0), can be derived from SSA measurements (Gallet and others, 2009). However, the definition of D_0 is based on optics, and its measurement is based on optical reflection from snow, which is not directly related, for example, to the scattering behaviour of radiation at microwave frequencies. On the other hand, empirical relations between E and the propagation of microwaves have been established in the past (Hallikainen and others, 1987). Physical snow models such as SNOWPACK are important for global derivation of snow properties that are difficult to observe in the field (e.g. grain size), for remote-sensing applications and hazard prediction systems. Therefore, a good correlation of manual measurements with the model is essential.

The main objective of the study was to compare E and D_0 to E_{sp} and D_{0sp}. Another objective was to define measurement errors of E and D_0. The measurements were made during the 2011/12 and 2012/13 winters in Sodankylä.

Layers simulated with SNOWPACK were not directly comparable with the manually determined layering structure, as simulation typically produced more layers with also a differing density profile. Furthermore, collected field data also exhibited the effects of spatial variability in natural snow. Therefore, averaged and weighted values for the whole snowpack were used in this study for intercomparison of measured and simulated values.

The temporal variation of measured and simulated values was similar in the time series (Fig. 8); however, in the first winter the average correlation was better. The largest difference between measured and simulated values occurred

in October–December and during the melting season in April and May. The magnitude of D_{0sp} was approximately twice as large as D_0, while the magnitude of E was almost the same for measured and simulated values (Table 3; Fig. 9). Calculated R^2 values were best between the same respective measured and simulated parameters, even though the magnitude of D_{0sp} was closer to E than D_0 (Table 4).

The largest uncertainties in both E estimations and D_0 measurements were estimated to occur in the bottom layer of the snowpack, where the grains were large and loose. The IceCube calibration error was 0.05 mm on average. The effect of other errors (sampling method, sample surface smoothness and observer) on D_0 was <0.1 mm in our preliminary unpublished results. E for an average grain was estimated to the nearest 0.25 mm. The magnitude of error in E was suspected to be in the millimetre range (Fig. 11).

This study suggests that SNOWPACK was able to simulate with reasonable accuracy the magnitude and trend of traditional grain-size profiles for boreal forest/taiga snow in midwinter. In the case of optical grain size, SNOWPACK simulations exhibited a notably large bias compared to measured values; however, the correlation between measured and simulated values exceeded that of the classical grain size.

ACKNOWLEDGEMENTS

We thank the WSL Institute for Snow and Avalanche Research SLF and especially Mathias Bavay and Martin Schneebeli for the opportunity to use the SNOWPACK model. We also thank the staff of FMI Arctic Research Centre in Sodankylä for performing the in situ measurements.

REFERENCES

Adams EE and Brown RL (1982) A model for crystal development in dry snow. *Geophys. Res. Lett.*, **9**(11), 1287–1289 (doi: 10.1029/GL009i011p01287)

Arnaud L and 7 others (2011) Measurement of vertical profiles of snow specific surface area with a 1 cm resolution using infrared reflectance: instrument description and validation. *J. Glaciol.*, **57**(201), 17–29 (doi: 10.3189/002214311795306664)

Baunach T, Fierz C, Satyawali PK and Schneebeli M (2001) A model for kinetic grain growth. *Ann. Glaciol.,* **32**, 1–6 (doi: 10.3189/172756401781819427)

Brown RD (2000) Northern Hemisphere snow cover variability and change, 1915–97. *J. Climate*, **13**(7), 2339–2355 (doi: 10.1016/S0165-232X(01)00032-5)

Brown RL, Edens MQ and Barber M (1999) Mixture theory of mass transfer based upon microstructure. *Defence Sci. J.*, **49**(5), 393–409

Brown RL, Satyawali PK, Lehning M and Bartelt P (2001) Modeling the changes in microstructure during metamorphism. *Cold Reg. Sci. Technol.*, **33**(2–3), 91–101 (doi: 10.1016/S0165-232X(01)00032-5)

Brun E, David P, Sudul M and Brunot G (1992) A numerical model to simulate snow-cover stratigraphy for operational avalanche forecasting. *J. Glaciol.*, **38**(128), 13–22

Chang ATC, Foster JL, Hall DK, Rango A and Hartline BK (1982) Snow water equivalent estimation by microwave radiometry. *Cold Reg. Sci. Technol.*, **5**(3), 259–267 (doi: 10.1016/0165-232X(82)90019-2)

Chen S and Baker I (2010) Evolution of individual snowflakes during metamorphism. *J. Geophys. Res.*, **115**(D21), D21114 (doi: 10.1029/2010JD014132)

Colbeck SC (1982) An overview of seasonal snow metamorphism. *Rev. Geophys. Space Phys.*, **20**(1), 45–61 (doi: 10.1029/RG020i001p00045)

Colbeck SC (1991) The layered character of snow covers. *Rev. Geophys.*, **29**(1), 81–96 (doi: 10.1029/90RG02351)

Colbeck SC and 7 others (1990) *The international classification for seasonal snow on the ground*. International Commission on Snow and Ice, International Association of Scientific Hydrology, Wallingford

De Vries DA (1963) Thermal properties of soils. In Van Wijk WR ed. *Physics of plant environment*. North-Holland Publishing Co., Amsterdam

Debye P, Anderson HR and Brumberger H (1957) Scattering by an inhomogeneous solid II. The correlation function and its application. *J. Appl. Phys.*, **28**(6), 679–683 (doi: 10.1063/1.1722830)

Domine F, Cabanes A, Taillandier AS and Legagneux L (2001) Specific surface area of snow samples determined by CH_4 adsorption at 77 K and estimated by optical microscopy and scanning electron microscopy. *Environ. Sci. Technol.*, **35**(4), 771–780 (doi: 10.1021/es001168n)

Domine F, Salvatori R, Legagneux L, Salzano R, Fily M and Casacchia R (2006) Correlation between the specific surface area and the short wave infrared (SWIR) reflectance of snow. *Cold Reg. Sci. Technol.*, **46**(1), 60–68 (doi: 10.1016/j.coldregions.2006.06.002)

Domine F and 7 others (2008) Snow physics as relevant to snow photochemistry. *Atmos. Chem. Phys.*, **8**(2), 171–208 (doi: 10.5194/acp-8-171-2008)

Dozier J and Painter TH (2004) Multispectral and hyperspectral remote sensing of alpine snow properties. *Annu. Rev. Earth Planet. Sci.,* **32**, 465–494 (doi: 10.1146/annurev.earth.32.101802.120404)

Dozier J, Davis RE and Perla R (1987) On the objective analysis of snow microstructure. *IAHS Publ.* 162 (Symposium at Davos 1986 – *Avalanche Formation, Movement and Effects*), 49–59

Fierz C and 8 others (2009) *The international classification for seasonal snow on the ground*. (IHP Technical Documents in Hydrology 83) UNESCO–International Hydrological Programme, Paris

Flanner MG and Zender CS (2006) Linking snowpack microphysics and albedo evolution. *J. Geophys. Res.*, **111**(D12), D12208 (doi: 10.1029/2005JD006834)

Flin F and 9 others (2005) Adaptive estimation of normals and surface area for discrete 3-D objects: application to snow binary data from x-ray tomography. *IEEE Trans. Image Process.*, **14**(5), 585–596 (doi: 10.1109/TIP.2005.846021)

Gallet J-C, Domine F, Zender CS and Picard G (2009) Measurement of the specific surface area of snow using infrared reflectance in an integrating sphere at 1310 and 1550 nm. *Cryosphere*, **3**(2), 167–182 (doi: 10.5194/tc-3-167-2009)

Giddings JC and LaChapelle E (1961) Diffusion theory applied to radiant energy distribution and albedo of snow. *J. Geophys. Res.*, **66**(1), 181–189 (doi: 10.1029/JZ066i001p00181)

Grenfell TC and Warren SG (1999) Representation of a nonspherical ice particle by a collection of independent spheres for scattering and absorption of radiation. *J. Geophys. Res.*, **104**(D24), 31 697–31 709 (doi: 10.1029/2005JD005811)

Hall DK, Riggs GA and Salomonson VV (1995) Development of methods for mapping global snow cover using Moderate Resolution Imaging Spectroradiometer (MODIS) data. *Remote Sens. Environ.*, **54**(2), 127–140 (doi: 10.1016/0034-4257(95)00137-P)

Hall DK, Riggs GA, Salomonson VV, DiGirolamo N and Bayr KJ (2002) MODIS snow-cover products. *Remote Sens. Environ.*, **83**(1–2), 181–194 (doi: 10.1016/S0034-4257(02)00095-0)

Hallikainen MT, Ulaby FT and Van Deventer TE (1987) Extinction behavior of dry snow in the 18- to 90-GHz range. *IEEE Trans. Geosci. Remote Sens.*, **25**(6), 737–745 (doi: 10.1109/TGRS.1987.289743)

Hirashima H, Nishimura K, Yamaguchi S, Sato A and Lehning M (2008) Avalanche forecasting in a heavy snowfall area using the snowpack model. *Cold Reg. Sci. Technol.*, **51**(2–3), 191–203 (doi: 10.1016/j.coldregions.2007.05.013)

Huang C, Margulis SA, Durand MT and Musselman KN (2012) Assessment of snow grain-size model and stratigraphy representation impacts on snow radiance assimilation: forward modeling evaluation. *IEEE Trans. Geosci. Remote Sens.*, **50**(11), 4551–4564 (doi: 10.1109/TGRS.2012.2192480)

Jin Y-Q (1993) *Electromagnetic scattering modelling for quantitative remote sensing*. World Scientific, Singapore

Kokhanovsky AA and Zege EP (2004) Scattering optics of snow. *Appl. Opt.*, **43**(7), 1589–1602 (doi: 10.1364/AO.43.001589)

Langlois A and 8 others (2010) On the relationship between snow grain morphology and *in-situ* near infrared calibrated reflectance photographs. *Cold Reg. Sci. Technol.*, **61**(1), 34–42 (doi: 10.1016/j.coldregions.2010.01.004)

Langlois A, Royer A, Derksen C, Montpetit B, Dupont F and Goïta K (2012) Coupling the snow thermodynamic model SNOWPACK with the microwave emission model of layered snowpacks for subarctic and arctic snow water equivalent retrievals. *Water Resour. Res.*, **48**(12), W12524 (doi: 10.1029/2012WR012133)

Legagneux L, Cabanes A and Domine F (2002) Measurement of the specific surface area of 176 snow samples using methane adsorption at 77 K. *J. Geophys. Res.*, **107**(D17), 4335 (doi: 10.1029/2001JD001016)

Lehning M, Bartelt P, Brown B, Fierz C and Satyawali P (2002a) A physical SNOWPACK model for the Swiss avalanche warning. Part II: snow microstructure. *Cold Reg. Sci. Technol.*, **35**(3), 147–167 (doi: 10.1016/S0165-232X(02)00072-1)

Lehning M, Bartelt P, Brown B and Fierz C (2002b) A physical SNOWPACK model for the Swiss avalanche warning. Part III: meteorological forcing, thin layer formation and evaluation. *Cold Reg. Sci. Technol.*, **35**(3), 169–184 (doi: 10.1016/S0165-232X(02)00072-1)

Martinec J and Rango A (1986) Parameter values for snowmelt runoff modelling. *J. Hydrol.*, **84**(3–4), 197–219 (doi: 10.1016/0022-1694(86)90123-X)

Matzl M and Schneebeli M (2006) Measuring specific surface area of snow by near-infrared photography. *J. Glaciol.*, **52**(179), 558–564 (doi: 10.3189/172756506781828412)

Matzl M and Schneebeli M (2010) Stereological measurement of the specific surface area of seasonal snow types: comparison to other methods, and implications for mm-scale vertical profiling. *Cold Reg. Sci. Technol.*, **64**(1), 1–8 (doi: 10.1016/j.coldregions.2010.06.006)

Mätzler C (2002) Relation between grain-size and correlation length of snow. *J. Glaciol.*, **48**(162), 461–466 (doi: 10.3189/172756502781831287)

Mätzler C and Wiesmann A (1999) Extension of the microwave emission model of layered snowpacks to coarse-grained snow. *Remote Sens. Environ.*, **70**(3), 317–325 (doi: 10.1016/S0034-4257(99)00047-4)

Maurer EP, Rhoads JD, Dubayah RO and Lettenmaier D (2003) Evaluation of the snow-covered area data product from MODIS. *Hydrol. Process.*, **17**(1), 59–71 (doi: 10.1002/hyp.1193)

Mognard NM (2003) Global snow-cover evolution from twenty years of satellite passive microwave data. In *Proceedings of International Geoscience and Remote Sensing Symposium (IGARSS 2003), 21–25 July 2003, Toulouse, France, Vol. 4*. Institute of Electrical and Electronics Engineers, Piscataway, NJ, 2838–2840

Montpetit B and 8 others (2012) New shortwave infrared albedo measurements for snow specific surface area retrieval. *J. Glaciol.*, **58**(211), 941–952 (doi: 10.3189/2012JoG11J248)

Painter TH, Molotch NP, Cassidy M, Flanner M and Steffen K (2007) Contact spectroscopy for determination of stratigraphy of snow optical grain size. *J. Glaciol.*, **53**(180), 121–127 (doi: 10.3189/172756507781833947)

Picard G, Arnaud L, Domine F and Fily M (2009) Determining snow specific surface area from near-infrared reflectance measurements: numerical study of the influence of grain shape. *Cold Reg. Sci. Technol.*, **56**(1), 10–17 (doi: 10.1016/j.coldregions.2008.10.001)

Pielmeier C and Schneebeli M (2003) Stratigraphy and changes in hardness of snow measured by hand, rammsonde and snow micro penetrometer; a comparison with planar sections. *Cold Reg. Sci. Technol.*, **37**(3), 393–405 (doi: 10.1016/S0165-232X(03)00079-X)

Pirinen P, Simola H, Aalto J, Kaukoranta J-P, Karlsson P and Ruuhela R (2012) *Climatological statistics of Finland 1981–2012*. (Report No. 2012-1) Finnish Meteorological Institute, Helsinki

Pulliainen J and Hallikainen M (2001) Retrieval of regional snow water equivalent from space-borne passive microwave observations. *Remote Sens. Environ.*, **75**(1), 76–85 (doi: 10.1016/S0034-4257(00)00157-7)

Pulliainen JT, Grandell J and Hallikainen MT (1999) HUT snow emission model and its applicability to snow water equivalent retrieval. *IEEE Trans. Geosci. Remote Sens.*, **37**(3), 1378–1390 (doi: 10.1109/36.763302)

Rasmus S, Gronholm S, Lehning T, Rasmus M and Kulmala M (2007) Validation of the SNOWPACK model in five different snow zones in Finland. *Boreal Environ. Res.*, **12**(4), 467–488

Roy V, Goïta K, Royer R, Walker AE and Goodison BE (2004) Snow water equivalent retrieval in a Canadian boreal environment from microwave measurements using the HUT snow emission model. *IEEE Trans. Geosci. Remote Sens.*, **42**(9), 1850–1859 (doi: 10.1109/TGRS.2004.832245)

Schweizer J, Bellaire S, Fierz C, Lehning M and Pielmeier C (2006) Evaluating and improving the stability predictions of the snow cover model SNOWPACK. *Cold Reg. Sci. Technol.*, **46**(1), 52–59 (doi: 10.1016/j.coldregions.2006.05.007)

Shaffrey LC and 25 others (2009) U.K. HiGEM: the new UK high-resolution global environment model – model description and basic evaluation. *J. Climate*, **22**(8), 1861–1896 (doi: 10.1175/2008JCLI2508.1)

Stogryn A (1986) A study of the microwave brightness temperature of snow from the point of view of the strong fluctuation theory. *IEEE Trans. Geosci. Remote Sens.*, **24**(2), 220–231 (doi: 10.1109/TGRS.1986.289641)

Sturm M, Morris K and Massom R (1998) The winter snow cover of the West Antarctic pack ice: its spatial and temporal variability. In Jeffries MO ed. *Antarctic sea ice: physical processes, interactions and variability*. (Antarctic Research Series 74) American Geophysical Union, Washington, DC, 1–18

Sun S, Jin J and Xue Y (1999) A simple snow–atmosphere–soil transfer model. *J. Geophys. Res.*, **104**(D16), 19 587–19 597 (doi: 10.1029/1999JD900305)

Tedesco M and Kim EJ (2006) Intercomparison of electromagnetic models for passive microwave remote sensing of snow. *IEEE Trans. Geosci. Remote Sens.*, **44**(10), 2654–2666 (doi: 10.1109/TGRS.2006.873182)

Tsang L and Kong JA (1981) Scattering of electromagnetic waves from random media with strong permittivity fluctuations. *Radio Sci.*, **16**, 303–320 (doi: 10.1029/RS016i003p00303)

Tsang L, Kong JA and Shin RT (1985) *Theory of microwave remote sensing*. Wiley, New York

Vionnet V and 7 others (2012) The detailed snowpack scheme Crocus and its implementation in SURFEX v7.2. *Geosci. Model Dev.*, **5**(3), 773–791 (doi: 10.5194/gmd-5-773-2012)

Wiesmann A and Mätzler C (1999) Microwave emission model of layered snowpacks. *Remote Sens. Environ.*, **70**(3), 307–316 (doi: 10.1016/S0034-4257(99)00046-2)

Wiesmann A, Mätzler C and Weise T (1998) Radiometric and structural measurements of snow samples. *Radio Sci.*, **33**(2), 273–289 (doi: 10.1029/97RS02746)

Wiscombe WJ and Warren SG (1980) A model for the spectral albedo of snow. I. Pure snow. *J. Atmos. Sci.*, **37**(12), 2712–2733 (doi: 10.1175/1520-0469(1980)037<2712:AMFTSA>2.0.CO;2)

APPENDIX

Table 5. SNOWPACK.ini file parameters

Data step length	30 min	
Calculation step length	15 min	
Height of meteo values	2.0 m	
Height of wind value	22.0 m	
Enforce measured snow heights	True	
SW mode	2	Incoming and reflected shortwave radiation are both measured
Neutral	1	Force Monin–Obukhov formulation to assume neutral conditions
Canopy	False	Open area
Measure TSS	False	Measured surface temperature not available
Change BC	False	
Incoming longwave	False	
Snow redistribution	True	
SNP SOIL	True	Soil layers defined
Soil flux	False	
Geo heat	0.06	
Advanced settings	Default variant, default settings	

Table 6. SNOWPACK.sno file parameters

Latitude	7571768	Sodankylä, northern Finland
Longitude	484270	
Altitude	180 m	
Slope Angle	0.0°	
Slope Azi	0.0°	
nSoilLayerData	1	Soil homogeneous at least the first 1.5 m
nSnowLayerData	0	
Bare Soil z0	0.02	
Soil Albedo	0.2	
CanopyHeight	10.0 m	
CanopyLeafAreaIndex	0.0	
CanopyDirect-Throughfall	0.0	
WindScalingFactor	1.0	
Profiledate	01.08.2011	
Soil layer thickness	1.5 m	
Volume fraction ice	0.00	
Volume fraction water	0.15	Calculated from automatic soil moisture measurements
Volume fraction void	0.15	
Volume fraction soil	0.7	
Soil density	1700 kg m^{-3}	Soil approximated as compact sandy soil. Values estimated according to the volumetric fraction of water after de Vries (1963)
Soil heat conductivity	1.5 W m^{-1} K^{-1}	
Soil specific heat	1200 J kg^{-1} K^{-1}	

MS received 27 January 2014 and accepted in revised form 5 October 2014

Publication 5

A. Kontu, J. Lemmetyinen, J. Vehviläinen, L. Leppänen, J. Pulliainen. 2017. Coupling SNOWPACK-modeled grain size parameters with the HUT snow emission model. *Remote Sensing of Environment*, 194, 33-47. doi: 10.1016/j.rse.2016.12.021.

Remote Sensing of Environment 194 (2017) 33–47

Contents lists available at ScienceDirect

Remote Sensing of Environment

journal homepage: www.elsevier.com/locate/rse

Coupling SNOWPACK-modeled grain size parameters with the HUT snow emission model

Anna Kontu *, Juha Lemmetyinen, Juho Vehviläinen, Leena Leppänen, Jouni Pulliainen

Finnish Meteorological Institute, Arctic Research, Tähteläntie 62, 99600 Sodankylä, Finland

ARTICLE INFO

Article history:
Received 2 August 2016
Received in revised form 12 December 2016
Accepted 30 December 2016
Available online xxxx

Keywords:
Snow grain size
Microwave radiometry
SNOWPACK
HUT snow emission model

ABSTRACT

We studied whether the physical snow evolution model SNOWPACK could be used together with the HUT snow emission model to simulate microwave brightness temperatures (TB) of snow cover and to parameterize key a priori variables in the retrieval of snow water equivalent (SWE). We used the extensive in situ measurement data set collected in Sodankylä, Finland, during the Nordic Snow Radar Experiment (NoSREx) campaign in 2009–2013 to model the evolution of snow with SNOWPACK. Resulting snow profiles were validated with manual in situ measurements. Mean agreement scores (for a winter) were 0.85–0.91 for traditional grain size, 0.74–0.75 for optical grain size, 0.65–0.80 for density, and 0.71–0.83 for temperature. Grain sizes modeled with SNOWPACK were compared to effective grain size retrieved from tower-based microwave radiometer measurements. The bias and RMS error of SNOWPACK optical grain size were −0.03 mm and 0.20 mm, respectively, and those of SNOWPACK traditional grain size were 0.30 mm and 0.33 mm, respectively. SNOWPACK snow profiles were used as input to the HUT snow emission model for calculation of TB, which was compared to microwave radiometer measurements. TB calculated with SNOWPACK optical grain size exhibited lower biases (from −12.5 K to 16.2 K, depending on year and frequency) and RMS errors (from 3.3 K to 18.5 K) than TB calculated with SNOWPACK traditional grain size (bias from −42.2 K to −9.9 K, RMS error from 12.0 K to 44.7 K). Grain sizes, temperature, and density modeled with SNOWPACK were used as a priori snow data in the retrieval of SWE from tower-based microwave radiometer observations. The lowest overall bias and RMS error were reached when traditional grain size from SNOWPACK was used, either directly with modelled snow density and temperature (−33 mm and 58 mm, respectively) or with an effective grain size correction and static snow density and temperature applied (22 mm and 59 mm, respectively).

1. Introduction

Seasonal snow has a significant effect on the Earth's surface energy balance (Groisman et al., 1994) and surface-atmosphere interaction through its high albedo and low thermal conductivity. It also affects hydrological processes by storing and releasing water, making snow crucial to one-sixth of the world's population living in areas where solid precipitation dominates annual runoff (Barnett et al., 2005). The magnitude of snow feedback mechanisms on climate change remains uncertain (Qu and Hall, 2014). Therefore accurate information on snow cover parameters, especially snow water equivalent (SWE), is needed in many applications, e.g. as input and validation data for climate models.

Global snow data are available from in situ measurements and remote sensing observations. In situ measurement networks in the areas covered with seasonal snow are insufficient due to difficulties in maintaining and operating measurement stations in sparsely populated areas with minimal infrastructure. Moreover, measurements are concentrated in easily accessible areas, and point-wise measurements do not necessarily represent the overall snow conditions well. Remote sensing offers unique possibilities for global daily snow monitoring. Passive microwave remote sensing of SWE is based on the extinction of microwave radiation, originating from soil, in the snowpack. Extinction is a sum of absorption and scattering, which vary with frequency, the amount of snow, and its dielectric and structural properties. Retrieval of SWE is often achieved from the difference of a higher (typically 36.5 GHz) and a lower (typically 18.7 GHz) frequency brightness temperature (TB). The first algorithm to exploit this relationship between TB and SWE was introduced by Chang et al. (1987). The algorithm relies on an empirical, linear relationship of the frequency difference and SWE. Variants of the algorithm have been used with SSM/I (Special

* Corresponding author.
E-mail addresses: anna.kontu@fmi.fi (A. Kontu), juha.lemmetyinen@fmi.fi (J. Lemmetyinen), juho.vehvilainen@fmi.fi (J. Vehviläinen), leena.leppanen@fmi.fi (L. Leppänen), jouni.pulliainen@fmi.fi (J. Pulliainen).

http://dx.doi.org/10.1016/j.rse.2016.12.021
0034-4257/

Sensor Microwave Imager) and AMSR-E (Advanced Microwave Scanning Radiometer for Earth Observing System) (Kelly and Chang, 2003). However, the algorithm assumes constant snow density and grain size, and therefore exhibits large errors on areas where snow conditions differ from the assumptions (Davenport et al., 2012). In the newer AMSR-E algorithm (Kelly, 2009) this has been taken into account with coefficients adjusting with the measured TBs. This modification partially compensates for changes in snow microstructure and density.

An alternative method for SWE retrieval is to utilize an inversion of a forward model for microwave emission of snow-covered ground. Emission models published in the literature include Microwave Emission Model of Layered Snowpacks (MEMLS) (Wiesmann and Mätzler, 1999), Dense Media Radiative Transfer Multi-Layer (DMRT-ML) model (Picard et al., 2013), and the Helsinki University of Technology (HUT) snow emission model (Pulliainen et al., 1999). In this paper we focus on the HUT model. It is operationally used in the GlobSnow SWE retrieval algorithm, which also incorporates the assimilation of in situ snow observations with passive microwave retrievals (Pulliainen, 2006; Takala et al., 2011). We apply the original 1-layer version (Pulliainen et al., 1999) of the HUT model in the retrievals of an effective grain size and SWE, and the modified n-layer version (Lemmetyinen et al., 2010) in the TB simulations.

Snow microstructure is the key parameter affecting the scattering of microwave radiation in snow. Snow consists of a continuous ice structure and pore space (Fierz et al., 2009), and may contain ice, air, liquid water, water vapor, and impurities. After initial precipitation, natural snowpacks form complex structures of ice grains in different stages of metamorphism. The internal structural variations of snow at distances comparable to wavelength affect scattering of electromagnetic waves in the snowpack, and must therefore be incorporated in SWE retrieval algorithms. In microwave emission models, snow microstructure is typically described with a proxy parameter related to grain size: MEMLS uses correlation length (p_c), DMRT-ML uses the diameter of spheres representing snow grains together with a stickiness parameter, and the HUT model uses traditional grain size (E). Recently efforts have been made to simulate scattering behavior of microwaves in snow through applying a numerical solution to Maxwell's equations of simulated microstructures (Tsang et al., 2013). All the symbols for different snow parameters and their short descriptions are listed in Table A1 in the Appendix.

Arguably the best metric to describe the scattering behavior of microwaves in snow is the correlation length, p_c (Mätzler, 2002). Correlation length can be objectively determined from structural samples of natural snowpacks (Wiesmann et al., 1998) using e.g. microcomputed tomography (micro-CT) of snow samples (Heggli et al., 2009), but this method is time-consuming and not suitable for large-scale use. A novel method of extracting p_c from SnowMicroPen measurements (Proksch et al., 2015) shows promising results, but some problems with calibration yet remain. Another emerging method is to estimate correlation length from near-infrared (NIR) photography (Toure et al., 2008).

Traditional grain size E is the average of the greatest extension of individual grains in a layer (Fierz et al., 2009). It is measured in the field by comparing snow grains to a grid and estimating grain size visually. Empirical relationships between E and p_c can be established (Durand et al., 2008; Hallikainen et al., 1987), but they may not hold for the whole range of natural snow types. While it is possible to measure the size of a single grain with great accuracy, variability between observers arises e.g. from the definition of a single grain in case they are bonded, and from the definition of the average grain size of a layer, which is difficult if a wide distribution of different grain sizes and shapes exist in a layer, as is often the case with e.g. depth hoar. Thus the method is subjective, and the variation between estimations by different observers generally increases with the age of the snow sample (and the variation of grain sizes in a layer) (Baunach et al., 2001). Moreover, the greatest extension of a snow grain is not in all cases the appropriate measure governing the scattering of microwaves in snow (Mätzler, 2002); even though the diameter of a dendritic snow flake equals that of a large depth hoar crystal, we may assume that their effect on microwave scattering differs from one another. Despite these problems, observations of E were used in the development of the extinction coefficient model (Hallikainen et al., 1987) applied in the HUT snow emission model, and field measurements of E are therefore relevant to this study.

Optical grain size D_o is the diameter of identical ice spheres that have the same optical properties as the snow in question. The same properties are achieved when surface area to volume ratio (or specific surface area, SSA) of the spheres is equal to that of snow grains (Grenfell and Warren, 1999). SSA is becoming the most widely used microstructure parameter because it is clearly defined, reproducible, and relatively easy to measure in the field. It can be measured using several methods, including methane adsorption (Legagneux et al., 2002), NIR photography (Matzl and Schneebeli, 2006), spectroscopy (Painter et al., 2007) and IR reflectance (Gallet et al., 2009). In addition, D_o and SSA can be related to p_c through theoretical relations (Debye et al., 1957). However, the relation of microwave scattering in snow to p_c, derived through D_o, is not straightforward; empirical relations have been proposed by e.g. Mätzler (2002). Roy et al. (2013) argued that since larger particles scatter much more microwave radiation than smaller ones, a collection of identical spheres does not represent a collection of variable sized spheres with the same SSA in the microwave range.

The GlobSnow algorithm presents a method to compensate for the effects of spatio-temporal variations of snow microstructure in the retrieval of SWE. In the GlobSnow algorithm, an effective grain size (a proxy parameter for snow microstructure) is first retrieved for observations of TB coinciding with meteorological stations where in situ snow depth (HS) data are available. This is done by finding for each station the grain size value which minimizes the error of modeled TB compared to the satellite observation, giving an effective grain size applicable for each station location. Spatial (Kriging) interpolation is then used to extend the retrieved effective grain size over the whole area of interest. The spatially interpolated effective grain size values are then used as a priori information in the retrieval of SWE from the satellite observations. The method is thoroughly presented by Pulliainen (2006) and Takala et al. (2011) and (2016). However, the GlobSnow algorithm has been criticized (Richardson et al., 2014), since the retrieval of effective grain size using constant density is unphysical; all errors in e.g. density and vegetation modeling are corrected by adjusting the effective grain size. Nevertheless, Lemmetyinen et al. (2015) studied the ability of the HUT snow emission model to account for spatial and temporal changes in snow structure using ground-based and airborne radiometer measurements of snow. They found that while the effective grain size accounts for changes in snow structure, vegetation properties and other uncertainties, the retrieved effective grain size can still be related to physical properties of snow for a wide temporal and spatial scale of snow conditions, including satellite scale observations. This suggests that information on snow physical properties, obtained from a physical snow evolution model, may be used as a priori information to enhance a SWE retrieval scheme based on the HUT model. One such snow cover model is SNOWPACK (Bartelt and Lehning, 2002; Lehning et al., 2002a, 2002b). We applied it here to model grain size, density and temperature to be used as a priori data in the HUT snow emission model.

This study focused on the application of E and D_o in the context of forward simulations of microwave emission and retrieval of SWE. We studied the possibility to use snow parameters simulated with SNOWPACK with the HUT snow emission model to increase the accuracy of TB simulation and SWE retrieval. Specifically, we applied experimental data from four consecutive winters, from 2009 to 2013, to

1. validate SNOWPACK snow profiles by comparing them to in situ measurements;
2. compare E and D_o from SNOWPACK to effective grain size retrieved from tower-based microwave radiometer measurements;

3. compare tower-based radiometer measurements to TBs simulated with the HUT snow emission model using a priori snow data from SNOWPACK; and
4. apply snow data from SNOWPACK as a priori information in the inversion of SWE from tower-based microwave radiometer observations, and compare the results to field measurements of SWE.

A flow diagram of the work is shown in Fig. 1. The diagram includes the measurement data sets, the models and the parameters compared in each of the four steps. The measurement data sets and the measurement site are described in Section 2. Section 3 presents the models and their parameters. Results and methods used to derive them are detailed in Section 4. The results are discussed in Section 5, and conclusions are given in Section 6.

2. Data

2.1. Measurement sites

All data used in this study were measured at the Arctic Research Centre of the Finnish Meteorological Institute (FMI-ARC) at 67.368° N, 26.633° E in Sodankylä, Finland during the Nordic Snow Radar Experiment (NoSREx (Lemmetyinen et al., 2016a)). The area is mainly covered with sparse boreal pine forest. Measurements were conducted at two sites at the institute area: the Intensive Observation Area (IOA) and the weather station. The main measurement site, the IOA, is located in a forest opening with a diameter of about 40 m. The ground at the IOA is mainly covered with a thin (~2 cm) layer of lichen and some sparse, low (~10 cm) heather. Any tree saplings and other higher vegetation were removed every summer. The soil is composed of sand (70%), silt (29%) and clay (1%) with a thin organic layer on top. All the measurements at the IOA were conducted within 20 m of each other, but no in situ measurements were performed at the radiometer footprints. The weather station (WMO code 02836) is also situated in an opening surrounded by sparse pine trees at a distance of 500 m from the IOA.

Based on 30-year (1981–2010) meteorological averages (Pirinen et al., 2012), the first snow typically falls in Sodankylä in October, while snow melt-off takes place in mid-May. The snow maximum of about 80 cm occurs in late March. Snow structure, especially the existence of ice layers, varies significantly between winters, depending on air temperature changes before and during snow season. Air temperatures down to −40 °C are typical in January and February, while temperatures around 0 °C are possible in every month throughout the winter, often resulting in melt-refreeze ice layers.

2.2. Microwave radiometer measurements

Snow microwave TB was measured with a commercial four-frequency dual-polarization radiometer (RPG-8CH-DP) manufactured by Radiometer Physics GmbH, Meckenheim, Germany. The instrument was mounted on a 4.1 m high tower at the IOA and set to perform a scan from incidence angles of 30 to 70° off nadir in 5° steps every 3–4 h. Vertical polarization (V-pol) measurements at frequencies 18.7 and 36.5 GHz and an incidence angle of 50° were used in this study. The average value of 1 s samples, integrated over a period of 180 s at one incidence angle, is referred to as one measurement in the subsequent analysis. Due to malfunctions and maintenance of the instrument, there are several long gaps in the data. Altogether 2795 measurements in dry snow conditions (HS > 0 cm, $T_{air} < 0$ °C, $T_{snow} < 0$ °C) were used. The radiometer was calibrated with a cold target cooled with liquid nitrogen and a target at ambient temperature at the beginning of each snow season. The calibration was verified a few times during the winter by measuring the ambient temperature target. A detailed account of the

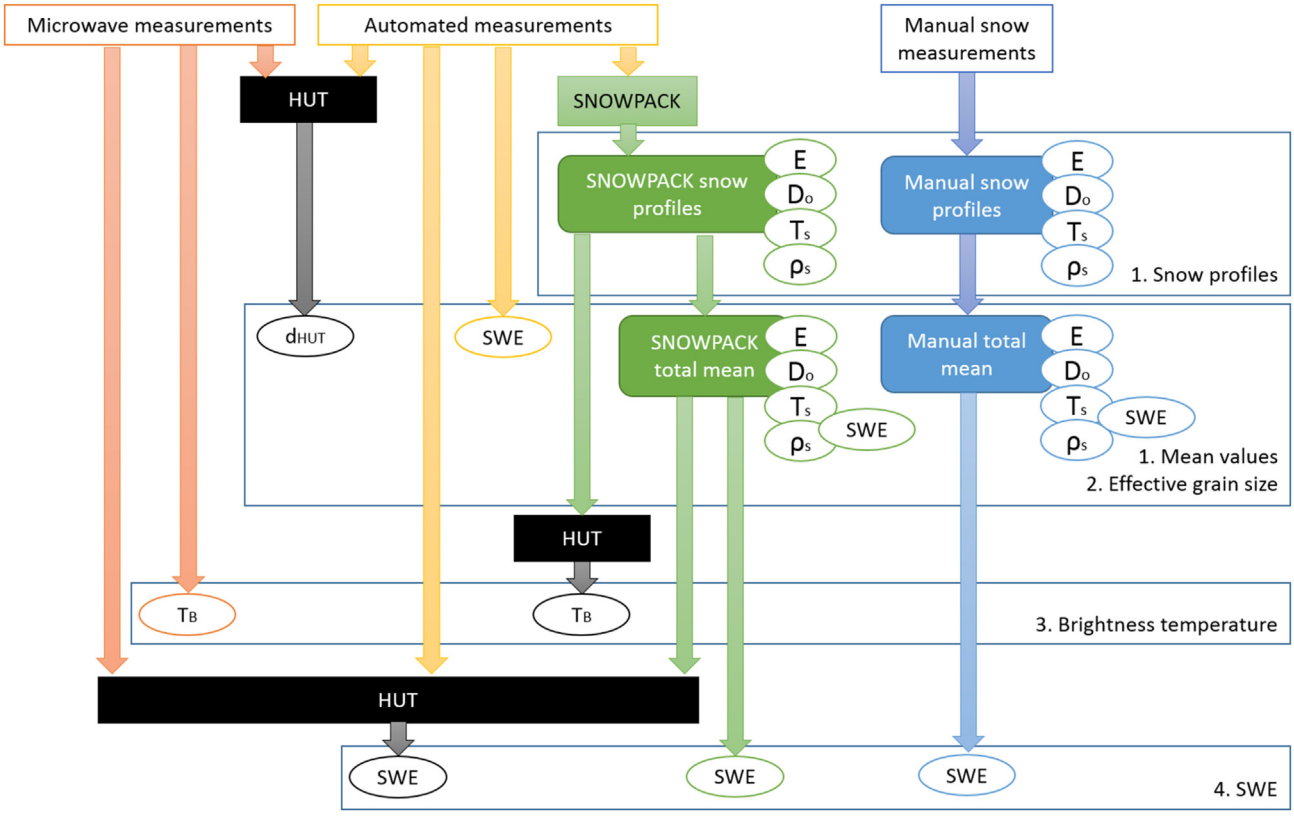

Fig. 1. Work and data flow. 'HUT' refers to the HUT snow emission model and 'SNOWPACK' to the physical snow model SNOWPACK, described in Section 3. The numbers on the right refer to the four goals of the paper, as well as to subsections in Section 4, where the compared parameters and their derivation are explained and the methods and results for each comparison are detailed. The symbols are explained in Appendix Table A1.

measurement protocols is given by Lemmetyinen et al. (2016a, 2016b, 2016c).

2.3. Snow profile

A snow pit was measured at least once a week during the winters. There were some intensive observation periods with more frequent snow pit measurements (even several times a day), especially during the winter of 2009–2010. Snow pit measurements were concentrated on an area of approximately 5 m × 5 m at the IOA outside the field of view of the radiometer. A new snow pit was dug every time at least 0.5 m off from the previous pits to avoid changes in the snow structure resulting from former measurements and effects of solar radiation and air temperature changes on the excavated pit wall. Thus, in addition to temporal changes, the snow pit data set also includes the effects of spatial variation due to uneven soil surface and vegetation.

The inspected snow pit wall was shadowed from direct sunlight. The wall was smoothed and layer boundaries were determined visually and manually from density, hardness, and grain size and type differences according to the guidelines of Fierz et al. (2009). A sample of snow (tens of grains) from each layer was placed on a screen with a 1-mm grid and macro-photographed. Grain size E was estimated in the field, but for this study, E_{pit} was reanalyzed from the photographs to reduce the random error in the original data induced by e.g. changing observers. There might be a difference between grain size interpretation from a photograph and from snow grains in the field, but this was assumed to be a minor error source compared to the random error in the original field observations.

After filtering out measurements of poor quality (e.g. photographs were missing or unfocused, or the number of layers deviated significantly from other measurements), 93 pits measured in dry snow conditions were used in this study. The manual measurement methods and instruments are described in detail by Leppänen et al. (2016). In addition to E_{pit}, profiles of snow temperature (T_s), density (ρ_s, measured with a 250 cm^3 wedge snow sampler and scales or the SnowFork (Sihvola and Tiuri, 1986)), and SWE, as well as bulk snow depth, density, and SWE, were recorded. All other profiles except E_{pit} were measured at fixed intervals of 5 cm (density and SWE from a sampler) or 10 cm (temperature, density from the SnowFork). Parameter values for each snow layer were calculated by linear interpolation from the values measured inside the layer, or (if there were no measurements inside the layer) of those directly above and below the layer. Density from the SnowFork was used if a sampler measurement was not available. Based on several years of comparison measurements (unpublished), typically density measured with the SnowFork is 40 kg/m^3 lower than density from the sampler. This difference was taken into account in the data processing by adjusting the densities measured with the SnowFork.

2.4. Specific surface area

Snow SSA was measured with the IceCube instrument, manufactured by A2 Photonic Sensors, Grenoble, France. The measurement is based on the reflectance of infrared (IR) radiation of a snow sample placed inside an integrating sphere (Gallet et al., 2009). A snow sample was taken from the snowpack into a sample holder, smoothed with a spatula and placed inside IceCube for measurement. The thickness of each snow sample was 3 cm, and the whole snowpack was sampled, excluding hard ice layers, which are extremely difficult to sample for IceCube measurement. SSA was measured from the same snow pit wall as E_{pit}. IceCube was calibrated by measuring the reflectances of six Spectralon plates (reflectances 0.076–0.986) before and after snow sampling. Optical grain size (D_{oIC}) profile was calculated from SSA measurements so that (Gallet et al., 2009)

$$D_{oIC} = 6/(\rho_{ice} \cdot SSA), \quad (1)$$

where $\rho_{ice} = 917$ kg/m^3 is the density of ice and SSA is given in m^2/kg. A total of 27 SSA profiles of dry snowpack were available since January 2012.

New very light snow needed to be compacted appropriately into the sample holder to avoid errors caused by absorption of the IR radiation to the sample holder walls (Gallet et al., 2009). The sampling of large depth hoar grains was also problematic: the laser may reflect from only a few grains on the sample surface, and in these cases the measurement is not repeatable for a sample or a layer. If highly varying values were noticed on the field, the bottom depth hoar layers (10–20 cm) were not measured. In addition, for an accurate measurement of IR reflectance, the snow sample surface needed to be smooth, which was difficult to achieve with large grains (Gallet et al., 2009) and nearly impossible with rough icy layers. The compaction of very light snow, problems with large crystals or icy layers, and different methods in snow sample preparation induced observer-related errors to IceCube measurements, but based on unpublished test measurements these were assumed to have a much smaller effect (in the worst case ±0.1 mm) on the resulting D_{oIC} than the observer-related errors in the measurement of E_{pit}. The calibration-related errors were small; based on Leppänen et al. (2015), the maximum difference in D_{oIC} caused by differences between calibrations before and after snow sampling was 0.113 mm, reflecting the stability of the IceCube instrument and the repeatability of D_{oIC} measurements.

2.5. Automated snow, meteorological, and soil measurements

Snow depth (Campbell SR50 acoustic sensor), snow temperature (Campbell 107-L), soil temperature (Vaisala QMT103), soil permittivity (Delta-T ML2x) and SWE were measured automatically at the IOA. SWE was measured with a prototype Gamma Water Instrument (GWI) manufactured by Astrock Oy, Sodankylä, Finland. The device measures the spectral response of a Cesium source placed at the soil surface. With build-up of snow cover, weakening of the detected radiation at certain spectral bands can be related to the water equivalent of snow in the signal path (Hatakka et al., 1998). These gamma radiation measurements were calibrated with weekly manual bulk SWE measurements. Soil permittivity (Delta-T Devices ML2x) was measured in two locations at the IOA at −2 cm depth. The average of these two sensors was used. The correction method described by Lemmetyinen et al. (2016b) was applied to the permittivity data. Air temperature (Vaisala PT100), relative humidity (Vaisala HMP), wind speed (Vaisala WAA25) and direction (Vaisala WAV15), and incoming and outgoing short wave radiation (Kipp&Zonen CM11) were measured at the weather station.

3. Models

3.1. SNOWPACK

SNOWPACK is a 1-D physically based finite-element snow evolution model developed at the WSL Institute for Snow and Avalanche Research (SLF), Switzerland. It calculates the evolution of snowpack from meteorological input parameters. The characteristics of numerical setup, snow microstructure, and initial and driving parameters of the model are described by Bartelt and Lehning (2002), Lehning et al. (2002a, 2002b) and Lehning et al. (2002a, 2002b), respectively.

SNOWPACK includes three types of snow metamorphism: equitemperature (ET, if temperature gradient $\partial T_s/\partial z < 5$ K/m), temperature gradient (TG, if temperature gradient $\partial T_s/\partial z \geq 5$ K/m) and wet snow metamorphism (if liquid water is present). Snow grains are described with two size parameters, grain size and bond size, and two shape parameters, dendricity (d) and sphericity (s). Dendricity describes the part of fresh and dendritic snow remaining in a snow layer, and sphericity describes the ratio of rounded versus faceted shapes. Dendricity and sphericity vary from 0 to 1, and are set to 1 and 0.5 for new snow, respectively. As snow gets older, snow develops either towards rounded

grains (sphericity increases) or faceted grains (sphericity decreases), depending on environmental conditions. Dendricity decreases in both cases. When dendricity reaches 0, snow consists of either rounded or faceted crystals, and the branched new snow forms have disappeared (Brun et al., 1992; Proksch, 2010). The following equations are used in SNOWPACK for the rate of change in sphericity ($\dot{s}$, unit 1/s) and dendricity ($\dot{d}$, unit 1/s) in ET and TG conditions (Proksch, 2010):

$$\dot{s}(t) = \begin{cases} 0.2 \cdot 10^8 e^{-\frac{6000}{T_s}} \left(5 - \left|\frac{\partial T_s}{\partial z}\right|\right), & \text{if } \frac{\partial T_s}{\partial z} < 5.0\,\text{K/m} \wedge s < 0.49 \\ 0.5 \cdot 10^8 e^{-\frac{6000}{T_s}} \left(5 - \left|\frac{\partial T_s}{\partial z}\right|\right), & \text{if } \frac{\partial T_s}{\partial z} < 5.0\,\text{K/m}, \\ -0.5 \cdot 10^8 e^{-\frac{6000}{T_s}} \left(\frac{\left|\frac{\partial T_s}{\partial z}\right| - 5}{17}\right), & \text{if } \frac{\partial T_s}{\partial z} \geq 5.0\,\text{K/m}, \end{cases} \quad (2)$$

$$\dot{d}(t) = \begin{cases} -2.5 \cdot 10^8 e^{-\frac{6000}{T_s}}, & \text{if } \frac{\partial T_s}{\partial z} < 5.0\,\text{K/m} \\ -3.5 \cdot 10^8 e^{-\frac{6000}{T_s}} \left(\frac{\left|\frac{\partial T_s}{\partial z}\right|}{7}\right), & \text{if } 5.0\,\text{K/m} \leq \frac{\partial T_s}{\partial z} < 15.0\,\text{K/m}, \\ -3.0 \cdot 10^8 e^{-\frac{6000}{T_s}} \left(\frac{\left|\frac{\partial T_s}{\partial z}\right|}{7}\right), & \text{else}, \end{cases} \quad (3)$$

where t is time and z is the height from the bottom of the snowpack. For new wet snow, the equations are (Lehning et al., 2002a, 2002b)

$$\dot{s}(t) = -0.5\dot{d}(t), \quad (4)$$

$$\dot{d}(t) = -\frac{\theta_m(t)^3}{16}, \quad (5)$$

where θ_m is the mass fraction of liquid water in snow. For old wet snow ($d = 0$) (Lehning et al., 2002a, 2002b),

$$\dot{s}(t) = \frac{\theta_m(t)^3}{16}. \quad (6)$$

Grain growth in ET metamorphism is based on the mixture theory model described by Brown et al. (2001) and (1999). Grain size in SNOWPACK (E_{SP}) in ET is the diameter of a sphere; however, it is not an "exact" grain size, but rather a mapping of parameters d and s to the grain size estimated manually in the field. Grain growth rate ($\dot{E}_{SP}$, unit m/s) in ET is (Lehning et al., 2002a, 2002b)

$$\dot{E}_{SP}(t) = s\left(A_1 + \frac{A_2}{r_g}\right) exp(A_3(1/T_R - 1/T_s)) \quad (7)$$

where $A_1 = 5.9 \cdot 10^{-12}$ m/s, $A_2 = 9.4 \cdot 10^{-17}$ m^2/s and $A_3 = 2.9 \cdot 10^3$ K are coefficients and $T_R = 273.15$ K.

Temperature gradient metamorphism used in SNOWPACK is described in Baunach et al. (2001). It assumes that snow grains grow as plates and the thickness of the plates stays constant. The length of a side of these plates is the TG grain size (E_{SP}) in SNOWPACK. Grain growth rate in TG ($\dot{E}_{SP}$, unit m/s) is (Proksch, 2010)

$$\dot{E}_{SP}(t) = \frac{0.5a^2\left(J_L(t) + \frac{a(t)}{\Delta z}\Delta J_{L2L}(t)\right)}{2 f_{gg} \rho_{ice} E_{SP}(0) E_{SP}(t)}, \quad (8)$$

where a is the lattice constant (distance between two grains in a regular body centered cubic structure (Baunach et al., 2001)), J_L is the intra-layer water vapor flux, ΔJ_{L2L} is the layer-to-layer water vapor transport, Δz is layer thickness, f_{gg} is an empirical geometrical factor for the approximation of real grain shape (Baunach et al., 2001; Lehning et al., 2002a, 2002b; Proksch, 2010), and $E_{SP}(0)$ is the initial grain size.

For wet snow, an empirical relationship (Brun, 1989; Lehning et al., 2002a, 2002b) for grain growth is used:

$$\dot{E}_{SP}(t) = \frac{\left(C_1 + C_2\theta_m^3\right)}{4\pi r_g(t)^2}, when\ s > 0.5, \quad (9)$$

where the two empirical constants are $C_1 = 1.11 \cdot 10^{-3}$ mm^3/day and $C_2 = 3.65 \cdot 10^{-5}$ mm^3/day. The equation and constants differ from Lehning et al. (2002a, 2002b), but they were verified from the SNOWPACK program code. There is no grain growth in wet snow in SNOWPACK before the sphericity of the grains reaches $s > 0.5$.

Calculation of the optical grain size (D_{oSP}) is based on empirical relations between parameters d, s, E_{SP} and D_{oSP} (Vionnet et al., 2012):

$$D_{oSP} = \begin{cases} 0.1 \cdot [d(1-d)(4-s)], \text{if } d > 0 \\ E_{SP} \cdot s + (1-s) \cdot max(0.4; E_{SP}/2), if\ d = 0. \end{cases} \quad (10)$$

SNOWPACK version 3.1.0 estimates both D_{oSP} and E_{SP} profiles of snow. In addition to grain sizes, SNOWPACK outputs profiles of layer thickness, density and temperature (and other parameters not used here) at 1 h intervals. We used automated measurements (detailed in Section 2.5) of air temperature, relative humidity, wind speed and direction, incoming and outgoing short wave radiation, snow depth, soil temperature and snow temperature as input parameters. Incoming and outgoing long wave radiation data were available, but large observational gaps hampered their application in simulations. SNOWPACK snow depth was forced with snow depth observations, since solid precipitation measurements (the other option for forcing) have large uncertainties (Wolff et al., 2015). The contents of model initialization files used here are listed in Appendix Tables A2 and A3.

3.2. HUT snow emission model

The HUT snow emission model calculates emissivity and TB of snow-covered ground from parameters describing soil, snow, vegetation, and atmosphere. We excluded vegetation effects from the simulations, since the measurement area was clear of vegetation protruding above the snow layer. Average downwelling atmospheric emission for the measured air temperature was calculated using a statistical model (Pulliainen et al., 1993). The soil reflectivity model is described in Section 3.3.

The original version of the HUT snow emission model considers snow as one homogenous layer on top of soil (Pulliainen et al., 1999). Later the possibility to simulate several snow, ice, and water layers was added (Lemmetyinen et al., 2010). This n-layer HUT snow emission model was used in the forward TB simulations, since profile snow data were available. The original 1-layer version was used in the SWE retrieval.

3.3. Soil reflectivity model

Soil surface reflectivity was calculated with a model by Wang and Choudhury (1981). In a recent comparison (Montpetit et al., 2015), the model was found to be frequency independent and easier to use than the model by Wegmüller and Mätzler (1999), often used with the HUT snow emission model. According to Wang and Choudhury (1981), soil surface reflectivity Γ_p at polarization p and incidence angle θ is

$$\Gamma_p = \left[(1-Q)\Gamma_p^{Fresnel} + Q\Gamma_q^{Fresnel}\right] exp\left(-Hcos^{N_p}\theta\right), \quad (11)$$

where $\Gamma_p^{Fresnel}$ and $\Gamma_q^{Fresnel}$ are Fresnel reflectivities at polarization p and q (if $p = H$, then $q = V$ and vice versa), and Q, H and N_p are parameters dependent on soil surface properties, and need to be determined for each site (Montpetit et al., 2015).

Parameters Q, H, and N_V were determined by minimizing the sum of squared error between TB simulations and 54 microwave radiometer measurements at 18.7 GHz V-pol made during 17th–25th November 2010. This period was selected since the soil was already frozen, but snowpack was shallow (snow depth 17–20 cm, SWE 34–54 mm) and dry. Automated measurements of soil permittivity, air, soil, and snow temperatures, and snow depth were used in TB simulations, as well as a grain size of $E_{pit} = 1.13$ mm (SWE-weighted mean of a snow pit measured on 23rd November 2010). The determined model parameter values were $Q = 0.01$, $H = 0.09$, and $N_V = 0.92$. With these parameters, the maximum error of the 54 simulations was 1.8 K.

4. Methods and results

This section describes how the four research goals set in Section 1 were studied. For each goal, the methods used and results obtained are shown.

4.1. Snow profiles

4.1.1. Methods

Snow parameters needed for the HUT snow emission model (grain sizes E and D_o, density ρ_s and temperature T_s), derived from SNOWPACK simulations and field measurements, were compared using agreement scores (Lehning et al., 2001). An agreement score between 0 (no agreement between measured and modeled profiles) and 1 (identical profiles) was calculated for each measured and coinciding SNOWPACK profile separately for each parameter. A SNOWPACK snow profile was first stretched to same height as the manually measured profile, and density was scaled accordingly to preserve snow mass. Scaling was not needed for temperature or grain sizes. Agreement scores were calculated only for dry snow profiles (volumetric water content in SNOWPACK profile = 0.0), since determining grain size or density of wet, melting snow on the field is highly inaccurate. Stretching, scaling and normalization of profiles were only used in the agreement score calculation; all further analysis is based on the original data.

For grain size E, the agreement score of a measured and coinciding modeled profile is (Lehning et al., 2001)

$$d^{E}_{profile} = \frac{1}{N}\sum_{l=1}^{N} d^{E_l^{obs}} \tag{12}$$

where N is the number of observed layers l and $d^{E_l^{obs}}$ are the agreement scores for each observed layer, which can be calculated from agreement measures (Lehning et al., 2001)

$$d^{E_l^{mod}} = 1 - |E_{pit,n} - E_{SP,n}| \tag{13}$$

with equations presented in Lehning et al. (2001). The agreement measure $d^{E_l^{mod}}$ is calculated from the normalized observed grain size $E_{pit,n}$ and the normalized modeled grain size $E_{SP,n}$ for each model layer combination that can be found from a height tolerance range around the observed layer, and the combination giving the best agreement measure is selected. This means that layers at the same height are not directly compared, but some tolerance is allowed for the location. The height of the tolerance range depends on total snow depth and the location of the layer in the snowpack; in the middle of the snowpack the range is wider, while close to surface or bottom it is narrower. In addition, individual layers are not directly compared, but a combination of one or more adjacent model layers may correspond to a single observed layer. Normalized grain size is the layer value divided by the maximum value in a profile. This is needed to scale the resulting agreement score between 0 and 1. Details of the selection of the tolerance range and the calculation of $d^{E_l^{obs}}$ from $d^{E_l^{mod}}$ can be found in Lehning et al. (2001).

For other snow parameters, the agreement scores were calculated similarly, except there was no need to search for matching layers. The selection of model values for each measurement followed the guidelines of Lehning et al. (2001): for point measurements (temperature and density from the SnowFork), linear interpolation of modeled parameter values around the measurement points was used, and for bulk measurements (D_{oIC} and density from the sampler), an average of the modeled parameter values at the measurement height range was used.

The calculated agreement scores were divided into bins of 0.05 width. The mode values presented in Section 4.1.2 are based on these binned values.

4.1.2. Results

Table 1 presents the mean and mode values of agreement scores for parameters E, D_o, ρ_s, and T_s. If each profile was normalized to its maximum grain size, as suggested by Lehning et al. (2001), the modes of agreement scores of grain size E for the winters of 2009–2010, 2010–2011, 2011–2012, and 2012–2013 were 0.8, 0.9, 0.85, and 0.7, respectively, and the mean agreement scores were 0.78, 0.82, 0.84, and 0.67, respectively. However, grain sizes can be normalized this way only if we assume that the differences between the modeled and observed profiles are due to a different definition of grain size (Lehning et al., 2001). If the largest grain size in a snow pit profile is erroneous, e.g. single snow grains are not identified properly, then all the other grain sizes from that pit are normalized incorrectly. Typically (e.g. Baunach et al., 2001; Leppänen et al., 2015) the variation of E_{pit} between observers increases as the value of E_{pit} increases, and thus the maximum grain size of a profile is prone to observation errors. If a measured and the corresponding modeled grain size profile were normalized to their common maximum, the modes of agreement scores for each winter were 0.9, 0.9, 0.9, and 0.95, respectively, as shown in Table 1. The mean agreement scores were 0.85, 0.87, 0.88, and 0.91, respectively. Based on this, the field measurements of grain size E_{pit} and the modeled E_{SP} profiles were quite similar every winter, but the similarity increased every winter towards the end of the experiment.

D_{oIC} measurements were available only from the last two winters, and the modes of agreement scores were 0.75 (2011 − 2012) and 0.80 (2012 − 2013), and the mean values were 0.75 and 0.74, respectively. Sometimes the depth hoar layers (bottom 10–20 cm of the snowpack) were not measured due to problems with large crystals (Section 2.4). In these cases the calculated agreement scores included only the top snow layers with smaller crystals. The agreement scores of D_o were

Table 1
Mean and mode values of agreement scores for each winter. 'n' refers to the number of samples. D_{oIC} measurements were available only from the last two winters.

Parameter	2009–2010			2010–2011			2011–2012			2012–2013		
	Mean	Mode	n	Mean	Mode	n	Mean	Mode	n	Mean	Mode	n
E	0.85	0.90	35	0.87	0.90	21	0.88	0.90	15	0.91	0.95	22
D_o	–	–	0	–	–	0	0.75	0.75	9	0.74	0.80	18
ρ_s	0.65	0.65	35	0.71	0.85	21	0.80	0.90	15	0.75	0.90	22
T_s	0.73	0.75	35	0.71	0.75	21	0.83	0.95	15	0.76	0.90	21

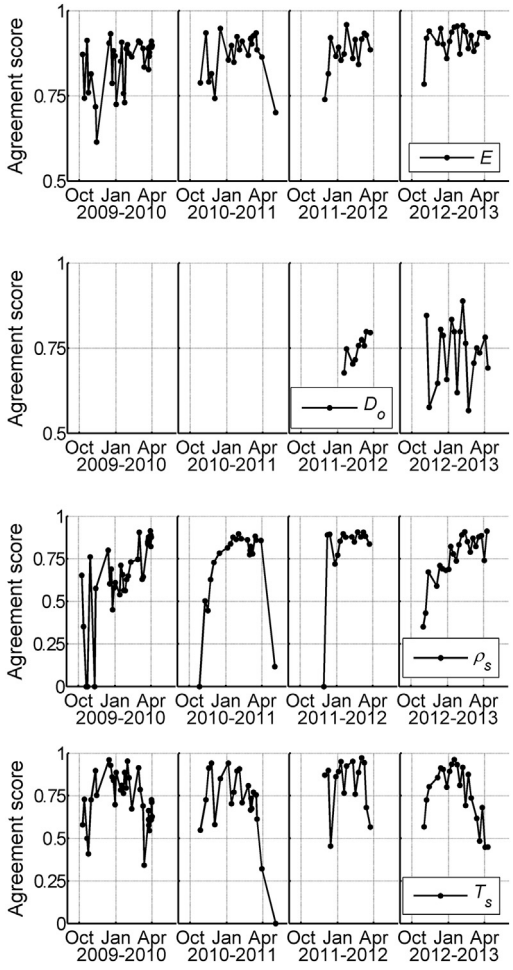

Fig. 2. Time series of agreement scores for grain sizes E (top panel) and D_o (second panel), density ρ_s (third panel) and temperature T_s (bottom panel). D_o observations were available only for the last two winters.

much lower than those of *E*. This could be explained with the grain size comparison results of Leppänen et al. (2015): while the scaling factor for 1-layer aggregates of E_{SP} and E_{pit} was $\beta_{E_{SP}} = 1.24$, that of D_{oSP} and D_{oIC} was $\beta_{D_{oSP}} = 2.11$ indicating a much larger difference between measured and modeled values in optical grain sizes. The reason for this inconsistency between IceCube measurements and SNOWPACK is yet unexplained.

The mean agreement score of density varied between 0.65 and 0.80, and the mode varied between 0.65 and 0.90. The same ranges for temperature were 0.71–0.83 and 0.75–0.95, respectively. In both cases, the highest mean and mode values were reached in the winter of 2011–2012.

Time series of agreement scores are shown in Fig. 2. The agreement scores of all parameters were lower (close to 0.5) in the beginning of each snow season than later in the winter (close to 1), suggesting that SNOWPACK had problems with early shallow snow, and possibly reflecting the variation in shallow snowpack due to low vegetation and uneven ground surface. Temperature agreement score was low (close to 0.5) also at the end of each snow season in April, when snow is melting.

Comparison of SNOWPACK total SWE to GWI measurement (Fig. 3) showed a high overestimation of SWE (up to 100 mm) in SNOWPACK especially at the time of the maximum snow height each winter. This was due to overestimation of snow density. Before snow maximum, the overestimation of SWE was ~20 mm. SNOWPACK overestimated snow densities (Fig. 3) in the first three winters, the highest overestimation (~100 kg/m^3) occurring in 2009–2010. As the difference in densities varies from year to year and the protocol for manual measurements remained the same, the overestimation is probably not due to erroneous field measurement protocol. In addition, the same difference can be seen in 2009–2010 in spite of the field instrument used (SnowFork or density sampler). As the equations for the density of new snow in SNOWPACK (Lehning et al., 2002a, 2002b) were developed for Alpine snow, they might not be directly applicable in the Arctic. However, most of the difference in densities originates from the bottom snow layers. Therefore we assume that in some, yet unspecified, meteorological or snow conditions, SNOWPACK models the settling of snow erroneously.

Early winter mean snow temperature from SNOWPACK agreed with manual measurements, with the exception of the winter of 2010–2011, when SNOWPACK overestimated snow temperature. SNOWPACK also overestimated snow temperature each spring during snowmelt; SNOWPACK mean snow temperature typically increased steadily with time, while the measured mean snow temperature often dropped a few times each spring due to cold air temperature. SNOWPACK snow surface temperature follows the measured air temperature closely, but there were larger differences between measured and modeled temperatures in the middle of the snowpack.

4.2. Effective grain size

4.2.1. Methods

Pulliainen (2006) introduced an effective value for grain size in the 1-layer HUT snow emission model to compensate for spatial and temporal changes in snow structure. This effective grain size (d_{HUT}) is the grain size value which minimizes error between the observed and

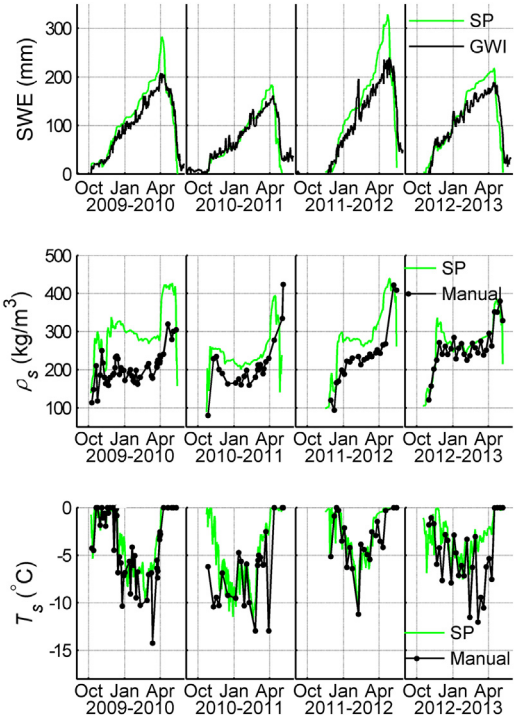

Fig. 3. Daily mean of total SWE calculated from SNOWPACK layer densities and thicknesses (SP, green) and from GWI measurement (black; top panel); daily mean snow density from SNOWPACK (SP, green) and from manual measurements (black; second panel); and daily mean snow temperatures from SNOWPACK (SP, green) and from manual measurements (black; bottom panel). Both dry and wet snow measurements are shown. (For interpretation of the references to color in this figure legend, the reader is referred to the web version of this article.)

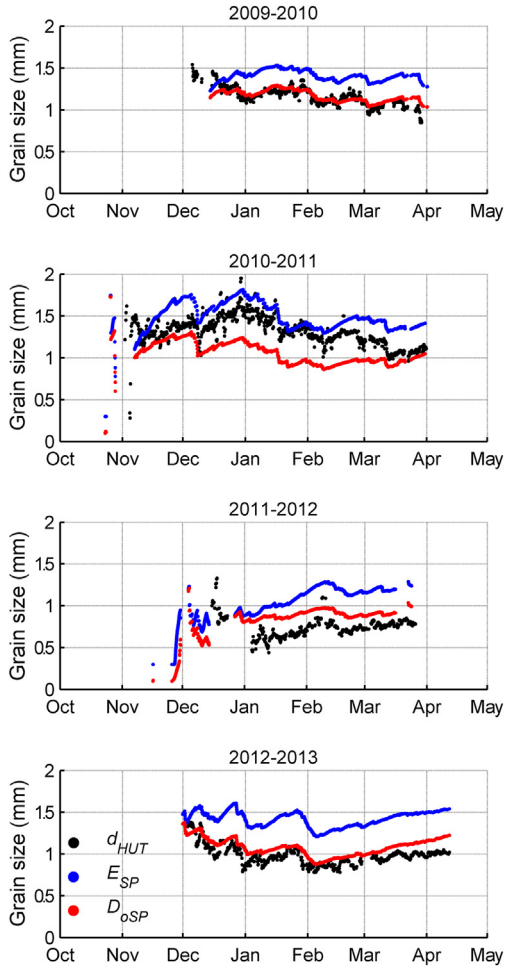

Fig. 4. Time series of the effective grain size from radiometer measurements (d_{HUT}, black) and 1-layer aggregates of grain sizes from SNOWPACK: E_{SP} (blue) and D_{oSP} (red). (For interpretation of the references to color in this figure legend, the reader is referred to the web version of this article.)

simulated TBs. We retrieved d_{HUT} by performing an iterative minimization of the cost function

$$F(d_{HUT}) = \left[\Delta T_{B,HUT}(d_{HUT}, x_1, \ldots, x_w) - \Delta T_{B,OBS}\right]^2, \quad (14)$$

where $\Delta T_{B,HUT}$ is the output of the 1-layer HUT snow emission model for channel difference V18.7-V36.5 at 50° incidence, $\Delta T_{B,OBS}$ is the observed channel difference, and x_w are snow a priori parameters. The channel difference V18.7-V36.5 was used, because the two frequencies have different penetration depths into snow. The 36.5 GHz frequency mostly reacts to snow volume, while the 18.7 GHz frequency penetrates into ground and provides the background. The use of the frequency difference mostly cancels out the effect of snow temperature. V-pol is less sensitive than H-pol to local ice lenses in the snowpack (Rees et al., 2010), which were difficult to model because the in situ snow measurements were not from the actual radiometer footprint. Automated observations of the bulk properties of snowpack (Section 2.5) were used as x_w. These observations included snow temperature (estimated as an average of air and soil surface temperatures), SWE (from GWI), and snow density (calculated from SWE and automated observations of HS). Retrieved d_{HUT} was limited between 0.01 and 3 mm. This method was similar to the retrieval of grain size in the GlobSnow algorithm (Takala et al., 2011).

The 1-layer HUT model was used since by allowing multiple layers the retrieved d_{HUT} would be ambiguous. For later use in SWE retrieval and to compare d_{HUT} with SNOWPACK output and field measurements, the modeled and manually measured snow profiles were aggregated to one layer using SWE-weighted means of layer values.

Table 2
The biases and RMS errors of the 1-layer aggregates of grain size from SNOWPACK compared to the effective grain size d_{HUT}. 'n' refers to the number of samples.

Year	Bias (mm)		RMS error (mm)		n
	D_{oSP}	E_{SP}	D_{oSP}	E_{SP}	
2009–2010	0.01	0.25	0.07	0.27	746
2010–2011	−0.27	0.17	0.30	0.21	828
2011–2012	0.19	0.42	0.20	0.42	382
2012–2013	0.10	0.44	0.12	0.45	703
2009–2013	−0.03	0.30	0.20	0.33	2659

4.2.2. Results

Visual comparison of d_{HUT} and the 1-layer aggregates of SNOWPACK grain size profiles (Fig. 4) showed that SNOWPACK modeled the trend of d_{HUT} well capturing the increases, decreases and locations of minima and maxima in grain size. This is partly a result from using the same snow depth, measured in situ, to drive both the SNOWPACK simulations and the retrieval of effective grain size in Eq. (14). The RMS error of SNOWPACK grain sizes compared to d_{HUT} (Table 2) varies from 0.07 mm (2009–2010) to 0.30 mm (2010−2011) for D_{oSP} and from 0.21 mm (2010–2011) to 0.45 mm (2012–2013) for E_{SP}. The bias varies from year to year, and especially the winter of 2010–2011 differs from the others with negative bias in D_{oSP} and smallest bias in E_{SP}. The differences might be related to snow structure, which depends on weather conditions before and during the snow season. During 2010–2011, the measurement site experienced the coldest temperatures combined with the shallowest snowpack resulting in significant depth hoar formation (Lemmetyinen et al., 2016b). As we compared only the 1-layer aggregates, snow layer structure and grain shapes were not taken into account. Another source of differences might be related to the problems that SNOWPACK had in modeling snow parameters in different years (Section 4.1.2). As all the snow properties are related, problems in modeling any snow parameter reflect to other parameters as well. The biases and RMS errors of the whole data set were −0.03 mm and 0.20 mm, respectively, for D_{oSP}, and 0.30 mm and 0.34 mm, respectively, for E_{SP}.

Scatter plots of d_{HUT} against the SNOWPACK grain sizes are shown in Fig. 5. Following relationships between the effective grain size and SNOWPACK grain sizes were defined using simple linear regression:

$$D_{oSP,eff} = 1.1090 \cdot D_{oSP} - 0.0875 \quad (15)$$

$$E_{SP,eff} = 1.1421 \cdot E_{SP} - 0.4965 \quad (16)$$

Eqs. (15) and (16) give the relationship of SNOWPACK-modeled grain sizes to the grain size needed in the HUT snow emission model. The RMS errors of the fitted equations were 0.19 mm for $D_{oSP,eff}$ and 0.15 mm for $E_{SP,eff}$. The correlation coefficients (r^2) were 0.34 and 0.59, respectively. It is to be noted that the Eqs. (15) and (16) apply only to the used data set. Especially the bias of D_{oSP} is highly dependent on year, being negative in 2010–2011 and positive in other years.

4.3. Brightness temperature

4.3.1. Methods

Snow TB was calculated using snow profiles modeled with SNOWPACK as input to the n-layer HUT model and compared to radiometer measurements. Full SNOWPACK profiles of layer thickness, temperature, density, and grain sizes were used. In addition to SNOWPACK profiles, automated measurements of air and soil temperature and soil

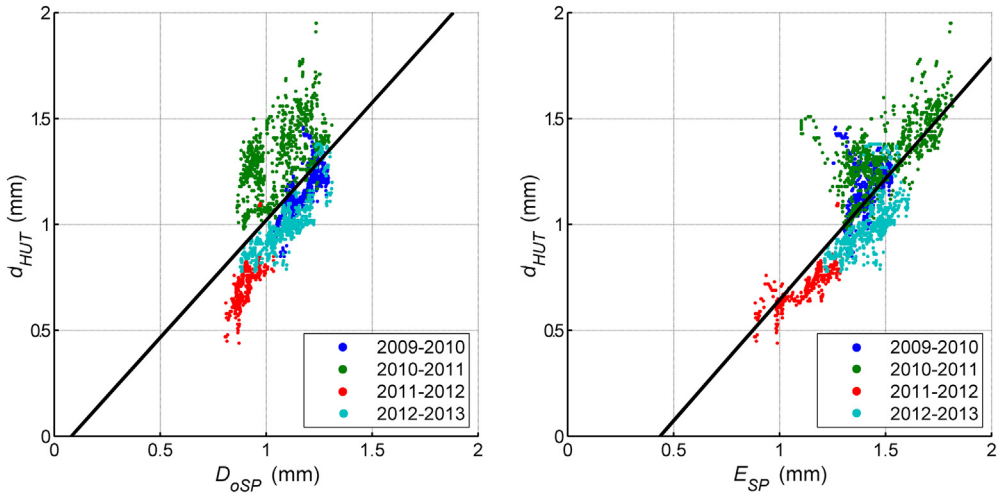

Fig. 5. The effective grain size d_{HUT} against the 1-layer aggregates of grain sizes from SNOWPACK: D_{oSP} (left) and E_{SP} (right). Lines fitted to all points (Eqs. (15) and (16)) are shown.

permittivity were used in the simulations. Other input data were always the same, but different grain size parameters were used:

1. D_{oSP} from SNOWPACK,
2. $D_{oSP,eff}$ from Eq. (15),
3. E_{SP} from SNOWPACK, and
4. $E_{SP,eff}$ from Eq. (16).

Eqs. (15) and (16) were applied separately to grain sizes of each layer.

4.3.2. Results

The simulated and measured TBs are shown in Fig. 6. Eqs. (15) and (16) both caused a maximum change of 0.45 mm in D_o and E, respectively. Due to nonlinearity of TB response to grain size, these resulted in maximum changes of 2 K and 9 K at 18.7 GHz, respectively, and 7 K and 32 K at 36.5 GHz, respectively.

Soil freezing (a drop in permittivity) was seen as an initial sharp increase in the simulated TB especially at 18.7 GHz in 2009 and 2010. In 2011 and 2012 no radiometer measurements were available from the soil freezing period, and therefore it is not visible in this figure. The measured TB at 18.7 GHz increased initially as well, but not as suddenly as the simulated one. This could be explained by inaccurately modeled soil processes: As the soil permittivity and temperature sensors were not in the radiometer footprint, it is possible that the timing and speed of soil freezing was different in these spots. In addition, residual liquid water in the ground might have an effect on the measured value.

Biases and RMS errors of the simulated TB time series are shown in Table 3. First we compared D_{oSP} to E_{SP}. The simulation with D_{oSP} had smaller biases and RMS errors than the one with E_{SP}, with the exception of V18.7-V36.5 in the winter of 2010–2011. When effective grain size equations were applied, the results were divided, and there was a lot of variation depending on year and frequency.

Second, we compared the simulations with effective grain sizes to the ones with SNOWPACK grain sizes. The simulation with $D_{oSP,eff}$ from Eq. (15) had lower simulation bias and RMS error than the one with $E_{SP,eff}$ only in the first two winters at V18.7-V36.5 and in the winter of 2010–2011 at 36.5 GHz. In all other cases the effective grain size increased errors. This was expected; as the bias in D_{oSP} compared to d_{HUT} varied a lot, different years would require different corrections. The simulation with $E_{SP,eff}$ from Eq. (16) always had lower errors than the one with E_{SP}. As the bias in E_{SP} compared to d_{HUT} was always positive, the Eq. (16) changes the grain sizes closer to the optimal value every year.

4.4. SWE retrieval

4.4.1. Methods

SWE was retrieved from the microwave radiometer measurements by applying a numerical inversion of the 1-layer HUT model. The cost function

$$F(SWE) = \left[\Delta T_{B,HUT}(SWE, x_1, \ldots, x_w) - \Delta T_{B,OBS}\right]^2 \quad (17)$$

was minimized. The used a priori snow data sets x_w are explained in detail in Table 4. In all cases, either one-layer aggregates of SNOWPACK snow profiles or fixed values were used. First, snow data from SNOWPACK were used (ID's D_{oSP} and E_{SP}). Then, the effective grain sizes were tested (ID's $D_{oSP,eff}$ and $E_{SP,eff}$). Last, only the effective grain sizes were used with fixed values to simulate an operational retrieval case. Only dry snow profiles were used in the retrieval.

The retrieved SWE values were compared to manual bulk SWE measurements and the total SWE modeled with SNOWPACK. Instead of measured soil permittivity values, a constant value of $\varepsilon_{soil} = 4 - j$ (a typical value for frozen ground) was used in the retrieval.

4.4.2. Results

Time series of retrieved, modeled and measured SWE are compared in Fig. 7, and biases and RMS errors of the retrievals and SNOWPACK modeling are shown in Table 5. There were notable differences between the retrievals and the years. Especially during the winter of 2010–2011, most of the retrievals showed 200–400 mm of SWE in January–March, even though the measured values were around 100 mm. Typically in the beginning of each winter the retrievals showed very high SWE values compared to the measured ones. This could be the effect of soil which is not yet completely frozen.

The retrievals with D_{oSP}, $D_{oSP,eff}$, and $D_{oSP,eff}$ *fix* all had very high RMS error (>110 mm) and bias (~100 mm) in the winter of 2010–2011. On the other hand, they had the lowest RMS errors in 2011–2012 and 2012–2013 (19–42 mm). In the D_{oSP} retrieval, total RMS error was 78 mm and bias was 48 mm. When the effective grain size $D_{oSP,eff}$ was applied, the total RMS error and bias decreased to 70 mm and 38 mm, respectively. In $D_{oSP,eff}$ *fix*, where fixed temperature and density values were applied, the total RMS error increased to 83 mm, but bias decreased to 24 mm.

The retrievals E_{SP}, $E_{SP,eff}$, and $E_{SP,eff}$ *fix* had a much lower RMS error in 2010–2011, but larger errors in 2011–2012 and 2012–2013, than D_{oSP}, $D_{oSP,eff}$, and $D_{oSP,eff}$ *fix*. In the E_{SP} retrieval, total RMS error was 58 mm and bias was −33 mm. When the effective grain size $E_{SP,eff}$ was applied,

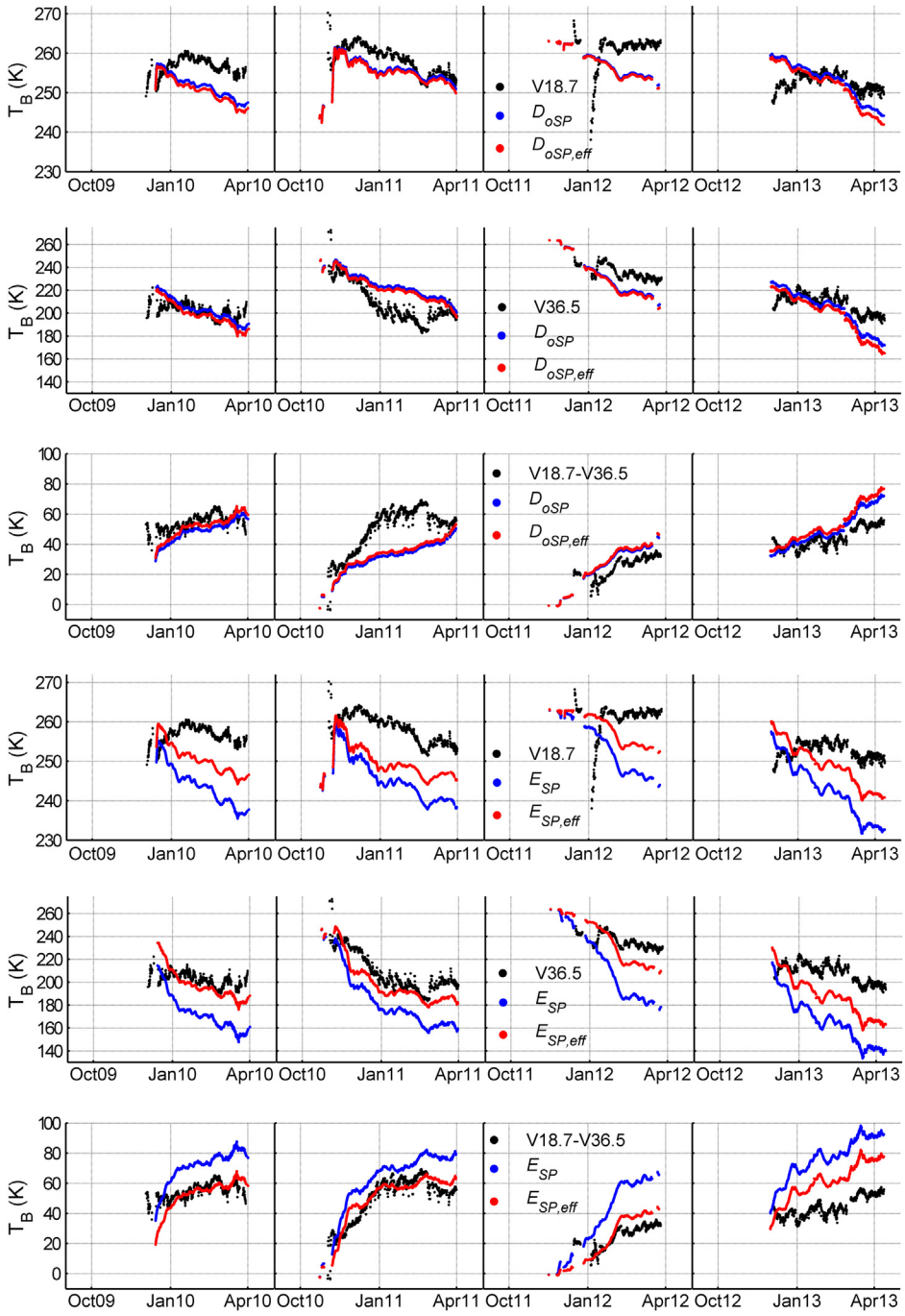

Fig. 6. Measured (V18.7, V36.5, black) and modeled TBs with different grain sizes: D_{oSP} (blue, top three panels), $D_{oSP,eff}$ from Eq. (15) (red, top three panels), E_{SP} (blue, bottom three panels), and $E_{SP,eff}$ from Eq. (16) (red, bottom three panels). Note the different scales on y-axes. One TB measurement is an integrated value of 180 1-s samples. (For interpretation of the references to color in this figure legend, the reader is referred to the web version of this article.)

total RMS error and bias increased to 73 mm and 43 mm, respectively. In $E_{SP,eff}$ *fix*, total RMS error was 59 mm and bias was 22 mm.

SNOWPACK modeled SWE better than any of the retrievals; it exhibited the lowest RMS error for every investigated year, as well as the lowest overall bias. The overestimation of SWE in SNOWPACK (Fig. 3) was at spring snowmelt time and is not seen in this comparison of dry snow cases.The good performance of SNOWPACK can at least be partly attributed to the high quality of input data (in particular, using measured snow depth in place of precipitation). E_{SP} retrieval had the lowest total RMS error (58 mm) of all the retrievals, and $E_{SP,eff}$ *fix* had the second lowest RMS error (59 mm) and the lowest total bias (22 mm).

5. Discussion

We used SNOWPACK to simulate snow temperature, density, and grain size profiles from meteorological data, because it includes most of the important physical processes governing evolution of snow structure, is widely used and validated (e.g. Groot Zwaaftink et al., 2013; Hirashima et al., 2008; Huang et al., 2012; Langlois et al., 2012; Rasmus et al., 2007) and is actively developed. The model requires numerous input parameters, and thus would not be suitable for an operational SWE algorithm over the whole Northern hemisphere. In an operational SWE retrieval scheme, a simple 1-layer snow model,

Table 3
The biases and RMS errors of the simulated TBs compared with the radiometer measurements. Four different grain sizes were used: D_{oSP} from SNOWPACK, $D_{oSP,eff}$ from Eq. (15), E_{SP} from SNOWPACK and $E_{SP,eff}$ from Eq. (16). 'n' refers to the number of samples. One TB measurement is an integrated value of 180 1-s samples.

Year	Grain size	Bias			RMS error			n
		V18.7	V36.5	V18.7-V36.5	V18.7	V36.5	V18.7-V36.5	
2009–2010	D_{oSP}	−4.9	2.0	−6.9	6.0	8.1	8.5	786
2010–2011		−2.5	16.2	−18.7	3.3	18.5	20.6	853
2011–2012		−4.7	−12.5	7.9	7.5	13.8	8.2	441
2012–2013		0.5	−4.8	5.2	4.4	11.8	8.4	715
2009–2010	E_{SP}	−12.6	−28.1	15.5	13.7	30.9	17.3	786
2010–2011		−12.7	−26.2	13.5	13.2	27.7	15.2	853
2011–2012		−10.2	−36.7	26.4	13.0	39.4	27.3	441
2012–2013		−9.9	−42.2	32.3	12.0	44.7	33.3	715
2009–2010	$D_{oSP,eff}$	−6.0	−2.1	−3.9	7.0	8.4	6.5	786
2010–2011		−3.1	13.7	−16.8	3.7	16.3	18.9	853
2011–2012		−5.0	−14.0	9.0	7.8	15.3	9.2	441
2012–2013		−0.7	−9.3	8.6	4.8	15.0	11.1	715
2009–2010	$E_{SP,eff}$	−6.2	−3.4	−2.8	7.5	11.8	7.7	786
2010–2011		−8.4	−9.2	0.8	8.9	11.9	6.4	853
2011–2012		−4.0	−9.1	5.1	7.9	14.4	7.2	441
2012–2013		−3.7	−20.4	16.8	6.4	23.8	18.2	715

which ideally would take as input only a limited amount of meteorological information and output reasonable estimates for bulk snow characteristics (e.g., grain size, temperature), would be more straightforward to apply. However, our goal was to study whether the HUT snow emission model could be coupled with a physical snow model to increase the accuracy of point scale simulations of TB. Since we had all the required input parameters available, we used SNOWPACK as a proof-of-concept.

Snow depth in SNOWPACK simulations can be constrained with either precipitation or snow depth measurements. The under-catch of precipitation gauges due to wind and other environmental factors is a known issue, and is emphasized in solid precipitation measurements (Sugiura et al., 2006; Wolff et al., 2015; Yang, 2014). Therefore precipitation measurements of snowfall are unreliable showing under-catch ratios of up to 50% even with proper wind shielding (Yang, 2014). This under-catch would result in a much smaller SWE in SNOWPACK than in reality (e.g. Langlois et al., 2012), and could produce a completely different snow microstructure, as snow layering and temperature profiles would change. Therefore we chose to constrain the SNOWPACK simulations with automated snow depth measurements, which is also the method recommended by SNOWPACK developers (Lehning et al., 2002a, 2002b). Considering large-scale operational use, measured snow depth is not widely available; in fact SWE retrieval from spaceborne measurements aims at providing this information. One option for an operational SWE retrieval scheme would be to run SNOWPACK or some simpler grain size model for the meteorological stations where in situ snow depth measurement data are available. The modeled grain size could replace or constrain grain size in the current GlobSnow method, which uses in situ snow depth data from meteorological stations to retrieve an effective grain size used in the final stage of SWE retrieval.

There were some discrepancies between snow parameters simulated by SNOWPACK and the measured values. The differences varied from winter to winter, as did the biases in 1-layer aggregate SNOWPACK grain sizes compared to d_{HUT}. The reason for these differences between measurements and modeling results are not fully explained yet. Further research is needed to find the meteorological conditions or snow properties (or some other underlying reason), which lead to these differences. A correction of these differences is also needed before SNOWPACK snow parameters are fully usable in an operational SWE retrieval scheme with the HUT snow emission model.

Our SWE retrievals assumed one homogeneous snow layer. This is unrealistic; SNOWPACK simulated up to 74 and our snow pit measurements recorded up to 16 layers in snow. There have been attempts to retrieve SWE from snow pit data using the number of snow layers as a free parameter (Durand and Liu, 2012), but no operational algorithm has solved the problem of multiple snow layers yet. In addition to the fact that no reliable snow layering information is available for e.g. the whole Northern hemisphere, snow micro- and macrostructure varies in scales from meters to tens of kilometers (Derksen et al., 2009; Hannula et al., 2016; Rutter et al., 2014), the scale of a single spaceborne radiometer footprint. It is uncertain how much improvement to a SWE estimate a homogeneous layer structure in a footprint scale would introduce.

We calculated regression equations (Eqs. (15) and (16)) for SNOWPACK grain sizes to relate them with the microwave effective grain size retrieved from radiometer observations. However, as the yearly biases in Table 2 highlight, the required correction highly depends on year. Therefore these regression equations are not general and cannot be directly applied to other locations or other years. As the TB simulations in Fig. 6 show, the simulation with $D_{oSP,eff}$ is quite similar to D_{oSP} (TB difference < 7 K), while the simulations run with $E_{SP,eff}$ and E_{SP} have a difference of up to 32 K at 36.5 GHz. Based on the SWE retrievals (Section 4.4.2), the lowest total RMS error of 58 mm in SWE is reached when E_{SP} is used with SNOWPACK density and temperature, and almost as low (59 mm) when $E_{SP,eff}$ is used with fixed density and temperature

Table 4
Input parameters to the HUT snow emission model in SWE retrieval.

ID	Grain size	Density	Snow temperature	Soil temperature	Air temperature
D_{oSP}	1-layer aggregate of D_{oSP}	1-layer aggregate of SNOWPACK profile	1-layer aggregate of SNOWPACK profile	Measured	Measured
$D_{oSP,eff}$	Eq. (15) applied to 1-layer aggregate of D_{oSP}	1-layer aggregate of SNOWPACK profile	1-layer aggregate of SNOWPACK profile	Measured	Measured
$D_{oSP,eff}$ *fix*	Eq. (15) applied to 1-layer aggregate of D_{oSP}	0.24 g/cm^3	−5 °C	−5 °C	−5 °C
E_{SP}	1-layer aggregate of E_{SP}	1-layer aggregate of SNOWPACK profile	1-layer aggregate of SNOWPACK profile	Measured	Measured
$E_{SP,eff}$	Eq. (16) applied to 1-layer aggregate of E_{SP}	1-layer aggregate of SNOWPACK profile	1-layer aggregate of SNOWPACK profile	Measured	Measured
$E_{SP,eff}$ *fix*	Eq. (16) applied to 1-layer aggregate of E_{SP}	0.24 g/cm^3	−5 °C	−5 °C	−5 °C

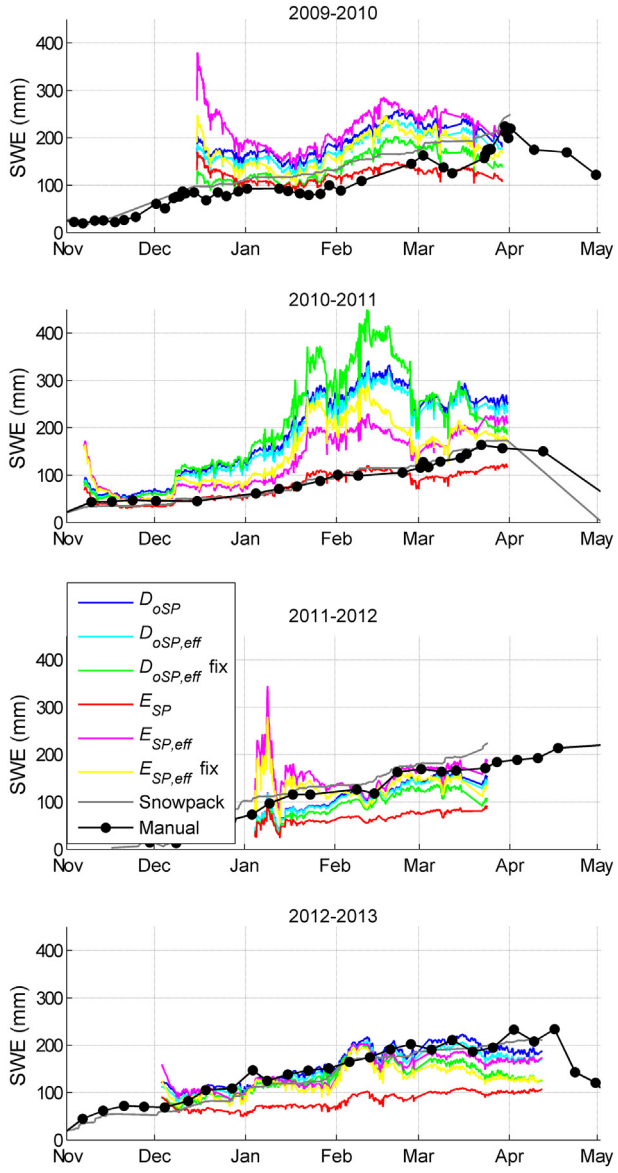

Fig. 7. Time series of SWE from the six retrievals (blue, cyan, green, red, magenta and orange, descriptions in Table 4) compared to the total SWE from SNOWPACK (gray) and manual measurements (black). (For interpretation of the references to color in this figure legend, the reader is referred to the web version of this article.)

values. However, $D_{oSP,eff}$ with fixed density and temperature had lower RMS error (36–42 mm) than $E_{SP,eff}$ fix in three winters out of four. These results suggest that the ability of SNOWPACK to model snow properties varies from year to year, but that grain sizes from SNOWPACK, with the corrections of Eqs. (15) and (16), are usable as input to HUT snow emission model with the fixed snow parameters.

Until tested elsewhere, these results are applicable only to our measurement and simulation setup. Different snow structure or simulation parameters could change the coefficients in the regression equations, as can be seen from the large variety of scaling factors between measured or simulated snow structural metrics and those suitable for microwave emission models reported in the literature (e.g. Mätzler (2002) for D_o-p_c; Brucker et al. (2011) for CROCUS-MEMLS; Langlois et al. (2012) for SNOWPACK-MEMLS; Huang et al. (2012) for SNOWPACK-MEMLS; Roy et al. (2013) for SSA-HUT and SSA-MEMLS; Leppänen et al. (2015) for D_o-SNOWPACK).

6. Conclusions

The presented study compared field measurements and modeled values for two metrics of snow grain size, i.e. optical grain size D_o and traditional grain size E. The modes of agreement scores of E_{pit} and E_{SP} profiles were 0.90–0.95 and the mean agreement scores were 0.85–0.91. The modes of agreement scores for D_{oIC} and D_{oSP} were 0.75 (2011–2012) and 0.80 (2012–2013), with mean values of 0.75 and 0.74, respectively. Lower agreement scores (mean values 0.65–0.83) were calculated for snow temperature and density profiles.

Furthermore, the applicability of the grain size measures in the context of simulating the microwave emission from snow using the HUT snow emission model was studied. It was expected that neither of the studied metrics for grain size would be directly applicable for the HUT snow model, since in the model the grain size is used as a proxy parameter to describe the microstructure of the whole snowpack in one single value. Thus correction equations were determined between the effective grain size retrieved from microwave observations, d_{HUT}, and D_{oSP} and E_{SP}. The TB simulation with D_{oSP} had lower bias and RMS error than the one with E_{SP}. The use of effective grain size $E_{SP,eff}$ decreased simulation bias by 35–88% and RMS error by 33–64% compared to using E_{SP} directly. However, since D_{oSP} had larger variation between the winters, the general correction equation often increased RMS error and bias. In SWE retrieval, the case with $E_{SP,eff}$ and fixed snow temperature and density had the lowest overall bias and the second lowest overall RMS error, while the case with $D_{oSP,eff}$ and fixed temperature and density had even lower RMS error and bias in three winters out of four.

Based on comparisons between the microwave effective grain size d_{HUT} and the SNOWPACK grain sizes, we conclude that SNOWPACK is able to simulate grain size evolution, even though the accuracy of simulations varies between years, and that its grain size values are applicable as input to the HUT snow emission model with proper scaling. The circumstances in which SNOWPACK models some snow parameters poorly still require further study.

Acknowledgment

We thank the WSL Institute for Snow and Avalanche Research SLF and especially Dr. Martin Schneebeli and Dr. Mathias Bavay for the possibility to use the SNOWPACK model. We also thank the staff of FMI Arctic Research Centre in Sodankylä for performing the in situ measurements.

Table 5
The biases and RMS errors of the SWE retrievals compared to manual measurements. The retrieval cases are described in Table 4. 'SP' refers to the total SWE modeled by SNOWPACK (no retrieval used) and 'n' to the number of samples.

Year	Bias (mm)							RMS error (mm)							n
	D_{oSP}	$D_{oSP,eff}$	$D_{oSP,eff}$ fix	E_{SP}	$E_{SP,eff}$	$E_{SP,eff}$ fix	SP	D_{oSP}	$D_{oSP,eff}$	$D_{oSP,eff}$ fix	E_{SP}	$E_{SP,eff}$	$E_{SP,eff}$ fix	SP	
2009–2010	68	53	16	4	100	48	27	76	63	37	43	112	63	32	52
2010–2011	108	98	120	−12	46	57	−1	123	113	146	21	55	73	16	24
2011–2012	−15	−19	−37	−68	28	3	17	19	22	39	71	52	41	21	22
2012–2013	1	−9	−29	−76	−14	−33	−12	22	25	42	83	33	48	17	28
2009–2013	48	38	24	−33	43	22	10	78	70	83	58	73	59	24	126

Appendix A. Appendix

Table A1
Symbols with units and definitions.

Symbol	Unit	Description
D_o	mm	Optical grain size, diameter of optically-equivalent spheres
D_{olC}	mm	Optical grain size measured with IceCube
D_{oSP}	mm	Optical grain size modeled with SNOWPACK
$D_{oSP,eff}$	mm	Effective optical grain size (SNOWPACK-modeled value scaled to fit TB observations and the HUT model)
d	–	Dendricity, parameter in SNOWPACK describing the fraction of dendritic (flake-like) snow
$d^{E_l^{mod}}$	–	Agreement measure for grain size E for an observed layer l
$d^{E_l^{obs}}$	–	Agreement score of grain size E for an observed layer l calculated from agreement measures
$d^{E}_{profile}$	–	Agreement score for a snow profile
d_{HUT}	mm	Effective grain size retrieved from microwave observations using the HUT snow emission model
E	mm	Traditional snow grain size, visual estimation of average grain diameter
E_{pit}	mm	Traditional snow grain size measured manually on the field
$E_{pit,n}$	–	Normalized traditional grain size from field observations
E_{SP}	mm	Traditional snow grain size modeled with SNOWPACK
$E_{SP,n}$	–	Normalized traditional grain size from SNOWPACK
$E_{SP,eff}$	mm	Effective traditional grain size (SNOWPACK-modeled value scaled to fit TB observations and the HUT model)
$\dot{E}_{SP}$	m/s or mm/day	Grain growth rate in SNOWPACK
F	K^2	Cost function
H	–	A parameter in soil reflectivity model of Wang and Choudhury (1981)
l	–	Current layer in SNOWPACK profiles
N	–	Total number of layers in SNOWPACK profile
N_p	–	A parameter in soil reflectivity model of Wang and Choudhury (1981) dependent on polarization p
n	–	Layer number (in SNOWPACK) or number of samples (in statistical calculations)
p	–	Polarization (either H or V)
p_c	mm	Correlation length
Q	–	A parameter in soil reflectivity model of Wang and Choudhury (1981)
s	–	Sphericity, parameter in SNOWPACK describing the fraction of rounded versus faceted grains
T_{air}	°C	Air temperature at 2 m
T_B	K	Brightness temperature
T_s	°C	Snow temperature
t	s	Time
x_w	–	Snow a priori parameters in the HUT snow emission model
z	m	Height from the bottom of snowpack
$\beta_{D_{oSP}}$	–	Scaling factor between measured and modeled optical grain size
$\beta_{E_{SP}}$	–	Scaling factor between measured and modeled traditional grain size
Γ_p	–	Soil reflectivity at polarization p
$\Delta T_{B,HUT}$	K	Modeled brightness temperature at frequency difference 18.7 V–36.5 V
$\Delta T_{B,OBS}$	K	Measured brightness temperature at frequency difference 18.7 V–36.5 V
ε_{soil}	–	Relative permittivity of soil
θ	rad	Incidence angle
θ_m	–	Mass fraction of liquid water in snow
ρ_{ice}	kg/m^3	Ice density
ρ_s	kg/m^3	Snow density

Table A2
SNOWPACK.ini file parameters.

Parameter	Value	Notes
Data step length	30 min	
Calculation step length	15 min	
Height of meteo values	2.0 m	
Height of wind value	22.0 m	
Enforce measured snow heights	True	
SW mode	2	Incoming and reflected shortwave radiation are both measured
Neutral	1	Force Monin-Obukhov formulation to assume neutral conditions
Canopy	False	Open area
Measure TSS	False	Measured surface temperature not available
Change BC	False	
Incoming longwave	False	
Snow redistrubution	True	
SNP SOIL	True	Soil layers defined
Soil flux	False	
Geo heat	0.06	
Advanced settings	Default variant, default settings	

Table A3
SNOWPACK.sno file parameters.

Parameter	Value	Notes
Latitude	7,571,768	Sodankylä in Northern Finland
Longitude	484,270	
Altitude	180 m	
Slope Angle	0.0°	
Slope Azi	0.0°	
nSoilLayerData	1	Soil homogenous at least the first 1.5 m
nSnowLayerData	0	
Bare Soil z0	0.02	
Soil Albedo	0.2	
CanopyHeight	10.0 m	
CanopyLeafAreaIndex	0.0	
CanopyDirectThroughfall	0.0	
WindScalingFactor	1.0	
Profiledate	01.08.2011	
Soil layer thickness	1.5 m	
Volume fraction ice	0.00	
Volume fraction water	0.15	Calculated from automated soil moisture measurements
Volume fraction void	0.15	
Volume fraction soil	0.7	
Soil density	1700 kg/m^3	Soil approximated as compact sandy soil. Values estimated according to the volumetric fraction of water after DeVries (1963)
Soil heat conductivity	1.5 W/(m·K)	
Soil specific heat	1200 J/(kg·K)	

References

Barnett, T.P., Adam, J.C., Lettenmaier, D.P., 2005. Potential impacts of a warming climate on water availability in snow-dominated regions. Nature 438 (7066):303–309 (http://doi.org/10.1038/nature04141).

Bartelt, P., Lehning, M., 2002. A physical SNOWPACK model for the Swiss avalanche warning: Part I: numerical model. Cold Reg. Sci. Technol. 35 (3):123–145. http://dx.doi.org/10.1016/S0165-232X(02)00074-5.

Baunach, T., Fierz, C., Satyawali, P.K., Schneebeli, M., 2001. A model for kinetic grain growth. Ann. Glaciol. 32:1–6. http://dx.doi.org/10.3189/172756401781819427.

Brown, R.L., Edens, M.Q., Barber, M., 1999. Mixture theory of mass transfer based upon microstructure. Def. Sci. J. 49 (5):393–409. http://dx.doi.org/10.14429/dsj.49.3854.

Brown, R.L., Satyawali, P.K., Lehning, M., Bartelt, P., 2001. Modeling the changes in microstructure of snow during metamorphism. Cold Reg. Sci. Technol. 33 (2–3):91–101. http://dx.doi.org/10.1016/S0165-232X(01)00032-5.

Brucker, L., Royer, A., Picard, G., Langlois, A., Fily, M., 2011. Hourly simulations of the microwave brightness temperature of seasonal snow in Quebec, Canada, using a coupled snow evolution-emission model. Remote Sens. Environ. 115 (8): 1966–1977. http://dx.doi.org/10.1016/j.rse.2011.03.019.

Brun, E., 1989. Investigation on wet-snow metamorphism in respect of liquid-water content. Ann. Glaciol. 13, 22–26.

Brun, E., David, P., Sudul, M., Brunot, G., 1992. A numerical model to simulate snow-cover stratigraphy for operational avalanche forecasting. J. Glaciol. 38 (128), 13–22.

Chang, A.T.C., Foster, J.L., Hall, D.K., 1987. Nimbus-7 SMMR derived global snow cover parameters. Ann. Glaciol. 9, 39–44.
Davenport, I.J., Sandells, M.J., Gurney, R.J., 2012. The effects of variation in snow properties on passive microwave snow mass estimation. Remote Sens. Environ. 118:168–175. http://dx.doi.org/10.1016/j.rse.2011.11.014.
Debye, P., Anderson, H.R., Brumberger, H., 1957. Scattering by an inhomogeneous solid. II. The correlation function and its application. J. Appl. Phys. 28 (6):679–683. http://dx.doi.org/10.1063/1.1722830.
Derksen, C., Sturm, M., Liston, G.E., Holmgren, J., Huntington, H., Silis, A., Solie, D., 2009. Northwest territories and Nunavut snow characteristics from a subarctic traverse: implications for passive microwave remote sensing. J. Hydrometeorol. 10 (2): 448–463. http://dx.doi.org/10.1175/2008jhm1074.1.
DeVries, D.A., 1963. Thermal properties of soils. In: Van Wijk, W.R. (Ed.), Physics of Plant Environment. North-Holland Publishing Co., Amsterdam.
Durand, M., Liu, D., 2012. The need for prior information in characterizing snow water equivalent from microwave brightness temperatures. Remote Sens. Environ. 126: 248–257. http://dx.doi.org/10.1016/j.rse.2011.10.015.
Durand, M., Kim, E.J., Margulis, S.A., 2008. Quantifying uncertainty in modeling snow microwave radiance for a mountain snowpack at the point-scale, including stratigraphic effects. IEEE Trans. Geosci. Remote Sens. 46 (6):1753–1767. http://dx.doi.org/10.1109/TGRS.2008.916221.
Fierz, C., Armstrong, R.L., Durand, Y., Etchevers, P., Greene, E., McClung, D.M., ... Sokratov, S.A., 2009. The international classification for seasonal snow on the ground. IHP-VII Technical Documents in Hydrology. Vol. 83. UNESCO-IHP, Paris.
Gallet, J.-C., Domine, F., Zender, C.S., Picard, G., 2009. Measurement of the specific surface area of snow using infrared reflectance in an integrating sphere at 1310 and 1550 nm. Cryosphere 3 (2):167–182. http://dx.doi.org/10.5194/tc-3-167-2009.
Grenfell, T.C., Warren, S.G., 1999. Representation of a nonspherical ice particle by a collection of independent spheres for scattering and absorption of radiation: 3. Hollow columns and plates. J. Geophys. Res. D: Atmos. 104 (D24):31697–31709. http://dx.doi.org/10.1029/2005JD005811\.
Groisman, P.Y., Karl, T.R., Knight, R.W., 1994. Observed impact of snow cover on the heat balance and the rise of continental spring temperatures. Science 263 (5144): 198–200. http://dx.doi.org/10.1126/science.263.5144.198.
Groot Zwaaftink, C.D., Cagnati, A., Crepaz, A., Fierz, C., Macelloni, G., Valt, M., Lehning, M., 2013. Event-driven deposition of snow on the Antarctic Plateau: analyzing field measurements with SNOWPACK. Cryosphere 7 (1):333–347. http://dx.doi.org/10.5194/tc-7-333-2013.
Hallikainen, M., Ulaby, F., Van Deventer, T., 1987. Extinction behavior of dry snow in the 18- to 90-GHz range. IEEE Trans. Geosci. Remote Sens. GE-25 (6):737–745. http://dx.doi.org/10.1109/TGRS.1987.289743.
Hannula, H.-R., Lemmetyinen, J., Kontu, A., Derksen, C., Pulliainen, J., 2016. Spatial and temporal variation of bulk snow properties in northern boreal and tundra environments based on extensive field measurements. Geosci. Instrum. Methods Data Syst. 5:347–363. http://dx.doi.org/10.5194/gi-5-347-2016.
Hatakka, J., Paatero, J., Viisanen, Y., Mattsson, R., 1998. Variations of external radiation due to meteorological and hydrological factors in Central Finland. Radiochemistry 40 (6), 515–519.
Heggli, M., Frei, E., Schneebeli, M., 2009. Snow replica method for three-dimensional X-ray microtomographic imaging. J. Glaciol. 55 (192):631–639. http://dx.doi.org/10.3189/002214309789470932.
Hirashima, H., Nishimura, K., Yamaguchi, S., Sato, A., Lehning, M., 2008. Avalanche forecasting in a heavy snowfall area using the snowpack model. Cold Reg. Sci. Technol. 51 (2–3):191–203. http://dx.doi.org/10.1016/j.coldregions.2007.05.013.
Huang, C., Margulis, S.A., Durand, M.T., Musselman, K.N., 2012. Assessment of snow grain-size model and stratigraphy representation impacts on snow radiance assimilation: forward modeling evaluation. IEEE Trans. Geosci. Remote Sens. 50 (11):4551–4564. http://dx.doi.org/10.1109/TGRS.2012.2192480.
Kelly, R., 2009. The AMSR-E snow depth algorithm: description and initial results. J. Remote Sens. Soc. Jpn. 29:307–317. http://dx.doi.org/10.11440/rssj.29.307.
Kelly, R., Chang, A., 2003. Development of a passive microwave global snow depth retrieval algorithm for Special Sensor Microwave Imager (SSM/I) and Advanced Microwave Scanning Radiometer-EOS (AMSR-E) data. Radio Sci. 38 (4):1–13. http://dx.doi.org/10.1029/2002RS002648.
Langlois, A., Royer, A., Derksen, C., Montpetit, B., Dupont, F., Goïta, K., 2012. Coupling the snow thermodynamic model SNOWPACK with the microwave emission model of layered snowpacks for subarctic and arctic snow water equivalent retrievals. Water Resour. Res. 48 (12):1–14. http://dx.doi.org/10.1029/2012WR012133.
Legagneux, L., Cabanes, A., Dominé, F., 2002. Measurement of the specific surface area of 176 snow samples using methane adsorption at 77 K. J. Geophys. Res. Atmos. 107 (17). http://dx.doi.org/10.1029/2001JD001016.
Lehning, M., Fierz, C., Lundy, C., 2001. An objective snow profile comparison method and its application to SNOWPACK. Cold Reg. Sci. Technol. 33 (2–3):253–261. http://dx.doi.org/10.1016/S0165-232X(01)00044-1.
Lehning, M., Bartelt, P., Brown, B., Fierz, C., Satyawali, P., 2002a. A physical SNOWPACK model for the Swiss avalanche warning part II. Snow microstructure. Cold Reg. Sci. Technol. 35 (3):147–167. http://dx.doi.org/10.1016/S0165-232X(02)00073-3.
Lehning, M., Bartelt, P., Brown, B., Fierz, C., 2002b. A physical SNOWPACK model for the Swiss avalanche warning: Part III: meteorological forcing, thin layer formation and evaluation. Cold Reg. Sci. Technol. 35 (3):169–184. http://dx.doi.org/10.1016/S0165-232X(02)00072-1.
Lemmetyinen, J., Pulliainen, J., Rees, A., Kontu, A., Qiu, Y., Derksen, C., 2010. Multiple-layer adaptation of HUT snow emission model: Comparison with experimental data. IEEE Trans. Geosci. Remote Sens. 48 (7):2781–2794. http://dx.doi.org/10.1109/TGRS.2010.2041357.
Lemmetyinen, J., Derksen, C., Toose, P., Proksch, M., Pulliainen, J., Kontu, A., ... Hallikainen, M., 2015. Simulating seasonally and spatially varying snow cover brightness temperature using HUT snow emission model and retrieval of a microwave effective grain size. Remote Sens. Environ. 156:71–95. http://dx.doi.org/10.1016/j.rse.2014.09.016.
Lemmetyinen, J., Schwank, M., Rautiainen, K., Kontu, A., Parkkinen, T., Mätzler, C., ... Pulliainen, J., 2016a. Snow density and ground permittivity retrieved from L-band radiometry: application to experimental data. Remote Sens. Environ. 180:377–391. http://dx.doi.org/10.1016/j.rse.2016.02.002.
Lemmetyinen, J., Kontu, A., Pulliainen, J., Vehviläinen, J., Rautiainen, K., Wiesmann, A., ... Davidson, M., 2016b. Nordic snow radar experiment. Geosci. Instrum. Methods Data Syst. http://dx.doi.org/10.5194/gi-2015-29.
Lemmetyinen, J., Kontu, A., Pulliainen, J., Vehviläinen, J., Rautiainen, K., Wiesmann, A., ... Davidson, M., 2016c. Nordic snow radar experiment. Geosci. Instrum. Methods Data Syst. 5:403–415. http://dx.doi.org/10.5194/gi-2015-29.
Leppänen, L., Kontu, A., Vehviläinen, J., Lemmetyinen, J., Pulliainen, J., 2015. Comparison of traditional and optical grain-size field measurements with SNOWPACK simulations in a taiga snowpack. J. Glaciol. 61 (225):151–162. http://dx.doi.org/10.3189/2015JoG14J026.
Leppänen, L., Kontu, A., Hannula, H.-R., Sjöblom, H., Pulliainen, J., 2016. Sodankylä manual snow survey program. Geosci. Instrum. Methods Data Syst. 5:163–179. http://dx.doi.org/10.5194/gi-5-163-2016.
Matzl, M., Schneebeli, M., 2006. Measuring specific surface area of snow by near infrared photography. J. Glaciol. 42 (179):558–564. http://dx.doi.org/10.3189/172756506781828412.
Mätzler, C., 2002. Relation between grain-size and correlation length of snow. J. Glaciol. 48 (162), 461–466.
Montpetit, B., Royer, A., Wigneron, J.P., Chanzy, A., Mialon, A., 2015. Evaluation of multi-frequency bare soil microwave reflectivity models. Remote Sens. Environ. 162: 186–195. http://dx.doi.org/10.1016/j.rse.2015.02.015.
Painter, T.H., Molotch, N.P., Cassidy, M.P., Flanner, M.G., Steffen, K., 2007. Contact spectroscopy for the determination of stratigraphy of snow grain size. J. Glaciol. 53 (180): 121–127. http://dx.doi.org/10.3189/172756507781833947.
Picard, G., Brucker, L., Roy, A., Dupont, F., Fily, M., Royer, A., Harlow, C., 2013. Simulation of the microwave emission of multi-layered snowpacks using the dense media radiative transfer theory: the DMRT-ML model. Geosci. Model Dev. 6 (4):1061–1078. http://dx.doi.org/10.5194/gmd-6-1061-2013.
Pirinen, P., Simola, H., Aalto, J., Kaukoranta, J.-P., Karlsson, P., Ruuhela, R., 2012. Climatological statistics of Finland 1981–2010. Reports. Vol. 2012:1. Helsinki: Finnish Meteorological Institute.
Proksch, M., 2010. Comparing CT Experiments and Field Observations With the SNOWPACK Microstructure. University of Innsbruck.
Proksch, M., Löwe, H., Schneebeli, M., 2015. Density, specific surface area, and correlation length of snow measured by high-resolution penetrometry. J. Geophys. Res. F: Earth Surf. 120 (2):346–362. http://dx.doi.org/10.1002/2014JF003266.
Pulliainen, J., 2006. Mapping of snow water equivalent and snow depth in boreal and sub-arctic zones by assimilating space-borne microwave radiometer data and ground-based observations. Remote Sens. Environ. 101 (2):257–269. http://dx.doi.org/10.1016/j.rse.2006.01.002.
Pulliainen, J., Kärnä, J.-P., Hallikainen, M., 1993. Development of geophysical retrieval algorithms for the MIMR. IEEE Trans. Geosci. Remote Sens. 31 (1):268–277. http://dx.doi.org/10.1109/36.210466.
Pulliainen, J., Grandell, J., Hallikainen, M., 1999. HUT snow emission model and its applicability to snow water equivalent retrieval. IEEE Trans. Geosci. Remote Sens. 37 (3 I): 1378–1390. http://dx.doi.org/10.1109/36.763302.
Qu, X., Hall, A., 2014. On the persistent spread in snow-albedo feedback. Clim. Dyn. 42 (1–2):69–81. http://dx.doi.org/10.1007/s00382-013-1774-0.
Rasmus, S., Grönholm, T., Lehning, M., Rasmus, K., Kulmala, M., 2007. Validation of the SNOWPACK model in five different snow zones in Finland. Boreal Environ. Res. 12 (4), 467–488.
Rees, A., Lemmetyinen, J., Derksen, C., Pulliainen, J., English, M., 2010. Observed and modelled effects of ice lens formation on passive microwave brightness temperatures over snow covered tundra. Remote Sens. Environ. 114:116–126. http://dx.doi.org/10.1016/j.rse.2009.08.013.
Richardson, M., Davenport, I., Gurney, R., 2014. Global snow mass measurements and the effect of stratigraphic detail on inversion of microwave brightness temperatures. Surv. Geophys. 35 (3):785–812. http://dx.doi.org/10.1007/s10712-013-9263-x.
Roy, A., Picard, G., Royer, A., Montpetit, B., Dupont, F., Langlois, A., ... Champollion, N., 2013. Brightness temperature simulations of the Canadian seasonal snowpack driven by measurements of the snow specific surface area. IEEE Trans. Geosci. Remote Sens. 51 (9):4692–4704. http://dx.doi.org/10.1109/TGRS.2012.2235842.
Rutter, N., Sandells, M., Derksen, C., Toose, P., Royer, A., Montpetit, B., ... Pulliainen, J., 2014. Snow stratigraphic heterogeneity within ground-based passive microwave radiometer footprints: Implications for emission modeling. J. Geophys. Res. Earth Surf. 119 (3):550–565. http://dx.doi.org/10.1002/2013JF003017.
Sihvola, A., Tiuri, M., 1986. Snow fork for field determination of the density and wetness profiles of a snow pack. IEEE Trans. Geosci. Remote Sens. GE-24 (5), 717–721.
Sugiura, K., Ohata, T., Yang, D., 2006. Catch characteristics of precipitation gauges in high winds. Bull. Am. Meteorol. Soc. 87 (9):1182–1183. http://dx.doi.org/10.1175/JHM542.1.
Takala, M., Luojus, K., Pulliainen, J., Derksen, C., Lemmetyinen, J., Kärnä, J.P., ... Bojkov, B., 2011. Estimating northern hemisphere snow water equivalent for climate research through assimilation of space-borne radiometer data and ground-based measurements. Remote Sens. Environ. 115 (12):3517–3529. http://dx.doi.org/10.1016/j.rse.2011.08.014.
Takala, M., Ikonen, J., Luojus, K., Lemmetyinen, J., Metsämäki, S., Cohen, J., ... Pulliainen, J., 2016. New snow water equivalent processing system with improved resolution over

Europe and its applications in hydrology. IEEE J. Sel. Top. Appl. Earth Obs. Remote Sens. (accepted f). 10.1109/JSTARS.2016.2586179.
Toure, A.M., Goïta, K., Royer, A., Mätzler, C., Schneebeli, M., 2008. Near-infrared digital photography to estimate snow correlation length for microwave emission modeling. Appl. Opt. 47 (36):6723–6733. http://dx.doi.org/10.1364/AO.47.006723.
Tsang, L., Ding, K., Huang, S., Xu, X., 2013. Electromagnetic computation in scattering of electromagnetic waves by random rough surface and dense media in microwave remote sensing of land surfaces. Proc. IEEE 101 (2):255–279. http://dx.doi.org/10.1109/JPROC.2012.2214011.
Vionnet, V., Brun, E., Morin, S., Boone, A., Faroux, S., Le Moigne, P., ... Willemet, J.M., 2012. The detailed snowpack scheme crocus and its implementation in SURFEX v7.2. Geosci. Model Dev. 5 (3):773–791. http://dx.doi.org/10.5194/gmd-5-773-2012.
Wang, J.R., Choudhury, B.J., 1981. Remote sensing of soil moisture content, over bare field at 1.4 GHz frequency. J. Geophys. Res. 86 (C6):5277. http://dx.doi.org/10.1029/JC086iC06p05277.
Wegmüller, U., Mätzler, C., 1999. Rough bare soil reflectivity model. IEEE Trans. Geosci. Remote Sens. 37 (3):1391–1395. http://dx.doi.org/10.1109/36.763303.
Wiesmann, A., Mätzler, C., 1999. Microwave emission model of layered snowpacks. Remote Sens. Environ. 70 (3):307–316. http://dx.doi.org/10.1016/S0034-4257(99)00046-2.
Wiesmann, A., Mätzler, C., Weise, T., 1998. Radiometric and structural measurements of snow samples. Radio Sci. 33 (2), 273–289.
Wolff, M.A., Isaksen, K., Petersen-Overleir, A., Odemark, K., Reitan, T., Braekkan, R., 2015. Derivation of a new continuous adjustment function for correcting wind-induced loss of solid precipitation: results of a Norwegian field study. Hydrol. Earth Syst. Sci. 19 (2):951–967. http://dx.doi.org/10.5194/hess-19-951-2015.
Yang, D., 2014. Double fence intercomparison reference (DFIR) vs. bush gauge for "true" snowfall measurement. J. Hydrol. 509, 94–100.

FINNISH METEOROLOGICAL INSTITUTE
Erik Palménin aukio 1
P.O. Box 503
FI-00101 HELSINKI
tel. +358 29 539 1000
WWW.FMI.FI

FINNISH METEOROLOGICAL INSTITUTE
CONTRIBUTIONS No. 144
ISBN 978-952-336-050-1 (paperback)
ISSN 0782-6117
Erweko
Helsinki 2018

ISBN 978-952-336-051-8 (pdf)
Helsinki 2018